Princeton University

Department of Mechanical and Aerospace Engineering

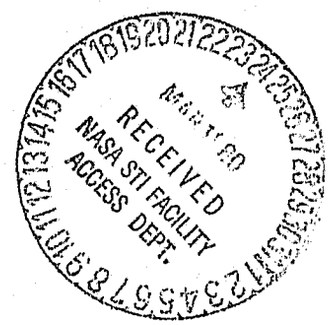

PRINCETON UNIVERSITY

DEPARTMENT OF MECANICAL AND AEROSPACE ENGINEERING

"RESONANT DOPPLER VELOCIMETER

Final Report

for

Grant NSG 1070

7-1-74 to 10-31-79

Principal Investigator: R. B. Miles

MAE Report No. T-1465

NASA/LANGLEY
Hampton, Virginia

RESONANT DOPPLER VELOCIMETER

Micha Zimmermann

A DISSERTATION

PRESENTED TO THE

FACULTY OF PRINCETON UNIVERSITY

IN CANDIDACY FOR THE DEGREE

OF DOCTOR OF PHILOSOPHY

RECOMMENDED FOR ACCEPTANCE BY THE

DEPARTMENT OF

MECHANICAL AND AEROSPACE ENGINEERING

March 1980

Abstract

The work presented in this thesis outlines the development of a new technique for visualization and for quantitative measurements of velocity, temperature and pressure of a gaseous flow. These are achieved by shining a single frequency laser beam into a flow which is seeded with an atomic species. The laser is tuned through the absorption frequencies of the seeded species and the absorption profile is detected by observing fluorescence as the atoms relax back to the ground state. The flow velocity is determined by observing the Doppler shift in the absorption frequency. Spectroscopic absorption line broadening mechanisms furnish information regarding the static temperature and pressure of the moving gas.

The primary motivation for the present study is the lack of an adequate diagnostic tool for high velocity flows. The technique is not limited to a particular flow density and is also nonintrusive since it does not introduce a local disturbance into the flow. Experiments have been conducted in the free stream and in the bow shock of a conical model mounted in a hypersonic wind tunnel. The results indicate that the experimental uncertainties in the measurement of average values for the velocity, temperature and pressure of the flow are 0.1, 5 and 10 percent respectively.

Acknowledgments

I would like to express my appreciation to the staff of the Gas Dynamics Laboratory. I especially wish to acknowledge my faculty advisor, Professor Miles, who started me on the course of my research, for his advice and assistance. John Thomas and Lou Pizzarello who went out of their way in extending their help to me. Bob Bogart who if he had eleven fingers instead of just ten might have been able to stop the twelfth leak in the helium system were he fast enough. Dr. Settles who transformed the Lab into a more livable environment. Finally the Gas Dynamics personnel, too numerous to mention, who turned my stay in the lab into a challenge. I would also like to thank Professor Bienkowski, Dr. Dolling, Professor Hama, Professor Kruger, Professor Lam, Professor Littman and Professor Smith. Assistance from Karen Praul in typing the manuscript is gratefully acknowledged.

This thesis carries the number T-1465 in the records of the Department of Mechanical and Aerospace Engineering.

Table of Contents

Page

Nomenclature

a	ratio of Lorentzian over Gaussian linewidths
$\tilde{a}$	speed of sound
A	area
A_J	magnetic hyperfine structure constant
b	impact parameter
B	magnetic field
B_J	electric quadrupole interaction constant
c	speed of light
c_p	specific heat at constant pressure
d	diameter
e	elementary charge
$\vec{E}$	electric field vector
g_i	degeneracy of level i
h	Planck's constant
$\hbar$	$= h/2\pi$
H	Hamiltonian
HWHM	half width at half maximum
I	intensity (power per unit solid angle)
j	total angular momentum quantum number
J	irradiance (power per unit area)
k	Boltzman's constant
$\vec{k}$	electromagnetic field propagation vector
Kn	Knudsen number
ℓ	length
ℓ	orbital angular momentum quantum number

L	total orbital angular momentum quantum number
m	mass of one atom
M	bulk mass
M	Mach number
n	index of refraction
n	number density
N_A	Avogadro's number
P	pressure
p	power
Q	quality factor
r	radius
R	universal gas constant
Re	Reynolds number
s	spin angular momentum quantum number
$\tilde{s}$	shift coefficient
S	total spin angular momentum quantum number
S^2	sample variance
t	time
T	temperature
u	velocity
v	voltage
V	volume
w	Gaussian beam waist diameter
W	atomic weight
x,y,z	cartesian coordinates
z	collision frequency
Z	atomic number

γ	ratio of specific heats
Γ	damping coefficient
δ_r	resonator losses
ϵ	permeativity
η	recovery ratio
Λ	mean free path
λ	wavelength
μ	mean value
μ	reduced mass
ν	frequency (Hertz)
ν	degrees of freedom
ρ	density
ρ_{mm}	density matrix element
σ_c	cross section
σ	standard deviation
σ^2	variance
ψ	wave function
ω	angular frequency (rad/sec)
Ω	solid angle

Chapter I

INTRODUCTION

The work presented in this thesis outlines the development of a new technique for visualization and for quantitative measurements of velocity, temperature and pressure of a gaseous flow. These are achieved by shining a single frequency laser beam into a flow which is seeded with an atomic species. The laser is tuned through the absorption frequencies of the seeded species and the absorption profile is detected by observing fluorescence as the atoms relax back to the ground state. The flow velocity is determined by observing the Doppler shift in the absorption frequency. Spectroscopic absorption line broadening mechanisms furnish information regarding the static temperature and pressure of the moving gas.

Traditional flow diagnostic techniques such as pitot probes, static pressure taps, total temperature probes, and hot wire anemometers introduce a disturbance at the measurement point in the fluid under investigation.[1] In contrast, the technique presented here does not introduce a probe into the flow and is therefore free of such local disturbances.

Laser induced fluorescence from dyes has been found useful for both flow visualization and quantitative studies in incompressible fluid flows.[2,3] For the gas phase, researchers have relied on electron beam fluorescence[4] and electric discharge induced fluorescence.[5] Of the two methods, electrom beam fluorescence has also given quantitative density,temperature[6] and velocity[7] information in low density gases. Index of refraction techniques[8] such as Schlieren, shadowgraph and interferometry have been applied to the gas phase for flow visualization and density measurements. Research is underway to extend these flow

visualization techniques to low density flows by using sodium vapor seeding to enhance the index of refraction.[9]

Tracer particles in a flowing gas have extensively been used in conjunction with the laser Doppler Velocimeter (LDV) in subsonic and transonic flows.[10] In the hypersonic regime, however, these particles tend to lose their ability to follow the flow. The "particle lag"[11] problem accentuates with increasing flow velocities and lower densities. To overcome this difficulty, smaller particles must be used. As the size of the particles decreases, however, their effectiveness as a light scatterer also decreases, thereby lowering the signal levels. The Resonant Doppler Velocimeter (RDV) technique presented in this thesis uses atomic size particles and therefore has virtually no particle lag problems. The RDV has been proposed by R. B. Miles[12] in 1975 and first demonstrated in 1977.[13]

Figure I.1 depicts the main features of the technique as applied to an idealized two level atom. When the laser frequency is tuned into the resonant absorption frequency in the frame of reference of the atoms, the atoms undergo an absorption process followed by fluorescence emission. The fluorescence signal is detected by a photomultiplier and recorded as a function of the laser frequency. The beam of the tunable laser is split in two directions. The lower beam in Figure I.1 perpendicularly intersects an atomic beam of sodium. As the laser is tuned, maximum absorption and therefore maximum fluorescence is observed from the atomic beam when the laser frequency equals the atom's rest frame absorption frequency. This is due to the fact that the atomic and laser beams are perpendicular so the atoms have zero average velocity in the direction of the laser beam. The upper beam in Figure I.1 intersects the seeded gas flow at an angle

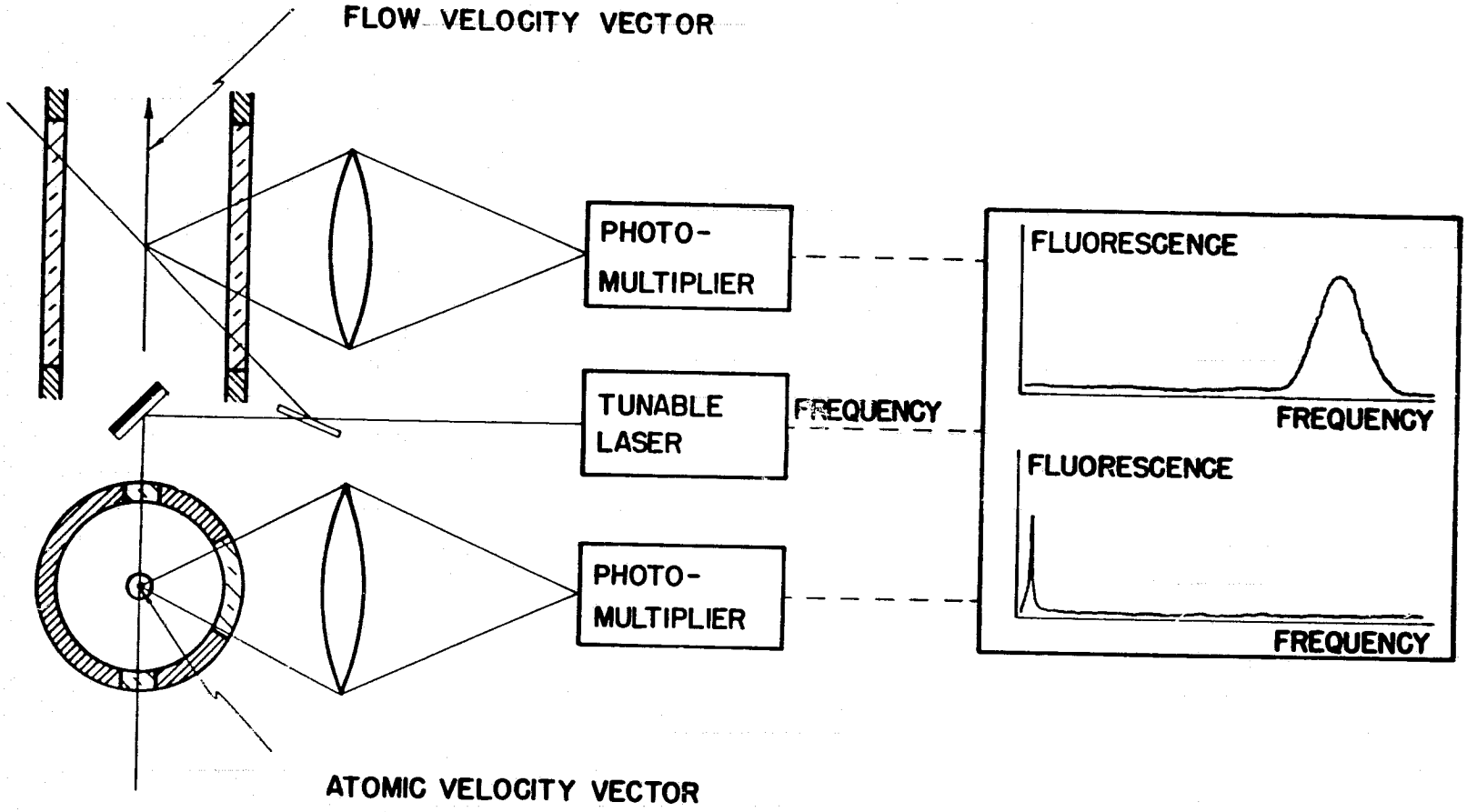
FLOW VELOCITY VECTOR
PHOTO-
MULTIPLIER
TUNABLE
LASER
FREQUENCY
PHOTO-
MULTIPLIER
FLUORESCENCE
FREQUENCY
FLUORESCENCE
FREQUENCY
ATOMIC VELOCITY VECTOR

Figure I.1

so that the fluorescence peak occurs at a different frequency due to the Doppler shifted absorption line center. A comparison of the two frequencies furnishes a quantitative value of the Doppler shift from which the velocity component of the flow along the laser beam may be determined.

An ensemble of two level atoms interact with an envelope of frequencies, an effect which is known as broadening of the spectral line. Various factors including temperature and pressure have a bearing on the broadening. Hence, the resolution of the different broadening components permits the determination of the static temperature and pressure of the flow.

Sodium is used as the seeded atomic species in this experiment for the reasons listed below. Sodium atoms possess two strongly absorbing line manifolds in the reddish-orange part of the spectrum.[14] These lines are so strong that number densities of several atoms per cubic centimeter have been detected in the laboratory.[15] Although sodium is not a two level atom, the structure of these lines is relatively uncomplicated simplifying the interpretation of the spectrum. The associated absorption frequencies are close to the frequency corresponding to the peak of the lasing range of the Rhodamine 6G dye laser pumped by the 5145 Å line of an argon ion laser.

The RDV technique has been demonstrated in helium flows since helium does not react with sodium and the quenching of sodium by helium is negligible.[16] Helium can also be expanded to very high Mach numbers from room temperature since it has a very low condensation temperature. This results in a low static temperature and pressure in the flow. Hence, the broadening is a small fraction of the Doppler shift, thereby enhancing the velocity measurement accuracy. The sodium follows the helium

flow well since it equilibrates thermally after only a few collisions.

Measurements of velocity, temperature, and pressure have been made in a free stream flow and in the vicinity of a model. The experimental components are described in Chapter II. Theoretical considerations presented in Chapter III are used to optimize the different operating parameters associated with the RDV and determine some of the limitations of the technique. The experimental results are presented in Chapter IV. Conclusions and suggestions for further study are discussed in Chapter V. The three sections of the appendix present a short discussion of atomic structure and broadening effects, statistical data analysis and the computer programs employed in the data reduction.

Chapter II

EXPERIMENTAL COMPONENTS

A. Introduction

The different elements included in the Resonant Doppler Velocimeter (RDV) experiment are presented in this chapter. The facility producing the hypersonic helium flow is described first (Section II.B). The pitot pressure and total temperature probe measurements are included in the same section. The measurements resulting from these classical flow diagnostic tools are compared to those obtained from the RDV in Chapter IV. The design of the atomic beam device and the factors affecting its performance are presented in the following section (Section II.C). The sodium seeding apparatus is described next (Section II.D). The optics employed in the experiment including the procedure for tuning the dye laser frequency to the sodium absorption frequency and monitoring its frequency stability are then discussed (Section II.E). The computer data acquisition scheme is presented in the final section (Section II.F).

B. Test Facility

1. Tunnel

The hypersonic helium flow investigated in this study was generated at Princeton University's six inch (0.152 m) diameter hypersonic facility, He3, located within the Gas Dynamics Laboratory. A constant stagnation temperature was maintained by passing the test gas through a 61 m coil of room temperature steel pipe upstream of the stagnation chamber. The helium was then expanded through a converging diverging nozzle which was contoured to provide a uniform free stream flow over the core region of the axisymmetric tunnel. All the data reported in this study were obtained at the set of operating conditions listed below.

P^t = 225±1 psi (1550±7 KPa) T^t = 295°±1°K

where P^t is the stagnation pressure and T^t is the stagnation temperature.

All measurements were made at one axial location in the test section, at a position 0.900±0.003 m downstream of the nozzle throat or 0.216±0.001 m from the end of the nozzle. This position will henceforth be referred to as the measuring station. The various classical and spectroscopic data scans were taken across the wind tunnel diameter. The test section diameter at that point was 0.151±0.001 m. The free stream conditions, listed below, were determined from pitot pressure, stagnation pressure and temperature and the assumption of the isentropic expansion of a perfect gas.

M	$n(1/m^3)$	T(°K)	P(torr, Pa)	u(m/sec)	$Re/\ell(1/m)$
13.8	7.5×10^{23}	4.55	0.34, 46	1736	8.5×10^{6}

M is the Mach number, n is the number density, T is the static temperature, P is the static pressure, u is the velocity and Re/ℓ is the Reynolds number per unit length. The run time of six minutes was limited by the steam ejector pumping system.

2. Pressure Measurements

During a run the stagnation pressure was monitored using a 500 psi Heise gauge graduated in 1 psi increments. It was held at 225 psi (1550 KPa). The static wall pressure in the plenum chamber 0.61±0.1 m downstream of the measuring station was monitored by a 800 torr Pennwalt (Wallace and Tiernan Division) Model FA160 gauge graduated in 5 torr increments. Both gauges are of the Bourdon tube type.

Pitot pressure surveys were made at the measuring station with two pitot probes. For free stream measurements, a probe with a circular cross section was used. The inside diameter of the tube was 0.023 (0.58 mm) and the outside diameter was 1/32" (0.79 mm). The tip had the shape of an inverted truncated cone with a 10° half angle. Surveys with a model installed in the test section on the tunnel axis were made with a pitot probe flattened to 1.0±0.2 mm external height and having an opening of 0.1±0.05 mm.

Two Pace transducers, of the reluctance type, with a range of 5 and 15 psi were used to monitor the pitot pressure. They were referenced to vacuum and calibrated using a mercury filled U tube manometer. The accuracy of the pitot pressure reading was 0.04 psi (270 Pa).

3. Temperature Measurement

The wall temperature was measured 0.09±0.003 m upstream of the survey station using 20 gauge chromed alumel thermocouple wires fastened to the tunnel wall through a brass plug. The stagnation temperature was monitored with a model CASS-18G-12 Omega thermocouple. Both thermocouples used an ice reference. The voltages of the wall and stagnation chamber thermocouples were read by a Hewlett Packard model 425 AR and model 413 AR multimeters. These voltmeters have a recorder output through which the temperatures

were monitored with the computer throughout the run (Section II.F).

A 0.005 inch (0.127 mm) diameter chromel/alumel thermocouple wire was used to measure the total temperature along a line extending from the wind tunnel wall into the core region. The spotwelded thermocouple junction was ground down to ensure that the wire, positioned perpendicular to the flow direction, would be of uniform diameter. This is a prerequisite for the unambiguous determination of the total temperature through the recovery ratio. The recovery ratio, η, is defined by[17]

$$\eta = \frac{T_{aw} - T}{T^t - T} \qquad \text{II.1}$$

where T is the static temperature, T^t is the stagnation temperature and T_{aw} is the adiabatic wall temperature. In the continuum flow regime the value of the adiabatic wall temperature falls between T and T^t. The temperature assumed by an insulated wall, past which flows a high speed gas stream, is controlled by physical phenomena in the boundary layer. Fluid layers far from the wall deliver viscous shear work to layers near the wall. The consequent temperature rise of the inner layer is necessarily accompanied by heat conduction away from the wall, thus tending to limit the temperature rise.[18]

The temperature at the thermocouple junction is relatively unaffected by end losses (heat conduction to the prongs supporting the wire) for large enough values of the L/D ratio where L is the wire length and D its diameter (in the present work it is equal to 30). The supporting prongs were 0.005 inch in diameter which is smaller than is commonly used, reducing the end losses even further. Hence it is reasonable to assume that the temperature measured by the thermocouple is the adiabatic wall temperature.

The recovery ratio is a function of the Knudsen number and in the hypersonic regime is independent of the Mach number.[19]

The nondimensional Knudsen number is defined by

$$Kn = \frac{\Lambda}{D} \qquad \text{II.2}$$

where Λ is the mean free path and D is the dimension of interest, the thermocouple wire diameter.

From kinetic theory, the viscosity, μ, is dependent on the mean free path[20]

$$\mu = \beta_\mu \rho \bar{u} \Lambda \qquad \text{II.3}$$

where ρ is the density, $\beta_\mu = 0.5$[20] and the average atomic speed is[20]

$$\bar{u} = \sqrt{\frac{8kT}{\pi m}} \qquad \text{II.4}$$

where k is the Boltzman's constant, T is the static gas temperature and m is the mass of one atom. By substituting equations II.3 and II.4 into II.2 one obtains

$$K_n = \sqrt{\frac{\pi\gamma}{2}} \frac{M}{Re} \qquad \text{II.5}$$

where γ is the ratio of specific heats and M and Re are the Mach and Reynolds numbers respectively. These results are used in Chapter IV to interpret the total temperature surveys.

C. Atomic Beam Device

An atomic beam device is used to create a directed beam of collision free particles. In the present experimental work it is used as a frequency reference. According to kinetic theory, the motion of an atom in a gas may be regarded as purely random and is accompanied by continual collisions of the atoms with each other and any surfaces present. Between collisions the atoms describe straight paths with uniform velocities which are distributed according to Maxwell's law. Corresponding to the average velocity there exists a mean free path Λ which is inversely proportional to gas pressure.

If a circular aperture with diameter less than Λ connects a gas filled vessel, with a highly evacuated chamber, the atoms colliding within one mean free path from the aperture and having velocity vectors directed towards the aperture will have a high probability of escaping into the evacuated region. The atoms then continue in straight paths, filling a solid angle which is determined by the collimating properties of the aperture.[22] The atoms which pass through a second aperture downstream of the first are constrained to move along nearly parallel paths defined by the two apertures and the distance between them. This forms an almost collisionless beam of atoms. Collisions in the highly evacuated regions occur only in those rare occasions when faster atoms overtake slower ones travelling along the same path.

The velocities of the atoms in the beam depend on the temperature of the source. Their distribution is not quite Maxwellian since the method of beam formation favours faster atoms. This is due to the fact that collisions taking place in and near the source aperture must be taken into account even when the mean free path in the source is considerably greater

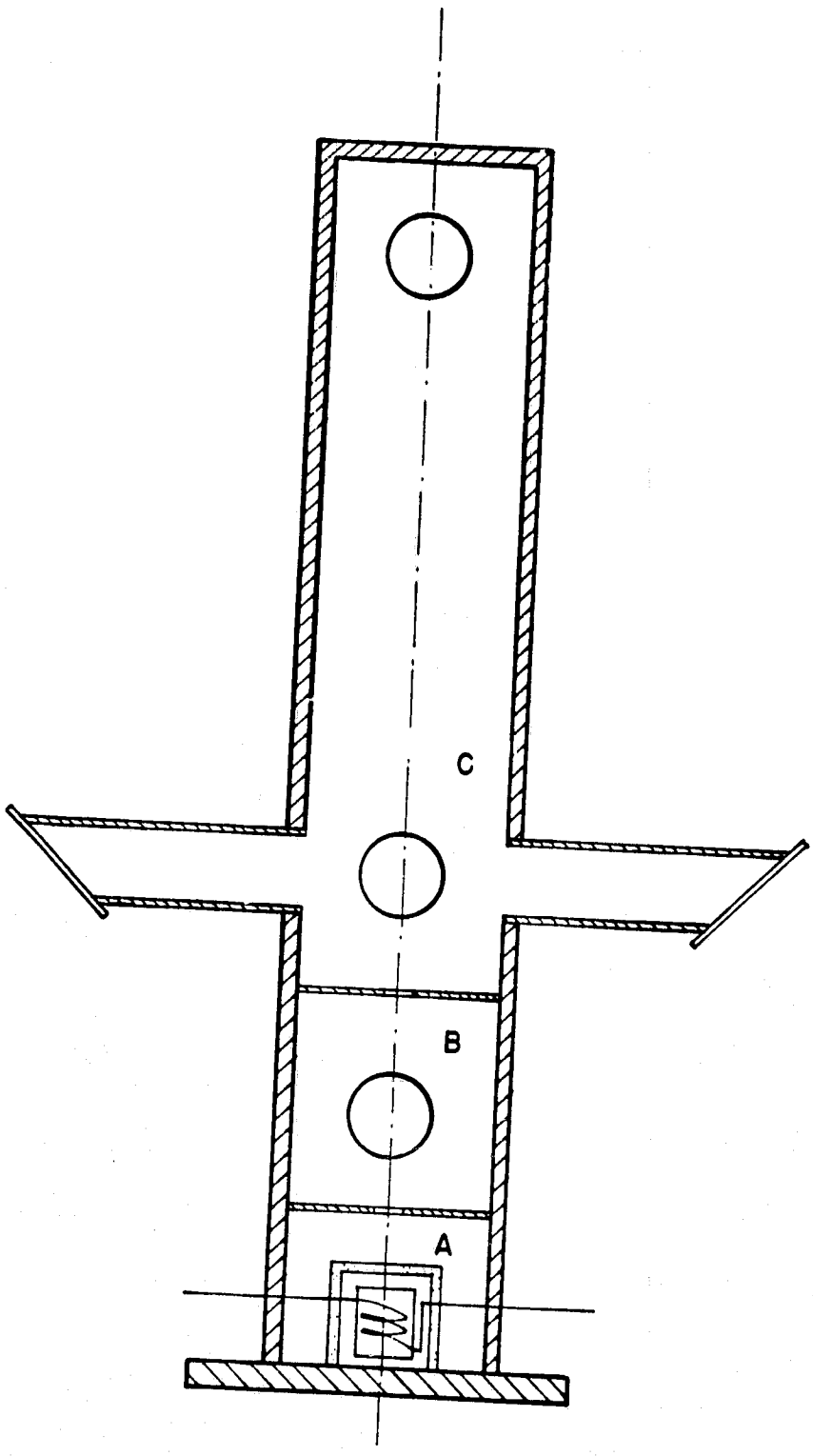

Figure II.1

than the aperture size. The probability of loss of atoms from the beam by this mechanism increases rapidly as the atomic velocity becomes less than the most probable velocity of the atoms in the source. This accounts for most of the low velocity deficiency.[23] The agreement between the Maxwellian and the experimental velocity distribution is quite good for velocities above the most probable velocity.

Figure II.1 is a schematic of the apparatus employed in the present study. Sodium metal contained in a quartz crucible is placed in a tungsten basket. A current applied to the basket heats the sodium to about 180°C. The temperature is monitored by a chromel/alumel thermocouple in physical contact with the crucible. The vaporized sodium atoms leave the surface in all directions, some of them reaching the bottom aperture. The top aperture produces a collimated beam in the test section. This atomic beam is intersected perpendicularly by the dye laser beam entering and exiting the device through Brewster angle windows. The detection optics are positioned perpendicularly to both the laser and atomic beam. A lens images the fluorescence signal onto a thermo-electrically cooled (Product for Research Model TE-104) RCA Model C31034 photomultiplier tube as depicted in Figure II.2.

Chambers B and C are evacuated by a Vactronic Econovac model 20 diffusion pump through ports welded to the walls of the device. Each vacuum line is immersed in a liquid nitrogen cold trap before joining at the pump. This prevents the circulation of sodium atoms between the chambers and enhances the vacuum by nearly an order of magnitude. The pressure recorded by a Vectronix model LDG-266 cold cathode gauge was 5×10^{-7} torr (7×10^{-5} Pa) at the pump's inlet port. The pressure in Chamber B, monitored with a Norton Vacuum Equipment model NRC 831 ion gauge using a NRC 507 tube

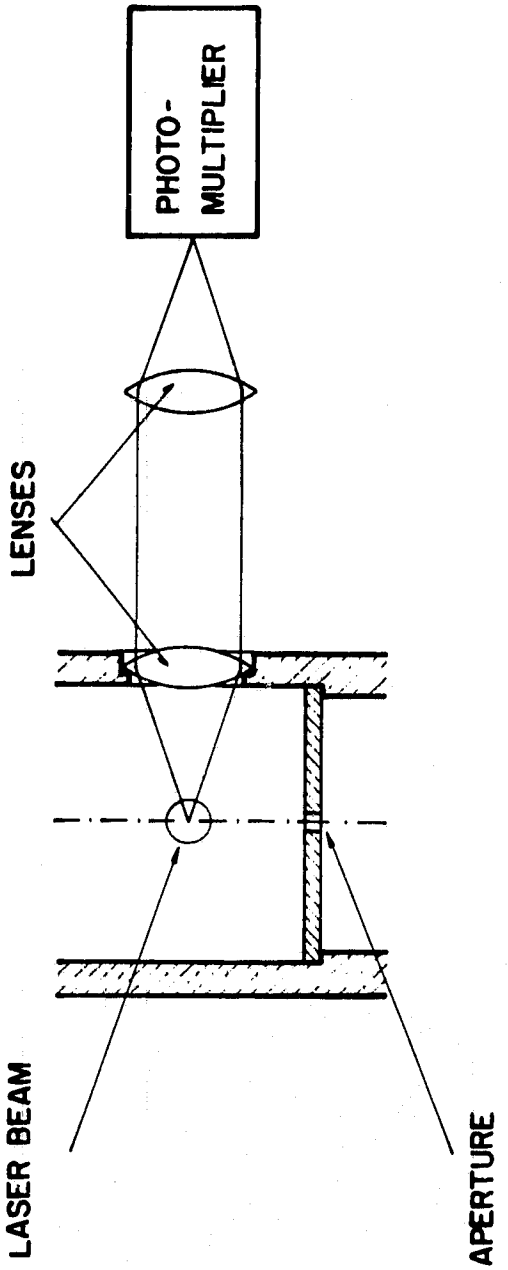

Figure II.2

was 10^{-6} to 10^{-5} torr (10^{-4} to 10^{-3} Pa). These pressure readings were taken with the sodium source at the operating temperature. At 180°C the vapor pressure of sodium is about 10^{-4} torr (10^{-2} Pa).[44] This corresponds to a mean free path Λ of[20]

$$\Lambda = \frac{1}{\sqrt{2}\pi d^2 n} = \frac{1}{\sqrt{2}\sigma_c n} = 3.5 \text{ cm} \qquad \text{II.6}$$

where $\sigma_c = 10^{-13}$ cm^2 [24] is the elastic collision cross section for a sodium sodium collision and n is the number density. (The helium-sodium collision cross section is one order of magnitude smaller.) As the distance from the crucible to the aperture is 22 mm and the diameter of the bottom aperture is 0.030" (0.76 mm) the majority of the sodium atoms leave chamber A without undergoing a collision. This insures some directionality to the beam in B and enhances its intensity. In B, at a pressure of 5×10^{-6} torr (7×10^{-4} Pa), the mean free path is of the order of 400 cm, which is appreciably longer than the upper aperture diameter of 0.020" (0.5 mm) and the distance to the observation region of 3.2 cm. These design conditions lower the probability of a collision taking place in the probe volume. The atomic beam possesses some divergence due to the finite dimension of the apertures and their separation. The maximum divergence angle α for a non-colliding atom is

$$\alpha = \tan^{-1}[(d_1+d_2)/\ell] \qquad \text{II.7}$$

where d_1, d_2 and ℓ are the lower and upper aperture diameters and their separation respectively. For a separation of ℓ = 8.6 cm the angle is α = 50'56". At worst this would correspond to a broadening half width half maximum (HWHM), $\Delta\nu$, of

$$\Delta\nu = \nu_{21}\frac{\bar{u}}{c}\sin\alpha = \sqrt{\frac{8kT}{\pi m}}\ \frac{\nu_{21}\sin\alpha}{c} \qquad \text{II.8}$$

where ν_{21} is the stationary absorption frequency, $\bar{u}$ and m are the sodium atom thermal velocity and mass respectively. c is the speed of light and T the temperature of the source. For a source temperature of 180°C and the sodium transition wavelength of 589 nm one obtains a HWHM of 16 MHz.

A HWHM of 10 MHz is obtained from the spectrum of the sodium line corresponding to the 589 nm wavelength. The natural and laser HWHM are 5 MHz each. Their sum is 10 MHz which equals the experimental width obtained from the atomic beam device spectra. To sum the natural and laser linewidths is a simplification which is not rigorously correct due to the fact that the laser linewidth is not Lorentzian (Section IV.4, Appendix A). Since the sum of the natural and laser linewidth equals the linewidth obtained from the spectra of the atomic beam device it is clear that the broadening contribution due an uncollimated atomic beam with an upper bound calculated by using equation II.8, is negligible. If the laser beam does not intersect the atomic beam perpendicularly, a frequency shift and additional broadening takes place. This is due to the fact that the atoms have a velocity distribution along the atomic beam. The broadening effect is negligible for small deviations from 90° but the resulting Doppler shift of the central absorption frequency has to be taken into account for velocity measurements (Section IV.B.3).

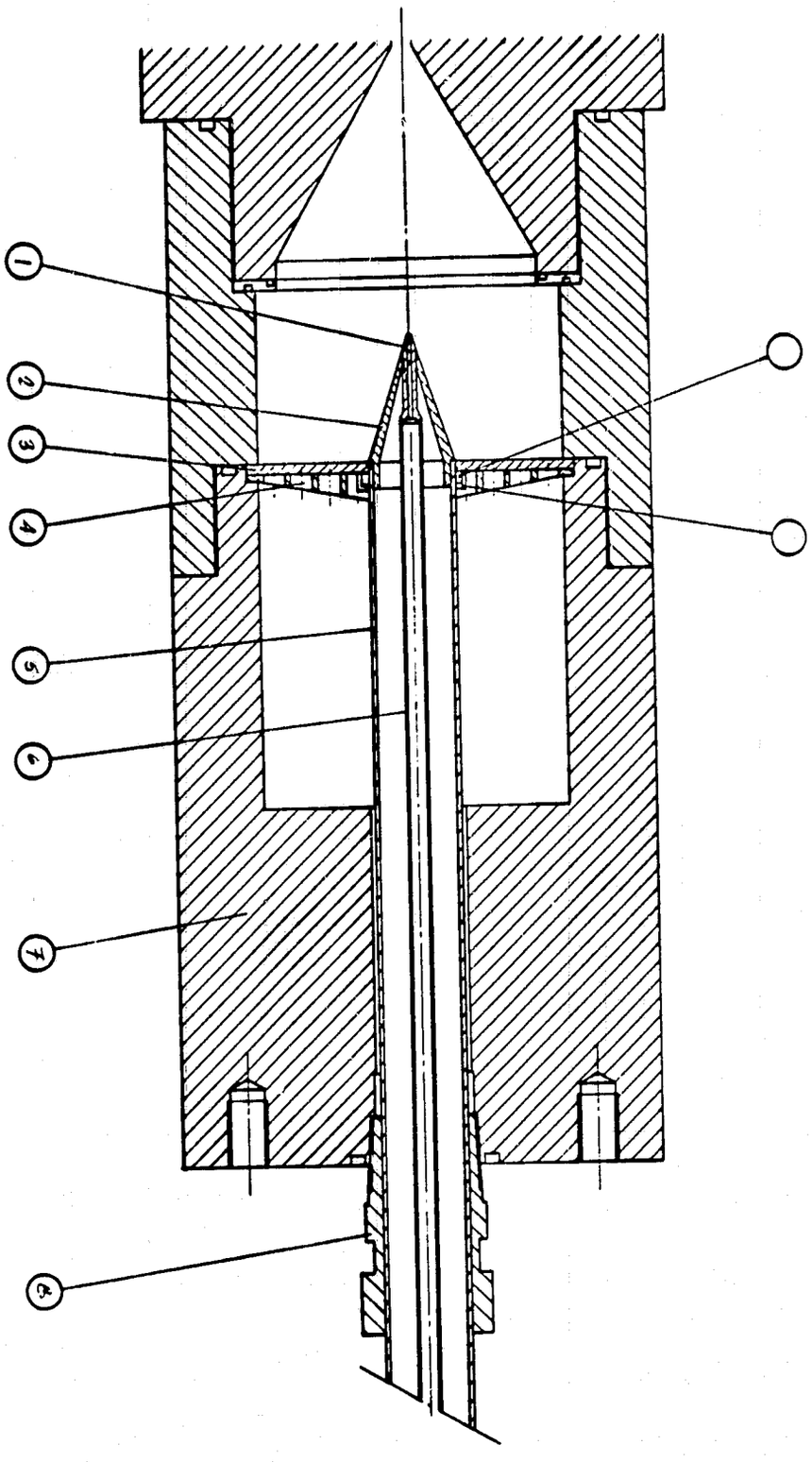

Figure II.3

D. Tunnel Seeding Apparatus

To facilitate seeding the flow through the stagnation chamber at high pressure the apparatus shown in Figures II.3 and II.4 was devised. A small amount of purge helium is used to produce a hot helium sodium mixture which is then seeded into the main helium supply. The oven is maintained external to the small stagnation chamber with only a needle penetrating into it.

The helium purge supply is preheated while passing through a 1/4" stainless steel coiled tube of 0.35" wall thickness (part 23) and then flows into the oven. In the oven the hot helium gas is forced to sweep very close to the sodium contained inside a quartz crucible (part 37). It therefore mixes with the sodium vapor and the mixture then flows towards the nozzle through the inner needle (part 6). This is a stainless steel 1/4" tube of 0.02" wall thickness which again is resistively heated.

The oven constitutes a heat sink as it contains a relatively large amount of metal. Due to its surface area it loses heat to the surroundings. To compensate for the above two losses an additional, independently powered, heating element (part 18) is installed inside the oven around the crucible containing the sodium.

The resistance of all heating elements are calculated so as to utilize the maximum power capability of the power supplies. A Mallory type VA-6000 DC power supply capable of 9600 watts at 48v is used for the coil. A Harrison Laboratory model 810-A capable of 450 watts at 60 volts DC and a Varian model 927-007 with a power output of 3 KVA at 20 volts AC are used to heat the oven and needle respectively. Figure II.5 is a schematic of the power and helium supplies. The voltage to the coil is applied between parts 26 and 45. The voltage to the inner needle is applied between parts 45 and ground. The outside jacket (part 22) is insulated electrically from

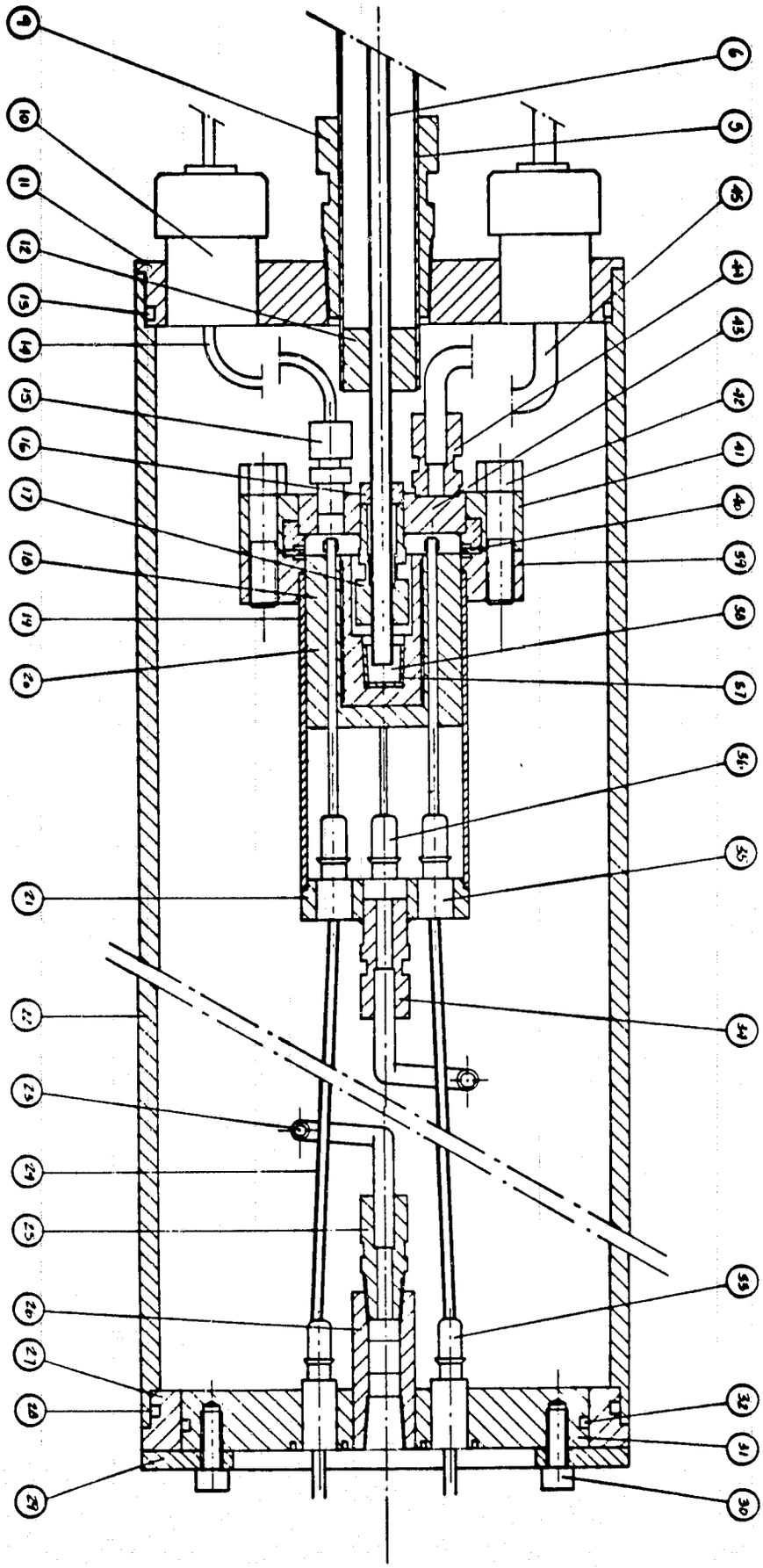

Figure II.4

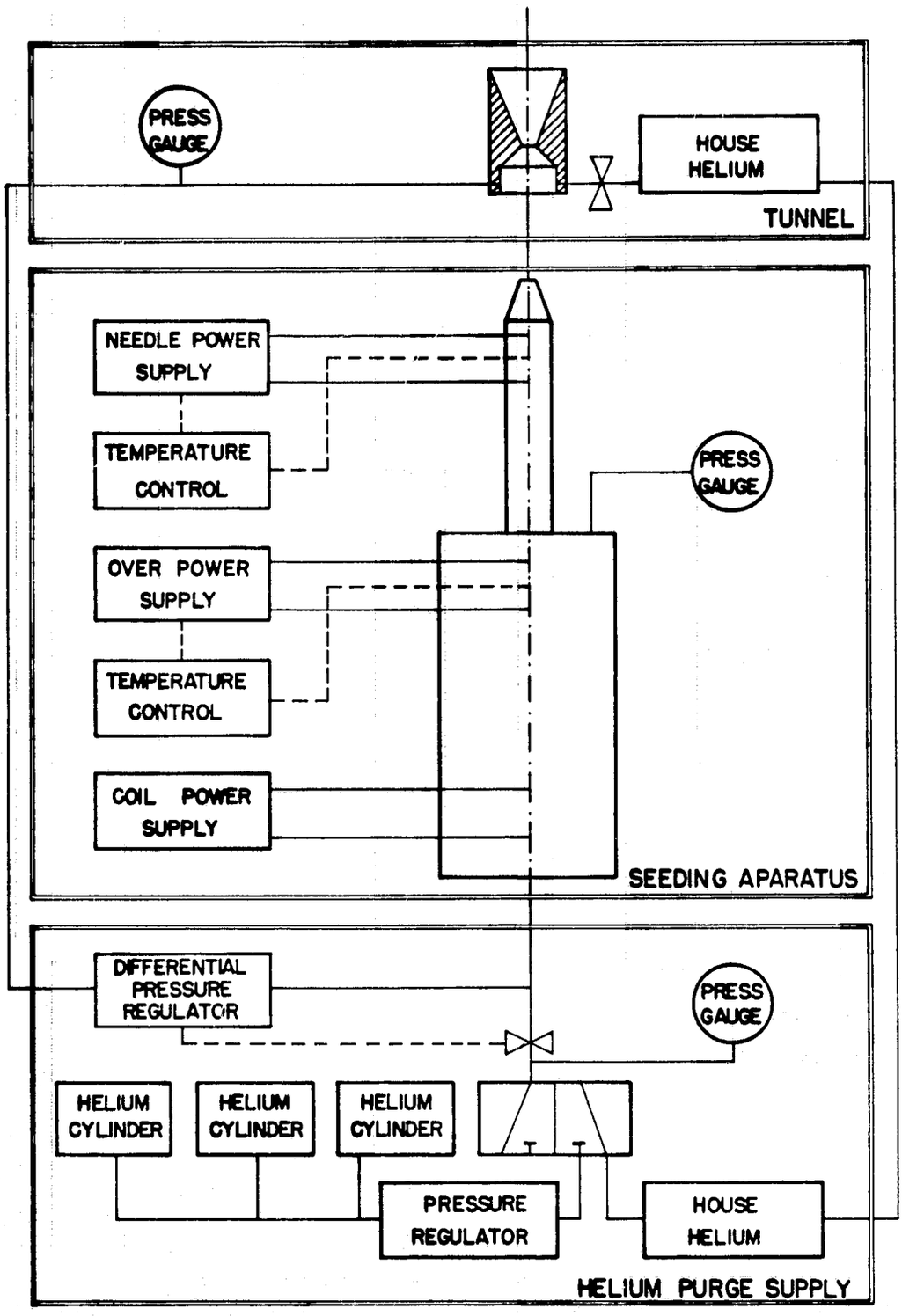
PRESS GAUGE
HOUSE HELIUM
TUNNEL
NEEDLE POWER SUPPLY
TEMPERATURE CONTROL
PRESS GAUGE
OVER POWER SUPPLY
TEMPERATURE CONTROL
COIL POWER SUPPLY
SEEDING APARATUS
DIFFERENTIAL PRESSURE REGULATOR
PRESS GAUGE
HELIUM CYLINDER
HELIUM CYLINDER
HELIUM CYLINDER
PRESSURE REGULATOR
HOUSE HELIUM
HELIUM PURGE SUPPLY

Figure II.5

the resistively heated elements by an electrical insulator (part 27). Thermal insulation is provided by the evacuated chamber between the inner and outer needles (parts 6, 5) and between the oven and coil assembly and the cylinder (part 22). The pressure inside the oven is monitored by a 500 psi Heise gauge of the Bourdon type graduated in one psi increments. It is maintained at 25 psi (0.17 MPa) above the stagnation pressure using a differential pressure regulator with a range of zero to 90 psi.

The temperatures of the preheated helium, of the bottom of the sodium crucible and of the needle are all monitored by chormel/alumel thermocouples. Two junctions are attached to the inner needle, one at about 25 mm from the tip on part 1 and the other at 5 cm from the tip on part 6. The oven thermocouple is operated in conjunction with an Omega model 50K on/off temperature controller with a 0-600°C range at 5°C increments. The thermocouple junction fastened to the 1/4" (0.0635 m) stainless steel needle (part 6) is connected to a Wheelco model 401C on/off temperature controller with a 0-1000°C range at 10°C increments. The purge flow is obtained from industrial grade helium delivered in bottles.

The tunnel starting procedure consists of several steps. First, the helium purge flow through the sodium loaded oven is established while the tunnel is evacuated by a 40 CFM Stokes pump. The power supplies to the seeding device are turned on until fluorescence is observed in the test section. At this stage the tunnel is started by gradually raising the stagnation pressure. The pressure in the oven increases simultaneously, controlled by the differential pressure regulator. Due to the large amount of the main helium flow through the stagnation chamber when the tunnel is operating, additional power has to be supplied to the seeding device to compensate for the convective heat losses.

During a run, the needle tip is maintained at approximately 700°C while the oven temperature is set to 250°C. It was found that the preheating coil does not have to be energized at all since enough heat is available from the other heated components. To determine the helium purge mass flow rate through the oven, the pressure drop in one of the supply cylinders is monitored as a function of time. If internal leaks in the pressure regulator are neglected then the mass flow rate, $\dot{M}$, is

$$\dot{M} = \frac{\Delta M}{\Delta t} = \frac{WV}{RT}\ \frac{\Delta P}{\Delta t} \qquad \text{II.9}$$

where M and W are the mass and atomic weight of sodium respectively, V and T are the cylinder volume and temperature, ΔP is the pressure drop in time Δt in the cylinder and R is the universal gas constant. For the seeding device injecting into vacuum, $\dot{M} = 4.3\text{x}10^{-5}$ Kgm/sec. When the tunnel is operating, $\dot{M} = 3.1\text{x}10^{-4}$ Kgm/sec. The difference is due to the fact that the needle tip is located inside the converging part of the nozzle and senses a pressure which is lower than the stagnation pressure when the tunnel is operating. This raises the flow rate through the oven.

To enhance the signal to noise ratio for the collection optics focused into the flow, the sodium density should be as high as possible. The limit, imposed by radiation trapping considerations is $8.2\text{x}10^{7}$ atoms/cc if one demands $K_\omega L = 0.1$ as determined in Chapter III. Clearly

$$\frac{\dot{M}_{Na}}{\dot{M}_{He}} = \frac{n_{Na} m_{Na}}{n_{He} m_{He}} \qquad \text{II.10}$$

where M is the total mass, n the number density and m is the mass of one atom. The helium number density is

$$n_{He} = 2.69\text{x}10^{19}\ \frac{P/P_o}{T/T_o}\ \frac{\text{atoms}}{\text{cc}} = 7.5\text{x}10^{17}\ \frac{\text{atoms}}{\text{cc}} \qquad \text{II.11}$$

where T_o = 273.15°K and P_o = 760 torr (1.013×10^5 Pa). T and P refer to the temperature and pressure in the test section. The mass flow in the tunnel is 0.0462 Kgm/sec based on the isentropic flow assumption and the physical throat area of the nozzle. Hence, the sodium mass flow rate equals 2.9×10^{-11} Kgm/sec. The above calculation assumes a uniform helium density across the test section and uniform mixing of the sodium atoms in the helium flow. Thus one obtains a seeding ratio of 6.3×10^{-4} parts per million on a mass basis.

E. Optics

A Spectra Physics model 580 single frequency tunable dye laser is pumped by a Coherent Radiation model 53A Argon ion laser. The pump laser is rated at 2.5 watts output at 5145 Å. At 1 watt input, the dye laser output ranges from 30 to 70 milliwatts, dependent on the quality of the alignment. A schematic of the setup is depicted in Figure II.6.

The output beam is split in several directions. The Spex 1700 Czerny-Turner monochromator is used for coarse wavelength adjustments. The obtainable resolution according to the manufacturer is 0.1 Å or 10 GHz at the sodium line corresponding to the 589 nm wavelength. A sealed pyrex ampule containing sodium metal under vacuum is used for finer wavelength adjustments. The cell is heated to raise the atomic vapor pressure. The resolution is determined by the linewidth of the sodium absorption profile in the cell. In this case the temperature broadening predominates and at 150°C one obtains a HWHM of 782 MHz. The sum of twice the HWHM plus the ground state hyperfine splitting provides a resolution of about 3.5 GHz. As the dye laser is capable of a 4 GHz linear frequency scan, it is relatively easy to find the sodium lines in the atomic beam device once fluorescence in the sodium cell has been observed. The longitudinal modes and frequency stability of the dye laser are monitored by a Jodon model SA-1500 confocal spectrum analyzer with a free spectral range of 1500 MHz and a linewidth of 7 MHz. A photodetector measures the laser intensity to record laser intensity fluctuations during a scan so that these may be removed during the data processing stage.

One of the beams is directed into the sodium seeded tunnel. The fluorescence signal from the seeded atoms is picked up by an EMI type 95745 photomultiplier tube. Fgure II.7 is a schematic of the tunnel collection

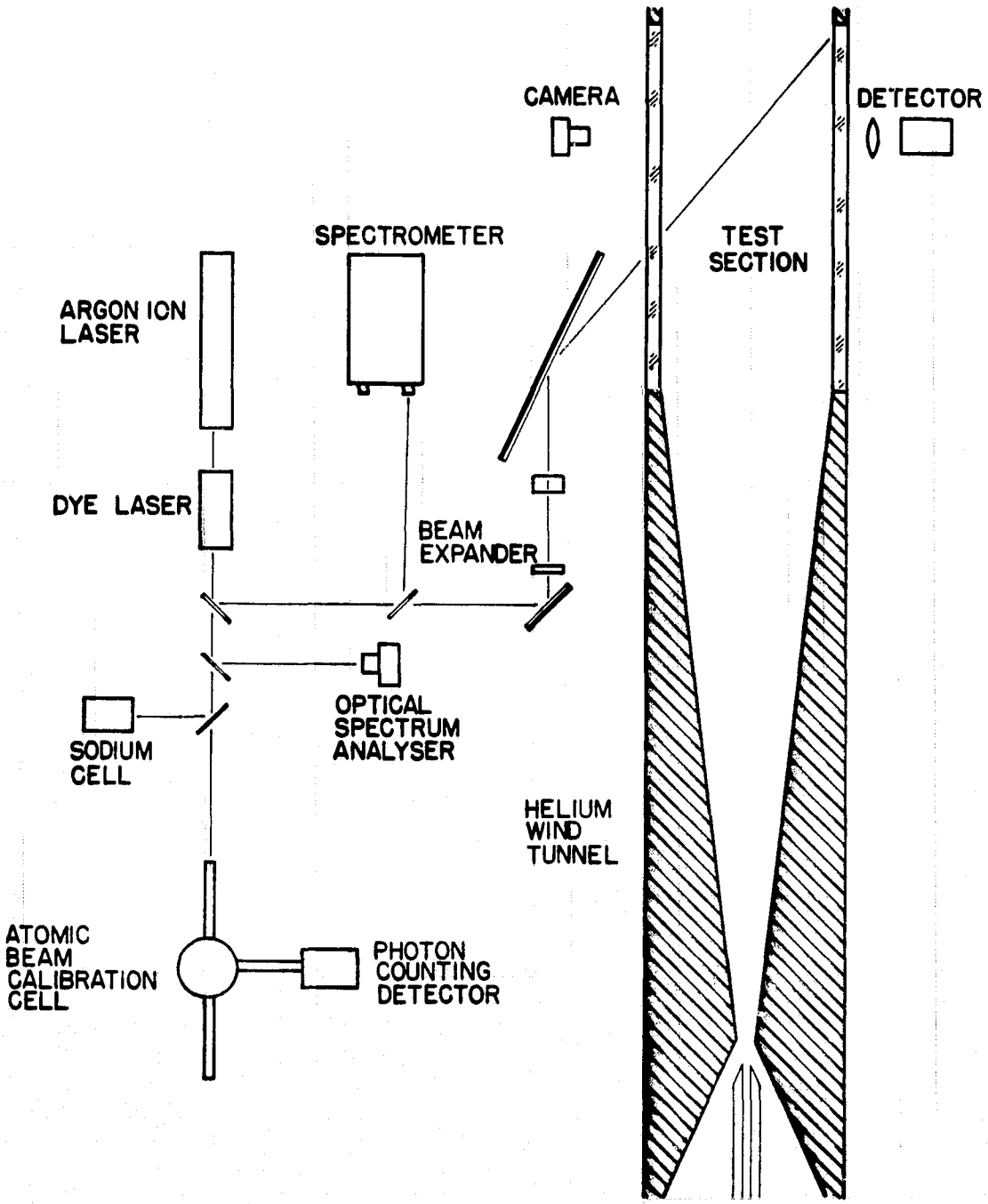
CAMERA
DETECTOR
SPECTROMETER
TEST SECTION
ARGON ION LASER
DYE LASER
BEAM EXPANDER
OPTICAL SPECTRUM ANALYSER
SODIUM CELL
HELIUM WIND TUNNEL
ATOMIC BEAM CALIBRATION CELL
PHOTON COUNTING DETECTOR

Figure II.6

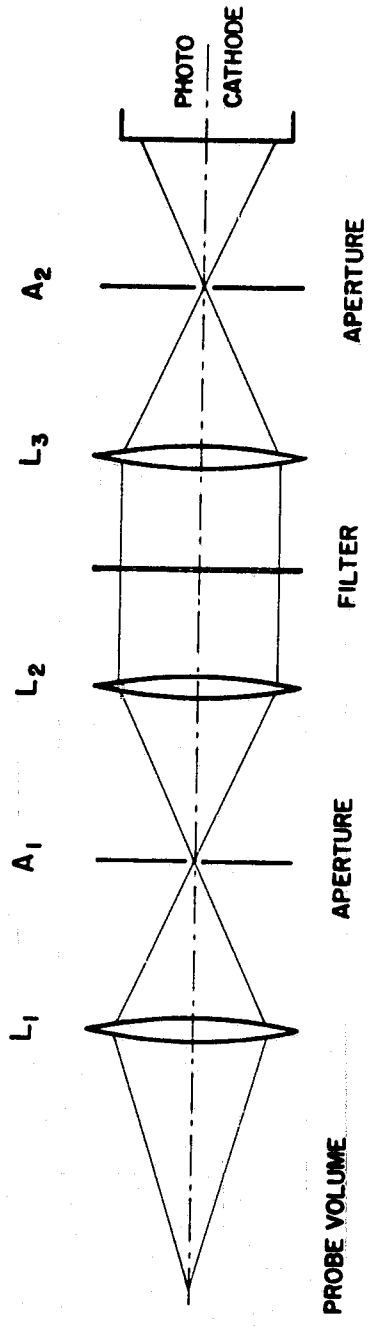
PHOTO
CATHODE
A_2
APERTURE
L_3
FILTER
L_2
A_1
APERTURE
L_1
PROBE VOLUME

Figure II.7

optics. L_1 is a 113 mm focal length, 53.3 mm diameter lens. The distances from the probe volume at the measuring station to L_1 and from L_1 to the 0.0135" (0.34 mm) diameter aperture A_1 are 22.2 and 23.2 cm respectively.

The detection acceptance solid angle is defined by

$$\Omega = \int_0^{\theta} \sin\theta d\theta \int_0^{2\pi} d\phi = 2\pi(1-\cos\theta) \qquad \text{II.12}$$

where

$$\tan\theta = \frac{\text{diameter of } L_1}{2x(\text{distance from probe volume to } L_1)} = \tan(6°50'43") \qquad \text{II.13}$$

The collection efficiency, $\Omega/4\pi$, equals 3.6×10^{-3}. The probe volume at the measuring station is 1.8×10^{-4} cm^3 for a laser beam perpendicular to the collection optics axis. This volume is defined by the laser beam radius at the e^{-1} points and the collecting aperture diameter, A_1. The two lenses between the aperture A_1 and the photomultiplier tube were matched so as not to degrade the collection efficiency of L_1. These lenses were employed to enable the use of an interference filter as depicted in Figure II.7.

The collection optics are mounted on an xyz translator. The laser beam position relative to that of the probe volume inside the tunnel defined by the aperture A_1 is kept constant by passing it through a mirror sequence as depicted in Figure II.8. Since the beam enters each translation stage parallel to its direction of movement, the following stage does not perceive any change in beam orientation. All the data presented in this experimental work was obtained using the xyz translator. Another possible configuration would be to expand the beam into a sheet of light and scan the position of the detection optics only. The disadvantage of this method is that while the signal is collected from the probe volume only, scattered light is contributed by the whole width of the beam.

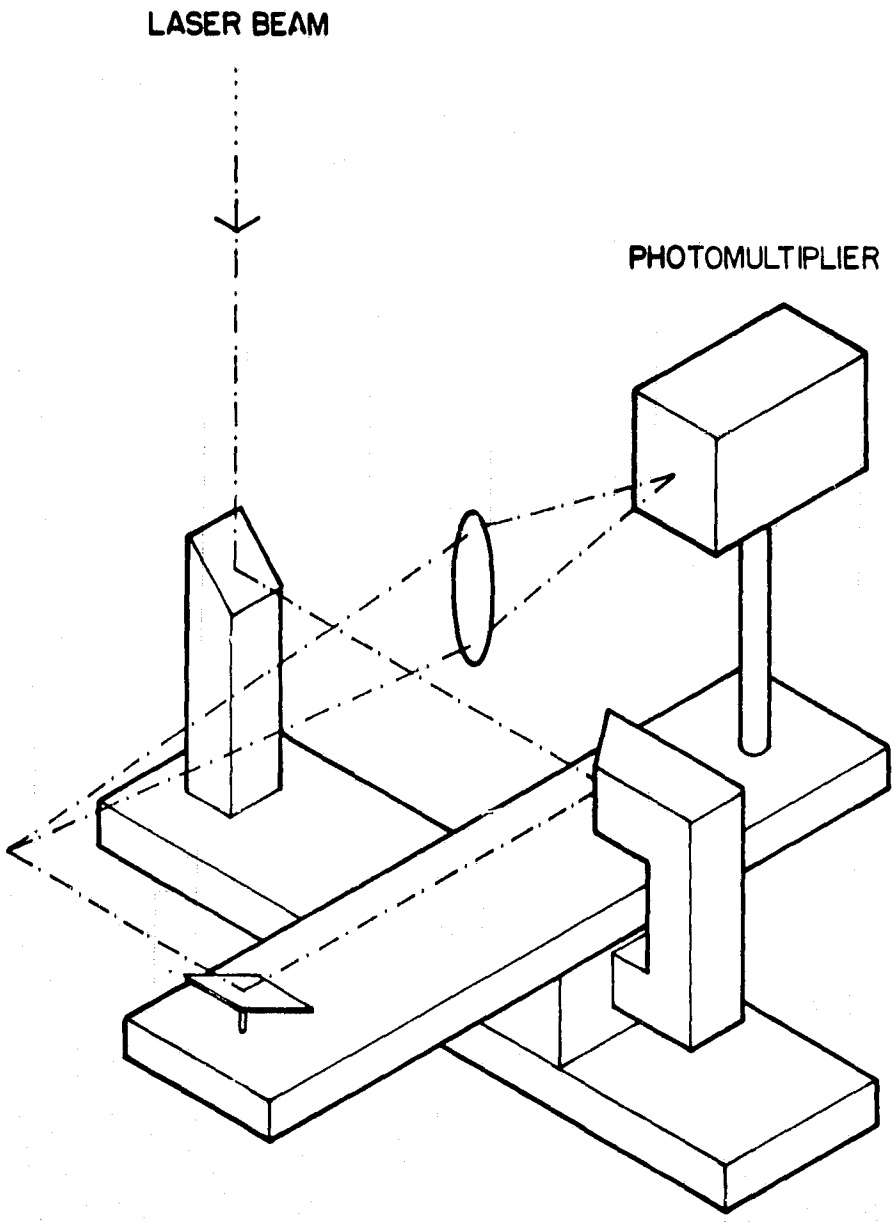

Figure II.8

F. Data Acquisition Scheme

A Hewlett-Packard 1000 16 bit minicomputer is incorporated into the experiment for data acquisition as shown in Figure II.9. Two A/D converters are used since all the data are in analogue form. A four channel 12 bit Preston model GMAD/1 with a variable sampling rate of 330 to 500,000 Hz for all channels is used to measure four inputs: the dye laser frequency scanning voltage ramp; the signals out of the two photomultipliers used to monitor the fluorescence intensities from the atomic beam device and the tunnel; and the output of the photodetector used to probe the laser intensity. The data from the set of four inputs are read simultaneously within a window of 10 nsec. A thousand points per channel at a rate of 330/4 Hz are obtained per laser frequency scan. Due to nonlinearities in the electronics producing the high voltage ramp driving the dye laser frequency scan, one obtains only about 600 useful points per channel. Hence the scan time is 7.3 sec.

Three additional channels are connected to the 14 bit Preston model GMAD/4 A/D converter which has a fixed total sampling rate of 1750 Hz and can read up to 64 channels sequentially. The inputs are the tunnel stagnation temperature, the test section wall temperature and the position along one axis of the xyz collection optics translator. The axis chosen determines the position of the probe volume along the tunnel diameter.

The input range of both A/D converters is ±10 v. Hence, to take advantage of the full resolution of these instruments, the weaker signals are passed through D.C. amplifiers. A Princeton Applied Research model 113 preamplifier is used for the laser intensity and two Dymec amplifiers model 2460A are used for the two photomultiplier signals.

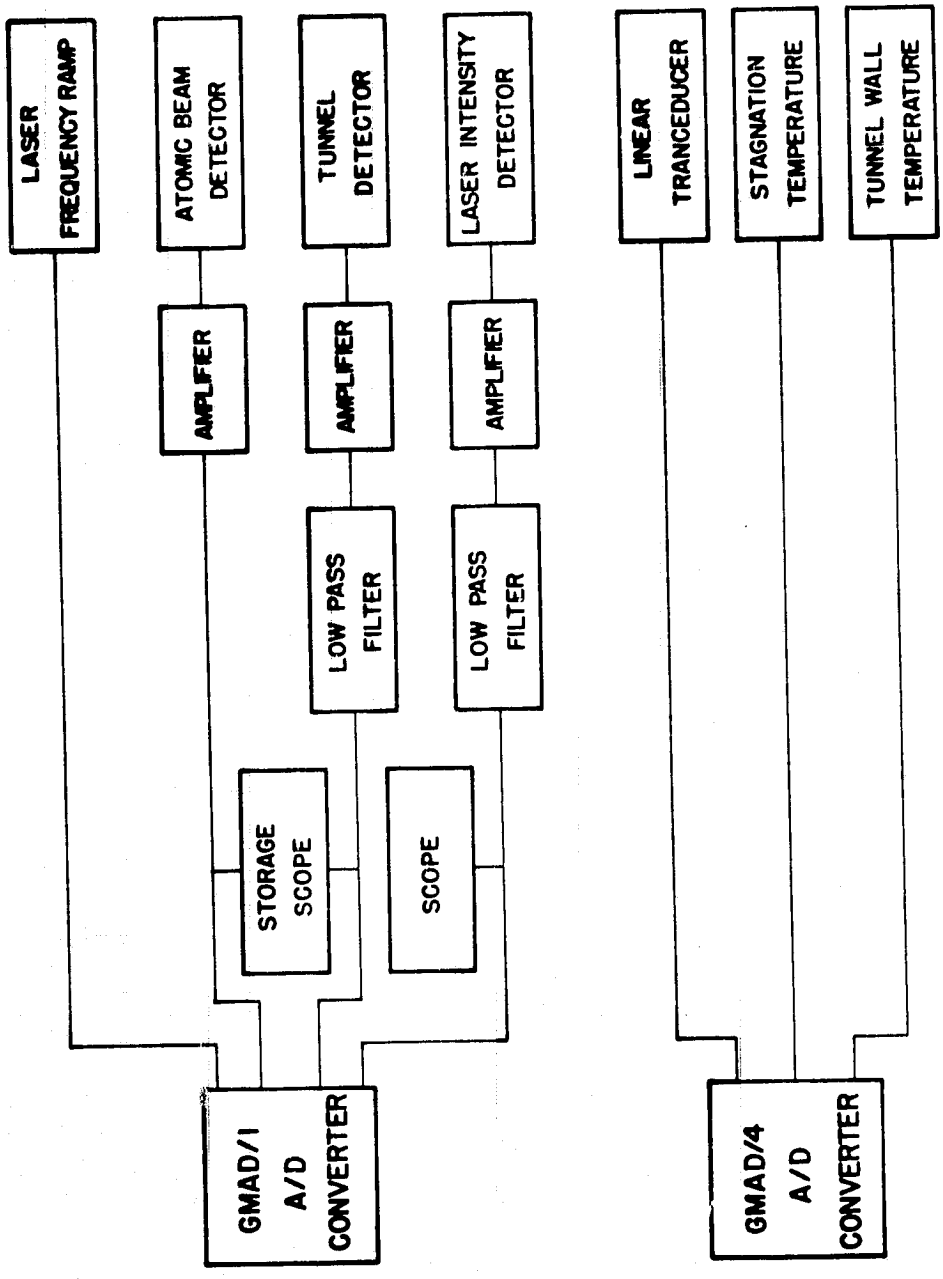
LASER FREQUENCY RAMP
ATOMIC BEAM DETECTOR
TUNNEL DETECTOR
LASER INTENSITY DETECTOR
LINEAR TRANCEDUCER
STAGNATION TEMPERATURE
TUNNEL WALL TEMPERATURE
AMPLIFIER
AMPLIFIER
AMPLIFIER
LOW PASS FILTER
LOW PASS FILTER
STORAGE SCOPE
SCOPE
GMAD/1 A/D CONVERTER
GMAD/4 A/D CONVERTER

Figure II.9

A Tektronics R564B storage oscilloscope with a dual trace vertical amplifier is used to monitor the two fluorescence signals from the photomultipliers during the laser scan. The horizontal amplifier is driven by the laser frequency scanning voltage ramp.

Chapter III

RESONANT DOPPLER VELOCIMETER OPERATING CONDITIONS

A. Introduction

A calculation for the determination of the optimal operating conditions for the RDV is presented in this chapter. The calculation is representative only since it applies to the He^3 facility in the Gas Dynamics Laboratory of Princeton University as described in Section II.B.

The procedure for deriving the velocity from the Doppler shift is discussed in the beginning of the following section. The effect of the number density of the seeded sodium on laser light absorption and radiation trapping is presented next. A discussion of the limit which has to be imposed on the laser power level to reduce saturated absorption and power broadening follows. Finally, the expected signal level based on the optimal sodium number density and laser power level is calculated. The phenomena of the sodium atoms lagging behind the helium flow, optical pumping and radiation quenching are also touched upon briefly.

B. Velocity Calculations

The velocity of the sodium atoms can be determined from the Doppler shifted absorption frequency. From equation A.29

$$\omega_{ki} = \omega(1-\hat{k} \cdot \frac{\vec{u}}{c}) \qquad \text{III.1}$$

where $\hat{k}$ is a unit vector in the direction of the propagation vector $\vec{k}$, $\vec{u}$ is the atomic velocity vector and c is the speed of light. The equation may be rewritten in terms of ω

$$\omega = \frac{\omega_{ki}}{1-\hat{k} \cdot \frac{\vec{u}}{c}} = \omega_{ki}[1+\hat{k} \cdot \frac{\vec{u}}{c} + (\hat{k} \cdot \frac{\vec{u}}{c})^2 + \ldots] \qquad \text{III.2}$$

For $\frac{|\vec{u}|}{c} << 1$

$$\omega \simeq \omega_{ki}(1+\hat{k} \cdot \frac{\vec{u}}{c}) \qquad \text{III.3}$$

Expressed in terms of a Doppler shift, $\Delta\omega$, the calculated velocity component, u, parallel to the propagation vector, $\vec{k}$, is

$$u = \Delta\omega \frac{c}{\omega_{ki}} = \frac{\Delta\omega}{2\pi} \lambda_{ki} \qquad \text{III.4}$$

where λ_{ki} is the absorption wavelength and $\Delta\omega$ equals $\omega-\omega_{ki}$.

The Doppler shift is measured by simultaneously scanning the dye laser frequency through the stationary absorption line in the reference cell and through the shifted absorption line in the wind tunnel while monitoring the fluorescence intensity from both. Since the ground state splitting is of the order of the velocity shift, one may use it to obtain a relative laser frequency calibration as detailed in Chapter IV. For accurate measurements of the Doppler frequency shifts, the reference frequency has to be determined as accurately as possible. The collimated atomic beam in the reference cell is collision free, hence the absorption linewidth is limited only

by the natural and instrumental broadening as discussed in Section II.C and Appendix A. The number of collisions a sodium atom undergoes in the tunnel during the time interval between injection and detection is an indication of how closely the sodium atom follows the helium flow. The smallest collision frequency and largest convective velocity should be used to obtain a lower bound on the number of collisions. These conditions are realized in the test section of the wind tunnel. The collision frequency per sodium atom, z, is

$$z = n_{He}\, \sigma_c \sqrt{\frac{8kT}{\pi\mu}} \qquad \text{A.58}$$

where n_{He} is the helium number density, σ_c is the sodium helium collision cross section, μ is the reduced mass, k is the Boltzman constant and T is the temperature. All the experimental investigations performed to determine the collision cross section for the sodium lines were carried out at temperatures of 400°K and higher. A cross section for the temperature range of only a few degrees Kelvin is measured in this experimental investigation (Section IV.D.1). For T = 4.55°K and $n_{He} = 7.5 \times 10^{23}$ $1/m^3$ determined from a pilot survey (Section IV.B.2) then z = 142 MHz. The cross section, $\sigma_c = 126 \times 10^{-16}$ cm^2, obtained by McCartan and Farr[25] at T = 415°K was used for a first iteration.

The velocity in the test section based on isentropic flow calculations is 1736 m/sec and the distance from the injection point to the probe volume is 0.93 m. A sodium atom therefore travels 5.4×10^{-4} sec before being detected. At the above calculated collision frequency, it undergoes at least 7.7×10^{4} collisions. One may thereby assume that the sodium atoms seeded in the tunnel follow the helium flow closely since they undergo many collisions between the point of their injection into the flow and the probe volume.

The two strong sodium lines with transition frequencies in the frequency range of the Rhodamine 6G dye laser are the D_1 at 5896 A° ($3^2S_{1/2} \rightarrow 3^2P_{1/2}$) and the D_2 at 5890 Å ($3^2S_{1/2} \rightarrow 3^2P_{3/2}$) transitions. A manifold of four and six hyperfine lines is associated with the D_1 and D_2 transitions respectively (Appendix A). The D_2 $3^2S_{1/2}$, F=2 $\rightarrow$ $3^2P_{3/2}$, F=3 hyperfine line is used for a frequency reference since it is almost three times more intense than the next strongest line.

C. Laser Power and Sodium Number Density Limits for RDV in Helium

The temperature and pressure may be determined by fitting a Voigt profile to the experimental points (Appendix A). The broadened lineshape may be distorted compared to the theoretical one by strong laser absorption, radiation trapping and power broadening in addition to optical pumping (Appendix A). These effects may be reduced by controlling the amount of seeded sodium and laser irradiance.

From the pitot survey and the stagnation conditions of 295±1°K and 225±1 psi (1550±7 KPa),one obtains T = 4.55±0.09°K, P = 6.7±0.2x10^{-3} psi (45±2 Pa) and M = 13.8±0.08 for the temperature pressure and Mach number existing in the test section. From equation A.31 the Doppler HWHM, $\Delta\nu_D$, is expected to be 81.8 MHz. From equation A.72 the collision HWHM, $\Delta\nu_c$, is expected to be 12.8 MHz where the cross section at a temperature of 415°K[25] has been used for a first iteration. The natural, $\Delta\nu_n$, and laser, $\Delta\nu_\ell$, are 5 MHz each. The total Lorentzian HWHM, $\Delta\nu_L$, is

$$\Delta\nu_L = \Delta\nu_c + \Delta\nu_n \qquad \text{III.5}$$

Assuming that the laser HWHM can be simply added to the Lorentzian component then the total Lorentzian HWHM

$$\Delta\nu_L = \Delta\nu_c + \Delta\nu_n + \Delta\nu_\ell = 22.8 \text{ MHz} \qquad \text{III.6}$$

The ratio of Lorentzian to Gaussian linewidths, a, is

$$a = \frac{\Delta\nu_L}{\Delta\nu_G/\sqrt{\ell n 2}} = 0.232 \qquad \text{A.108}$$

where $\Delta\nu_G$ is the Gaussian HWHM and $\Delta\nu_G$ equals $\Delta\nu_D$. From tables based on numerical calculations[26] one obtains the field free Voigt HWHM of

$$\Delta\nu_V(I=0) = 94.7 \text{ MHz} \qquad \text{III.7}$$

If a 1% error in the HWHM of the Voigt profile due to power broadening is acceptable, then

$$\Delta\nu_V(I \neq 0) = 1.01\ \Delta\nu_V(I = 0) = 95.6\ \text{MHz} \qquad \text{III.8}$$

and the linewidth ratio, a', is 0.248. The power broadened Lorenzian HWHM is

$$\Delta\nu_L'(I \neq 0) = a' \frac{\Delta\nu_G}{\sqrt{\ell n 2}} = 24.4\ \text{MHz} \qquad \text{III.9}$$

The saturation intensity, $I_s(\omega_{21})$, is

$$I_s(\omega_{21}) = \frac{1}{1 + \frac{g_2}{g_1}} \frac{8\pi^2 hc\Delta\nu_L}{\lambda_{21}^3} = 104.5\ \text{W/m}^2 \qquad \text{A.98}$$

where g is the degeneracy, h is Planck's constant, c is the speed of light, and λ_{21} is the transition wavelength. The subscripts 2 and 1 refer to the upper and lower states respectively. The laser intensity, I, is related to the saturation intensity by equation A.100 and may be calculated for the above conditions

$$I = I_s(\omega_{21})\{[\frac{\Delta\nu_L'(I \neq 0)}{\Delta\nu_L}]^2 - 1\} = I_s(\omega_{21})\{[\frac{a'(I \neq 0)}{a}]^2 - 1\} = 15\ \text{W/m}^2 \qquad \text{III.10}$$

The intensity distribution for a cylindrical beam with a Gaussian profile is[27]

$$I' = I_o e^{-2(\frac{r}{w})^2} = \frac{dP}{dA}$$

where w is the beam waist at the e^{-2} point and r is the radial distance from the laser beam axis. Therefore the power is

$$P = \int_o^\infty I' 2\pi r dr = \frac{\pi I_o w^2}{2}$$

The power equals 2.4×10^{-5} w assuming I_o equals 15 W/m^2 at a beam waist of 1 mm.

This then is the maximum total laser power that can be used to illuminate a 2 mm diameter cross section area in the flow without causing distortion of the data due to saturation and power broadening. The laser beam may alternatively be expanded into a sheet of light since enough power is available at the output of the dye laser to illuminate a large portion of the flow. The calculation was based on the values $g_2 = 5$ and $g_1 = 3$ which hold for the $3^2S_{1/2}$, F=1 → $3^2P_{3/2}$, F=2 transition. This transition provides the lowest saturation intensity. Hence, if the laser power is kept below $P = 2.4 \times 10^{-5}$ W (for a 1 mm waist), all other lines connecting levels $3^2S_{1/2}$ and $3^2P_{3/2}$ will possess an even smaller saturation broadening component.

The sodium D_2 transitions have different strengths (Figure A.2). The intensity of the laser beam at the probe volume is therefore dependent on the hyperfine line being pumped due to absorption along the beam's path as depicted in Figure III.1. A stronger line would absorb more of the laser beam power through its passage in the sodium seeded region towards the probe volume. Also, significant absorption of the fluorescence signal may take place between the probe volume and the detection optics. The last effect known as radiation trapping is also dependent on the line strength. If major differences in absorption are allowed for different transitions the interpretation of the spectra would become difficult. In order to avoid this problem the density of the sodium must be limited.

Due to broadening effects in the tunnel, the structure of the upper state $3^2P_{3/2}$ is not resolved. The relative strengths of the two transitions $3^2S_{1/2}$, F=1,2 → $3^2P_{3/2}$ are 12/48 and 20/48 respectively. From equation A.82 the ratio of the laser irradiances, after passing a distance L through the absorbing medium for an optical depth, $K_\omega L$, equal to 0.1 is

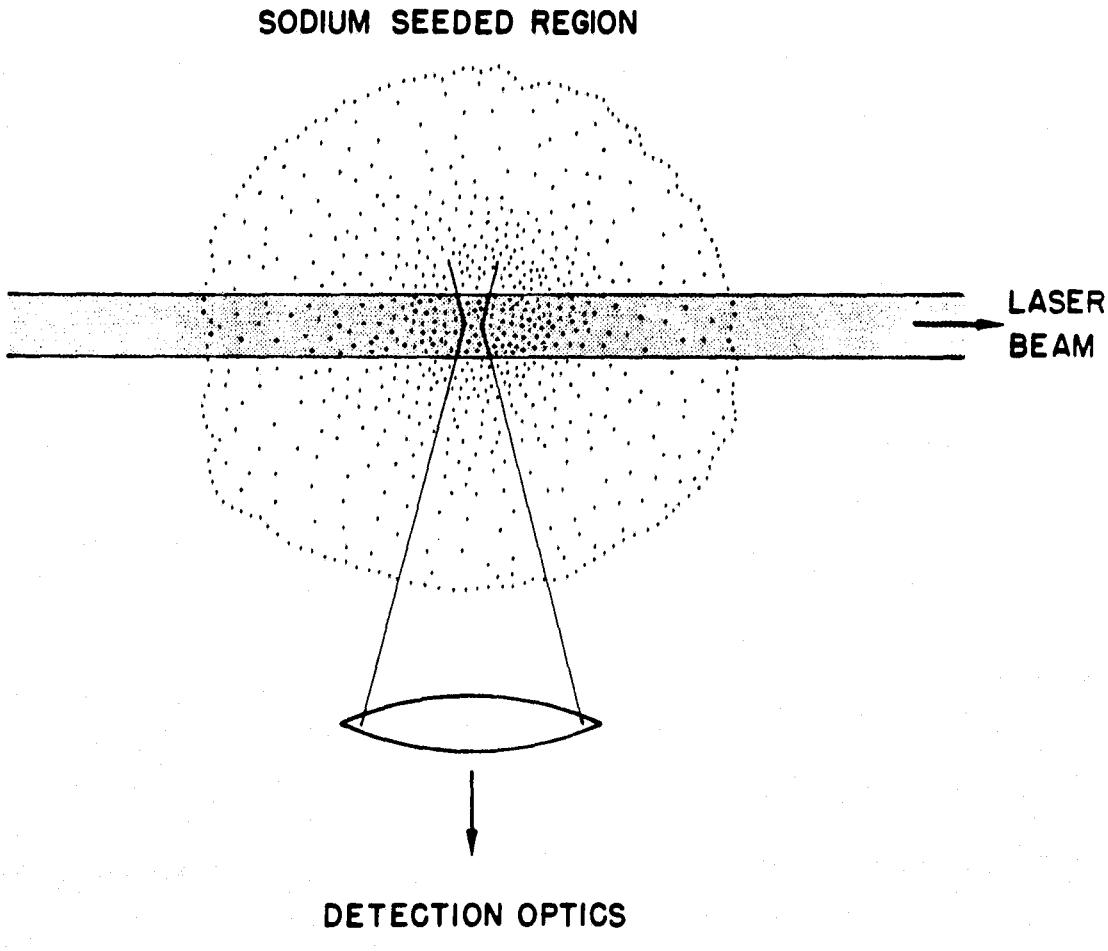

Figure III.1

given by

$$\frac{e^{-\frac{12}{48}\kappa_\omega L}}{e^{-\frac{20}{48}\kappa_\omega L}} = 1.017 \qquad \text{III.13}$$

One may calculate the maximum number density of sodium for an optical depth of 0.1 by using equations A.106 and A.111.

$$\kappa_\omega = \frac{\pi^2 c^2}{\omega_{21}^2} \frac{g_2}{g_1} A_{21} \left(\frac{n_1^o}{g_1} - \frac{n_2^o}{g_2}\right) \frac{1}{\sqrt{1 + \frac{I(\omega)}{I_s(\omega_{21})}}} \left[\frac{\ell n 2}{(\pi)^{3/2}} \frac{\Delta\nu_L}{\Delta\nu_G^2} \int_{-\infty}^{\infty} \frac{e^{-y^2}}{(x-y)^2+a^2} dy\right]$$

where κ_ω is the absorption frequency, c is the speed of light, ω_{21} is the transition frequency, g is the degeneracy, A is the Einstein coefficient for spontaneous emission and n^o is the zero field number density, a was defined in equation A.108. The detuning, x, is

$$x = \frac{\nu - \nu_{21}}{\Delta\nu_G/\sqrt{\ell n 2}} \qquad \text{A.109}$$

The term in square brackets is the Voigt integral (Appendix A). On line center x = 0. Then

$$\kappa_\omega = 2\pi^2 c r_o f_{12} \left(\frac{n_1^o}{g_1} - \frac{n_2^o}{g_2}\right) \frac{1}{\sqrt{1 + \frac{I(\omega)}{I_s}}} \left\{\sqrt{\frac{\ell n 2}{\pi}} \frac{1}{\Delta\nu_G} e^{-\left(\frac{\Delta\nu_L}{\Delta\nu_G}\right)^2 \ell n 2}\right.$$

$$\left.\left[1 - \operatorname{erf}\left(\frac{\Delta\nu_L \sqrt{\ell n 2}}{\Delta\nu_G}\right)\right]\right\} \qquad \text{III.15}$$

The last result has been derived employing the identity[28]

$$\frac{a}{\pi} \int_{-\infty}^{\infty} \frac{e^{-y^2}}{y^2+a^2} dy = e^{a^2} [1 - \operatorname{erf}(a)] \qquad \text{III.16}$$

Use has also been made of equation A.15 and A.16 to obtain

$$A_{21} = -3f_{21}\ 2\Gamma = 3\ \frac{g_1}{g_2}\ f_{12}\ \frac{2}{3}\ r_o\ \frac{\omega^2}{c} \qquad \text{III.17}$$

where $r_o = 2.82\text{x}10^{-15}$ m is the classical electron radius, f_{12} and f_{21} are the absorption and emission oscillator strengths and Γ is the natural HWHM.

From equation III.15 for L on the order of 0.1 m and $\kappa_\omega L = 0.1$

$$\frac{n_1^o}{g_1} - \frac{n_2^o}{g_2} = 8.19\text{x}10^{13}\ \text{atom/m}^3 \qquad \text{III.18}$$

At equilibrium, for $\lambda = 589\text{x}10^{-9}$ m and a temperature of $4.55°\text{K}$[29]

$$\frac{n_2^o}{g_2} = \frac{n_1^o}{g_1}\ e^{-\frac{\hbar\omega}{KT}} = \frac{n_1^o}{g_1}\ 10^{-2293} \qquad \text{III.19}$$

The thermal upper state number density may be neglected. Hence

$$\frac{n_1^o}{g_1} = 8.19\text{x}10^{13}\ \text{atoms/m}^3 \qquad \text{III.20}$$

The laser power available at the probe volume varies less than 1.6% for the two ground states of $3^2S_{1/2}$ if the sodium density is kept below the calculated value. The ratio of the detected fluorescence emission intensity of the stronger transition manifold to the weaker transition manifold, if trapping is included for the same optical depth of 0.1 is from equation A.82

$$\left[\frac{I_o e^{-\frac{20}{48}\kappa_\omega L}}{I_o e^{-\frac{12}{48}\kappa_\omega L}}\right]\left[\frac{1-e^{-\frac{20}{48}\kappa_\omega L}}{1-e^{-\frac{12}{48}\kappa_\omega L}}\right] = 1.63 \qquad \text{III.21}$$

where the first bracket relates to the absorption of the laser beam and the second bracket to radiation trapping. The ratio obtained from an infinitely short absorption length equals the ratio of the relative strengths, 20/12. The difference between the two ratios is 2.5%. For $\kappa_\omega L = 1$ and

0.01 the ratios are 1.304 and 1.662 which differ from the ideal value by 22% and 0.25% respectively. In the present experimental investigation the optical depth is of the order of 0.1.

The power absorbed by the sodium atoms is given by equation A.87. It also equals the energy of a single photon multiplied by the net photon absorption rate. The number of photons emitted equals the number absorbed, times a radiation quenching factor defined by

$$Q = \frac{\text{Intensity of fluorescence with foreign gas}}{\text{Intensity of fluorescence without foreign gas}}$$

Quenching is a result of nonradiative decay of the upper state due to inelastic collisions with foreign atoms or molecules. Quenching occurs when the atomic excitation energy is converted to translational, rotational or vibrational energy. The rate per unit volume of spontaneously emitted photons, $\dot{n}$, is

$$\dot{n} = \frac{I}{\hbar\omega} \frac{(\kappa_\omega L)}{L} Q = 4.5\text{x}10^{19} \text{ 1/sec-m}^3 \qquad \text{III.22}$$

The values used for this calculation are the sodium D_2 transition frequency, $I = 15 \text{ W/m}^2$, $\kappa_\omega L = 0.1$, and $L = 0.1$ m. Sodium quenching by helium is negligible[16] and therefore $Q \simeq 1$.

The detection optics are discussed in Chapter II. The rate of collected photons, $\dot{N}$, if the probe volume and the collector solid angle are taken into account, is

$$\dot{N} = \dot{n} \cdot V \cdot \frac{\Omega}{4\pi} \qquad \text{III.23}$$

From the above calculations, the sodium density has to be kept below $8.2\text{x}10^{13}$ atoms/m^3 to eliminate the distortion of the absorption lineshape. The laser power has to be kept below $2.4\text{x}10^{-5}$ W so as not to add an appreciable saturation component to the Lorentzian linewidth. Under these

conditions one obtains 2.9×10^{7} photons/sec for a probe volume of 1.8×10^{-10} m^3 and a collection efficiency of 3.6×10^{-3} (Section II.D).

Chapter IV

RESULTS

A. Introduction

The experimental results are presented in this chapter. Pitot pressure and total temperature surveys were taken to determine the effect of sodium seeding on the helium flow in the wind tunnel. The characteristics of the atomic beam and the laser spectral purity are then analysed since they affect the quality of the data obtained from the wind tunnel. A discussion of the data analysis procedure is presented next and is followed by the results obtained from three different experimental configurations.

The atomic beam device is used for velocity measurements in the free stream flow of the wind tunnel in the first experiment. A laser double pass configuration in the free stream flow of the wind tunnel is employed next and dispenses with the use of the atomic beam device. The first configuration is applied in the third experiment to perform measurements in the vicinity of a shock wave surrounding a conical model placed in the wind tunnel.

B. System Calibration

1. Total Temperature Surveys

Two total temperature surveys were taken at the measuring station (Section II.B.1), without and with sodium seeding through the needle, as depicted in Figure IV.1 and IV.2 respectively. The ordinate represents the adiabatic wall temperature and the abscissa is the distance along the wind tunnel diameter from the wall into the hypersonic core.

The adiabatic wall temperature measured in the free stream without sodium injection was 278±2°K. Hence the recovery ratio, η (equation II.1) is 0.95±0.008. This value is based on a measured stagnation chamber temperature of 295±1°K and a static temperature of 4.55±0.09°K calculated from isentropic relations based on the stagnation temperature and the Mach number.

The Knudsen number, Kn (equation II.2), obtained in this experimental work is 0.02 where the Reynolds number, Re (equation II.5), is based on the wire diameter. The recovery ratio obtained by P. Materna[30] for the same Knudsen number was 0.96.

The injection needle tip was maintained at 700°C while the survey of Figure IV.2 was taken. The injection system is responsible for some heating of the center of the flow. The heating manifests itself through a peak in the core region as depicted in Figure IV.2. The total temperature at the peak is 305±3°K (taking into account the recovery ratio). It is also clear that some asymmetry is present in the flow, as discussed in the following section.

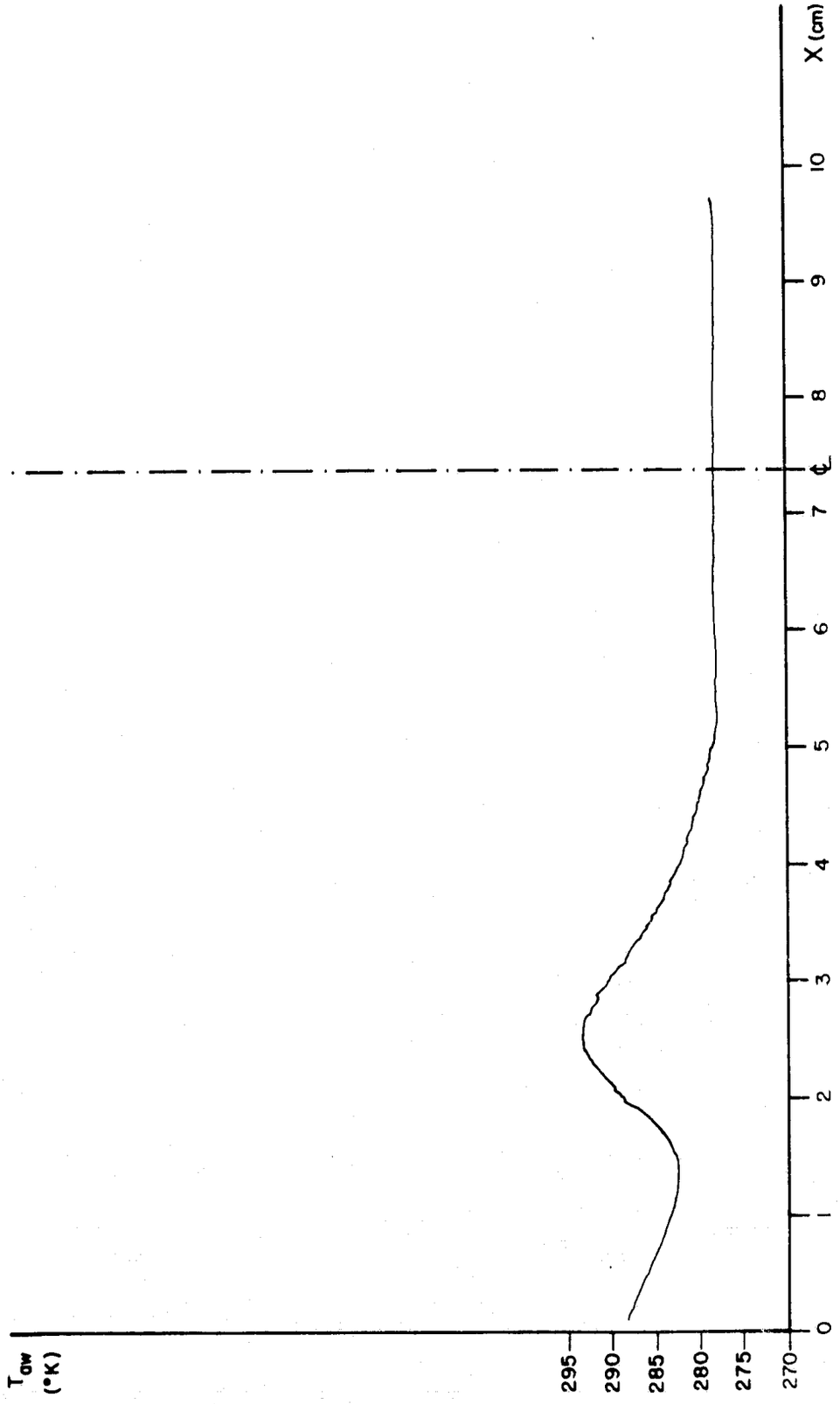

Figure IV.1

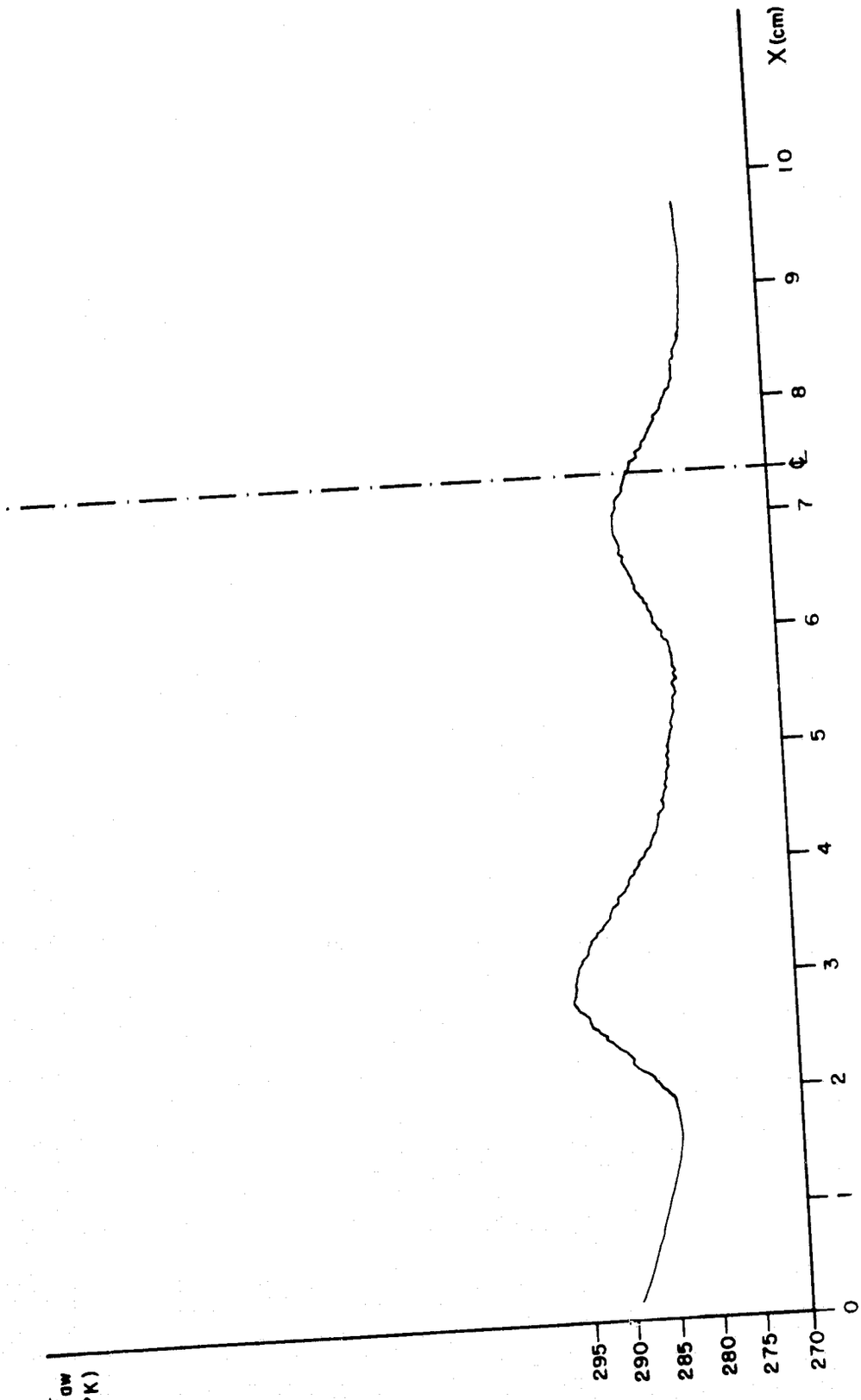

Figure IV.2

2. Pitot Surveys

The measuring station, as discussed previously (Section II.B.1), is maintained at 0.216 m downstream of the nozzle exit because of experimental constraints. This position facilitates scanning the optics along the tunnel diameter as far as possible towards the tunnel wall. Most of the previous experiments performed by other workers in the He3 facility were conducted closer to the nozzle exit than the measuring station. Hence, two sets of pitot surveys were taken to compare the flow conditions at the measuring station (Figure IV.3 to Figure IV.5) to those existing at 0.049±0.001 m downstream of the nozzle exit (Figure IV.6 to Figure IV.8). Figure IV.3 and IV.6 are the surveys obtained with the injection needle removed, corresponding to the normal mode of operation of the wind tunnel without sodium seeding. The injection needle was positioned 0.1 inches upstream of the nozzle in Figure IV.4 and IV.7 with no injection. Sodium injection was taking place in Figure IV.5 and IV.8. The abscissa is the distance from the tunnel wall and the ordinate is the pitot pressure. There is no apparent difference between Figures IV.7 and IV.8 and between Figures IV.4 and IV.5 apart from the vicinity of the compression wave. The concave part of the expanding side of the nozzle produces compression waves as depicted in Figure IV.9. The pitot probe which is scanned across the tunnel diameter, 0.216 m downstream of the nozzle exit, senses these compression waves and registers them as a pressure peak on both sides of the inviscid core. The compression wave really surrounds the inviscid core since the tunnel is axisymmetric. It appears that the presence of the needle in the stagnation chamber increased the diameter of the inviscid core in the test section and also reduced the compression wave strength near the core boundary. This effect was particularly noticeable at the measuring

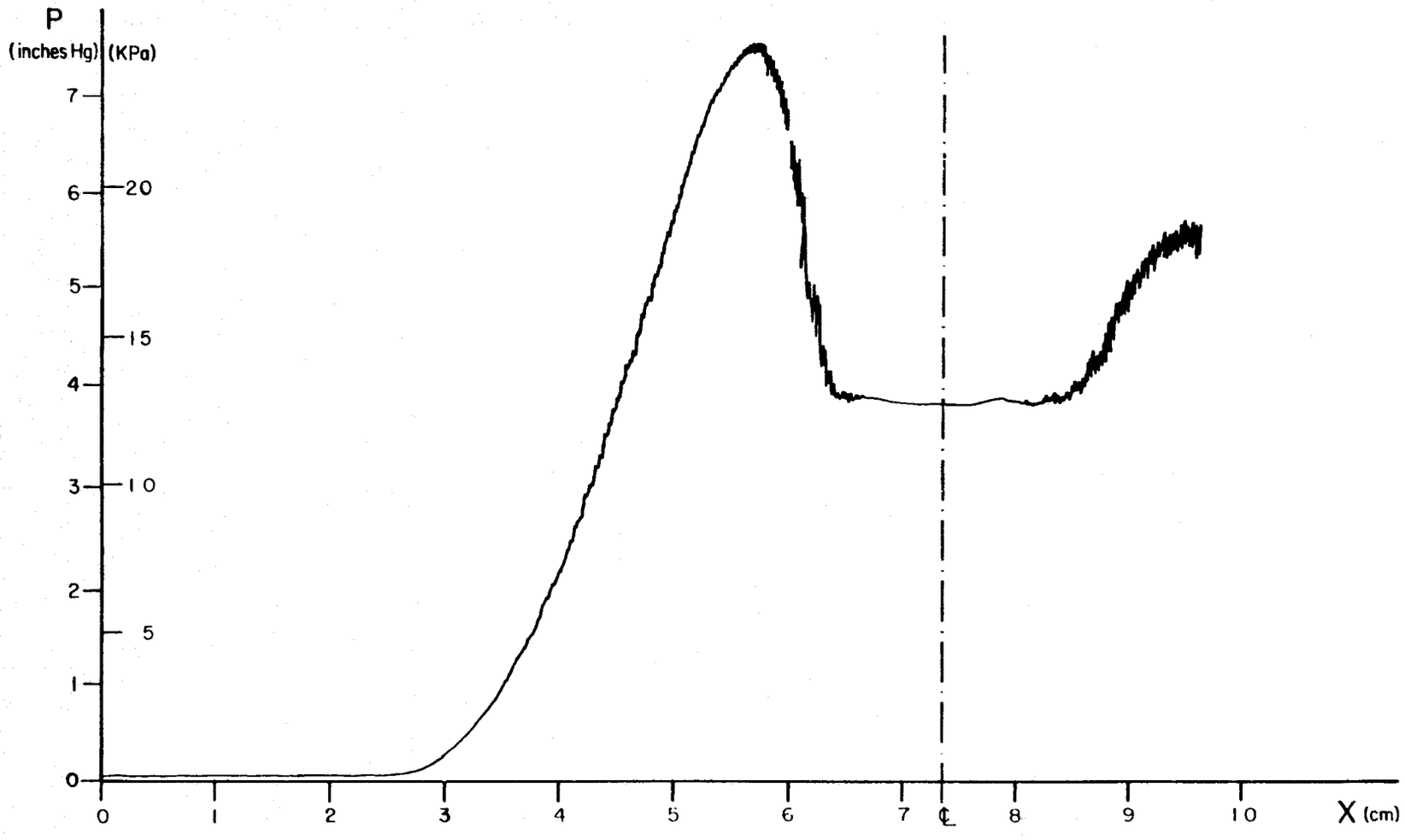

Figure IV.3

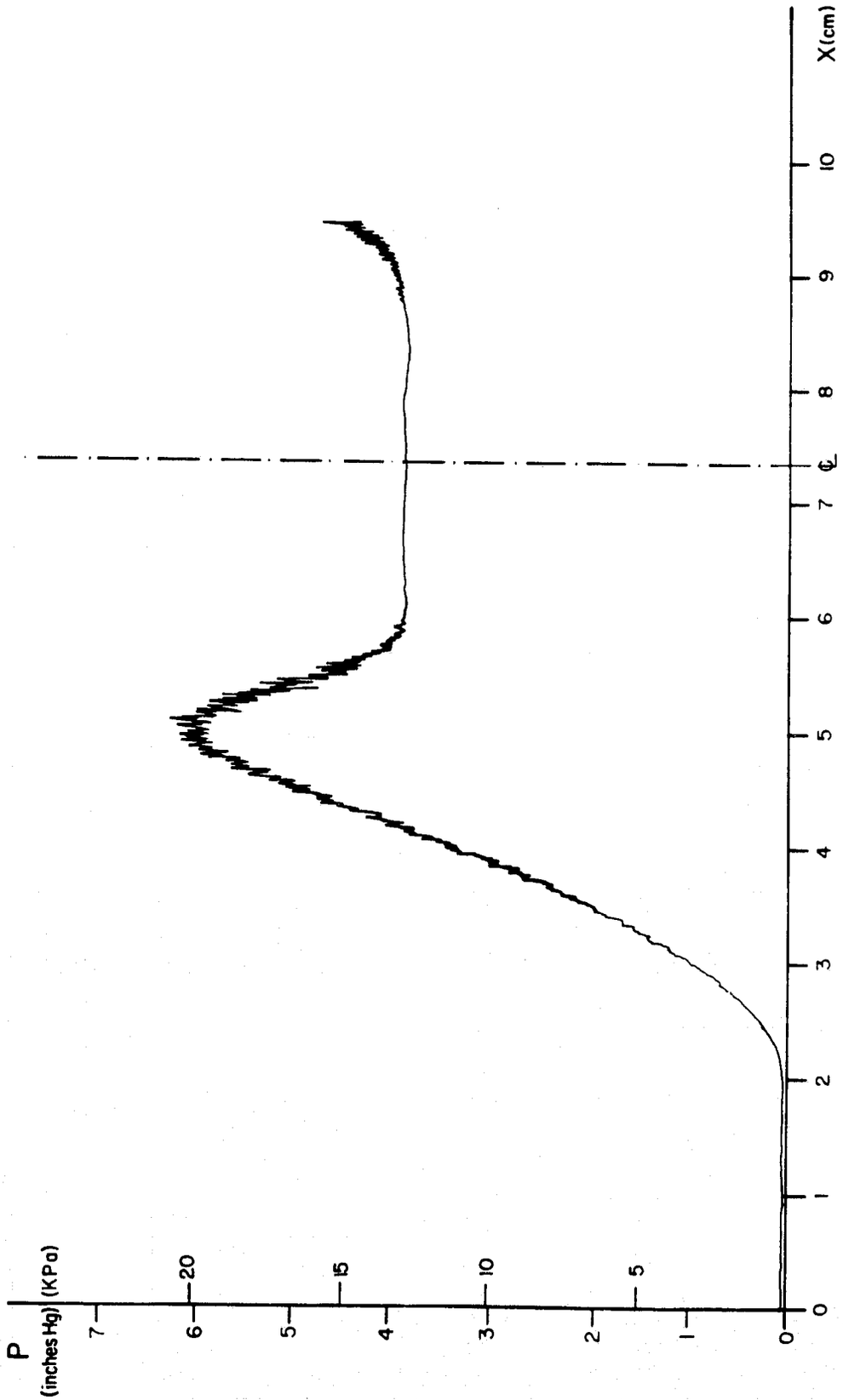

Figure IV.4

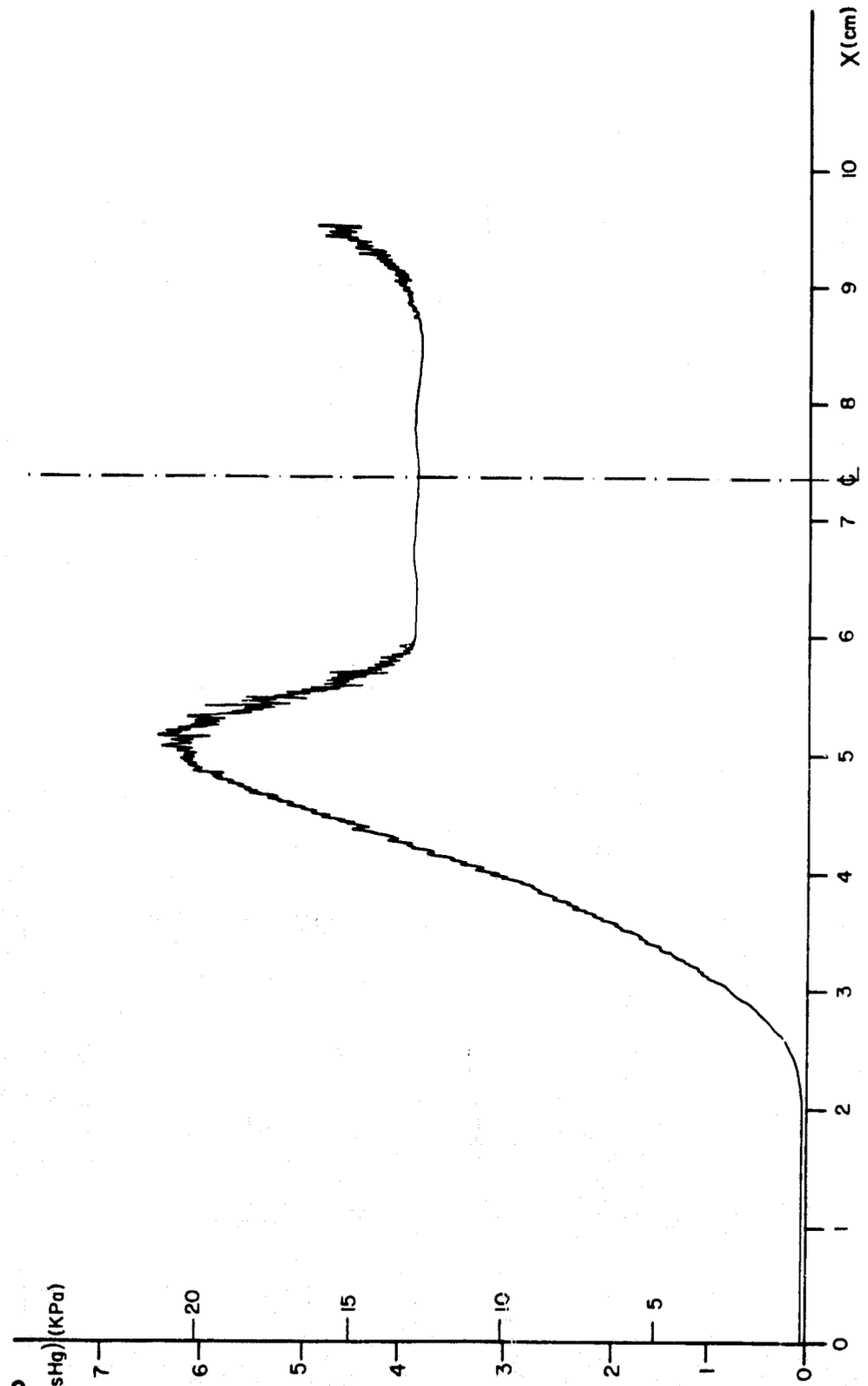

Figure IV.5

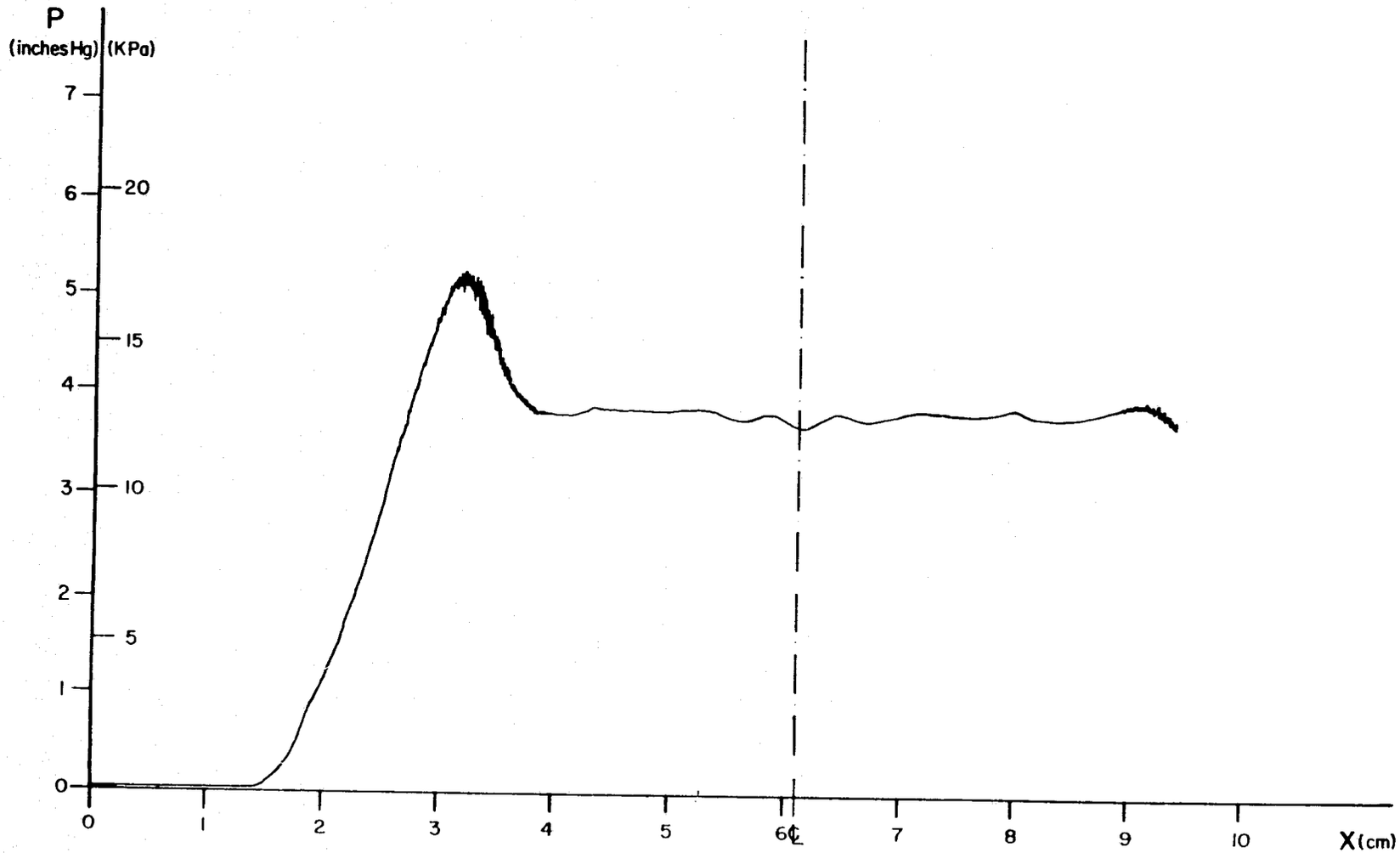

Figure IV.6

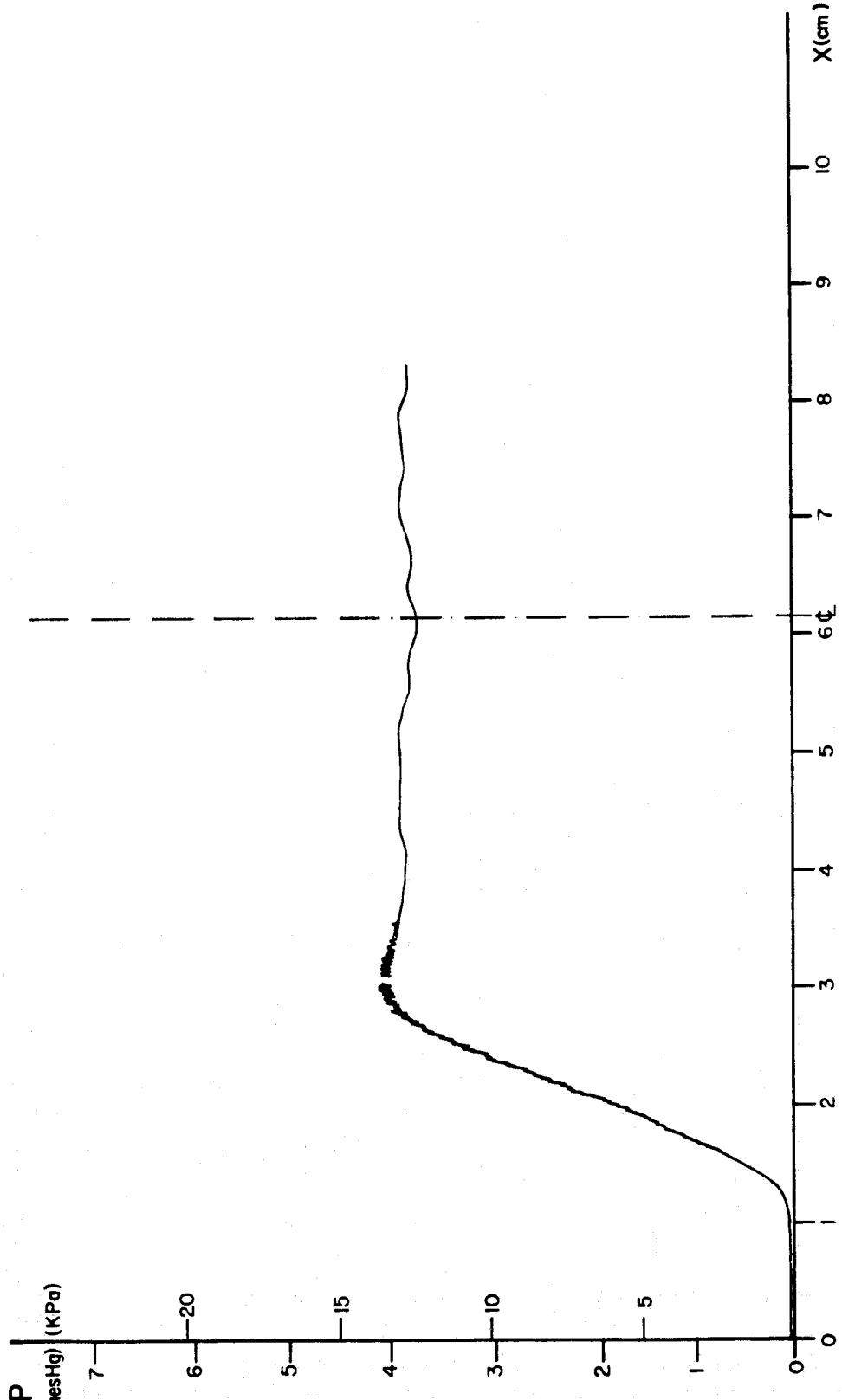

Figure IV.7

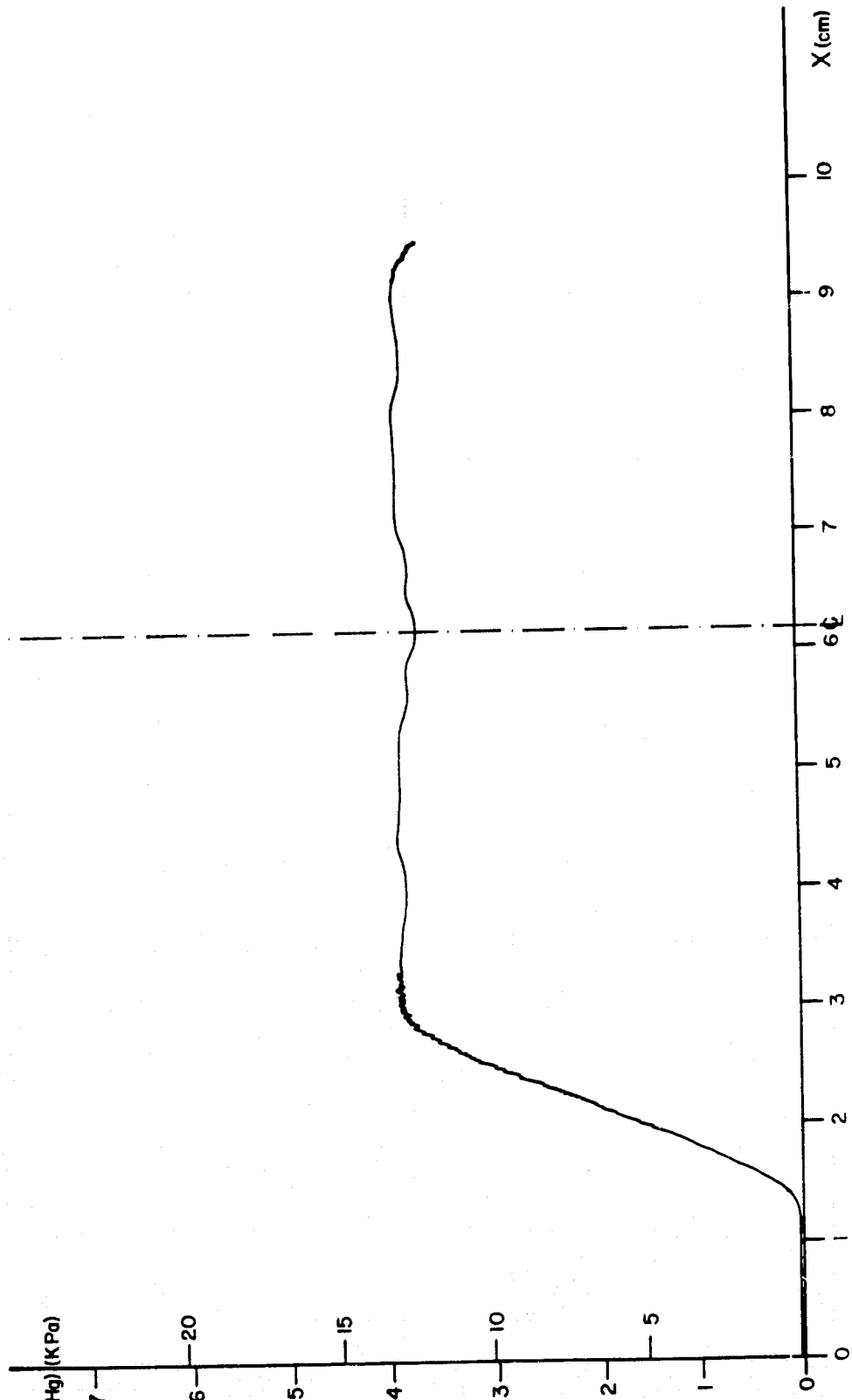

Figure IV.8

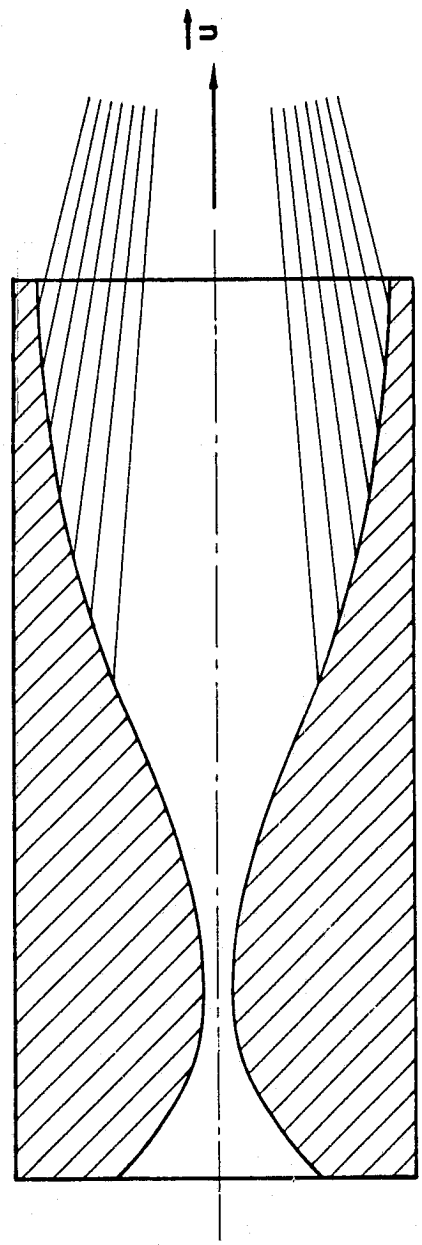

Figure IV.9

station. The pitot surveys also indicated the presence of flow asymmetry as previously observed with the temperature survey. The compression wave surrounding the inviscid core is not of uniform magnitude.

To determine the Mach number from the Pitot pressure, P_2^t, one has to calculate the ratio[31]

$$\frac{P_2^t}{P_1^t} = \left(\frac{P_1}{P_1^t}\right) \left(\frac{P_2}{P_1}\right) \left(\frac{P_2^t}{P_2}\right) \qquad \text{IV.1}$$

P with the superscript t is a stagnation pressure and without it a static pressure. The subscripts 1 and 2 refer to the pressure upstream and downstream of the shock standing in front of the pitot probe. The expansion from the stagnation chamber towards this shock is not isentropic when sodium seeding takes place as is evident from Figure IV.2 since the flow is not adiabatic. Then clearly P_1^t is not the stagnation chamber pressure but an unknown quantity. Therefore when the flow is seeded the Mach number may not be found from equation IV.1 by substituting the stagnation chamber pressure for P_1^t. The pitot pressures measured in the hypersonic core for all the six different surveys are the same to within the experimental error and are equal to 3.9±0.08 inches Hg (13200±270 Pa). The four surveys performed with no seeding taking place may be used for Mach number determination. The Mach number obtained in the inviscid core, based on the pitot and stagnation pressure is M = 13.8±0.1 assuming an isentropic expansion of a perfect gas. The area ratio of the nozzle is 2.7×10^{-3} which corresponds to a Mach number of 17.95. The nozzle is designed for a Mach number of 16. The difference between the value of 17.95 and 16 is due to the fact that the boundary layer thickness is taken into account which limits the expansion. The measured Mach number of 13.8 is lower than the design

value of M = 16. To determine whether this was due to contaminated helium, the same gas was used in the He2 facility and in the He3 facility with its original nozzle and with the He4 nozzle. All these nozzles were designed to operate at Mach 16. The resulting pitot pressures in the core are summarized in Table IV.1

Table IV.1

configuration	He2 tunnel He2 nozzle	He3 tunnel He3 nozzle	He3 tunnel He4 nozzle
pitot pressure (inches Hg)	2.4±0.08	3.9±0.08	2.4±0.08
Mach number	16.2±0.1	13.8±0.1	16.2±0.1

The He3 nozzle is 6 inches longer than the He2 and He4 nozzles. Hence the displacement thickness at its exit is larger which would tend to decrease the expansion. It is thus the nozzle's design which is responsible for the lower than expected Mach number. In the presence of seeding, the Mach number may be found spectroscopically as discussed in Section IV.C. It is reduced from the above measured value due to the injection process (Section IV.B.1).

3. Atomic Beam Device and Frequency Calibration

The atomic beam spectra of the D_2 line of sodium is depicted in Figure IV.10 for three different laser scan starting frequencies. Each of the larger and smaller peaks contain three hyperfine transitions associated with the $3^2S_{1/2}$, F=2 and $3^2S_{1/2}$, F=1 ground state respectively.

The $3^2S_{1/2}$, F=2 → $3^2P_{3/2}$, F=3 hyperfine transition is mainly responsible for the larger peak in the spectra, since it is almost three times stronger than the next strongest hyperfine transition. The hyperfine lines in each peak are closely spaced in relation to the spectral purity of the

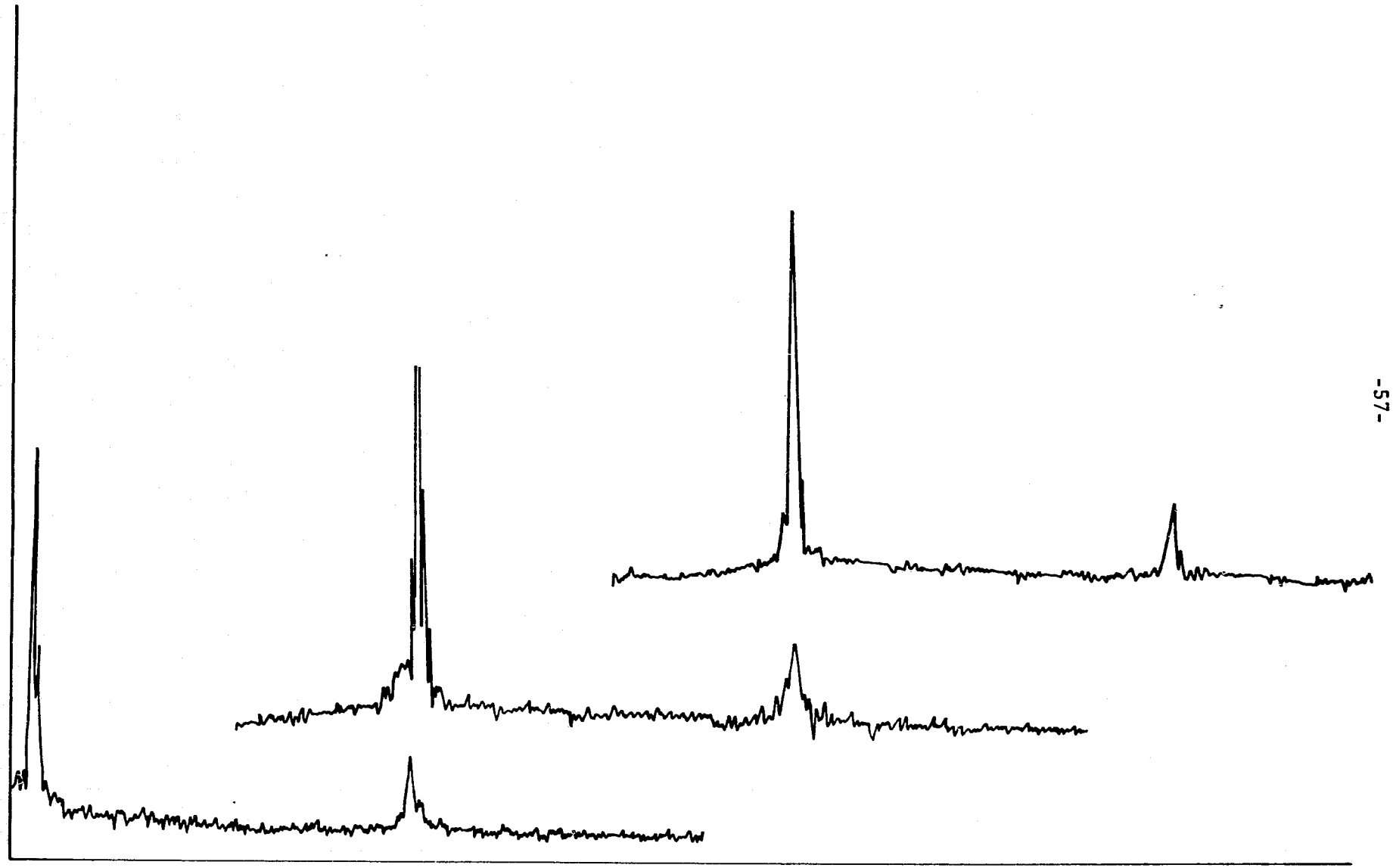

Figure IV.10

laser. The natural width of the transitions causes some overlap between them. These reasons in addition to the fact that only 10 sampling points were used to map the spike and the fact that a large amount of scattering existed in the atomic beam probe volume, are responsible for the unresolved structure of the line.

The experimentally observed HWHM of the large peak is 10 MHz. The natural HWHM is 5 MHz (Appendix A). If the large peak represents the $3^2S_{1/2}$, F=2 → $3^2P_{3/2}$, F=3 hyperfine transition only, then the experimental contribution to the HWHM is 5 MHz. This implies that the laser HWHM is 5 MHz if it is assumed that the laser linewidth may be simply added to the Lorentzian natural linewidth.

The three lines emanating from the $3^2S_{1/2}$, F=1 state are not resolved for the same reasons. Since the line strengths of the two transitions $3^2S_{1/2}$, F=1 → $3^2P_{3/2}$, F=1,2 (Figure A.2) are comparable, one may not assign the peak to any transition in particular. Therefore, for velocity measurement purposes it is the $3^2S_{1/2}$, F=2 → $3^2P_{3/2}$, F=3 transition which provides the best accuracy as a frequency reference.

The dye laser frequency is tuned by applying a high voltage ramp to a piezoelectric crystal which translates one of the end mirrors of the cavity. The intracavity etalon installed to facilitate single frequency operation has to be tuned so as to track the cavity mode. Since the frequency-voltage relation is nonlinear, it has to be calibrated. Figure A.10 depicts the calibration procedure which is performed in conjunction with the atomic beam device. First, the minimum laser frequency is adjusted so that the strongest transition ($3^2S_{1/2}$, F=2 → $3^2P_{3/2}$) appears just as the laser starts scanning. The laser is then tuned to a lower initial frequency so that the absorption line corresponding to the strongest transition falls

on top of that of the second transition ($3^2S_{1/2}$, F=1 → $3^2P_{3/2}$) of the first scan. This is repeated a third time for the last frequency range, providing a piecewise calibration. Linear interpolation was used for frequencies falling between the four calibrated points. The determination of these four points is again subject to the error sources mentioned in relation to the atomic beam device spectrum. For frequency calibration purposes the computer collects 2000 points instead of a mere 1000 for a regular run to enhance the resolution.

A more accurate calibration scheme, which averages over the laser frequency fluctuations is presented in Section IV.D.2.

4. Laser Spectral Purity

The jitter obtained with the Spectra Physics model 580 dye laser is within the resolution of the Jodon 7 MHz linewidth spectrum analyser. In the absence of amplitude noise and frequency jitter, a scanning interferometer would display a perfect bell-shaped curve. When the frequency jitter of the dye laser has a single component at a frequency which is lower than the sweep rate of the interferometer, several of these bell-shaped curves will appear on the oscilloscope screen, one for each spectrum analyser scan, as depicted in Figure IV.11.a. When the dye laser has a jitter at a frequency which is higher than the interferometer scan rate, the interferometer transmission varies rapidly with time as the dye laser frequency jitters back and forth over various portions of the bell-shaped response curve as shown in Figure IV.11.b.

The utilization of the spectrum analyser to measure dye laser jitter as outlined is not accurate. It was used however to obtain an upper limit on the laser frequency jitter. The maximum frequency excursions are about

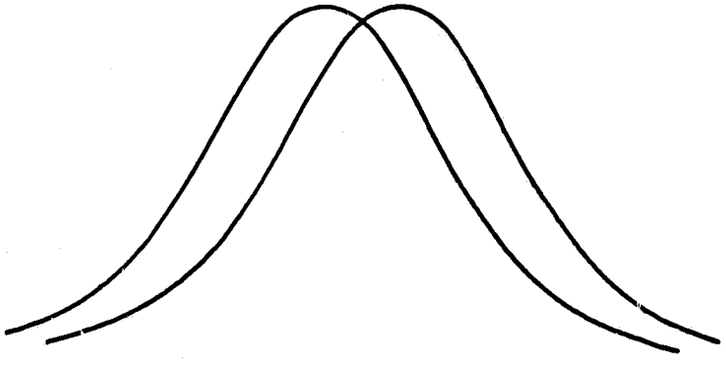

Figure IV.11.a[32]

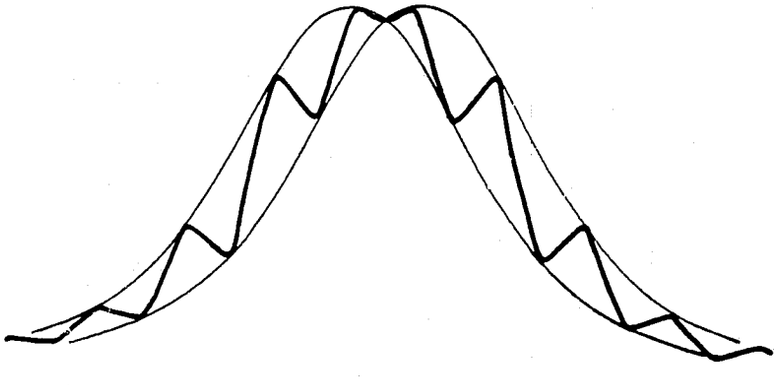

Figure IV.11.b[32]

25 MHz and occur at a rate of about 5 Hz. The frequency excursions due to frequency jitter introduce an offset in the velocity measurement since the center of the absorption lineshape varies from scan to scan. A 25 MHz frequency excursion corresponds to a velocity measurement error of 15 m/sec at the sodium D_2 transition wavelength. More reliable information regarding the error is obtained in Section IV.D.1 and IV.D.2.

C. Data Analysis

The data consisting of somewhat more than 600 points per laser scan were reduced by fitting with a Voigt profile, V(x). x is the detuning[33] normalized by the Voigt HWHM, $\Delta\nu_V$.

$$x = \frac{\nu-\nu_o}{\Delta\nu_V} \qquad \text{IV.2}$$

where ν_o is the line center frequency.

The fitting function was generated using an approximation devised by Kielkopf[33] which is accurate to within 0.0001 of the peak value of the function. The function is defined so that

$$V(x = 0) = 1 \qquad \text{IV.3}$$

$$V(x = 1) = 1/2 \qquad \text{IV.4}$$

Each of the six hyperfine transitions (Section II.B, Appendix A) comprising the D_2 line was frequency shifted and intensity weighted (Figure A.2) to generate the complete theoretical spectrum. The best fit was determined by a computer program incorporating a least squares routine ZXSSQ[34] supplied by I.M.S.L.[35] and described in Appendix B.

A minimum of five parameters, needed to fit a complete D_2 spectrum are listed below.

1) The ratio of Lorentzian over Gaussian HWHM, a (equation A.108), determines the shape of the curve.
2) The Voigt HWHM determines the frequency scale.
3) The frequency, F_1, of the $3^2S_{1/2}$, F=2 → $3^2P_{3/2}$, F=1 transition determines the position of the Doppler shifted spectrum along the frequency axis.
4) The background intensity, I_o, determines the base line.
5) The intensity normalization factor, I_1, determines the intensity scale.

Once an optimal value for the parameters has been established one may determine the Lorentzian (LHWHM) and Gaussian HWHM (GHWHM) from the Voigt HWHM and a by using the relations[33]

$$\varepsilon = 0.099$$

$$\ell = \frac{2}{1 + \varepsilon\, \ell n2 + \sqrt{(1-\varepsilon \ell n2)^2 + \frac{4\ell n2}{a^2}}} \qquad \text{IV.5}$$

$$g^2 = \frac{1 - (1+\varepsilon\ell n2)\ell + \varepsilon\ell n2\ \ell^2}{\ell n2} \qquad \text{IV.6}$$

$$\text{LHWHM} = \ell \cdot \text{HWHM}$$

$$\text{GHWHM} = g\ \text{HWHM}\ \sqrt{\ell n2} \qquad \text{IV.8}$$

The collisional and natural broadening mechanisms are Lorentzian. Their combined linewidth is therefore a sum of the collisional (CHWHM) and natural (NHWHM) HWHM (Appendix A.). For simplicity it is assumed that the laser HWHM (IHWHM) may be added to the Lorentzian broadening component. This could be justified based on the analysis of the atomic beam device spectra (Section IV.B.3). The result is

$$\text{CHWHM} = \text{LHWHM} - \text{NHWHM} - \text{IHWHM} \qquad \text{IV.9}$$

The temperature, T, is given by

$$T = T_o\left(\frac{\text{GHWHM}}{628}\right)^2 \qquad \text{A.35}$$

where T_o is 273°K and GHWHM is in MHz.

If the large spike in the atomic beam spectrum of frequency FREFL is due to the $3^2S_{1/2}$, F=2 → $3^2P_{3/2}$, F-3 transition, equation A.29 and the data from Figure A.2 may be used to find the velocity component, u, in the laser beam direction.

$$u = [\text{F1} + (60+34)\text{x}10^6 - \text{FREFL}] \cdot \lambda_{21} \qquad \text{IV.10}$$

where λ_{21} is the transition wavelength. The Mach number can be determined from the relation[36]

$$M = \frac{u}{\tilde{a}} = \frac{u}{\sqrt{\frac{\gamma RT}{W}}} \qquad \text{IV.11}$$

where $\tilde{a}$ is the velocity of sound, γ is the ratio of specific heats for helium, R is the universal gas constant and, W is the atomic weight of helium. The static pressure, P, is given by[37]

$$P = P^t\left[\left(\frac{\gamma+1}{2}\right)M^2\right]^{-\frac{\gamma}{\gamma-1}}\left[\frac{\gamma+1}{2\gamma M^2-(\gamma-1)}\right]^{-\frac{1}{\gamma-1}} \qquad \text{IV.12}$$

where P^t is the pitot pressure. Since M is the result of a spectroscopic measurement the value of P is based on local quantities (P^t, M) and not on the stagnation chamber pressure (Section IV.B.2). Finally, a value for the pressure broadening cross section, σ_c, can be calculated. From equation A.67

$$\sigma_c = \text{CHWHM}\left(\frac{P/P_o}{\sqrt{T/T_o}}\right)^{-1}\left[P_o\sqrt{\frac{2}{\pi k T_o \mu}}\right]^{-1} \qquad \text{IV.13}$$

where P and T are the static pressure and temperature respective, T_o is 273°K and P_o is 760 torr (1.01×10^5 Pa). k is the Boltzmann constant and μ is the sodium helium reduced mass.

The least squares fitting method, described in Appendix B, involves the calculation of the sum of squares, χ^2

$$\chi^2 = \sum_{j=1}^{N}\left[\frac{y_{ij}-f(x_j)}{\sigma_j}\right]^2 \qquad \text{B.20}$$

where N is the number of sample points, y_{ij} is the fluorescence intensity from the tunnel at a frequency x_j, $f(x_j)$ corresponds to the theoretical model and σ_j is the standard deviation. An estimate of σ_j, the consequence of counting statistics and instrumental uncertainties, has to be

found. The fluctuations in the observations as a result of the counting statistics are not due to any imprecision in measuring the time interval or counting the number of events. Rather they are a result of the fact that a random sample of events distributed randomly in time contains numbers of events which fluctuate from sample to sample. Physically this is due to the discrete nature of the photons in the laser and fluorescence electromagnetic field, the sodium atoms seeded in the flow and the photoelectrons produced in the photomultiplier tube. These fluctuations follow the Poisson distribution[38] as discussed in Appendix B.

The instrumental uncertainties are due mainly to the laser frequency jitter and to noise induced in the shielded cables, 25m long, connecting the experiment to the A/D converter (Section II.F). The sum of squares, χ^2, may also be expressed in terms of the variance of the fit $S_\nu'^2$ and the variance of the data $\overline{\sigma^2}$ (Appendix B).

$$\chi^2 = (N-n) \frac{S_\nu'^2}{\overline{\sigma^2}} \qquad \text{B.22}$$

where n is the number of parameters. $\overline{\sigma^2}$ is a characteristic of the dispersion of the data y_{ij} in the parent population j and is not descriptive of the fit. $S_\nu'^2$ is a characteristic of the spread of the data about the fit but is also an estimate of $\overline{\sigma^2}$. χ^2 is the ratio of the estimated variance to the parent variance, times N-n, which makes it a convenient measure of the goodness of the fit. If the fitting function is a good estimate of the parent function, $S_\nu'^2$ should agree with $\overline{\sigma^2}$ and

$$\chi^2 \simeq N-n \qquad \text{IV.14}$$

The parent distribution standard deviations, σ_j, have to be used in equation B.20 to be able to take advantage of the "Goodness of Fit" test.

The fitting programs are executed for two standard deviations. Using $\sigma_j = 1$ one clearly does not obtain $\chi^2 = N-n$. Assuming that the model describes the physics and that the data are consistent with the model, then $\chi^2 = N-n$, if the value[39] $\sigma_j = \sigma = \chi^2/(N-n)$ is chosen. The parameter uncertainties are then[40]

$$\sigma_k = [(\bar{\bar{\alpha}})^{-1}]_{kk}^{1/2} \cdot \sigma \quad (k = 1....,n) \qquad \text{IV.15}$$

where σ_k relates to parameter β_k. $\bar{\bar{\alpha}}$ is defined in Appendix B. For small residuals $\bar{\bar{\alpha}}$ may be approximated by

$$(\bar{\bar{\alpha}})_{\ell k} = \sum_{j=1}^{N} \frac{\partial f_o(x_j)}{\partial \beta_\ell} \frac{\partial f_o(x_j)}{\partial \beta_k} \qquad \text{IV.16}$$

where the fitting function f is evaluated at the solution to the least squares problem as designated by the subscript o. This approximation is incorporated into the computer program of Appendix C to calculate the uncertainties in equation IV.15.

No counting was performed in the present experiment, though the photomultiplier used to monitor the tunnel fluorescence is inherently a digital device. The output was passed through an integrator, and a voltage was measured. Using $\sigma_j = \sqrt{y_{ij}}$, where y_{ij} is the observed voltage, one again cannot use the χ^2 "Goodness of Fit" test since the ratio of the number of counts to the output voltage is unknown. Making the same assumptions as for the choice $\sigma_j = 1$, then

$$\sigma_k = [(\bar{\bar{\alpha}})^{-1}]_{kk}^{1/2} \cdot \sigma_{\sqrt{y_{ij}}} \qquad (k = 1,...,n) \qquad \text{IV.16}$$

where

$$\sigma_{\sqrt{y_{ij}}} = \frac{\chi^2_{\sqrt{y_{ij}}}}{N-n} \qquad \text{IV.17}$$

and

$$\chi^2_{\sqrt{y_{ij}}} = \sum_{j=1}^{N} \left[\frac{y_{ij}-f(x_j)}{\sqrt{y_{ij}}}\right]^2 \qquad \text{IV.18}$$

The residues are defined as

$$R_j = \frac{y_{ij}-f(x_j)}{\sigma_j} \qquad \text{IV.19}$$

Each y_{ij} belongs to a different parent population with mean $f(x_j)$. Once $[y_{ij}-f(x_j)]$ is divided by σ_j, all the residuals are encompassed into one parent population. The residuals are plotted versus x_j for every fit. They would be randomly distributed around zero for a good fit.

A histogram of the residuals was drawn for each fit. The range of the residuals was divided into a hundred slots. The histogram was fitted with a Gaussian using three parameters.

1) mean of histogram
2) standard deviation of histogram
3) probability normalization factor.

A good fit should have a histogram which follows the Gaussian envelope closely.[40]

An additional criteria for the consistency of the data is that the observations be randomly distributed within the histogram. The data points are plotted in sequential order, versus their histogram frequency of occurrence.

Apart from using two different standard deviations, the fits were performed for the following cases:

1) Using all the generated data points.
2) Neglecting the points surrounding the smaller peak corresponding to transitions involving the $3^2S_{1/2}$, F=1 state.

3) With one set of intensity normalization factor, Voigt HWHM and ratio of Lorentizian over Gaussian HWHM.

4) With two sets as in 3 , one for each peak in the D_2 line.

The errors in the quantities calculated through the parameters are obtained by using[41]

$$\sigma_x^2 = \sum_{k=1}^{n} \left(\frac{\partial x}{\partial \beta_k}\right)^2 \Delta\beta_k^2 \qquad \text{IV.20}$$

where x is the quantity of interest, β_k is the parameter, $\Delta\beta_k^2$ is the variance of the parameter and n is an integer signifying the number of parameters. Equation IV.20 holds if the parameters are uncorrelated. For errors including a systematic component equation IV.20 yields too large a standard deviation. Systematic errors will occur if optical pumping, saturation effects, absorption effects or excessive laser frequency jitter are present.

D. Experiment

1. Free Stream Flow Investigation

The Doppler shifted spectrum obtained by shining the laser into the seeded flow and collecting the fluorescence signal from the probe volume is depicted in Figure IV.12. There are somewhat more than 600 data points represented by the crosses. The continuous line is a fitted Voigt function discussed in section IV.C, and Appendix A. The two noisy spectra on the left are due to the unshifted sodium D_2 line obtained from the atomic beam device. The three vertical lines inside each peak corresponding to the tunnel spectrum represent the theoretical line strength and location along the frequency axis of each hyperfine transition as determined by the fitting routine.

The Doppler shift furnishes the velocity component along the laser beam direction. For Mach number calculations, the total velocity vector has to be determined. A velocity vector in a plane parallel to the tunnel axis was measured by using two different laser beam angles.

The bottom of figure IV.12 includes a plot of the residuals. Figures IV.13 and IV.14 depict the histogram and the frequency of occurrence of the observation points within the histogram respectively. It was established that using $\sigma_i = \sqrt{y_i}$ is preferred over $\sigma_i = 1$ (Section IV.C), since then the histogram follows the Gaussian envelope more closely and the distribution of data points within the histogram is more random. These two tests are not very sensitive since they do not indicate the presence of systematic errors very well. By fitting one peak out of the two in Figure IV.12 and comparing the other with that predicted by the fit one can determine whether optical pumping, absorption effects, saturation or laser frequency jitter have affected the measurement.

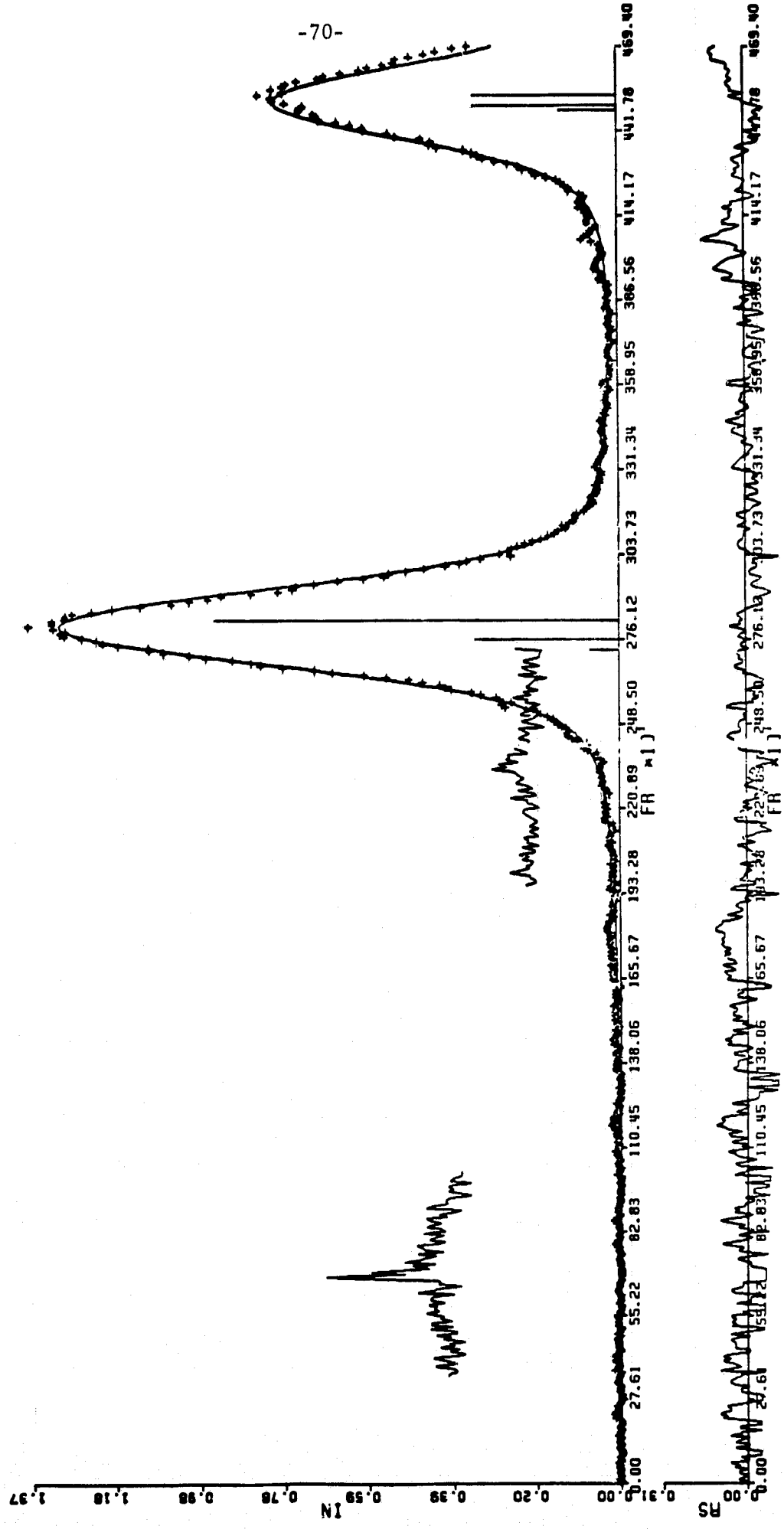
IN
0.00
0.20
0.39
0.59
0.78
0.98
1.18
1.37
RS
0.00
0.31
27.61
55.22
82.83
110.45
138.06
165.67
193.28
220.89
248.50
276.12
303.73
331.34
358.95
386.56
414.17
441.78
469.40
FR (1)

Figure IV.12

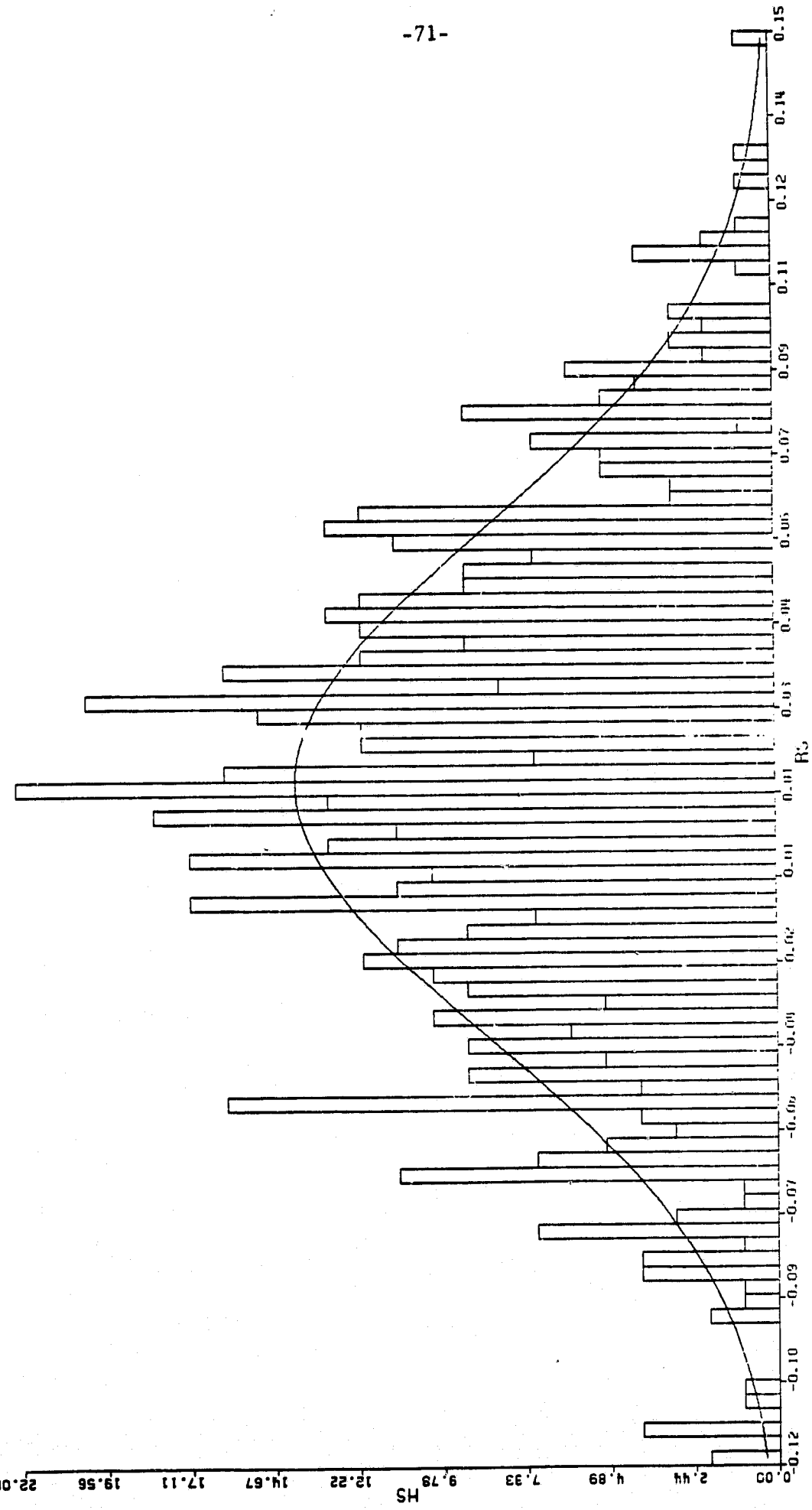
0.03
2.44
4.89
7.33
9.79
12.22
14.67
17.11
19.56
22.00
HS
0.15
0.14
0.12
0.11
0.09
0.07
0.06
0.04
0.01
-0.02
-0.04
-0.06
-0.07
-0.09
-0.10
-0.12
RS

Figure IV.13

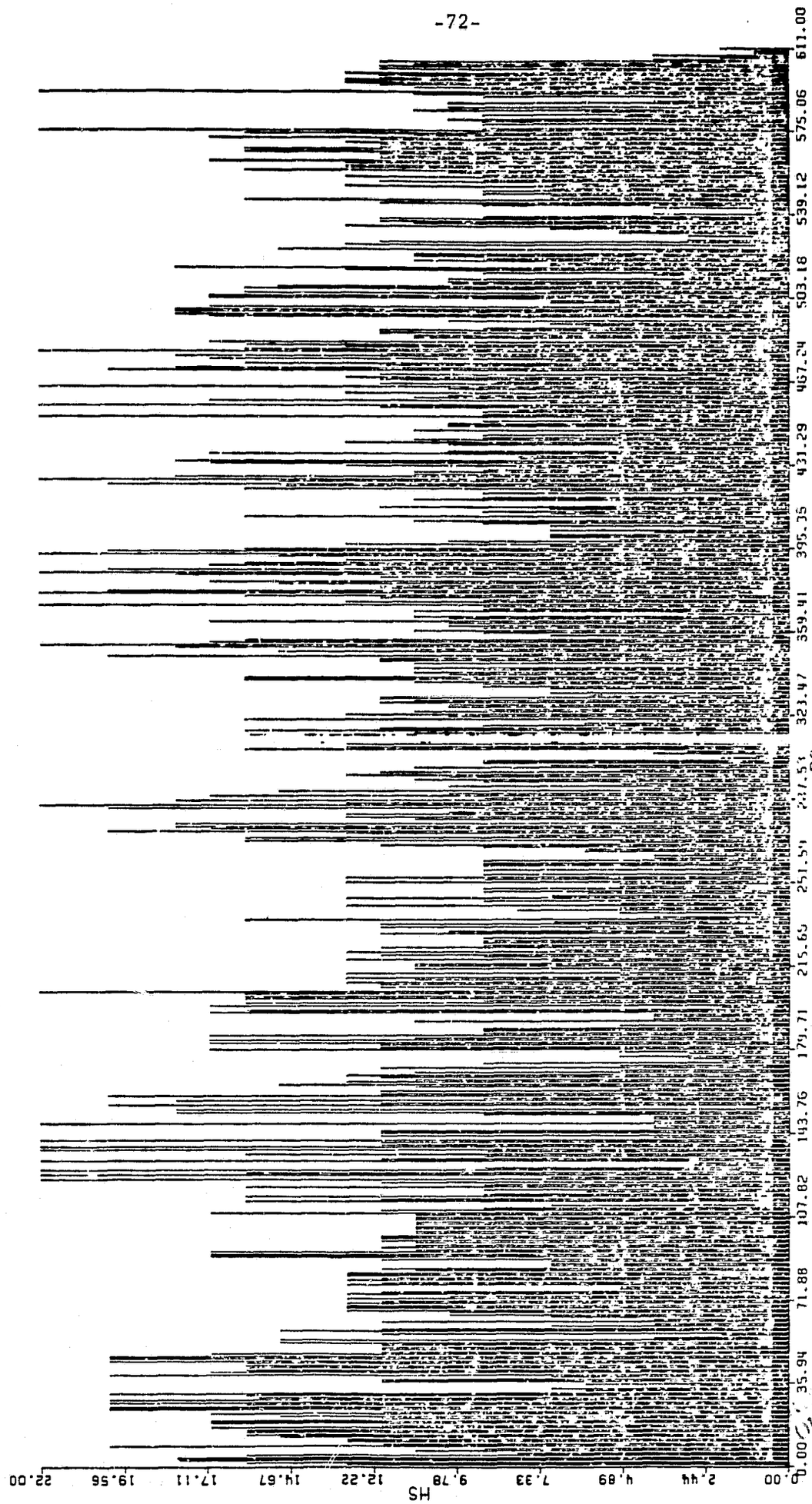

Figure IV.14

The larger peak has been chosen for the fit since it contains more points, particularly in the low frequency tail. The tail of the spectrum is affected mostly by the Lorentzian component of the HWHM as discussed in Appendix A. Absorption effects tend to raise the intensity of the experimental observations of the smaller peak. Optical pumping tends to lower the intensity of the experimental observations of the smaller peak, a similar effect is observed due to the laser frequency jitter. Laser frequency jitter also tends to distort the lineshape.

The quality of the data does not have much of an affect on velocity and Voigt HWHM measurement, but has a strong affect on the ratio of Lorentzian to Gaussian linewidths. These three quantities, the velocity, the Voigt HWHM and the ratio of Lorentzian to Gaussian linewidths, remain constant within the experimental accuracy throughout the hypersonic core in the tunnel. By applying the single peak fit criterion of "Goodness of Fit" one obtains the values based on four fits summarized in Table IV.2.

The velocity uncertainty is based on the laser frequency jitter as determined from the atomic beam device spectrum. The uncertainty of ±16 m/sec is an absolute error and does not depend on the value of velocity measured.

Time of flight broadening is neglected as it contributes less than 0.5 MHz to the HWHM for a Gaussian beam waist radius of 0.001 m. (equation A.55). The scaling of the collision cross section, σ_c, with temperature may be determined by the expression

$$\Delta w_c = \sigma_c n \bar{u} \qquad \text{A.66}$$

where Δw_c is the collision HWHM, n is the number density and $\bar{u}$ is the relative atomic velocity. The collision HWHM is clearly a function of two

Table IV.2

Voigt HWHM (Half Width at Half Maximum)	141±2 MHz
Ratio of Lorentzian over Gaussian HWHM	0.43±0.03
Collisional HWHM	48±3 MHz
Gaussian HWHM	107±3 MHz
Temperature	8±0.4°K
Pressure	0.56±0.03 torr (75±4 Pa)
Mach Number	11±0.3
Collisional Cross Section	$(187\pm14)\ 10^{-6}\ cm^2$
Velocity Component Along Laser Beam	1265±16 m/sec
Velocity Vector	1749±28 m/sec

thermodynamic variables; the density and the temperature, T, since the relative velocity, $\bar{u}$, is a function of temperature

$$\bar{u} = \sqrt{\frac{8kT}{\pi\mu}} \qquad \text{A.64}$$

where k is the Boltzmann constant and μ is the reduced mass. Equation A.66 may be expressed in terms of the collision HWHM over the density.

$$\frac{\Delta w_c}{n} = \sigma_c \bar{u} = KT^{\alpha} \qquad \text{IV.21}$$

where K and α are constants. This equation was fitted to two data sets. One obtained during this experimental investigation at 8°K (Table IV.2) and the other obtained by McCartan and Farr[25] at 415°K. The value obtained for α is 0.38±0.03 which is lower than α = 0.41 as calculated by Lewis and McNamara[42] (Appendix A).

2. Double Beam Experiment

The spectrum obtained by shining the laser into the tunnel with a mirror reflecting the beam back on itself is shown in Figure IV.15. The first and second peaks are the Doppler down shifted D_2 manifold. The third and fourth peaks are the Doppler upshifted D_2 manifold. The downshifted peaks are smaller in intensity since they are due to the reflected laser beam which has undergone more transmission and reflection losses.

The same computer fitting routine is used as that for the single beam experiment with two additional parameters. One is the frequency, F2, of the $3^2S_{1/2}$, F=2 → $3^2P_{3/2}$, F=1 transition and the other is the intensity normalization factor, I2, corresponding to the downshifted laser beam.

The ratio of the Lorentzian to Gaussian width and the Voigt HWHM are assumed equal for all transitions. The different variables are obtained in the same manner as before. The velocity may also be calculated by

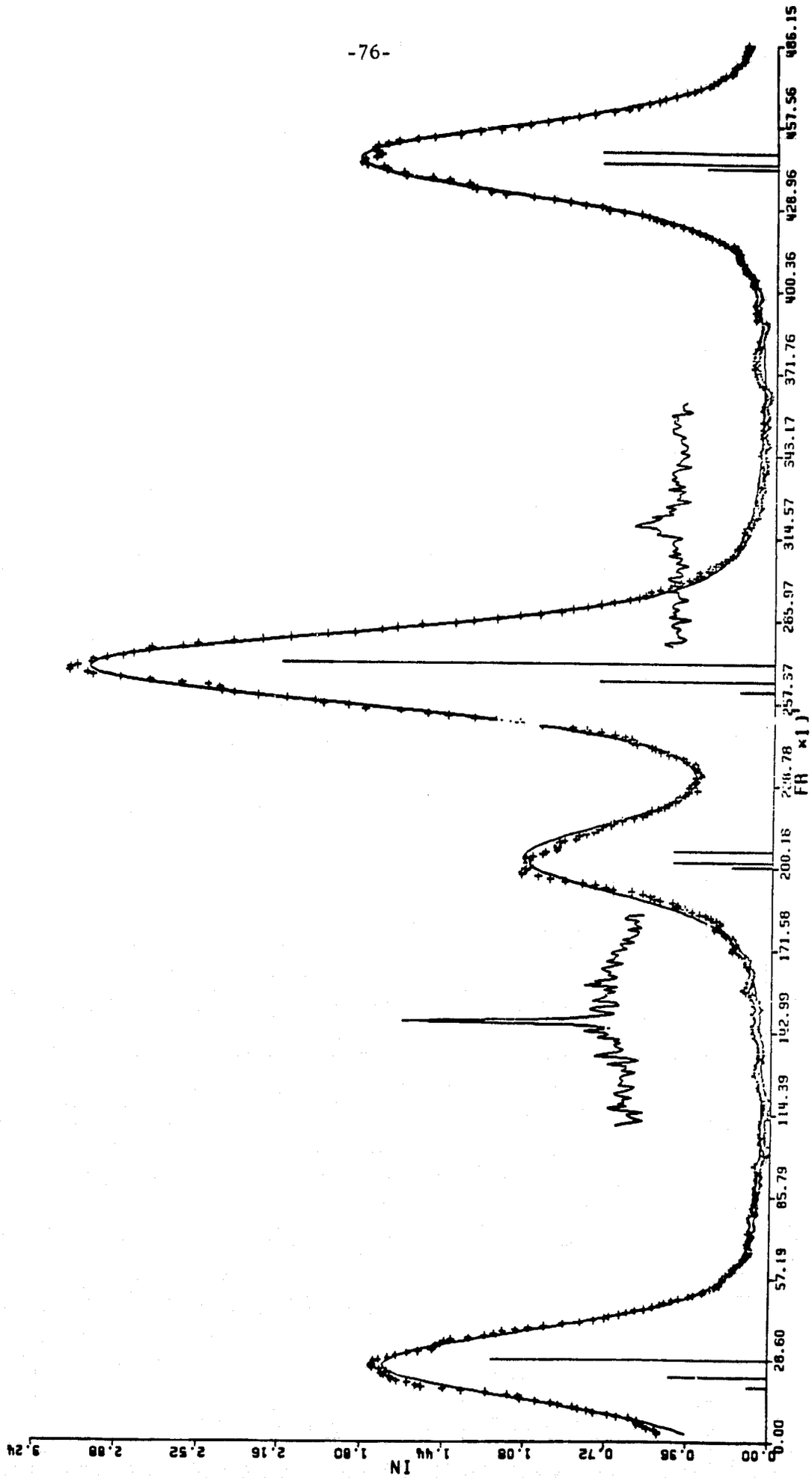
IN
0.00
0.36
0.72
1.08
1.44
1.80
2.16
2.52
2.88
3.24
0.00
28.60
57.19
85.79
114.39
142.99
171.58
200.18
228.78
257.37
285.97
314.57
343.17
371.76
400.36
428.96
457.56
486.15
FR ×1)

Figure IV.15

halving the Doppler shift between any two transitions connecting the same hyperfine levels. The values obtained by deconvoluting the spectrum are essentially the same as for the single beam experiment of the last section apart from the velocity sensitivity which is appreciably improved. The improvement in the velocity measurement accuracy is due to a more accurate frequency calibration scheme. Calibration is established in this experiment by assuming a frequency (ν) versus ramp voltage (v) relation of the form

$$\nu = c_1 v^2 + c_2 v \qquad \text{IV.22}$$

The constant c_1 and c_2 are additional parameters determined by the least squares routine. Figure IV.16 depicts the calibration method performed in conjunction with the fitting process. For this presentation only one transition per peak is assumed. The top graph is the spectrum intensity versus ramp voltage. The bottom graph is the laser frequency versus the ramp voltage. The frequency separation in the manifold, $\Delta\nu$, is known from the literature. One may therefore write

$$\begin{aligned} \Delta\nu &= c_1(v_2^2 - v_1^2) + c_2(v_2 - v_1) \\ \Delta\nu &= c_1(v_4^2 - v_3^2) + c_2(v_4 - v_3) \end{aligned} \qquad \text{IV.23}$$

c_1, c_2, v_1, v_2, v_3 and v_4 are all determined by the least squares routine. In the present experimental work all the hyperfine transitions in the D_2 manifold are utilized for the calibration. Nine instead of just seven parameters are used the two additional ones being c_1 and c_2. The effect of laser frequency drift is also minimized by the calibration scheme. This calibration is employed in the interpretation of all the spectra.

Since the laser frequency jitter is associated with a time which is much shorter than the one second scan time through one of the broadened peaks, this frequency jitter is averaged. The averaging process is an additional reason for a better velocity measurement accuracy. The uncertainty obtained is ±2 m/sec, an absolute error which does not depend on the value of the measured velocity. The total temperature, T^t, of the flow is calculated using the expression[36]

$$T^t = \frac{u^2}{2c_p} + T \qquad \text{IV.24}$$

where u is the flow velocity, c_p is the specific heat at constant pressure and T is the static temperature. The spectroscopically calculated values are depicted in Figure IV.17, by the crosses which signify error bars. The ordinate represents the total temperature, T^t, and the abscissa is the distance from the center line. The errors are mainly due to an uncertainty in the measurement of the angle between the laser beam and the wind tunnel axis. The five crosses with a black dot in their centers are measurements taken on the center line during five, six minute duration, wind tunnel runs. Each corresponds to an average taken over three to seven laser scans. The five are separated along the abscissa for graphical presentation only. The solid line represents the thermocouple total temperature measurement. The shaded area is the error associated with that measurement. It is due to an uncertainty of ±2°K and ±0.008 in the value of the adiabatic wall temperature and the recovery ratio respectively. The total temperature and its uncertainty based on the thermocouple measurement are not sensitive to the value of the static temperature. The static temperature obtained from isentropic calculations (Section II.B) was used. The discrepancy between the crosses and the solid line are due to a systematic

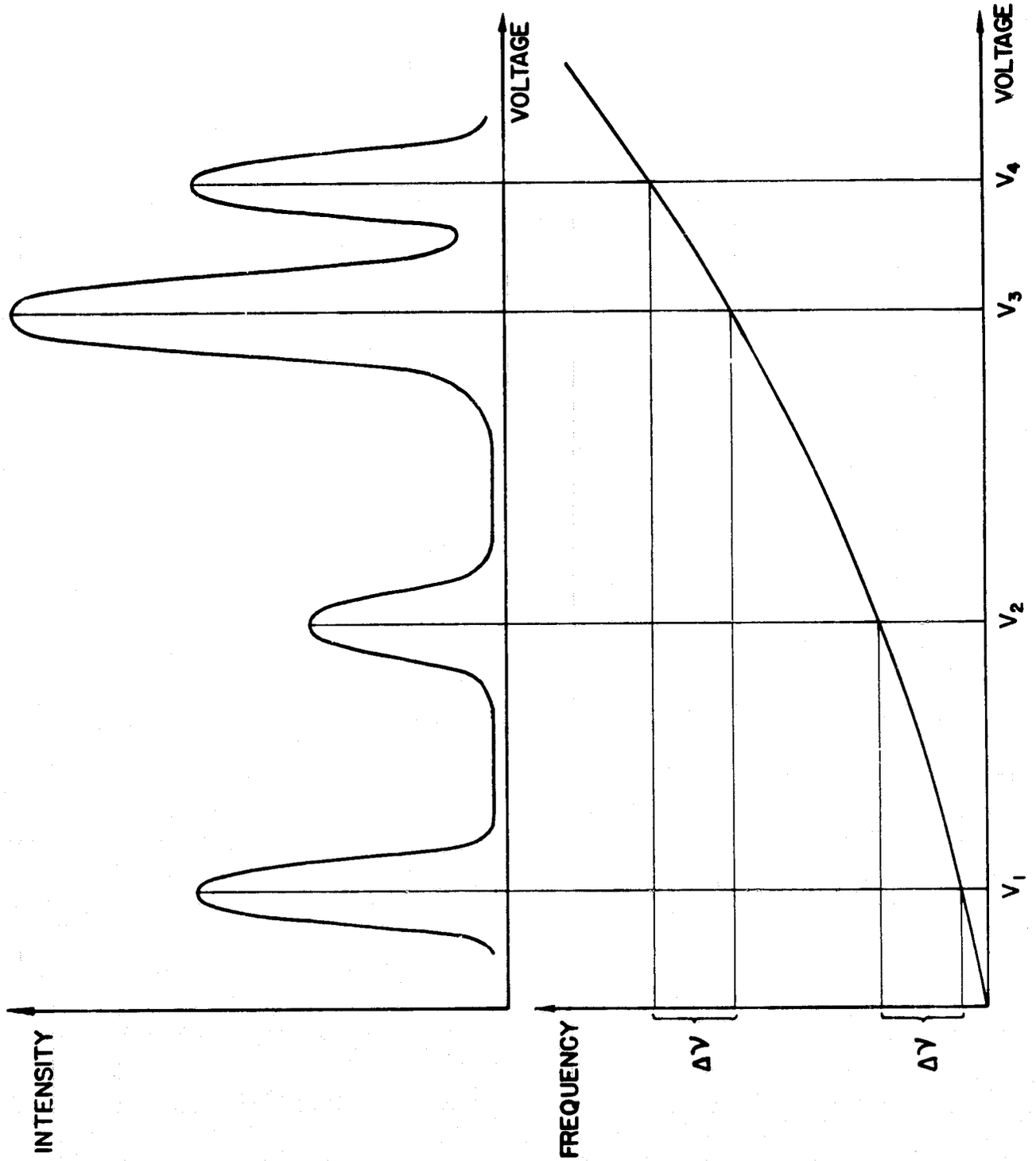

Figure IV.16

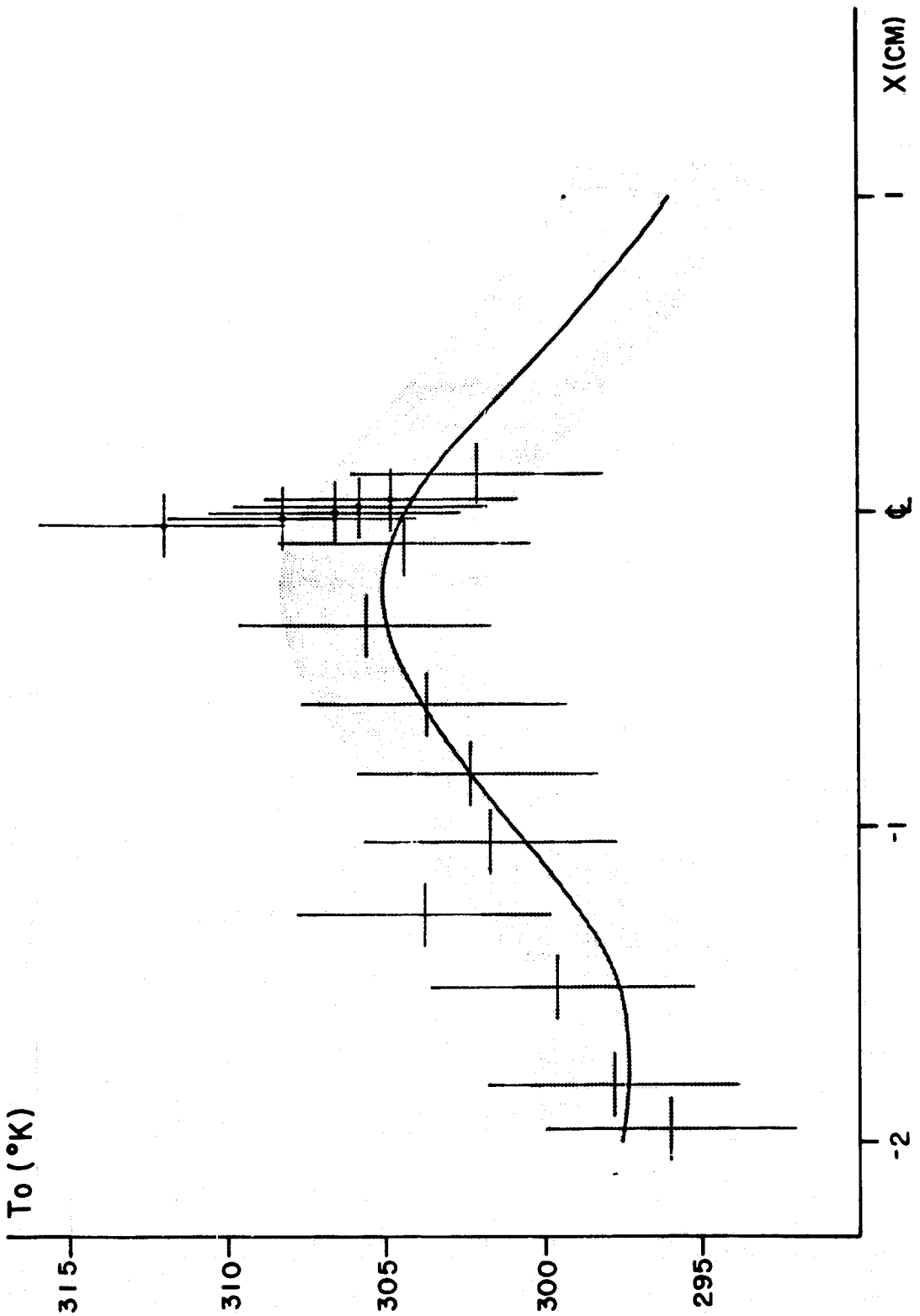

Figure IV.17

error in the measurement of the angle between the laser beam and the wind tunnel axis of symmetry.

3. Cone Flow Field Investigation

A 10° half angle cone was mounted in the test section, with the apex 0.067±0.001 m upstream of the measuring station. The pitot probe survey at the measuring station is shown in Figure IV.18. The abscissa is the distance from the wall and the last point is the cone surface. The probe volume was scanned across the tunnel diameter from the inviscid region into the shock and boundary layer of the cone. The temperature and velocity of the flow were calculated from the spectroscopic data as in Section IV.D.1. The sodium helium collision cross section obtained from the free stream flow conditions was used to spectroscopically determine the pressure in the vicinity of the shock and inside the boundary layer. This is a good approximation since the main temperature dependence of the pressure broadening mechanism is due to relative velocity and density effects and not to the cross section as discussed in Appendix A. The results are presented in Table IV.D.3.

The uncertainties in the relative position of the points are 0.003 inches. The position of the cone surface is known to within 0.01 inch. The static pressure in the free stream based on the pitot survey is calculated using the spectroscopically determined Mach number. The velocity vector in the free stream is inclined at an angle, α, of 43°40' from the laser beam. The velocity vector downstream of the shock is calculated assuming a (maximum) stream line turning angle of 10°. This changes α to 44°30' (maximum). The pressure and temperature on the cone surface from compressible flow relations are 4.1 torr (547 Pa) and 27.7°K respectively.

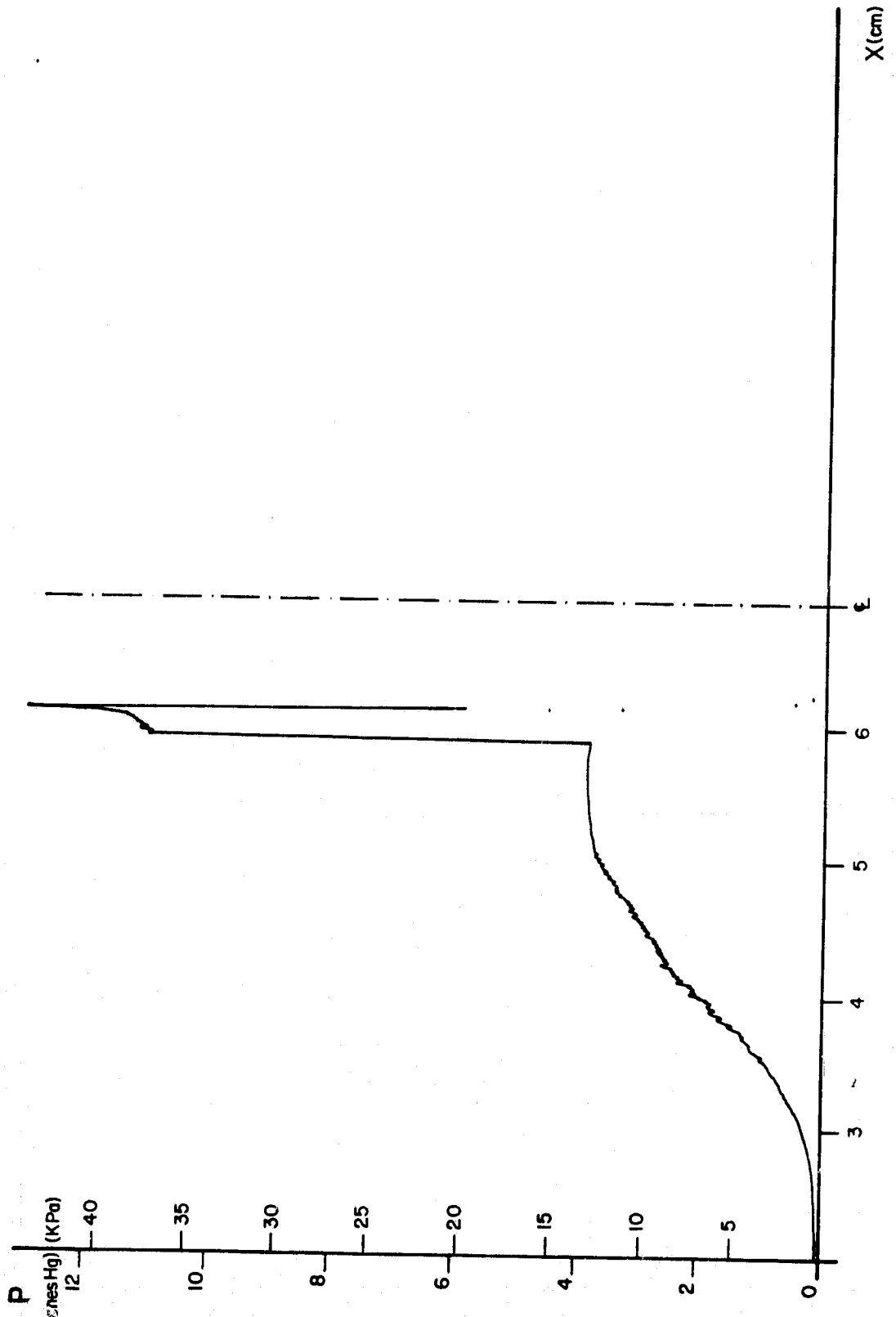

Figure IV.18

Table IV.2

Distance from center line (cm)	1.97	1.69	1.20	1.09	1.05	1.01	0.97
Distance from cone surface (cm)	1.16	0.88	0.39	0.28	0.24	0.20	0.15
Spectroscopic static temperature (°K)	7.7±0.3	8±0.2	7.7±0.3	14.3±1.5	28.4±1.6	42.5±3.6	
Spectroscopic static pressure (torr)	0.53±0.03	0.56±0.03	0.56±0.03	1.08±0.12	2.16±0.14	3.23±0.29	
Spectroscopic static pressure (Pa)	71±4	75±4	75±4	144±16	288±19	431±39	
Velocity component (m/sec)	1289±16	1260±16	1248±16	1215±16	1208±16	1206±16	1177±16
Velocity vector (m/sec) $\alpha = 43°40'$	1782±28	1742±28	1725±28				
$\alpha = 44°30'$				1703±28	1694±28	1691±28	1650±28
Spectroscopic Mach number	11.3±0.3	10.9±0.2	11±0.3	7.9±0.4	5.6±0.2	4.5±0.2	

The calculation is based on the free stream Mach number obtained from the pitot surveys.

The pressure, P, temperature T, velocity component, u_L, velocity vector, u and Mach number, M, are depicted in Figures IV.19 and IV.20 along the ordinate. The solid line is the pitot pressure survey drawn for position comparison while the abscissa is the distance from the cone's surface. The data near the cone's surface is less reliable due to strong light scattering and a weakening of the fluorescence signal which may be due to a depletion in the number of sodium atoms. The source of this drop in signal intensity is unknown, but may be caused by loss of sodium to the cone's surface.

For flow visualization purposes the laser beam is expanded into a sheet of light by using two cylindrical lenses as shown in Figure II.6 The normal to the light sheet lies in the plane of the figure. A 10° half angle cone was mounted in the test section. The resulting picture is shown in figure IV.21. Since the shock forms a cone around the model, its intersection with the sheet of light produces an ellipse. The long axis of this ellipse is hidden by the model. The fluorescence is more intense downstream of the shock since the density is larger and the laser is tuned to a frequency which highlights the particular velocity existing behind the shock. The shock angle measured by drawing a line from the cone tip tangent to the fluorescing ellipse is 13°50'±10'. This corresponds to a Mach number of[31] 7.34±0.34. The Mach number obtained from the spectroscopic calculation is 11±0.3. The discrepancy is related to hypersonic interaction. Since the shock angle in hypersonic flows is very shallow, the shock interacts with the boundary layer near the tip of the cone. The cone appears to the flow with a virtual half angle which is larger than the

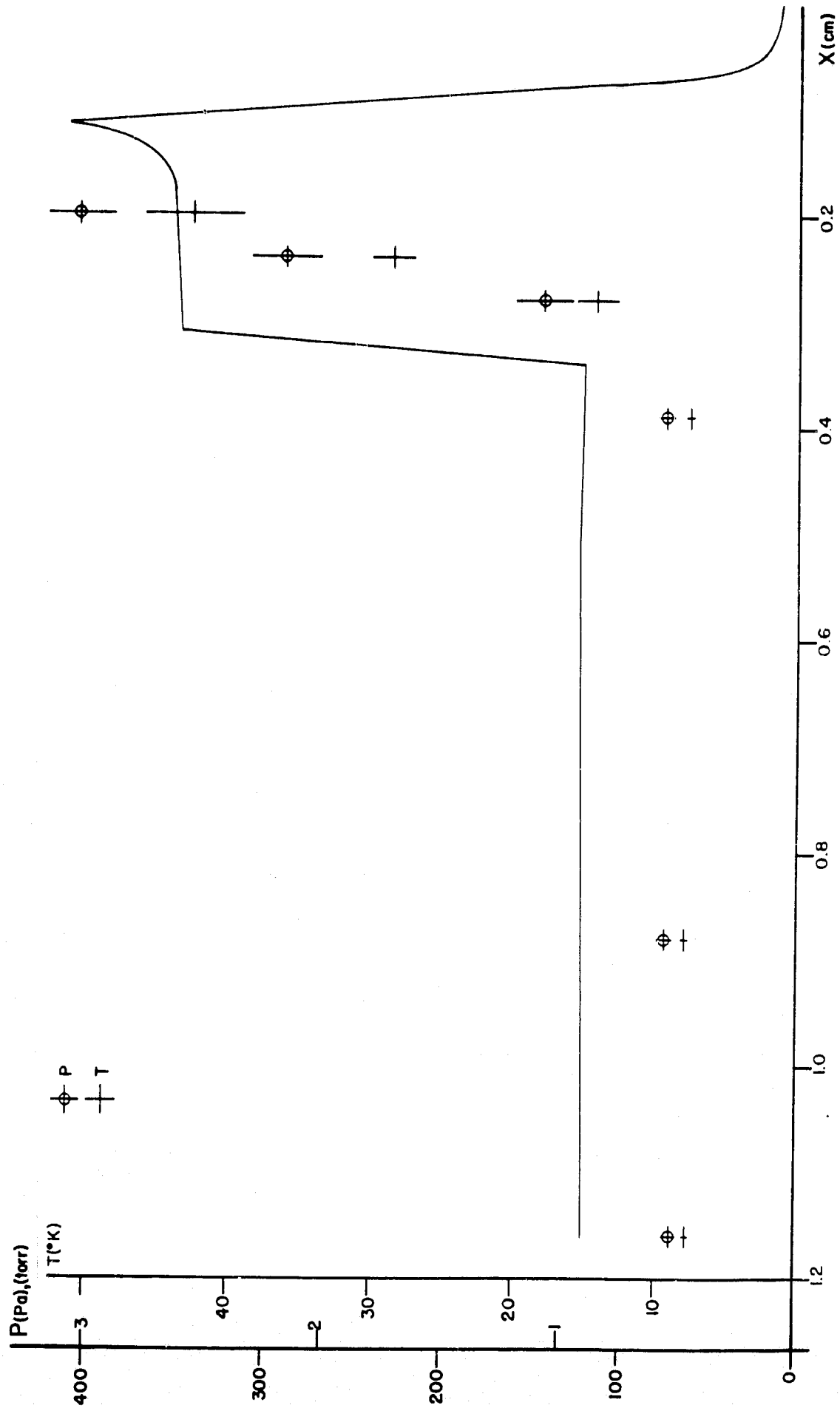
P(Pa),(torr)
T(°K)
400
300
200
100
0
3
2
1
40
30
20
10
P
T
0.2
0.4
0.6
0.8
1.0
1.2
X(cm)

Figure IV.19

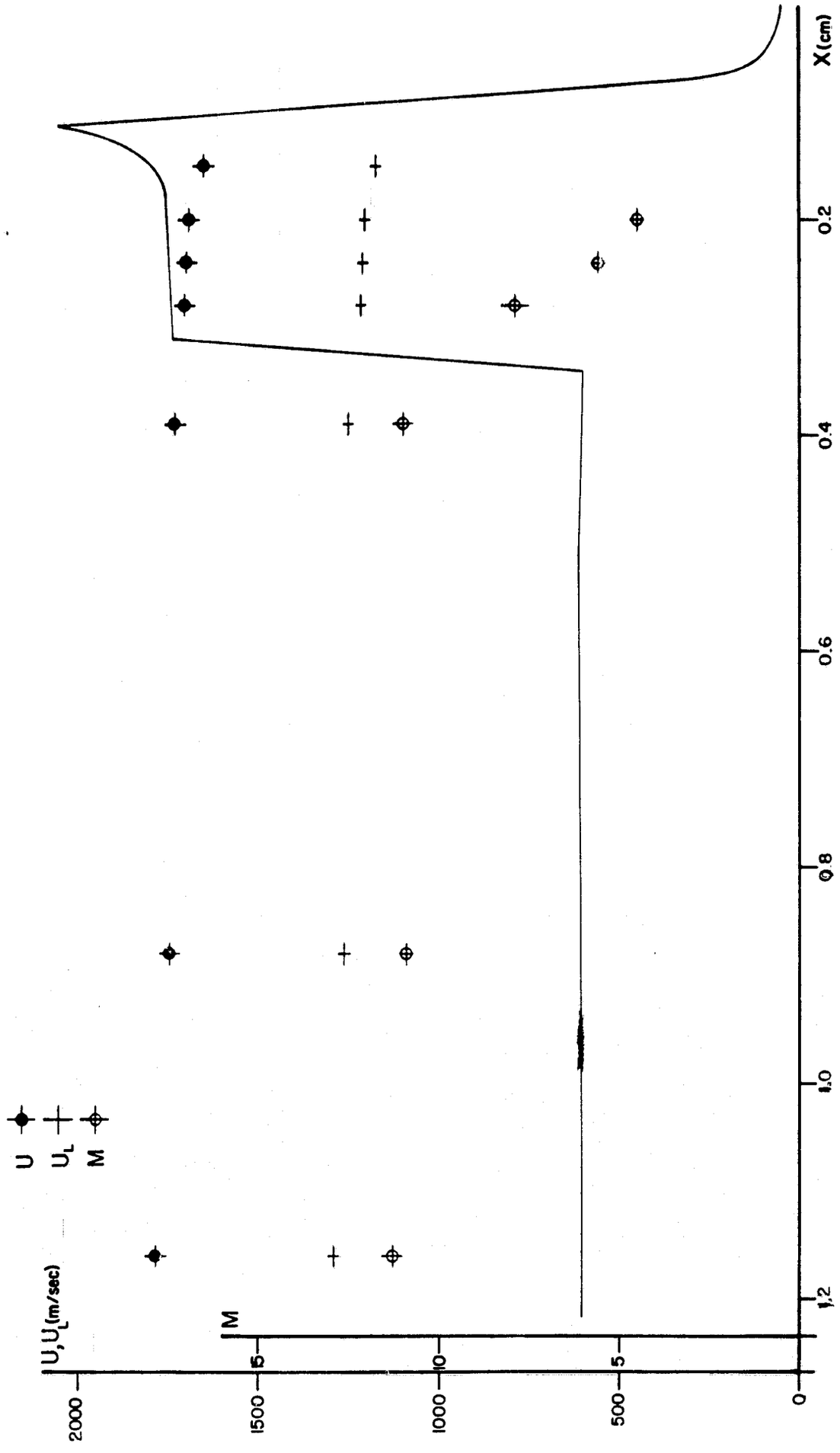

Figure IV.20

C-2

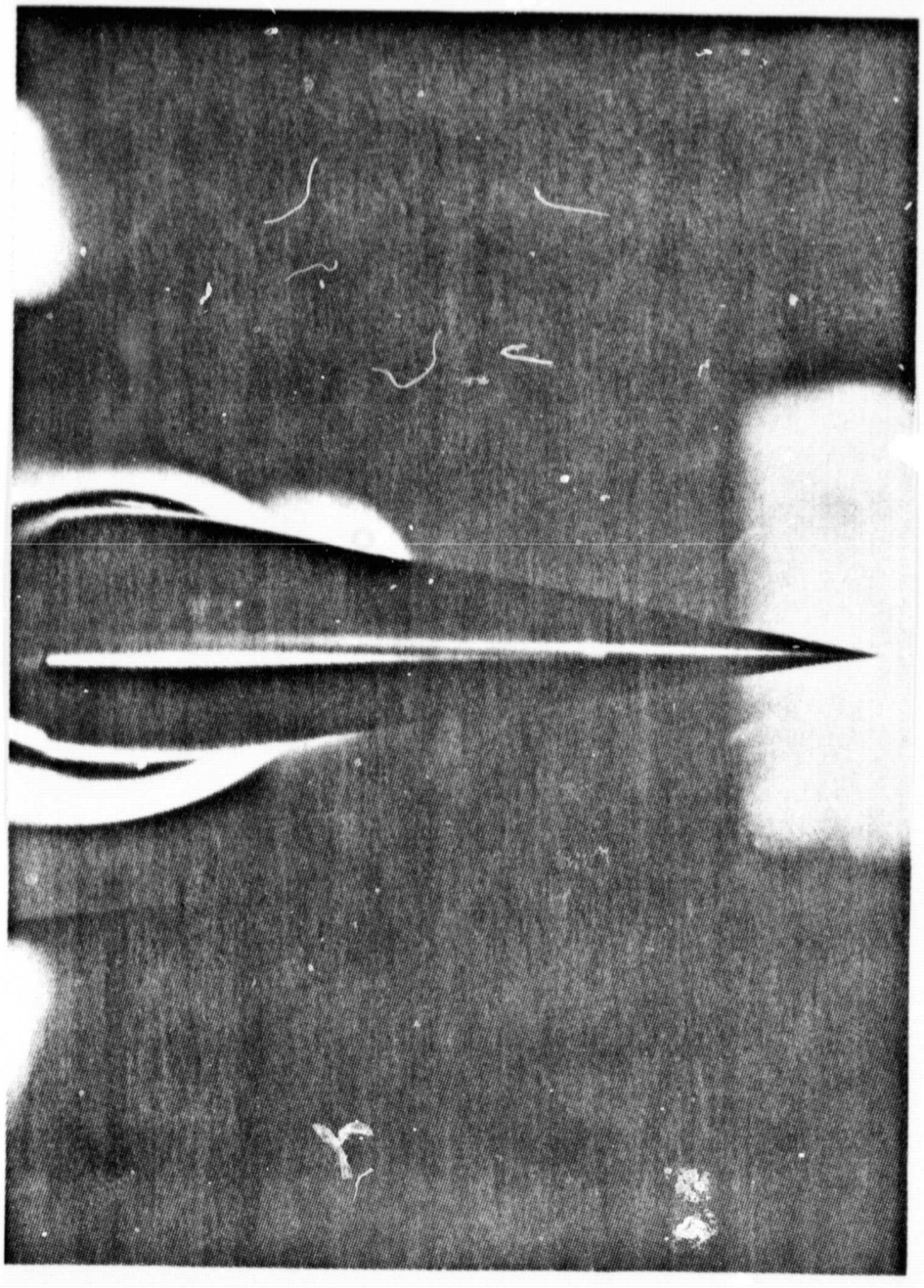

Figure IV.21

real half angle. The interaction weakens further downstream since the shock moves into the inviscid flow. The shock is therefore curved especially near the tip and one may not calculate its angle as outlined.

Chapter V

CONCLUSIONS AND SUGGESTIONS FOR FURTHER STUDY

A. Conclusions

1. Introduction

As a result of the experimental work described in this thesis, the Resonant Doppler Velocimeter (RDV) technique has been established as a means of measuring average components of temperature and velocity in compressible helium flows. Furthermore, the sodium helium collision cross section at low temperature was determined using the spectroscopically measured temperature and collision line broadening coupled with a pitot tube measurement of the pressure in the free stream.

Using the cross section data, the RDV technique is capable of simultaneously measuring velocity, temperature and pressure. This was demonstrated by mapping the flow field in the vinicity of a conical model.

2. Doppler Shift Uncertainty

The Doppler shift and the resulting velocity uncertainties are summarized in Table V.1.

Table V.1

	single beam	double beam
Doppler shift uncertaintiy (MHz)	28	3
Velocity uncertainty (m/sec)	16	2

The experimental uncertainties are due to counting statistics, instrumental uncertainties and systematic errors. An inspection of the Doppler

shift data indicates that the position of the spectra (from the atomic beam device and the wind tunnel) along the frequency axis and not their shape is responsible for the uncertainty in measurement. The limiting factor influencing the position of the spectra is the laser frequency jitter and drift. The error in velocity measurements is thus absolute. Hence, the larger the measured velocity component, the smaller the relative error.

No averaging of the frequency jitter was performed with the atomic beam spectra since the jitter was larger than twice the natural HWHM of sodium. Frequency jitter averaging was possible with the tunnel spectra (through the use of the data reduction scheme with the Least Square routine) since twice the Voigt HWHM is an order of magnitude larger than the laser frequency jitter. The large velocity uncertainty associated with the single beam experiment reflects the lack of averaging with the atomic beam device spectra.

Were the laser frequency jitter and drift and systematic errors to be eliminated, then the sensitivity for average velocity measurements would be limited by counting statistics and turbulence. The effect of turbulence on the average measurements depends on the relative value of the characteristic turbulence time and the time it takes the laser to scan through the spectrum. If these times are of the same order, then the turbulence would be manifested through an erroneous linewidth measurement. For a scanning time shorter than the turbulence time, scan to scan inconsistencies would occur in the velocity measurement though the linewidths would not be appreciable effected. Random noise is added to the counting statistics if the scanning time is longer than the turbulence time. The scanning time has to be adjusted for the latter possibility since only then can averaging be performed. Longer scans also improve counting statistics.

With an actively stabilized laser incorporating a feedback loop one can easily obtain jitter which is smaller than 1 MHz. This is smaller than the natural HWHM of sodium. Since the natural lineshape is a Lorentzian it may be fitted using a Least Squares routine to find the position of all the hyperfine transition frequencies within the sodium D_2 manifold. A lower than 0.59 m/sec velocity uncertainty can be expected using a laser stabilized to 1 MHz. This is due to the fact that frequency jitter averaging is then facilitated not only with the wind tunnel spectra but also with the atomic beam spectra through the fitting process.

3. Linewidth Uncertainties

The temperature, cross section and pressure sensitivities due to linewidth measurement uncertainties are summarized in Table V.2.

Table V.2

Temperature Uncertainty	5%
Cross Section Uncertainty	9%
Pressure Uncertainty	10%

The quantities in Table V.2 are calculated from the Lorentzian and Gaussian linewidths (Section IV.C). These in turn are derived from the Voigt HWHM and the parameter which is defined (Appendix A) as the ratio of the Lorentzian over the Gaussian widths. An inspection of the Lorentzian and Gaussian linewidth data indicates that their measurement sensitivity was limited by the uncertainty in the parameter a and not the Voigt HWHM. The value of a is influenced appreciably by the presence of systematic errors in the spectrum (Section IV.C) and by a low signal to noise ratio (due to counting statistics).

4. Scan Limitations

The tunnel operating time of six minutes was too short to allow for the optimization of the power supply settings (to maximize the signal to noise ratio or to suppress absorption effects). It takes the temperatures of the different components in the seeding device time to equilibrate. Also, the power supply settings vary from run to run since the quality of helium deteriorates with increasing numbers of purification cycles. Hence only a few laser frequency scans per run were taken.

The tunnel fluorescence intensity was fed to the GMAD/1 which samples during a time smaller than 10 nsec at 330 Hz. The small value of the duty cycle raises severe signal to noise ratio problems. An integrator with a time constant of the order of the reciprocal of the sampling frequency was used in order to alleviate this difficulty. Too large a time constant in some of the laser scans gave rise to spectrum distortions which also caused scan to scan inconsistencies in the value of a.

An improvement can be obtained by scanning the laser in discrete steps and using a photon counting device to collect the signal for a preset time at each frequency. The information stored in the photon counter would be transferred to the computer before the laser shifts to a new frequency. This would eliminate the integrator and the systematic errors associated with its time constant. Since counting is performed, the "Goodness of Fit" criterion (Appendix B and Section IV.C) may be applied to the data.

Photon counting enhances the signal to noise ratio allowing a reduction in the seeded sodium number densities and laser power. A lower sodium density and laser power would suppress the systematic errors due to absorption effects, saturation and power broadening.

5. Flow Perturbation

About 850 watts are injected into the main helium flow in the stagnation chamber with the purge helium flowing through the sodium seeding device. The mass ratio of the two helium flows is less than 0.01. The effect of mass and energy injection into the flow is discussed in this section.

No disturbance to the flow due to sodium injection manifests itself in the pitot surveys (Section IV.B.2). On the contrary, the diameter of the core region seems to enlarge as a result of the presence of the injection needle. The needle tip was positioned 0.1 inch upstream of the throat. The improvement in the core area may be due to the main helium flow undergoing two expansions while flowing past the needle tip. The first expansion occurs at the base and the second at the tip of the truncated cone (part 2, Figure II.C.1). The resulting expansion waves could interact favorably with the compression waves downstream of the throat thus enlarging the core region.

Mach number information cannot be derived from the pitot pressure scans obtained while sodium injection was taking place since the flow then is not isentropic (Section IV.B.2). An additional cause resulting in stagnation pressure loss is the presence of compression waves. The expansion waves emanating from the needle tip are reflected off the nozzle wall. These reflected waves could turn into compression waves if the curvature of the nozzle wall is concave enough.

The Mach numbers obtained from the spectroscopic measurements (Section IV.D.1) and from the interpretation of the cone flow picture (Section IV.D.2) are summarized in Table V.3.

Table V.3

Spectroscopic measurement	11±0.3
Shock angle measurement	7.34±0.34

The shock angle measurement as outlined in Section IV.D.3 is incorrect due to the hypersonic interaction effect. An accurate measurement may be obtained by illuminating the complete flow with an expanded collimated laser beam instead of a sheet of light (Section IV.D.3). The shock angle should then be measured far enough downstream from the cone tip where the hypersonic interaction is negligible. This picture was not taken because of helium supply limitations. A picture of a shock surrounding a pitot probe is presented in Figure V.1 . No quantitative results can be obtained from that picture since the shape of the pitot probe is not a simple one.

Figure IV.17 indicates good agreement between the total temperature thermocouple measurement and the total temperature calculated from the spectroscopic measurements.

6. The Utility of the Technique

The technique has been demonstrated in a hypersonic wind tunnel since the experimental uncertainty in the velocity measurement, limited by laser frequency jitter (Section V.A.2) is absolute. Hence the higher the measured velocity the lower the relative error.

A meaningful deconvolution of the Voigt profile to obtain both the temperature and the pressure can be performed only for a parameter a on the order of one (Appendix A). This requirement dictates the preferred range of values for the temperature and pressure in the test section of the wind tunnel.

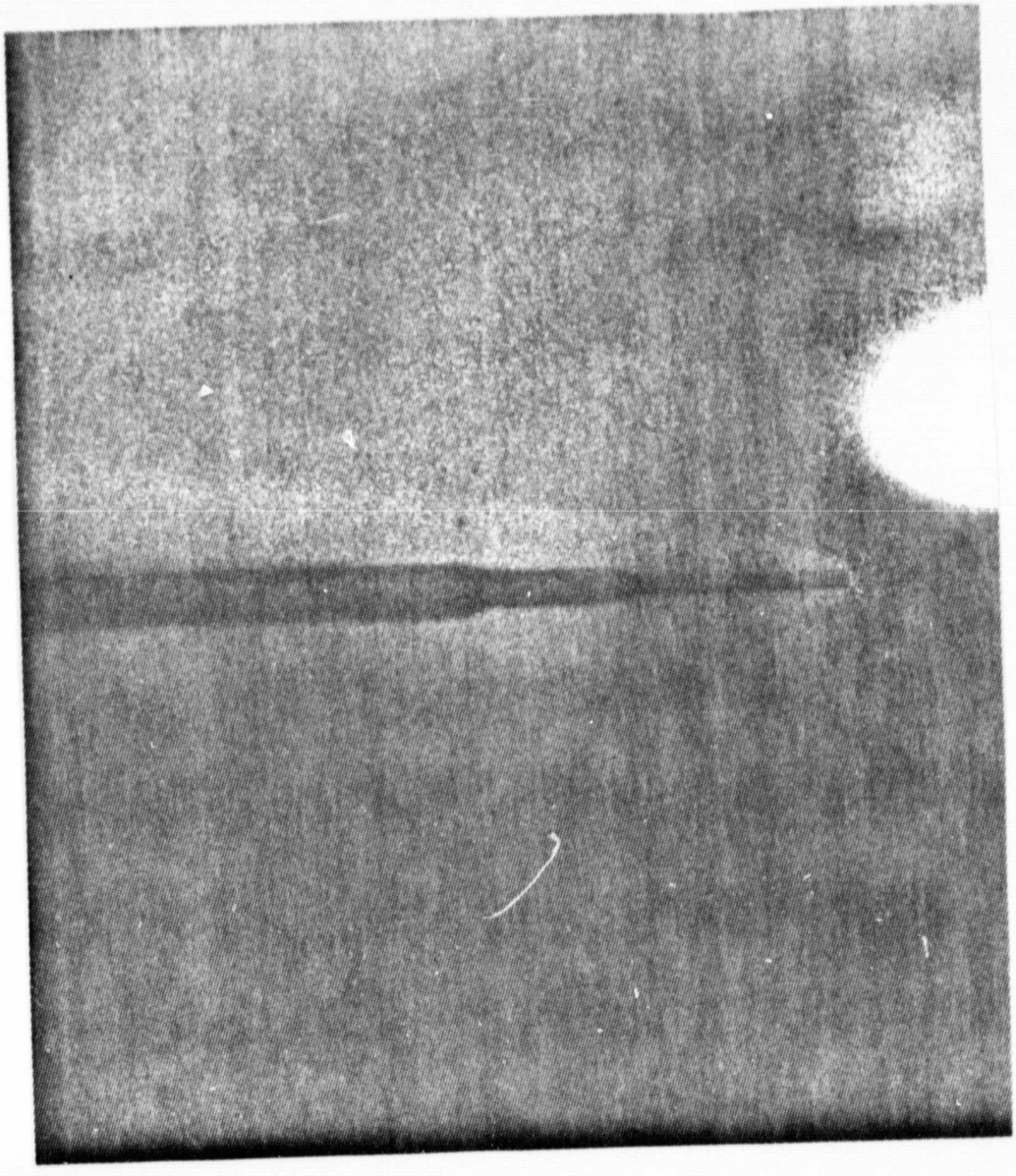

Figure V.1

Helium was used as the flowing gas since it neither reacts with nor quenches sodium.

As discussed in Section V.A.2, accuracies of the order of centimeters per second can be expected with a 1 MHz linewidth laser. Hence the measurement of velocities much lower than those encountered in this experimental investigation would be possible while still keeping the relative error down. The experimental facility is currently undergoing modification in an effort to utilize the technique in a Mach 2.9 nitrogen flow.

B. Suggestions for Further Study

1. Simultaneous Multipoint Data Collection

The spatial resolution in the flow field measurements are due to the lens aperture combination mounted in front of the photomultiplier tube and the focusing of the laser beam. The flow field properties in a plane can be measured by illuminating a plane with an expanded laser beam and imaging into a photodiode array. The size of the plane is determined by the magnification of the collection optics and the area of the array. The spatial resolution will be limited by the matrix density of the array and the number of channels which the data acquisition system is able to handle.

2. Multiple Velocity Components

The Doppler shift facilitates the measurement of the velocity component along the laser beam. Three laser beams intersecting at different angles in the flow will be needed to obtain the velocity vector. A chopper can be used to block all but one beam at a time. The fluorescence intensity picked up by the photomultiplier tube may be fed into the computer and gated by the chopper to separate the components. Using a chopper wheel with two holes along a diameter, one may split the laser beam into three components designated in Figure V.2 by the black dots. The dimensions of the apertures should be such that only one beam at a time intersects the seeded flow.

3. Elimination of the Doppler Effect

Two photon spectroscopy by two counter propagating laser beams has been used to eliminate Doppler broadening.[43] Circularly polarized light has to be employed to suppress the Doppler background from single beam two photon absorption if this type of experiment is performed in a cell.

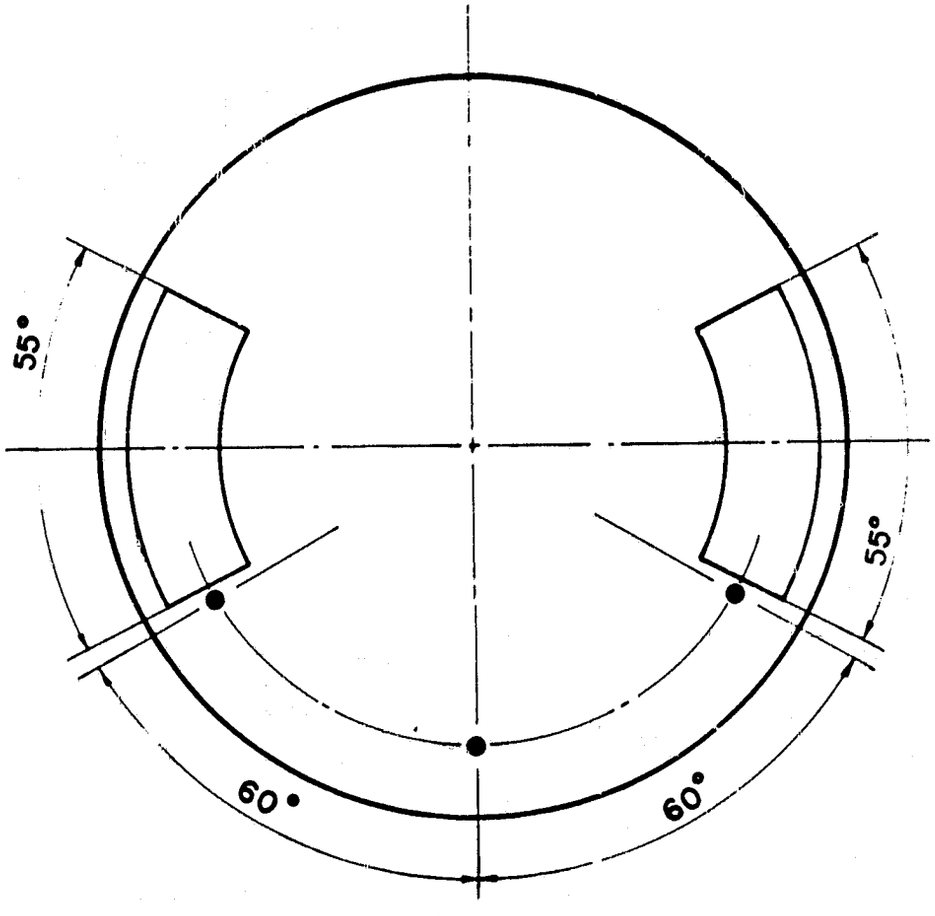

Figure V.2

By applying this technique to spectroscopy in the tunnel, one may eliminate not only the Doppler broadening component but also the Doppler shift due to the convective velocity of the atoms. The use of linearly polarized light causes two Doppler shifted and broadened spectra to appear on both sides of the Doppler free absorption peak in the wind tunnel. Each is due to two photon absorption by a single linearly polarized beam, and, as compared to the spectrum in a simple cell, both of these spectra are well removed from the Doppler free peak.

The velocity may be calculated using as a reference frequency the unshifted absorption peak as in the single beam experiment (Section IV.D.1). The velocity may also be calculated by dividing the shift between the two Doppler broadened spectra into two, to obtain the Doppler shift as in the double beam experiment. The Lorentzian linewidth component is provided by the Doppler free absorption peak. It can be compared to the deconvoluted value obtained from the two side spectra from which the temperature can be determined.

The technique could be useful in turbulence measurements since the pressure and temperature broadening mechanisms can be decoupled.

An additional advantage of two photon spectroscopy is that the excitation and fluorescence frequency are different. Laser scattering can thus be strongly filtered facilitating measurements near surfaces.

The sodium two photon transition with the largest cross section which is accessible with the R6G dye laser is 3S → 4D. The total cross section integrated over the frequency response of the atom is $\sigma_T = 2.8 \times 10^{-19}$ cm^2 MHz (W/cm^2)$^{-1}$.[44] For an irradiance of 15 W/m^2 used in the calculations of Chapter III one obtains $\sigma_T = 4.5 \times 10^{-22}$ cm^2 MHz. The total cross section for the sodium D_2 line is 1.1×10^{-7} cm^2 MHz which is fifteen orders of

magnitude larger.

To improve the signal strength one could seed the flow with more atoms. This is possible due to the fact that trapping is less of a problem for the 3s → 4p transition (3302 Å) than for the D lines since the absorption oscillator strength, f, is only[45] 0.0152 for the 3S → 4P transition. The laser scanning time in this experiment was about 7.3 seconds. Longer scanning times would improve the statistical averaging procedure. The laser power used for a 1 mm Gaussian beam radius was 2.4×10^{-5} W. The power available from the dye laser used in this experimental investigation for a 1 W argon laser pump beam is 50 mW. With this power and with tighter focusing the light intensity could easily be raised much higher, strongly increasing the two photon absorption cross section.

4. Accurate Frequency Calibration

A hot low pressure sodium vapor cell may be used in place of the atomic beam device for a frequency reference. Doppler broadening would predominate in such a cell. A temperature of 373°K results in a Gaussian HWHM of 734 MHz (equation A.31). The laser frequency jitter would be averaged (Section V.A.2) since it is an order of magnitude smaller (Section IV.B.4) than twice the Doppler linewidth in the cell. The calibration of the frequency scale would become possible in a manner similar to the one employed in the double beam experiment (Section IV.D.2) by using the Least Square procedure. A velocity measurement sensitivity of the order of 2 m/sec would be attainable using the suggested experimental setup. Saturation spectroscopy in a sodium cell may also be used as a frequency reference. The advantage to be gained over ordinary absorption spectroscopy in a cell is that the linewidths are adjustable over a wider range. The disadvantage is that

the spectrum is complicated by cross over terms. Saturation spectroscopy of the D_2 line furnishes twelve instead of just six peaks.

A frequency reference cell and its related detection optics is not needed in a double beam experiment. In this case the laser beam has to be reflected back on itself, an experimental requirement which it is not always possible to fulfill. This constraint is removed by employing a hot sodium cell as a frequency reference.

Appendix A

Spectroscopic Properties of Sodium

1. Introduction[46]

Sodium has an atomic number of 11, an atomic weight of 22.9898, a melting point of 97.81°C and a boiling point of 882.9°C. Sodium is a soft bright, silvery metal which floats on water with a specific gravity of 0.97. It decomposes water with the evolution of hydrogen and the formation of NaOH. The flame, characteristic of this reaction in air, is due to the reaction of hydrogen with oxygen to form H_2O. Sodium may or may not ignite spontaneously on water depending on the relative amount of oxide to metal surface area exposed to the water. It normally does not ignite spontaneously in dry air at temperatures below 115°C. Seven isotopes are recognized but only $_{11}Na^{23}$ exists naturally.

The electronic energy levels of sodium and optical pumping are discussed in the next section. Broadening mechanisms are presented in Section VI.A.3. The complete absorption line shape including natural temperature and pressure broadening is derived in Section VI.A.4. The derivation also incorporates saturation and power broadening. This is followed by a short discussion of radiation trapping.

2. Energy Levels of Sodium

The electronic configuration of sodium is $1s^2\ 2s^2\ 2p^6\ 3s^1$. Only the outer shell electron is involved in the transitions corresponding to the visible region of the spectrum. By treating sodium as a hydrogen-like atom with a coulomb potential one obtains energy levels which are dependent on the principal quantum number n = 1, 2, ... only. The orbital angular momentum quantum number (ℓ) degeneracy present in hydrogen is lifted by taking the screening effect of the outer shell electrons into account using the central field approximation. For a definite value of n, then ℓ = 0, 1, ...n-1. Spectroscopic notation associates ℓ = 0, 1, 2, 3, 4, 5, ... with the letters ℓ = s, p, d, f, g, h, ...

Corresponding to each angular momentum $\vec{\ell}\hbar$ there is an associated magnetic moment $\vec{\mu}_\ell$ generated by the motion of the electrons around the nucleus. The electron itself has an intrinsic magnetic moment $\vec{\mu}_s$ by virtue of its charge and spin angular momentum $\vec{s}\hbar$. As a result of the electron's motion in the central electronic field it experiences a magnetic field $\vec{\beta}_\ell$ proportional to its orbital angular momentum $\vec{\ell}\hbar$. The perturbation Hamiltonian is given by

$$E_{\ell s} = -\vec{\mu}_s \cdot \vec{\beta}_\ell = a\vec{s} \cdot \vec{\ell} \qquad \text{A.1}$$

where a is a constant which may be calculated if the central field potential is known.

Capital letters are used to denote total angular momenta for atoms. With this notation

$$E_{LS} = a\vec{S} \cdot \vec{L} \qquad \text{A.2}$$

The angular momenta $\vec{L}\hbar$ and $\vec{S}\hbar$ are coupled by this interaction. To evaluate the energy shifts, linear combinations of the wave functions $|\gamma, L,$

$S, M_L, M_S\rangle$ are taken to form a new zeroth order wavefunction $|\gamma, L, S, J, M_J\rangle$. The total angular momentum quantum number, J, corresponding to the total angular momentum operator

$$\vec{J} = \vec{L} + \vec{S} \qquad \text{A.3.}$$

and the quantum number M_J corresponding to projection of the operator $\vec{J}$ are both good quantum numbers for the new set of wavefunctions. γ represents all other quantum numbers needed to specify the configuration. The values of the quantum number J are restricted to

$$|L - S| \leq J \leq L + S \qquad \text{A.4.}$$

by the usual angular momenta sum rule. As S = 1/2 for a single electron atom, one clearly obtains two values of J for each $L \neq 0$. This interaction together with the relativistic correction to the kinetic energy operator $-\frac{\hbar^2}{2\mu}\nabla^2$ is responsible for the fine structure of the alkali spectra. Specifically each orbital angular momentum quantum number, apart from the ground state has associated with it two energy levels. For example if L = 1 then J = 1/2, 3/2. The usual spectroscopic notation for the atomic fine structure energy levels is $^{2S+1}L_J$. $\vec{L}\hbar$, $\vec{S}\hbar$ and $\vec{J}\hbar$ represent the resultant of all electronic orbital angular momentum $\vec{\ell}_i\hbar$, spin angular momentum $\vec{s}_i\hbar$ and total angular momentum $\vec{j}_i\hbar$ of the individual electrons. The values of $|\vec{S}|$, $|\vec{L}|$, $|\vec{J}|$ are obtained by the usual angular momenta sum rules. The expression $2|\vec{S}|+1$ is known as the multiplicity and represents the number of fine structure energy level splittings. Figure A.1. depicts the energy levels of Na.

Although the spin orbit interaction accounts for the primary splitting of the energy levels, additional effects exist which modify the energy levels still further. In the discussion so far the only property of the

nucleus used was its charge Ze where e is the elementary charge and Z is the atomic number. There are three additional properties of the nucleus which affect the electronic energy levels. First, the energy levels depend on the mass of the nucleus and hence on the specific isotope being used. Second, the nucleus possesses an intrinsic angular momentum $\vec{I}\hbar$. The magnetic moment associated with $\vec{I}$ interacts with $\vec{\beta}_\ell$ the magnetic field produced by the electrons at the nucleus. Third, the nuclear electric quadrapole moment interacts with the electronic electric field gradient produced at the nucleus. The last two effects lead to the hyperfine structure and their corresponding perturbation Hamiltonian is given by [48]

$$H_{HFS} = A_J \vec{I}\cdot\vec{J} + \frac{B_J}{2I(2I-1)J(2J-1)}\{3(\vec{I}\cdot\vec{J})^2 + \frac{3}{2}(\vec{I}\cdot\vec{J}) - I(I+1)J(J+1)\} \qquad \text{A.5.}$$

where the magnetic hyperfine structure constant, A_J, is determined experimentally. The electric quatrupole interaction constant, B_J, is defined by

$$B_J = eQ\langle\frac{\partial^2 V}{\partial z^2}\rangle \qquad \text{A.6.}$$

where Q is the nuclear electric quadrupole moment and $\langle\frac{\partial^2 V}{\partial z^2}\rangle$ is the average of the field gradient at the nucleus over the valence electron. B_J vanishes for I = 0, 1/2 as the nuclear charge distribution is spherically symmetric in these cases. Similarly $B_J$is also zero if J = 0, 1/2 for then the electronic charge density is spherically symmetric and $\langle\frac{\partial^2 V}{\partial z^2}\rangle$ vanishes. Schneider et. al.[49] foung A_J = 18.9 ± 0.3 MHz and B_J = 2.4 ± 0.3 MHz. The angular momenta $\vec{I}\hbar$ and $\vec{J}\hbar$ are coupled by this interaction. To evaluate the energy shift linear combinations of the functions $|\gamma, J, I, M_J, M_I\rangle$ are taken to form a new zeroth order wavefunctions $|\gamma, J, I, F, M_F\rangle$. The total angular momentum quantum number

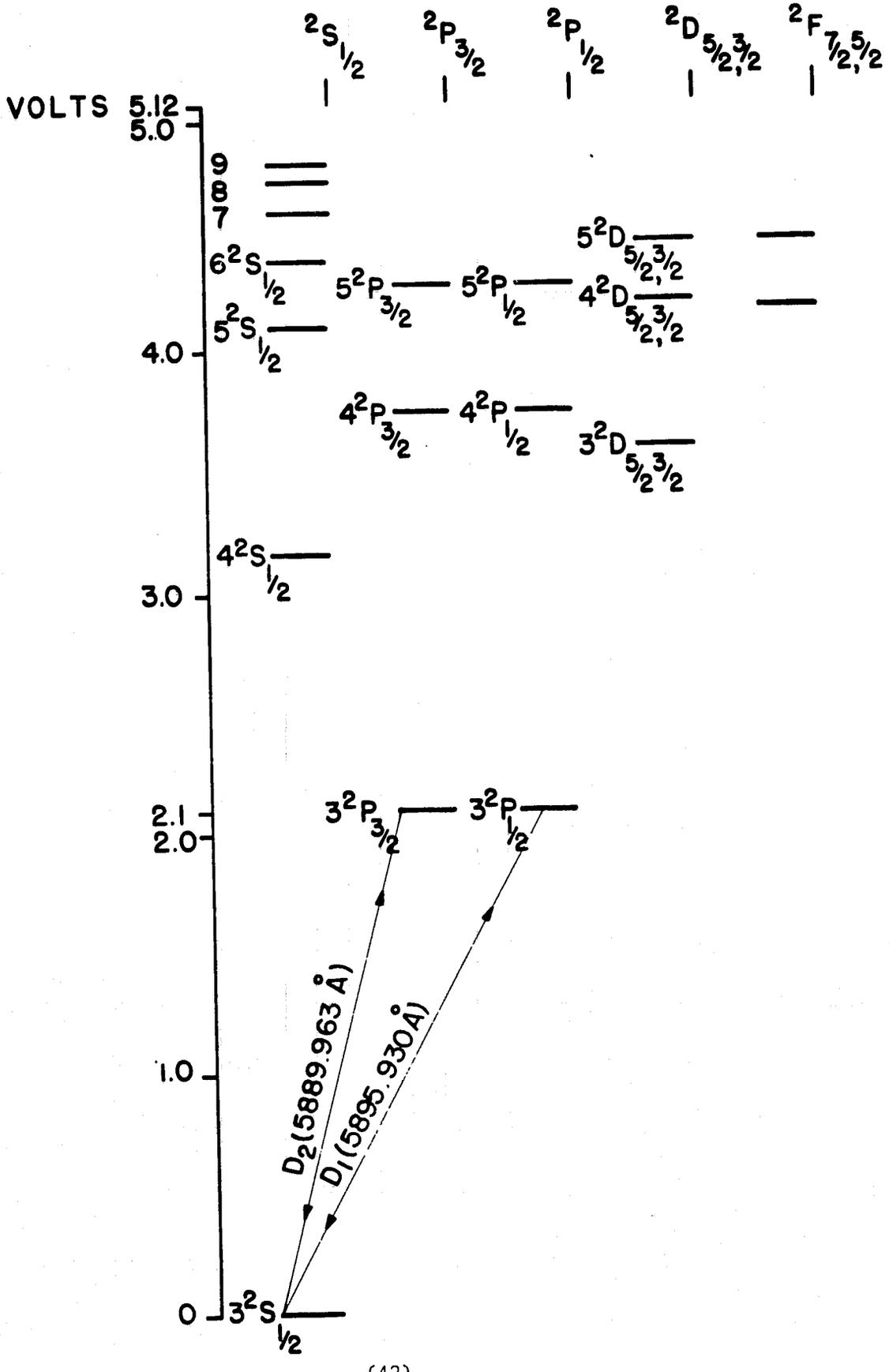
$^2S_{1/2}$
$^2P_{3/2}$
$^2P_{1/2}$
$^2D_{5/2,3/2}$
$^2F_{7/2,5/2}$
VOLTS
5.12
5.0
9
8
7
$6^2S_{1/2}$
$5^2D_{5/2,3/2}$
$5^2P_{3/2}$
$5^2P_{1/2}$
$4^2D_{5/2,3/2}$
$5^2S_{1/2}$
4.0
$4^2P_{3/2}$
$4^2P_{1/2}$
$3^2D_{5/2,3/2}$
$4^2S_{1/2}$
3.0
2.1
2.0
$3^2P_{3/2}$
$3^2P_{1/2}$
D_2(5889.963 Å)
D_1(5895.930Å)
1.0
0
$3^2S_{1/2}$

Figure A.1[42]

corresponding to the total angular momentum operator

$$\vec{F} = \vec{J} + \vec{I} \qquad \text{A.7.}$$

and the quantum number M_F corresponding to the projection of the operator $\vec{F}$ are both good quantum numbers for the new set of wavefunctions. The values of the quantum number F are restricted to

$$|J - I| \leq F \leq J + I \qquad \text{A.8.}$$

The hyperfine structure of the sodium $3^2S_{1/2}$, $3^2P_{1/2}$ and $3^2P_{3/2}$ states are shown in Figure A.2.[15]. The numbers on the arrows representing the allowed transitions correspond to the theoretical line strengths.

The total angular momentum quantum number, F, dipole selection rules are $\Delta F = 0, \pm 1$. These give rise to a phenomenon known as Optical Pumping. Exciting the transition $3^2S_{1/2}$, $F = 1 \rightarrow 3^2P_{3/2}$, $F = 1$, allows a decay channel into the $3^2S_{1/2}F = 2$ level, for then $\Delta F = 1$. This process removes the atom from the $3^2S_{1/2}$, $F = 1$ state so that it will not be available for another pumping cycle from $3^2S_{1/2}$, $F = 1$.

Tuning the laser frequency to the $3^2S_{1/2}$, $F = 2 \rightarrow 3^2P_{3/2}$, $F = 3$ transition eliminates this problem, as then the upper level can only decay to the lower level by $\Delta F = -1$. The magnetic quantum number, M_F, dipole selection rules for spontaneous emission are $\Delta M_F = -1, 0, +1$. For absorption and stimulated emission the selection rules are $\Delta M_F = 0$ if $\Delta F \neq 0$ for linearly polarized light, $\Delta M_F = -1$ for right circularly polarized light and $\Delta M_F = +1$ for left circularly polarized light. The transition $3^2S_{1/2}$, $F = 2 \rightarrow 3^2P_{3/2}$, $F = 1$ will optically pump atoms into the energy levels $3^2S_{1/2}$, $F_1 = 2$, $M_{F_1} = \pm 2$ if linearly polarized light is used. This is depicted in Figure A.3. where the heavy and thin lines correspond to absorption and spontaneous emission respectively. From the figure

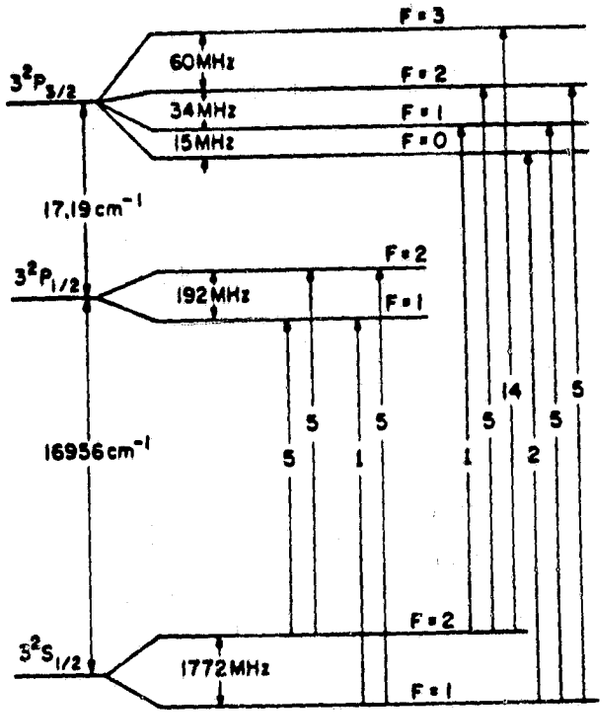
F = 3
60MHz
F = 2
$3^2P_{3/2}$
34MHz
F = 1
15MHz
F = 0
17.19 cm^{-1}
F = 2
$3^2P_{1/2}$
192MHz
F = 1
16956 cm^{-1}
5
5
5
1
5
1
14
5
2
5
F = 2
$3^2S_{1/2}$
1772MHz
F = 1

Figure A.2[15]

it is clear that once the atom has undergone one excitation cycle and has ended up in the $F_1 = 2$, $M_{F_1} = \pm 2$ levels, it is no longer available for another cycle since the selection rule for stimulated absorption for linearly polarized light is $\Delta M_F = 0$.

If the transit time of an atom through the excitation volume defined by the narrow linewidth laser beam is much longer than the upper state lifetime, the fluorescence signal will be considerably reduced. This is due to the fact that the atom while in the laser beam will undergo several excitation cycles with a high probability that it will finally end up in a trap level.

If a linearly polarized laser is tuned to the $3^2S_{1/2}$, $F = 2 \rightarrow 3^2P_{3/2}$, $F = 3$ transition, levels $3^2P_{3/2}$, $F = 3$, $M_F = \pm 3$ will not be excited, but no trapping of atoms in the ground state will take place. A simple analysis will show that apart from this one transition, all others in the two sodium D lines trap atoms due to optical pumping.

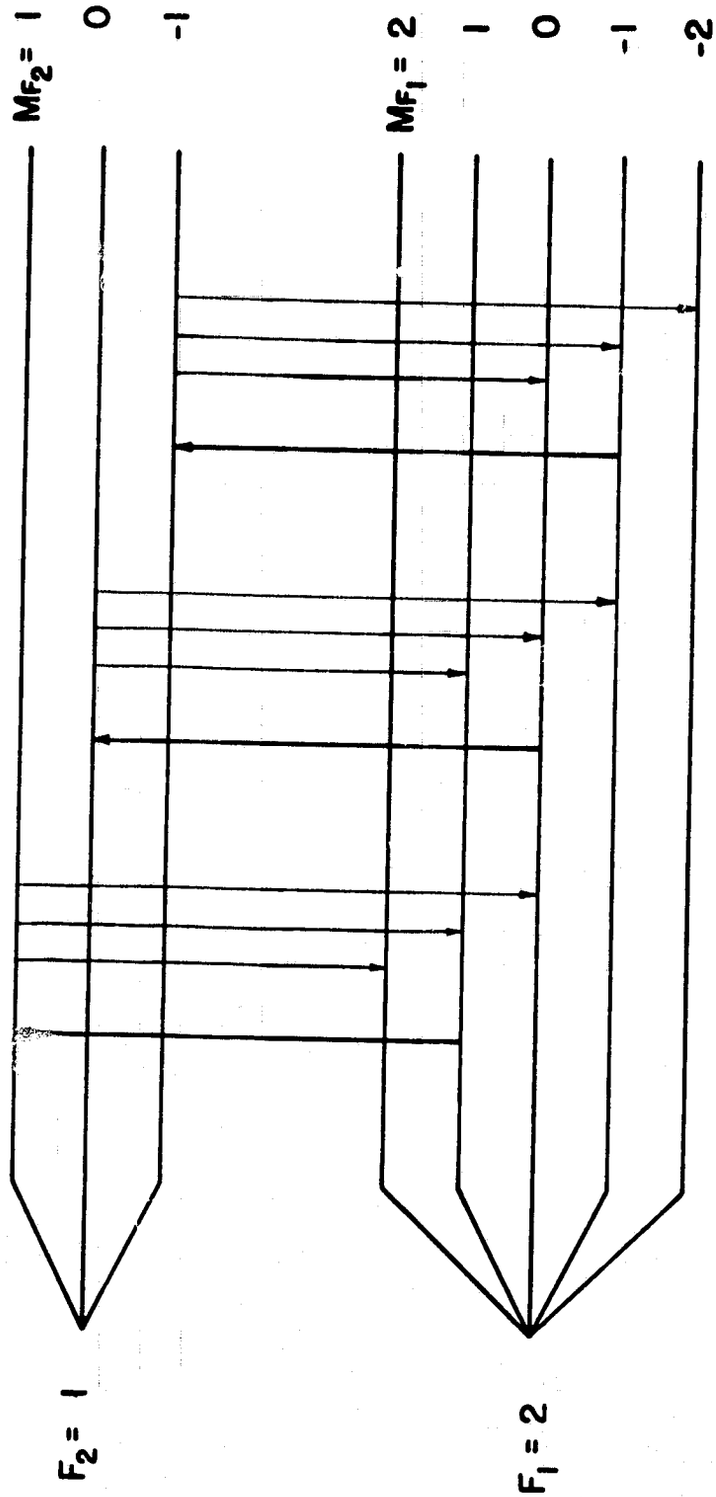

Figure A.3

3. Broadening Effects

a. Natural Broadening

One may show[50] that the expectation value of the dipole moment $\langle e\vec{r} \rangle$ of a two level atomic system behaves very much like a classical oscillator. With this in mind consider a classical oscillator consisting of an electron on a spring under the influence of an applied electromagnetic field. Since the electron performs a time dependent motion it acts like an antenna radiating an electromagnetic field and causing the dipole to lose energy, that is, the dipole is damped. The equation of motion is

$$\ddot{x}(t) + 2\Gamma \dot{x}(t) + \omega_o^2 x(t) = \frac{eE_o}{m} \cos \omega t \qquad \text{A.9.}$$

ω_o corresponds to the transition frequency, ω is the forcing frequency, E_o is the electromagnetic field amplitude and Γ is the damping coefficient[51].

$$\Gamma = \frac{1}{3} \frac{e^2\omega_o^2}{4\pi\varepsilon_o c^3 m} \frac{1}{3} \frac{\omega_o^2 r_o}{c} \qquad \text{A.10.}$$

where m is the electron's mass and $r_o = 2.82 \times 10^{-15}$m is the classical electron radius.

The average rate of work done by the field on the atom is given by the power expressions

$$P = \frac{1}{2\pi/\omega} \int^{2\pi/\omega} dt\ \dot{x}\ eE_o \cos \omega t = \frac{\pi(eE_o)^2}{2m} \frac{\Gamma/\pi}{(\omega-\omega_o)^2+(\Gamma)^2} > 0 \qquad \text{A.11.}$$

This shows that the steady state forced oscillator absorbs radiation dissipating it in the damping process. For radiative damping this involves (following the classical treatment) scattering the incident radiation in a doughnut pattern characteristic of a dipole. The absorbed power is proportional to a Lorenzian lineshape which is a normalized function

defined by

$$L(\omega-\omega_o\ \Gamma) = \frac{\Gamma/\pi}{(\omega-\omega_o)^2+(\Gamma)^2} \qquad \text{A.12.}$$

The half width at half maximum (HWHM) for the sodium D2 line using equation A.10. is found to be $\Delta\nu = \frac{\Gamma}{2\pi} = 5.1$ MHz.

A quantum mechanical treatment was first obtained by Weisskopf and Wigner[52]. It shows that the frequency distribution of the intensity, $I_{ki}(\omega)$, of a transition taking place between an upper level k and a lower level i is

$$I_{ki}(\omega) = I_o \frac{\Gamma_{ki}/\pi}{(\omega-\omega_{ki})^2+(\Gamma_{ki})^2} \qquad \text{A.13.}$$

where I_o is the total intensity of the line, ω_{ki} is the transition frequency and Γ_{ki} is the HWHM of the Lorentzian lineshape. If A_{ij} is the quantum mechanical transition rate from level i to j, then

$$\Gamma_{ki} = \sum_j A_{kj} + \sum_h A_{ih} \quad k > j \ , \ i > h \qquad \text{A.14.}$$

For a transition from an upper level k to a lower level i one defines the emission oscillator strength f_{ki} as the ratio between the quantum mechanical and classical rates[45]

$$f_{ki} = -\frac{A_{ki}}{3\Gamma} = -\frac{2m\omega_{ki}}{3hg_k} \sum_{m_i m_k} |\langle km_k|\vec{r}|im_i\rangle \qquad \text{A.15.}$$

where m_k is the quantum number associated with the degeneracy of level k and g_k is the degeneracy of level k. For absorption one defines

$$g_i f_{ik} = -g_k f_{ki} \qquad \text{A.16.}$$

For the sodium D lines, i is the ground state and k the first excited state. Thus

$$\frac{\Gamma_{10}}{2\pi} = \frac{A_{10}}{2\pi} = \frac{3\Gamma}{2\pi}\frac{g_o}{g_1} f_{01} = 5 \text{ MHz} \qquad \text{A.17.}$$

where Γ is the damping coefficient calculated in equation A.10. and $f_{01} = 0.982$[45]. The quantum mechanical rate is close to the classical

result since the oscillator strength, f_{01}, is close to unity for the sodium D lines. The time uncertainty relation may not be derived using Heisenberg's rule only since time is not an operator. The equation of motion for the expectation value of the operator A is

$$i\hbar \frac{d}{dt}\langle A\rangle = \langle [A,H]\rangle + i\hbar \langle \frac{\partial A}{\partial t}\rangle \qquad \text{A.18.}$$

Heisenberg's uncertainty relation is

$$\Delta A \, \Delta' \geq \left|\frac{1}{2}\langle i[A,H]\rangle\right| \qquad \text{A.19.}$$

where the root mean square deviation of A is defined by

$$(\Delta A)^2 = \langle \psi | \, (A-\langle A\rangle)^2 | \psi\rangle = \langle A^2\rangle - \langle A\rangle^2 \qquad \text{A.20.}$$

If A does not depend explicitly on time one obtains from A.18 and A.19

$$\tau_A \cdot \Delta H \geq \frac{\hbar}{2} \qquad \text{A.21.}$$

provided[53]

$$\tau_A = \frac{\Delta A}{d\langle A\rangle/dt} \qquad \text{A.22}$$

τ_A appears as a time characteristic of the evolution of the statistical distribution of A. It is the time required for the center $\langle A\rangle$ of this distribution to be displaced by an amount equal to its "HWHM" ΔA. Kibble et.al.[54] measured the lifetime of the upper state $3^2P_{3/2}$ of sodium to be $\tau = (16.0 \pm 0.5)10^{-9}$ sec. From the uncertainty relation one may obtain the HWHM

$$\Delta\nu_n = \frac{\Delta E}{2\pi\hbar} \geq \frac{1}{4\pi\tau} = 5 \pm 0.16 \text{ MHz} \qquad \text{A.23}$$

b. Doppler Broadening

At any time each atom has some instantaneous velocity. This causes the atomic absorption frequency ν_{ik} to be Doppler shifted to a new frequency. Consider an inertial coordinate frame K and a moving one K'. The phase of a planewave is an invariant quantity. This is because the elapsed phase

of a wave is proportional to the number of wave crests that have passed the observer. Since this is merely a counting operation, it must be independent of the coordinate frame. A planewave of frequency ω and wave vector $\vec{k}$ in the inertial frame K will in general have a different frequency ω' and wave vector $\vec{k}'$ in the moving frame K'. The phase of the wave ϕ is invariant. Hence

$$\phi = \omega t - \vec{k} \cdot \vec{x} = \omega' t' - \vec{k}' \cdot \vec{x}' \qquad \text{A.24.}$$

After substituting the Lorentz transformation into equation A.24. one obtains the Doppler shift formulas for light waves[51]

$$\tan \theta' = \frac{\sin \theta}{\gamma(\cos\theta - \beta)} \qquad \text{A.25.}$$

$$\omega' = \gamma\omega(1 - \beta\cos\theta) \qquad \text{A.26.}$$

where θ is the direction of $\vec{k}$ relative to the velocity vector $\vec{u}$ and

$$\beta = \frac{|\vec{u}|}{c} \qquad \text{A.27.}$$

$$\gamma = (1 - \beta^2)^{-1/2} \qquad \text{A.28.}$$

For nonrelativistic gas dynamics $\beta << 1$. Then

$$\theta' \cong \theta$$

$$\omega' = \omega(1 - \beta\cos\theta) \qquad \text{A.29.}$$

The condition for the largest probability of absorption is that ω' correspond to the transition frequency in the atom's rest frame.

Assuming a Maxwellian velocity distribution function one obtains[27] the absorbed irradiance, J,

$$J = J_o \frac{c}{\nu_{ik}} \sqrt{\frac{m}{2\pi kT}} \exp\left[\frac{-m}{2kT} \left(\frac{c}{\nu_{ik}}\right)^2 (\nu - \nu_{ik})^2\right] \qquad \text{A.30.}$$

where m is the weight of one atom, T is the temperature of the sample and J_o is the incident irradiance. The Doppler HWHM is

$$\Delta\nu_D = \frac{\nu_{ik}}{c} \sqrt{\frac{2kT \ \ln 2}{m}} \qquad \text{A.31.}$$

Rewriting equation A.30 in terms of the HWHM, one obtains

$$J = J_o \, G(\nu-\nu_{ik}, \Delta\nu_D) \qquad \text{A.32}$$

where the Gaussian is a normalized function defined by

$$G(\nu-\nu_{ik}, \Delta\nu_D) = \frac{1}{\Delta\nu_D}\sqrt{\frac{\ln 2}{\pi}}\; e^{-\ln 2\left(\frac{\nu-\nu_{ik}}{\Delta\nu_D}\right)^2} \qquad \text{A.33}$$

Equation A.31 may be used to determine the temperature as a function of the Doppler linewidth.

$$T = (\Delta\nu_D, \lambda_{ik})^2 \frac{m}{2k \ln 2} \qquad \text{A.34}$$

Normalizing by the broadening HWHM, $\Delta\nu_{Do}$, at $T_o = 273°K$, then for the sodium D_2 line

$$T = T_o\left(\frac{\Delta\nu_D}{\Delta\nu_{Do}}\right)^2 = T_o\left(\frac{\Delta\nu_D}{628}\right)^2 \qquad \text{A.35}$$

for $\Delta\nu_D$ in MHz.

c. Time of Flight Broadening[55]

At low pressures an absorbing atom may interact coherently, without undergoing collisions, during its entire transit through the laser excitation region. As in the discussion of natural broadening, one obtains a time of flight limited HWHM which cannot be less than $(4\pi\Delta t)^{-1}$ where Δt is the duration of the perturbation. Consider a Gaussian beam with a waist w and for simplicity assume a plane wave behavior. The field may be represented by

$$\vec{E}(x,y,z,t) = \hat{\epsilon} E \; e^{-(r/w)^2} \cos(kz-\omega t) \qquad \text{A.36}$$

where $\hat{\epsilon}$ is the polarization direction, r is the radial distance from the beam axis and z is the distance along the beam.

The plane wave assumption holds for particles under the influence of approximately uniform phase fronts. It is thus suitable for particle with a lifetime which is short compared to the transit time through the laser beam.

Since each particle interacts with the laser beam independently of all the others one may translate the coordinates of each in time and rotate them in the x-y plane. Choosing $u_y = 0$, the particle enters the laser excitation region with velocity u_x at an impact parameter of $y = b$ as illustrated in Figure A.4. The time axis is translated so that at $t = 0$ the particle lies on the y axis. The transverse dependence of the spatial field is transform to

$$E[r(t)] = E_o e^{-(r/w)^2} = E_o e^{-\frac{b^2+(u_x t)^2}{w^2}} = E_o e^{-(\frac{b}{w})^2} e^{-(\frac{u_x t}{w})^2} \qquad A.37$$

This is the field the particle experiences in the zero pressure limit. The time dependence is the same for all particles and does not depend on the impact parameter b. In other words, each particle of a given velocity subgroup will have the same time of flight residual HWHM.

In the absorber's rest frame

$$E(b,z,u_x,u_z,t) = \hat{\varepsilon}\, E_o e^{-(\frac{b}{w})^2} e^{-(\frac{u_x t}{w} + \phi)^2} \cos[kz-\omega(1 + \frac{u_z}{c})t] \qquad A.38$$

The phase angle ϕ has been introduced to represent the phase of the alternating optical field upon entry of a given particle characterized by b, u_x and u_z. The number of optical cycles during a transit time is given by

$$\frac{w/u}{T} = \frac{w\nu}{u} \simeq 3.10^8 \qquad A.39$$

where u is the convective gas velocity. As this number is large, one may assume the effect of ϕ to be negligible. The Schrodinger equation has the

form

$$i\hbar \frac{\partial \psi}{\partial t} = (H_o + H')\psi \qquad A.40$$

where H_o and H' are the field free and perturbing Hamiltonian respectively. Consider a two level atom with unperturbed eigenfunctions $\psi_1(\vec{r})$ and $\psi_2(\vec{r})$. Then

$$\psi(\vec{r},t) = a_1(t)e^{-i\omega_1 t}\,\psi_1(\vec{r}) + a_2(t)e^{-i\omega_2 t}\,\psi_2(\vec{r}) \qquad A.41$$

where $a_i(t)$ is slowly varying compared to oscillating term. In the dipole approximation

$$H' = e\vec{r}\cdot\vec{E} \qquad A.42$$

H' is antisymmetric and thus has only nondiagonal matrix elements

$$\dot{a}_1 = -\frac{i}{\hbar} \langle 1|H'|2\rangle\, e^{i\omega t}\, a_2 \qquad A.43$$

$$\dot{a}_2 = -\frac{i}{\hbar} \langle 2|H'|1\rangle\, e^{-i\omega t}\, a_1 \qquad A.44$$

The density matrix is defined by the products

$$\rho = \begin{pmatrix} \rho_{11} & \rho_{12} \\ \rho_{21} & \rho_{22} \end{pmatrix} = \begin{pmatrix} |a_1|^2 & a_1 a_2^* \\ a_2 a_1^* & |a_2|^2 \end{pmatrix} \qquad A.45$$

Then[50]

$$\dot{\rho}_{11} = +\frac{i}{\hbar} \langle 1|H'|2\rangle\, e^{i\omega t}\, \rho_{21} + CC \qquad A.46$$

$$\dot{\rho}_{22} = -\frac{i}{\hbar} \langle 1|H'|2\rangle\, e^{i\omega t}\, \rho_{21} + CC \qquad A.47$$

$$\dot{\rho}_{21} = +\frac{i}{\hbar} \langle 1|H'|2\rangle\, e^{i\omega t}\, (\rho_{22}-\rho_{11}) \qquad A.48$$

The wavelength of the electric field is long compared to atomic dimensions in the optical frequency range. Inasmuch as the electric field does not depend on the atomic coordinates (electric dipole approximation), the

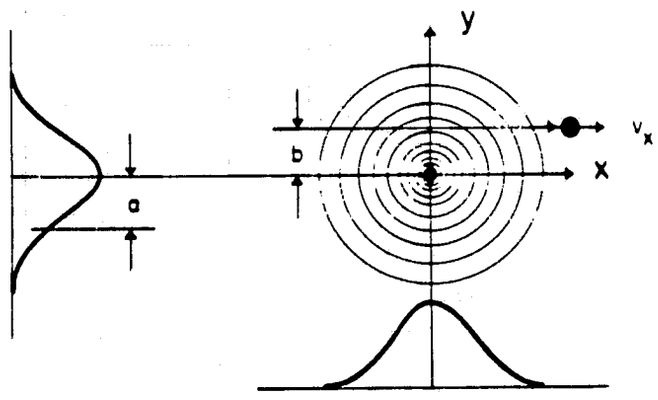

Figure A.4[55]

matrix element reduces to

$$\langle 1|H'|2\rangle = eE_o\langle 1|x|2\rangle e^{-(\frac{b}{w})^2} e^{-(\frac{u_x t}{w})^2} \cos[kz-\omega(1+\frac{u_z}{c})t] \qquad A.49$$

assuming $\vec{E}_o$ to be polarized along the x direction. The density matrix relates to a definite velocity class of absorbers. The absorbed power is given by

$$P = \hbar\omega F\rho_{22} \qquad A.50$$

As ρ_{22} varies during transit through the laser beam it has to be averaged over time. Hence,

$$P = \hbar\omega F \int_{-\infty}^{\infty} \frac{d\rho_{22}}{dt}\, dt \qquad A.51$$

F is the rate at which the atoms are injected into the volume in velocity space. An inspection of equations A.47, A.48 and A.49 shows that for small saturation (Using a lower laser intensity, the upper state population is negligible and $\rho_{22}-\rho_{11} \simeq -1$.) the absorbed power is roughly proportional to $[\exp-(\frac{u_x t}{w})^2]^2$. Instead of performing the density matrix integration, one could calculate the distribution of frequencies in the atomic rest frame, resulting from the action of $\exp-(\frac{u_x t}{w})^2$ on the sharp laser frequency in the laboratory rest frame.

$$C(\omega) = \int_{-\infty}^{\infty} e^{-2(\frac{u_x t}{w})^2} e^{-i\omega t}\, dt \qquad A.52$$

The above expression should be averaged over the velocity distribution. The average random velocity in the wind tunnel for the present experiment is

$$\bar{u} = \sqrt{\frac{8kT}{\pi m}} = 156 \text{ m/sec} \qquad A.53$$

This value is less than 10% of the convective velocity of 1736 m/sec.

Hence, no averaging is performed and for a first approximation one may use

$$C(\omega) = \frac{a}{\sqrt{2}\, u_x} e^{-\frac{1}{2}\left(\frac{w\omega}{u_x}\right)^2} \qquad A.54$$

The HWHM is[55]

$$\Delta\nu_T = \frac{1}{2\pi} \sqrt{2\ \ln 2}\ \frac{u_x}{w} \qquad A.55$$

For a beam waist of 0.1 mm and a velocity of 1736 m/sec then $\Delta\nu_T$ = 3 MHz.

d. Pressure Broadening and Shift

The classical model represents an atomic radiator as an elastically bound oscillating electron. The problem of collisional broadening is to calculate the absorption of such an oscillator when it is disturbed by colliding with the other atoms. The equation of motion is

$$\ddot{x} + 2\Gamma\dot{x} + \omega_o^2 x = \frac{eE}{m} \cos \omega t \qquad A.9$$

where Γ is related to the natural HWHM, ω_o is the atomic resonance frequency, e is the elementary charge, m is the electron mass and E and ω are the driving field amplitude and frequency respectively.

One assumes that the collisions do not change the amplitude of the oscillator, only its phase.[56] The atom continues its driven motion after a collision with a completely random phase between 0 and 2π. The instances at which collisions take place are also randomly distributed with an average time between collisions equal to T_2. By solving equation A.9, one may then average over the random phases and collision times. The time averaged power absorbed by the oscillator from the driving electromagnetic field is then[57]

$$\bar{P} = \frac{1}{2\pi/\omega} \int_0^{\frac{2\pi}{\omega}} (eE \cos \omega t)\dot{x}\, dt = \frac{eE}{2m} L(\omega-\omega_o, \frac{1}{T_2} + \Gamma) \qquad A.56$$

The contribution to the Lorentzian HWHM due to dephasing is given by the reciprocal of the average time between collisions T_2. From the kinetic theory of gases, the collision frequency per unit volume, $\tilde{z}_{ab}$, between atom a and b is[20]

$$\tilde{z}_{ab} = n_a n_b \sigma_c \sqrt{\frac{8kT}{\pi\mu_{ab}}} \qquad A.57$$

where σ_c and μ_{ab} are the collision cross section and reduced mass of the two atoms. The collision frequency per atom a is

$$z_{ab} = \frac{\tilde{z}_{ab}}{n_a} = n_b \sigma_c \sqrt{\frac{8kT}{\pi\mu_{ab}}} \qquad A.58$$

Thus the HWHM due to collision is

$$\Delta\nu_c = \frac{1}{2\pi T_2} = \frac{n_b \sigma_c}{2\pi} \sqrt{\frac{8kT}{\pi\mu_{ab}}} \qquad A.59$$

Experimentally it was found that the central frequency of a line shifts with increasing foreign gas density.[56] To incorporate this into the theory one again assumes a classical oscillator with natural frequency ω_o. As the collisions induce phase shifts, the oscillation frequency is a function of time. The oscillation displacement, x(t), is

$$x(t) = x_o e^{i \int_o^t \omega'(t')dt'} \qquad A.60$$

where x_o is the oscillation amplitude. From the Larmor formula[51] for the power radiated by an accelerating charge and taking a Fourier component of the displacement one obtains

$$P(\omega) = \frac{1}{4\pi\epsilon_o} \frac{e^2\omega^4}{3\pi c^2} x_o^2 \left| \int_{-\infty}^{\infty} dt\, e^{i\int_o^t \omega'(t')dt' - i\omega t} \right|^2 \qquad A.61$$

This expression has to be averaged over the phase shifts $\Delta\omega'$ defined by

$$\omega'(t) = \omega_o + \Delta\omega'(t) \qquad A.62$$

and over the number of collisions. The power radiated by an accelerating charge may then be written as[56]

$$P(\omega) = \frac{2\omega^4 (ex_o)^2}{3\pi\, c^3} \frac{n\bar{u}\sigma_c}{[\omega - (\omega_o + n\bar{u}\tilde{S})]^2 + (n\bar{u}\sigma_c)^2} \qquad A.63$$

where n is the number density of the perturbing gas and $\bar{u}$ is the relative velocity defined by

$$\bar{u} = \sqrt{\frac{8kT}{\pi\mu_{ab}}} \qquad A.64$$

The Lorentzian in equation A.63 is shifted from resonance by

$$\Delta\nu_s = \frac{n\,\bar{u}\,\tilde{S}}{2\pi} \qquad A.65$$

where $\tilde{S}$ is a constant having the dimension of an area which can be determined experimentally. The Lorentzian has a HWHM of

$$\Delta\nu_c = \frac{n\bar{u}\sigma_c}{2\pi} \qquad A.66$$

which is the same expression as in equation A.59. From the perfect gas law

$$n = \frac{N}{V} = \frac{P}{kT} \qquad A.66$$

one obtains

$$\Delta\nu_c = \frac{1}{2\pi} P_o \sqrt{\frac{8}{\pi k T_o \mu_{ab}}}\, \sigma_c \frac{P/P_o}{\sqrt{T/T_o}} \qquad A.67$$

For helium and sodium at the reference condition of 760 torr and 273°K

$$\Delta\nu_c = 5.57 \cdot 10^{23}\ \sigma_c \frac{P/P_o}{\sqrt{T/T_o}} \qquad A.68$$

for σ_c in cm^2 and $\Delta\nu_c$ in Hz.

Experiments by McCartan and Farr[25] for sodium in helium indicate a HWHM per number density n of

$$\frac{\Delta\omega_c}{n} = (2.03\pm0.1)10^{-9}\ \frac{\text{rad/sec}}{\text{atoms/cm}^3} \qquad A.69$$

at 415°K for the $3^2P_{3/2}$ state up to a density of 11.5×10^{18} atoms/cc. Equation A.59 may be rewritten in terms of σ_c.

$$\sigma_c = \frac{\Delta\omega}{n}\sqrt{\frac{\pi\mu_{ab}}{8kT}} = (126\pm6)10^{-16}\ cm^2 \qquad A.70$$

At a temperature of 460°K they obtained

$$\frac{\Delta\omega_c}{n} = (2.18\pm0.2)10^{-9}\ \frac{\text{rad/sec}}{\text{atoms/cc}} \qquad A.71$$

The collision cross section using equation A.70 would then be $(128\pm12)10^{-16}$ cm^2. The value for σ_c from equation A.70 may be substituted back into equation A.68

$$\Delta\nu_c = (7.04\pm0.34)10^{9}\ \frac{P/P_o}{\sqrt{T/T_o}}\ \text{Hz} \qquad A.72$$

For the shift at T = 460°K they obtained[25]

$$\frac{\Delta\omega_s}{n} = (-0.07\pm0.03)10^{-19}\ \frac{\text{rad/sec}}{\text{atoms/cc}} \qquad A.73$$

By exchanging $\tilde{S}$ with σ_c in equation A.70 one obtains

$$\tilde{S} = (-2.1\pm0.9)10^{-16}\ cm^2 \qquad A.74$$

and the shift is

$$\Delta\nu_s = -(1.1\pm0.5)10^{8}\ \frac{P/P_o}{\sqrt{T/T_o}}\ \text{Hz}. \qquad A.75$$

The cross section is a function of the temperature. This dependence is amplified at low temperature since the colliding particle is then brought under the influence of the long range part of the potential. The theoretical investigation by Lewis and McNamara,[42] based on the interaction potential calculated by Bayliss[58] for the ground state and resonance states of sodium perturbed by helium, indicates that the broadening rates per unit number density (HWHM/number density) scale as $T^{0.41}$. From the spectroscopic measurements performed in this experimental investigation (Section IV.D.1) the rates per unit number density scale as $T^{0.38}$.

e. Instrumental Broadening

The laser linewidth is influenced by the resonator in which lasing takes place. To find the resonator linewidth one must consider a collimated beam of radiation of intensity I launched inside a laser parallel to the resonator axis. After one round trip the intensity of the beam falls down to $I-I\delta_r$ where δ_r represents diffraction, absorption, scattering and output transmission losses. For a resonator of length L

$$\frac{dI}{dt} = - \frac{I\delta_r}{2L/c} \qquad \text{A.76}$$

and

$$I = I_o \, e^{- \frac{t}{2L/c\delta_r}} \qquad \text{A.77}$$

The resonator decay time is given by $\frac{2L}{c\delta_r}$ and the expression obtained for the passive resonator HWHM is[48]

$$\Delta\nu_r = \frac{1}{2\pi} \frac{c\delta_r}{2L} \qquad \text{A.78}$$

If it is assumed that the reflection at the optical surfaces and the output coupling represent the main loss mechanism in the resonator, then for the

Spectra Physics model 580 dye laser δ_r is approximately 0.04 which results in a HWHM of 3.2 MHz. The laser linewidth is narrower then the passive resonator linewidth since the gain is nonlinearly related to the frequency dependent resonator losses. The resonator losses not only determine the conditions for the oscillation threshold, but also the theoretical spectral purity of the laser output. By considering the noise output produced by spontaneous emission into a resonator mode, which cannot be separated from the power derived by stimulated emission the following laser HWHM, $\Delta\nu_\ell$, is obtained[59]

$$\Delta\nu_\ell = \frac{hc}{\lambda} (2\pi)^2 \frac{(\Delta\nu_r)^2}{2P} \qquad A.79$$

where P is the laser output power. The laser HWHM obtained by using equation A.79 is $2.3\text{x}10^{-3}$ Hz for the dye laser tuned to the sodium D_2 wavelength with a power output of 30 mW. The narrowest linewidth achieved to date is 2kHz R.M.S.[60] The reasons for the discrepancy between the experimental and theoretical linewidths are due to external influences. The main ones are the thermal and acoustical disturbances to the cavity length and the fluctuations in the thickness, position and index of refraction of the dye jet. The single mode frequency ν is given by

$$\nu = \frac{mc_o}{2\ell n} \qquad A.80$$

where m is an integer, ℓ is the cavity length and n is the index of refraction of the medium assumed to be filling the complete cavity. Then

$$\left|\frac{\Delta\nu}{\nu}\right| = \left|\frac{\Delta\ell}{\ell}\right| = \left|\frac{\Delta n}{n}\right| \qquad A.81$$

To keep a 0.3 m long laser stable to within $\Delta\nu$ = 1 MHz the laser cavity length has to remain constant to within $\Delta\ell = 6\text{x}10^{-10}$ m for frequencies in the visible range of the spectrum. A model 580 single frequency Spectra

Physics dye laser was used in this experimental investigation. A short term linewidth of $\Delta\nu_c = \pm 7$ MHz should be obtainable according to the manufacturer's specifications. To achieve this narrow linewidth an accumulator to damp mechanical, pump-induced, dye pressure fluctuations and a vibration isolated optical table was used. In the commercial laser, the dye was contained between two windows in the laser cavity. The laser was redesigned to incorporate a free jet dye stream to eliminate window burning. This also reduced the occurrence of mode hops but degraded the frequency stability of the laser.

The quality of the absorption spectrum depends on the ratio of the absorption width to the laser frequency jitter and on the rate at which the laser frequency is made to scan across the absorption profile.

4. Absorption, Saturation, Power Broadening and Radiation Trapping

The complete absorption line shape including natural, Doppler and pressure broadening, is derived in this section. The derivation also incorporates saturation and power broadening. This is followed by a short discussion of radiation trapping.

The solution to the steady state equation of radiation transfer may be written as[48]

$$I_\omega(L) = I_\omega(0)e^{-\kappa_\omega L} + \frac{\varepsilon_\omega}{\kappa_\omega}(1-e^{-\kappa_\omega L}) \qquad \text{A.82}$$

provided κ_ω and ε_ω are independent of position x. $I_\omega(0)$ and $I_\omega(L)$ are the impinging and emitted intensity from a column of gas of length L. κ_ω and ε_ω are the volume absorption and emission coefficients respectively, given by

$$\varepsilon_\omega = \frac{\hbar\omega}{4\pi} A_{21}\, n_2\, g(\omega) \qquad \text{A.83}$$

and

$$\kappa_\omega = \frac{\hbar\omega}{4\pi} B^I_{12}\, g_1\left(\frac{n_1}{g_1} - \frac{n_2}{g_2}\right) g(\omega) \qquad \text{A.84}$$

A_{21} and B^I_{12} are the Einstein coefficients, n is the atomic number density, g is the degeneracy, $g(\omega)$ is a linewidth factor and the subscripts 1 and 2 refer to the lower and upper levels respectively. $\kappa_\omega L$ is known as the optical thickness of the absorber. It determines the amount by which a collimated beam of intensity $I_\omega(0)$ is attenuated as it passes through the medium. For $\kappa_\omega L \ll 1$

$$I_\omega(L) = I_\omega(0)(1-\kappa_\omega L) + \varepsilon_\omega L \qquad \text{A.85}$$

The net absorbed intensity is

$$I_{\omega,abs} = I_\omega(0)\kappa_\omega L - \varepsilon_\omega L \qquad \text{A.86}$$

Neglecting the intensity injected into the beam by spontaneous emission

which is emitted in all directions

$$I_{\omega,abs} = I_{\omega}(0)\ \kappa_{\omega} L \qquad A.87$$

To evaluate the above expression, the population difference has to be calculated. The rate equation for the upper state of a two level system is given by

$$\frac{dn_2(u)}{dt} = S_2(u) - n_2(u)A_{21} - [n_2(u)B_{21}^I - n_1(u)B_{12}^I]\ \frac{I(\omega)g(u,\omega)}{4\pi} \qquad A.88$$

where $S_2(u)$ describes the rate at which atoms in the velocity class u, u+du are created. The number density and linewidth factor are velocity dependent since an electromagnetic wave of frequency ω, propagating through an ensemble of atoms, interacts with a restricted class of atoms having a velocity component u along the propagation vector $\vec{k}$ given by equation A.29

$$u = \frac{\omega-\omega_{21}}{k} \qquad A.89$$

where ω_{21} is the transition frequency. The steady state number density of the upper level is given by (equation A.88)

$$n_2(u) = \frac{S_2(u) + n_T(u)B_{12}^I\ \frac{I(\omega)\ g(u,\omega)}{4\pi}}{A_{21} + (B_{21}^I+B_{12}^I)\ \frac{I(\omega)\ g(u,\omega)}{4\pi}} \qquad A.90$$

where $n_T(u)$ is the total number density of sodium atoms with velocity u. The steady state inversion density is given by

$$\frac{n_2(u)}{g_2} - \frac{n_1(u)}{g_1} = -\frac{(\frac{n_T}{g_1} - \frac{S_2}{g_1 A_{21}})\ P(u)}{1 + (1+\frac{g_1}{g_2})\ \frac{B_{12}^I}{A_{21}}\ \frac{I(\omega)\ g(u,\omega)}{4\pi}} \qquad A.91$$

The total number of atoms in a certain velocity group, $n_T(u)$, may be written as a function of the total number of atoms, n_T, as

$$n_T(u) = n_T\ P(u) \qquad A.92$$

using the velocity distribution function P(u). S_2 is defined in a similar manner. The total inversion density, $\frac{n_2^o}{g_2} - \frac{n_1^o}{g_1}$, existing under zero field conditions (I = 0), may be obtained by integrating over the total range of velocities.

$$\frac{n_2^o}{g_2} - \frac{n_1^o}{g_1} = \int_{-\infty}^{\infty} [\frac{n_2(u)}{g_2} - \frac{n_1(u)}{g_1}]du = -(\frac{n_T}{g_1} - \frac{S_2}{g_1 A_{21}}) \qquad \text{A.93}$$

If the thermal population of the upper level is neglected, S_2 vanishes and n_1^o equals n_T. Equation A.91 may now be presented in different form.

$$\frac{n_2(u)}{g_2} - \frac{n_1(u)}{g_1} = \frac{(\frac{n_2^o}{g_2} - \frac{n_1^o}{g_1})\ P(u)}{1 + \frac{I(\omega)}{I_s(u,\omega)}}$$

$I_s(u,\omega)$ is the saturation intensity which is the intensity at which the population difference, $\frac{n_2(u)}{g_2} - \frac{n_1(u)}{g_1}$, drops to one half its zero field value. Sodium radiation quenching is not included in equation A.88 since the quenching of sodium by helium is negligible and sodium sodium collisions are unlikely for the densities encountered in the experiment.

The explicit expression for the saturation intensity using the Einstein A and B coefficients is given by

$$I_s(u,\omega) = \frac{1}{1 + \frac{g_2}{g_1}} \frac{8\pi\hbar c}{\lambda_{21}^3} \frac{1}{g(u,\omega)} \qquad \text{A.94}$$

where g is velocity dependent and λ_{21} is the transition wavelength. The travelling electromagnetic wave interacts with the homogeneous part of the lineshape which is Lorentzian. The homogeneous lineshape is

$$g(u,\omega) = \frac{1}{\pi} \frac{\Delta\nu_L}{(\omega_s - \omega_{21})^2 + (\Delta\nu_L)^2} \qquad \text{A.95}$$

where $\Delta\nu_L$ is the HWHM (i.e. natural plus collision broadening) and

$$\omega_s = \omega - ku \qquad \text{A.96}$$

The preceding results may be substituted into equation A.84 to obtain the absorption coefficient $\kappa_\omega(u)$.

$$\kappa_\omega(u) = \frac{\hbar\omega}{4\pi} B_{12}^I \, g_1 \, \frac{\frac{n_1^o}{g_1} - \frac{n_2^o}{g_2}}{g_1} \, \frac{P(u)}{1 + \frac{I}{\frac{1}{1 + \frac{g_2}{g_1}} \frac{8\pi hc}{\lambda_{21}^3} \frac{1}{g(u,\omega)}}} \, g(u,\omega) \qquad \text{A.97}$$

By defining

$$I_s(\omega_{21}) = \frac{1}{1 + \frac{g_2}{g_1}} \, \frac{8\pi^2 \hbar c \Delta\nu_L}{\lambda_{21}^3} \qquad \text{A.98}$$

one obtains after some manipulations

$$\kappa_\omega(u) = \frac{\hbar\omega}{4\pi} B_{12}^I \left(\frac{n_1^o}{g_1} - \frac{n_2^o}{g_2}\right) \frac{1}{\sqrt{1 + \frac{I(\omega)}{I_s(\omega_{21})}}} \, \frac{1}{\pi} \, \frac{\Delta\nu_L \sqrt{1 + \frac{I(\omega)}{I_s(\omega_{21})}}}{(\omega - \omega_{21} - ku)^2 + \Delta\nu_L^2 [1 + \frac{I(\omega)}{I_s(\omega_{21})}]} \, P(u) \qquad \text{A.99}$$

Therefore the absorption coefficient is proportional to a Lorentzian, with a HWHM of

$$\Delta\nu_L' = \Delta\nu_L \sqrt{1 + \frac{I(\omega)}{I_s(\omega_{21})}} \qquad \text{A.100}$$

To find the contribution of all velocities, expression A.99 has to be integrated over all u. Even though sodium sodium collisions are neglected, the sodium is assumed to be in translational equilibrium with the helium atoms. In this case P(u) is a Gaussian and since only the velocity component, u, in the direction of propagation $\vec{k}$ is of interest, the velocity distribution function is given by the one dimensional Maxwell Boltzman distribution.[20]

$$P(u) = \sqrt{\frac{m}{2\pi kT}}\, e^{-\frac{m}{2kT}u^2} \qquad A.101$$

A new variable is defined to simplify the notation

$$\Delta = ku = \frac{\omega u}{c} \qquad A.102$$

Then

$$P(u)du = \frac{1}{\sqrt{\pi}\,\delta}\, e^{-(\frac{\Delta}{\delta})^2}\, d\Delta \qquad A.103$$

where

$$\delta = \frac{\omega}{c}\sqrt{\frac{2kT}{m}} \simeq \frac{\omega_{21}}{c}\sqrt{\frac{2kT}{m}} = \frac{\Delta\nu_D}{\sqrt{\ell n 2}} \qquad A.104$$

$\Delta\nu_D$ is the Doppler HWHM and is defined by equation A.31. The last approximation holds for

$$\left|\frac{\omega-\omega_{21}}{\omega_{21}}\right| = 10^{-5} << 1 \qquad A.105$$

as the maximum frequency scan of the dye laser is 5 GHz. Finally

$$\kappa_\omega = \frac{\pi^2 c^2}{\omega_{21}^2}\,\frac{g_2}{g_1}\,A_{21}\left(\frac{n_1^o}{g_1} - \frac{n_2^o}{g_2}\right)\frac{1}{\sqrt{1+\frac{I(\omega)}{I_s(\omega_{21})}}} \cdot V(x) \qquad A.106$$

where

$$V(x) = \int_{-\infty}^{\infty}\left\{\frac{1}{\pi}\,\frac{\Delta\nu_L\sqrt{1+\frac{I(\omega)}{I_s(\omega_{21})}}}{(\omega-\omega_{21}-\Delta)^2+\Delta\nu_L^2\left[1+\frac{I(\omega)}{I_s(\omega_{21})}\right]}\right\}\left\{\sqrt{\frac{\ell n 2}{\pi}}\,\frac{1}{\Delta\nu_D}\, e^{-\ell n 2(\frac{\Delta}{\Delta\nu_D})^2}\right\}d\Delta \qquad A.107$$

The integral, V(x), in equation A.107 is a convolution of a Lorentzian and a Gaussian lineshape known as the Voigt profile.[61] It is normalized, since both the Lorentzian and the Gaussian are normalized. The following nondimensional quantities are introduced to simplify the notation[62]

$$a = \frac{\Delta\nu_L'}{\Delta\nu_G/\sqrt{\ell n 2}} \qquad \text{A.108}$$

$$x = \frac{\nu-\nu_{21}}{\Delta\nu_G/\sqrt{\ell n 2}} \qquad \text{A.109}$$

$$y = \frac{\Delta}{\Delta\nu_G/\sqrt{\ell n 2}} \qquad \text{A.110}$$

After some manipulation one obtains

$$V(x) = \frac{\ell n 2}{(\pi)^{3/2}} \frac{\Delta\nu_L'}{\Delta\nu_G^2} \int_{-\infty}^{\infty} \frac{e^{-y^2}}{(x-y)^2+a^2}\,dy = \frac{1}{(\pi)^{3/2}} \frac{a^2}{\Delta\nu_L'} \int_{-\infty}^{\infty} \frac{e^{-y^2}}{(x-y)^2+a^2}\,dy \qquad \text{A.111}$$

where $\Delta\nu_L'$ is defined by equation A.100.

The shape of V(x) is determined by the parameter a only. The linewidths $\Delta\nu_G$ and $\Delta\nu_L'$ determine the scale of the frequency and intensity axis. The Voigt profile cannot be expressed in analytical form but has been evaluated numerically.[33]

The data analysis procedure employed in this experimental investigation requires the deconvolution of the natural and collisional lineshapes which are Lorentzian. The special case of a convolution of two Lorentzians provides a Lorentzian with a linewidth equal to the sum of the individual widths. The convolution of two Gaussians provides a Gaussian with a linewidth squared equal to the sum of the squares of the individual widths.

Values of the Lorentzian and Gaussian profiles versus detuning off line center in HWHM units, i $\Delta\nu$, where i is an integer, are presented in Table A.1.

Table A.1

i	0.1	0.2	0.4	1	2	4	10
$\pi\Delta'\nu_L L(i\Delta\nu_L', \Delta\nu_L')$	0.99	0.96	0.86	0.5	0.2	0.06	0.01
$\sqrt{\frac{\pi}{\ell n 2}}\,\Delta\nu_G G(i\Delta\nu_G, \Delta\nu_G)$	0.99	0.97	0.89	0.5	0.065	1.5×10^{-5}	8×10^{-31}

The Gaussian clearly falls off much faster off line center. For $\Delta\nu_L' << \Delta\nu_G$ the line profile would be Gaussian to about three Doppler widths before changing over to the more slowly decreasing Lorentzian shape. For the opposite case, $\Delta\nu_L' >> \Delta\nu_G$, the profile would be approximately Lorentzian over the entire lineshape. When $\Delta\nu_L' \simeq \Delta\nu_G$ it is possible to determine both $\Delta\nu_L'$ and $\Delta\nu_G$ from a detailed comparison of the experimental and theoretical line profiles.[48]

Due to the presence of the electromagnetic field, the value of κ_ω drops and its frequency response broadens. The broadening may be related to the shortening of the lifetime of the upper state by stimulated emission and of the lower state by absorption.[63] The smaller value of κ_ω is due to absorption followed by the reduction in the number density of the ground state. These effects, induced by the laser electromagnetic field, are known as saturation of the absorption line and power broadening.

In the present experimental work the absorption line is obtained by scanning the laser frequency and monitoring the spontaneous emission intensity. A hyperfine structure is associated with each D line of sodium. Since the hyperfine lines are of different strengths, the radiation emitted by the focal volume might be reabsorbed differently by each transition. This would distort the spectrum. The effect is known as radiation trapping[62] and is discussed more fully in Chapter III.

Appendix B

DATA REDUCTION BY LEAST SQUARES[41]

1. Introduction

Errors are the difference between a calculated or observed value and the true value of some quantity. Since the true value is unknown one has to compare the results to those of other experiments or to a theoretical calculation. One may identify two types of errors.

1) Systematic errors which are reproducible and can result from faulty calibration, background light scattering, etc. Statistical methods are useless in this case. The systematic errors have to be estimated by analyzing the experimental conditions. The systematic errors are then added to the statistical ones.

2) Random errors are due to instrumental uncertainties or counting statistics. These errors may be reduced by using more reliable instruments or counting more events.

It is usually of interest to extract the most reasonable estimate of the theoretical parameters from the experimental observations, compute the uncertainties in the calculations based on the random errors and evaluate the confidence in the final result. The accuracy of an experiment is a measure of how close the result of the experiment comes to the true value. Therefore it is a measure of the correctness of the result. The precision of an experiment is a measure of how exactly the result is determined, without reference to what the result means. Precision is also a measure of how reproducible a result is. Clearly the uncertainties in the estimates of the theoretical parameters are related to precision while the confidence in the final result pertains to the accuracy of the experiment.

2. Distributions

One defines a parent distribution which determines the probability of obtaining any particular observation in one measurement. The parent population is a collection of an infinite number of measurements from which the parent distribution is obtained. In practical experiments the finite number of measurements is a sample from the parent population. Even if one cannot determine the true value, one would like to describe the parent distribution as well as possible.

The experimental parent distribution is assumed to equal the theoretical one in the limit of an infinite number of observations. Denoting by y_i the i^{th} observation of y and by N the number of observations, one defines the mean μ by

$$\mu = \lim_{N\to\infty} \frac{1}{N} \sum_{i=1}^{N} y_i \qquad \text{B.1}$$

the median $\mu_{1/2}$ by

$$\text{probability}(y_i \leq \mu_{1/2}) = \text{probability}(y_i \geq \mu_{1/2}) = 50\% \qquad \text{B.2}$$

the most probable value μ_{max} by

$$\text{probability}(\mu_{max}) \geq \text{probability}(y_i) \qquad i = 1,\ldots,N \qquad \text{B.3}$$

If the probability distribution is symmetric then μ, $\mu_{1/2}$ and μ_{max} are all equal to the true value of the quantity of interest apart from systematic errors. For a nonsymmetric distribution, additional information pertaining to the causes for the deviations has to be supplied to determine which of μ, $\mu_{1/2}$ or μ_{max} if any represents the true value. By definition, μ , $\mu_{1/2}$ and μ_{max} are just parameters specifying the probability distribution. It is μ which by convention is considered to be the best estimate of the true value.

The variance σ^2 is defined by

$$\sigma^2 \equiv \lim_{N\to\infty} \frac{1}{N} \Sigma(y_i-\mu)^2 = \lim_{N\to\infty} (\frac{1}{N} \sum_{i=1}^{N} y_i^2) - \mu^2 \qquad \text{B.4}$$

The sample mean includes only a finite number of observations and

$$\bar{y} = \frac{1}{N} \sum_{i=1}^{N} y_i \qquad \text{B.5}$$

For large N

$$\bar{y} \simeq \mu \qquad \text{B.6}$$

The sum of the deviations from y_o, squared, is

$$\sum_{i=1}^{N} d^2 = \sum_{i=1}^{N} (y_i-y_o)^2 \qquad \text{B.7}$$

This sum is minimized for $y_o = \bar{y}$. The sample variance is defined by

$$S^2 = \frac{1}{N} \sum_{i=1}^{N} (y_i-\mu)^2 \qquad \text{B.8}$$

However μ is unknown. By substituting $\bar{y}$ for μ one underestimates the sample variance. This is evident for N equals one since the sample variance vanishes. Hence one defines a corrected sample variance.

$$S_\nu^2 = \frac{1}{\nu} \sum_{i=1}^{N} (y_i-\bar{y})^2 \qquad \text{B.9}$$

ν is the number of observations in excess of those needed to determine the parameters appearing in the equations.[39] If $\bar{y}$ is substituted for μ, at least one observation is needed to determine $\bar{y}$. Thus $\nu = N-1$ and

$$S_\nu^2 = \frac{1}{N-1} \sum_{i=1}^{N} (y_i-\bar{y})^2 \simeq \sigma^2 \qquad \text{B.10}$$

The last expression grows without bounds for a single measurement which is more in keeping with an idea of a variance. The most useful distributions are defined below.

a. Binomial Distribution

If the probability for the success of a single event is p then the probability $P_B(\ell,n,p)$ for the success of ℓ events out of n is

$$P_B(\ell,n,p) = \frac{n!}{\ell!(n-\ell)!} p^{\ell}(1-p)^{n-\ell}$$

and

$$\mu = np$$

$$\sigma^2 = np(1-p)$$

The maximum variance is obtained for p = 1/2. Then

$$P_B(\ell,n,1/2) = \frac{n!}{\ell!(n-\ell)!} \frac{1}{2^n}$$

$$\mu = n/2$$

$$\sigma^2 = n/4 = \mu/2$$

and the probability distribution is symmetric. The probability distribution is asymmetric for $n \neq 1/2$ and the variance is smaller then $\mu/2$. The ratio

$$\frac{\mu}{\sigma} = \frac{np}{\sqrt{np(1-p)}} = \sqrt{\frac{p}{1-p}}\sqrt{n} \qquad \text{B.11}$$

improves as the size of the sample, n, is enlarged.

b. Poisson Distribution

This represents a limiting case of the binomial distribution where the average number, μ, of successful events, ℓ, is much smaller than the possible number, n, since the probability for a single successful event, p, is vanishingly small. Then

$$P_p(\ell,\mu) = \frac{\mu^{\ell}}{\ell!} e^{-\mu} \qquad \text{B.12}$$

$$\sigma^2 = \mu \qquad \text{B.13}$$

The advantage of this distribution is that it is specified by the mean only. It is useful in counting experiments under the above mentioned conditions. The ratio

$$\frac{\mu}{\sigma} = \sqrt{\mu} \qquad \text{B.14}$$

improves as the square root of the mean.

c. Gaussian Distribution

This represents a limiting case of the binomial distribution for an infinite number of possible events with a finite probability for the success of a single event. Then

$$P_G(y,\mu,\sigma) = \frac{1}{\sqrt{2\pi}\,\sigma} e^{-\frac{1}{2}\left(\frac{y-\mu}{\sigma}\right)^2} \qquad \text{B.15}$$

The distribution is relatively simple and is accepted by convention and experimentation to be the most likely distribution for most experimental conditions where the Poisson distribution is inappropriate. The advantage of this distribution is that the most probable estimate of the mean, μ, from a random sample of observations, y, is the sample mean, $\bar{y}$. Generally one assumes either a Gaussian or a Poisson distribution for the measurement around the mean. Since these distributions are indistinguishable for most physical situations ($\mu \gg 1$), one assumes that the Gaussian distribution is obeyed. This is done due to the fact that the Gaussian distribution is more amenable to mathematical manipulations. μ is a parameter describing the parent distribution. By convention it is considered to be the best estimate of the true value.

3. Method of Maximum Likelihood

It is often of interest to determine one characteristic of an experiment y as a function of some other quantity x. That is to find the function f such that

$$y = f(x) \tag{B.16}$$

Instead of making a number of measurements of the quantity y for one particular value of x, one makes a series of N measurements y_{ij} one for each value of the quantity $x = x_j$, where j is an index that runs from 1 to N and i in this case is one. The procedure is depicted in Figure B.1 for a measurement y_{ij} at a single point x_j. y_{ij} is one value from the parent population associated with the parent distribution, P_j.

If one assumes a Gaussian distribution, the probability for obtaining a data point y_{ij} around the true value μ_j with uncertainty σ_j is

$$P_j = P(y_{ij},\mu_j,\sigma_j) = \frac{1}{\sqrt{2\pi}\sigma_j} e^{-\frac{1}{2}\left(\frac{y_{ij}-\mu_j}{\sigma_j}\right)^2} \tag{B.17}$$

It is assumed that the mean of y_{ij}, for all i in the parent population, is given by the fitting function f at x_j. That is

$$\mu_j = f(x_j) \tag{B.18}$$

σ_j has to be determined from an analysis of the experimental conditions.

The probability for making the observed set of measurements of the N values of y_{ij} is the product of these probabilities, which is known as the likelihood function

$$P = \left[\prod_{j=1}^{N} \frac{1}{\sqrt{2\pi}\sigma_j}\right] e^{-\frac{1}{2}\sum_{j=1}^{N}\left[\frac{y_{ij}-f(x_j)}{\sigma_j}\right]^2} \tag{B.19}$$

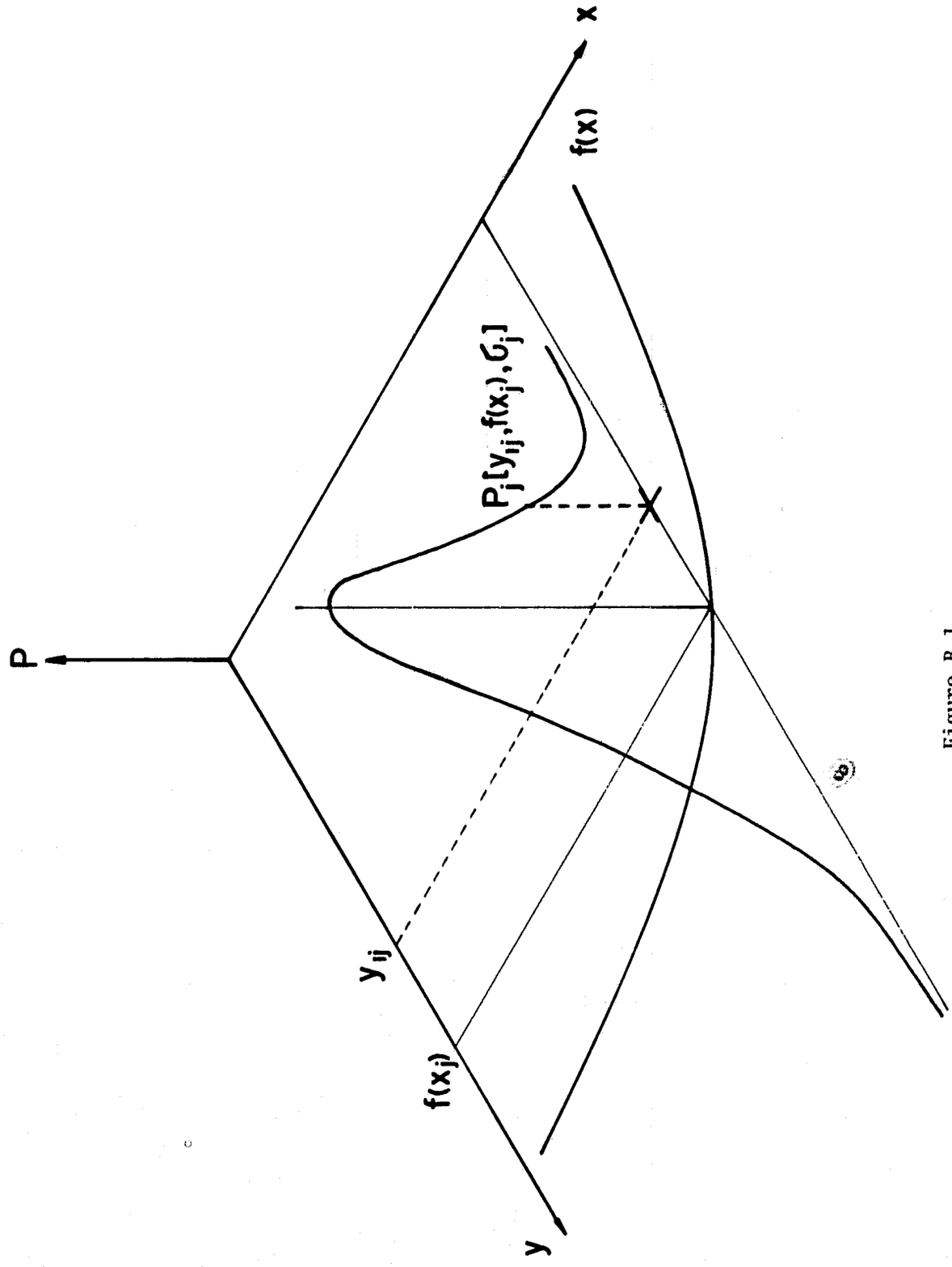

Figure B.1

The method of maximum likelihood assumes that the observed measurements are more likely to have resulting from a fitting function representing the parent distribution then from any other fitting function of the same form but with different coefficients. Hence, the fitting function representing the parent distribution is obtained by maximizing the probability or minimizing the sum of squares, χ^2,

$$\chi^2 = \sum_{j=1}^{N} \left[\frac{y_{ij}-f(x_j)}{\sigma_j}\right]^2 \qquad \text{B.20}$$

The same procedure can be applied to a Poisson distribution. Since the resulting expressions are more difficult to manipulate, one generally assumes that the shape of the individual Poisson distributions governing the distribution of each observation y_{ij} around its mean $f(x_j)$ are nearly Gaussian. The uncertainties are still assumed to be those associated with a Poisson distribution, $\sigma_j^2 = y_{ij}$.

4. Goodness of the Fit

The sum of squares is characterized by the variance of the fit, $S_\nu'^2$, which is an estimate of the variance of the data $\overline{\sigma^2}$. By definition

$$S_\nu'^2 = \frac{1}{N-n} \frac{1}{\frac{1}{N}\sum_{j=1}^{N}\frac{1}{\sigma_j^2}} \sum_{j=1}^{N} \frac{1}{\sigma_j^2}[y_{ij}-f(x_j)]^2 \qquad \text{B.21}$$

The square bracket on the right hand side is the deviation of point i out of the j^{th} parent population, y_{ij}, from the mean of the j^{th} parent population, $f(x_j)$. $1/\sigma_j^2$ is a weighting factor which reduces the N different distribution into one to enable the sum over j to be taken. The sum in the denominator is a normalization factor. The expression for the reduced sum of squares, χ_ν^2, is

$$\chi_\nu^2 = \frac{\chi^2}{N-n} = \frac{1}{N-n} \sum_{j=1}^{N} \left[\frac{y_{ij}-f(x_j)}{\sigma_j}\right]^2 = \frac{S_\nu'^2}{\overline{\sigma^2}} \qquad \text{B.22}$$

where

$$\overline{\sigma^2} = \frac{1}{\frac{1}{N}\sum_{j=1}^{N}\frac{1}{\sigma_j^2}} \qquad \text{B.23}$$

which for equal uncertainties $\sigma_j = \sigma$ reduces to

$$\overline{\sigma^2} = \sigma^2 \qquad \text{B.24}$$

$\overline{\sigma^2}$ is a characteristic of the dispersion of the data y_{ij} about the parent distribution j and is not descriptive of the fit. $S_\nu'^2$ is a characteristic of the spread of the data about the fit but is also an estimate of $\overline{\sigma^2}$. χ_ν^2 is the ratio of the estimated variance to the parent variance which makes it a convenient measure of the goodness of the fit.

If the fitting function is a good estimate of the parent function, $S_\nu'^2$ should agree with $\overline{\sigma^2}$ and $\chi_\nu^2 \simeq 1$. If the fitting function is not a

good approximation, the deviations will be larger, yielding too large a value for $\chi^2_\nu (\chi^2_\nu > 1)$. $\chi^2_\nu < 1$, does not indicate an improvement of the fit. It is simply a consequence of the uncertainty in the determination of σ_j.

The probability distribution for χ^2 with ν degrees of freedom is given by[64]

$$P(\chi^2,\nu) = \frac{(\chi^2)^{\frac{\nu-2}{2}} e^{-\frac{\chi^2}{2}}}{2^{\nu/2}\,\Gamma(\nu/2)} \qquad \text{B.25}$$

More important is the integral probability distribution for χ^2 defined by

$$P_\chi(\chi^2,\nu) = \int_\chi^\infty P(x^2,\nu)dx \qquad \text{B.26}$$

This function describes the probability that a random set of N points from the parent population would yield a value of χ^2 as large or larger. The probability P_χ of obtaining $\chi^2_\nu = 1$ is about 0.5. A larger value of χ^2_ν would yield a smaller value of P_χ.

There are three sources of error contributing to the size of χ^2.

1) The observations i from the j^{th} parent population, y_{ij}, are a random sample from the parent population. Each y_{ij} is measured at a certain x_j and has associated with it an expected value $\langle y_{ij} \rangle$ given by the population distribution and assumed to be equatl to $f(x_j)$. The fluctuations of the y_{ij}-s about the expected value may be greater or less than the uncertainties σ_j due to statistics. The value of χ^2 may be improved by repeating the experiment.

2) The parameters associated with the function have to be estimated accurately. This may be done using the least square method to minimize χ^2.

3) The choice of the functional behavior of the analytical fitting

function f(x) as an approximation to the true function <f(x)> will influence the value of χ^2. The resultant value of χ^2 for several different functions f(x) can be compared to determine the most probable form for f(x).

5. Nonlinear Least Squares

The least squares solution is straightforward if the fitting function is linear in the coefficient. For an arbitrary function one may extrapolate to the method of nonlinear least squares.

χ^2 is considered a continuous function of the n parameters β_k (k = 1,...,n) describing a hypersurface in n dimensional space. The space must be searched for the appropriate minimum of χ^2. More than one minimum for χ^2 may exist within a reasonable range of the parameters β_k. It is then advantageous to conduct a coarse grid mapping of the parameter space to locate the main minima and identify the desired range of parameters over which to refine the search. Once this has been done, one may follow three methods to obtain the minimum of χ^2.

a. Gradient Search

All parameters β_k are incremented simultaneously with their relative magnitudes adjusted so that the resultant direction of travel is along the local gradient of χ^2.

$$\nabla\chi^2 = \sum_{k=1}^{n} \frac{\partial\chi^2}{\partial\beta_k} \Delta\hat{\beta}_k \qquad \text{B.27}$$

where $\Delta\beta_k$ characterizes the variation of χ^2 with β_k. Then define a dimensionless gradient

$$\vec{\gamma}_k = \frac{\frac{\partial\chi^2}{\partial\beta_k}\hat{\beta}_k}{\sum_{k=1}^{n} \left(\frac{\partial\chi^2}{\partial\beta_k}\right)^2} \qquad \text{B.29}$$

The procedure involves assuming an initial set of parameters and computing χ^2 and γ_k. Then incrementing the parameters simultaneously by

$$\delta\beta_k = -\gamma_k \Delta\beta_k \qquad \text{B.30}$$

and recalculating χ^2 and γ_k. These steps are continued until χ^2 is minimized.

b. Linearization of the Sum of Squares

Instead of searching the χ^2 hypersurface for the minimum one may look for an analytical approximation to the hypersurface and use it to locate the minimum directly.

Expanding χ^2 to first order around some starting point $(\beta_k)_o$.

$$\chi^2 = \chi^2_o + \sum_{k=1}^{n} \left.\frac{\partial\chi^2}{\partial\beta_k}\right|_o [\beta_k - (\beta_k)_o] = \chi^2_o + \sum_{k=1}^{n} \left.\frac{\partial\chi^2}{\partial\beta_k}\right|_o \delta\beta_k \qquad \text{B.31}$$

where

$$\delta\beta_k = \beta_k - (\beta_k)_o$$

Equation has to be differentiated to locate the minimum. At the minimum of χ^2, the derivatives $\frac{\partial\chi^2}{\partial\beta_\ell}$ vanish

$$\frac{\partial\chi^2}{\partial\beta_\ell} = \left.\frac{\partial\chi^2}{\partial\beta_\ell}\right|_o + \sum_{k=1}^{n} \left.\frac{\partial^2\chi^2}{\partial\beta_\ell\partial\beta_k}\right|_o \delta\beta_k = 0 \qquad (\ell = 1,\ldots,n) \qquad \text{B.32}$$

One may introduce the matrix elements.

$$(\bar{b})_\ell = -\frac{1}{2} \left.\frac{\partial\chi^2}{\partial\beta_\ell}\right|_o \quad ; \qquad \text{B.33}$$

$$(\delta\beta)_k = \delta\beta_k \quad ; \qquad \text{B.34}$$

$$(\bar{\bar{\alpha}})_{k\ell} = \frac{1}{2} \frac{\partial^2\chi^2}{\partial\beta_k\partial\beta_\ell} \qquad \text{B.35}$$

Then

$$\bar{b} = \bar{\delta\beta}\ \bar{\bar{\alpha}} \qquad \text{B.36}$$

The procedure involves assuming an initial set of parameters and calculating

$\bar{\bar{\alpha}}$ and $\bar{b}$. Then by solving the matrix equation one can obtain the new values of the parameters. These steps are continued until convergence is obtained. The gradient method suffers near the minimum as the evaluation of the derivatives by finite differences consists of the subtraction of almost equal numbers. The linearization scheme works best near the minimum when only first order terms may be kept. Marquardt[34.b] shows that the path direction for the gradient and linearization schemes are nearly perpendicular. Thus the optimum search direction is somewhere in between. A program provided by I.M.S.L.[35, 33.c] has been used in this experimental investigation.

c. Linearization by Expanding the Fitting Function

Instead of expanding χ^2 one could linearize the fitting function f(x). The function, f(x), expanded to second order is

$$f(x) = f_o(x) + \sum_{k=1}^{n} \frac{\partial f_o(x)}{\partial \beta_k} \delta\beta_k + \frac{1}{2} \sum_{\ell=1}^{n} \sum_{k=1}^{n} \frac{\partial^2 f_o(x)}{\partial \beta_k \partial \beta_\ell} \delta\beta_k \delta\beta_\ell \qquad \text{B.37}$$

If the above equation is substituted into equation B.20 and differentiated with respect to the parameter increments $\delta\beta_s$ (s is an integer) for minimization purposes one obtains

$$\frac{\partial \chi^2}{\partial \delta\beta_s} = -\sum_{j=1}^{N} 2\left[\frac{y_{ij} - f(x_j)}{\sigma_j}\right]\left(\frac{1}{\sigma_j}\right)\left[\frac{\partial f_o(x_j)}{\partial \beta_s} + \frac{1}{2}\sum_{k=1}^{n} \frac{\partial^2 f_o(x_j)}{\partial \beta_k \partial \beta_s} \delta\beta_k\right.$$

$$\left. + \frac{1}{2}\sum_{\ell=1}^{n} \frac{\partial^2 f_o(x_j)}{\partial \beta_s \partial \beta_\ell} \delta\beta_\ell\right] = -2 \sum_{j=1}^{N} \frac{1}{\sigma_j^2}\left[y_{ij} - f_o(x_j) - \sum_{k=1}^{n} \frac{\partial f_o(x_j)}{\partial \beta_k}\right. \qquad \text{B.38}$$

$$\left. - \frac{1}{2}\sum_{\ell=1}^{n}\sum_{k=1}^{n} \frac{\partial^2 f_o(x_j)}{\partial \beta_k \partial \beta_\ell} \delta\beta_k \delta\beta_\ell\right]\left[\frac{\partial f_o(x_j)}{\partial \beta_s} + \sum_{k=1}^{n} \frac{\partial^2 f_o(x_j)}{\partial \beta_j \partial \beta_s} \delta\beta_k\right]$$

At the minimum $\frac{\partial \chi^2}{\partial \delta \beta_s}$ vanishes. Then if terms of order higher than one in the parameter increments are neglected one obtains

$$\sum_{j=1}^{N} \frac{1}{\sigma_j^2} [y_{ij}-f_o(x_j)] \frac{\partial f_o(x_j)}{\partial \beta_s} = \sum_{j=1}^{N} \frac{1}{\sigma_j^2} \{ \sum_{k=1}^{n} \frac{\partial f_o(x_j)}{\partial \beta_k} \delta\beta_k \frac{\partial f_o(x_j)}{\partial \beta_s}$$

$$- [y_{ij}-f_o(x_j)] \sum_{k=1}^{n} \frac{\partial^2 f_o(x_j)}{\partial \beta_k \partial \beta_s} \delta\beta_k \} \qquad \text{B.39}$$

The above result may be put into the matrix form of equation B.36 after defining

$$(\bar{\beta})_k = \sum_{j=1}^{N} \frac{1}{\sigma_j^2} [y_{ij}-f_o(x_j)] \frac{\partial f_o(x_j)}{\partial \beta_k} = - \frac{1}{2} \sum_{j=1}^{N} \frac{1}{\sigma_j^2} \frac{\partial}{\partial \beta_k} [y_{ij}-f_o(x_j)]^2$$

$$= - \frac{1}{2} \frac{\partial \chi_o^2}{\partial \beta_k} \qquad \text{B.49}$$

$$\alpha_{k\ell} = \sum_{j=1}^{N} \frac{1}{\sigma_j^2} \{ \frac{\partial f_o(x_j)}{\partial \beta_k} \frac{\partial f_o(x_j)}{\partial \beta_\ell} - [y_{ij}-f_o(x_j)] \frac{\partial^2 f_o(x_j)}{\partial \beta_k \partial \beta_\ell} \} = \frac{1}{2} \frac{\partial^2 \chi_o^2}{\partial \beta_k \partial \beta_\ell} \qquad \text{B.50}$$

These are the same definitions as in equations B.33 to B.35

6. Uncertainties in the Parameters

The χ^2 criterion can be rigorously applied to evaluate the validity of the model only if the data are uncorrelated and represent a statistical distribution. Conversely, if one accepts that the model fully describes the physics, χ^2 may be used to measure the consistency of the data. Unfortunately in most physical applications both of these conditions break down.

Choosing the data to be correct, χ^2 may be directly related to the model parameters. Define the error in the model parameter β_k as

$$\Delta\beta_k = [(\bar{\bar{\alpha}}^{-1})_{kk}]^{1/2} \qquad (k = 1,\ldots,n) \qquad \text{B.42}$$

where $\bar{\bar{\alpha}}$ is the matrix in equation VI.B.35. Changing β_k by $\Delta\beta_k$ while optimizing all the other parameters $\beta_\ell \neq k$ for minimum χ^2, then the new value of χ^2 will be 1 greater than the old value. Denoting the likelihood function by P, then[40]

$$\beta_k \rightarrow \beta_k + \Delta\beta_k \quad , \quad \chi^2 \rightarrow \chi^2 + 1 \quad , \quad P \rightarrow \frac{1}{\sqrt{e}} P \qquad \text{B.43}$$

Hence $\Delta\beta_k$ corresponds to a standard deviation since by definition, the Gaussian probability distribution at $\mu\pm\sigma$ drops in value by $\sqrt{e}^{-1}$ compared to its value at μ.

To use the method of least squares one has to assume that the uncertainties are in the dependent variable, y.

$$\frac{\sigma_x}{x_{j_1} - x_{j_2}} << \frac{\sigma_y}{y_{ij_1} - y_{ij_2}} \qquad \text{B.44}$$

where the subscripts j_1 and j_2 correspond to two representative measurements. The above assumption does not always hold. The fitting will still be correct if the uncertainties in the dependent and independent variable are combined and assigned to the dependent variable. If the uncertainties in the

independent variable is larger than in the dependent variable it would be beneficial to switch their roles.

Appendix C

COMPUTER PROGRAMS

1. Data Acquisition

The program reads NCH1 channels, NPPC1 samples per channel from the GMAD/1 A/D converter and NCH4 channels, NPPC4 samples per channel from the GMAD/4 A/D converter. The results are stored in binary form on tape. The records on tape are arranged in the following order.

ITITLE (19) - contains the date and time, the run number, the sampling rate for the GMAD/1 and the total sampling time for the GMAD/1.

HEAD (10) - contains the calibration of the linear position transducer and the laser frequency calibration.

IPT (180) - Includes the position, stagnation temperature and wall temperature in sequential order. The first half of the array contains data preceding the GMAD/1 scan and the second half contains data taken after the GMAD/1 scan.

IVOLT (4000) - Includes the laser voltage ramp, the atomic beam device photomultiplier intensity, the tunnel photomultiplier intensity and the laser intensity in sequential order.

```
0001  FTN4,L
0002        PROGRAM AD0
0003  C     DATA AQUISITION PROGRAM USING THE GMD1 AND THE GMD4
0004  C     THE PROGRAM READS NCH1 CHANNELS, NPPC1 SAMPLES PER CHANNEL FROM
0005  C     THE GMAD/1 A/D CONVERTER FOR RAMP, C.C. TUNNEL, INTENSITY.
0006  C     THE PROGRAM READS NCH4 CHANNELS, NPPC4 SAMPLES PER CHANNEL FROM
0007  C     THE GMAD/4 A/D CONVERTER FOR POSITION, TEMPERATURE.
0008        COMMON ICOM(196)
0009        REAL CAL(6),POS(4),HEAD(10)
0010        INTEGER IBUFR(4000),IB(14),ITITLE(19),IPT(180),
0011       1        PARMS(5),TRIG(2)
0012        EQUIVALENCE (IB,ITITLE),(IRUN,ITITLE(15)),(HERTZ,ITITLE(16)),
0013       1            (ETIME,ITITLE(18)),
0014       2            (HEAD,POS),(HEAD(5),CAL)
0015        DATA CAL /3.69,2137.,5.476,1066.,8.09,1525./
0016        DATA LUMT,LUAD1,LUAD4 /8,10,9/
0017        DATA NCH1,NPPC1 /4,1000/
0018        DATA NCH4,NPPC4 /3,30/
0019        DATA ETIME /1.0E+03/
0020      1 FORMAT (9I10)
0021      2 FORMAT (1P10E12.4)
0022      3 FORMAT (10F12.4)
0023      4 FORMAT (" PRESS CR TO CONTINUE. ENTER 1 TO CALIBRATE")
0024      5 FORMAT (" ENTER POSITION IN INCHES ←")
0025      6 FORMAT (" PRESS CR TO RUN. ENTER -1 OTHERWISE")
0026      7 FORMAT (" ENTER DESIRED GMAD/1 SAMPLING RATE IN HERTZ ←")
0027      8 FORMAT (" ACTUAL SAMPLING RATE IS ",G10.4," HERTZ")
0028  C
0029  C
0030  C...  DETERMINE INPUT CRT
0031  C
0032        CALL RMPAR (PARMS)
0033        IF (PARMS(1) .GT. 0) LUCRT=PARMS(1)
0034  C
0035  C
0036  C...  SET GMAD/4 TO SEQUENTIAL MODE WITH FIRST AND LAST CHANNELS
0037  C...  DETERMINED BY FRONT PANEL SWITCHES
0038  C
0039        CALL EXEC(3,LUAD4+1300B)
0040  C
0041  C
0042  C...  CALIBRATE POSITION
```

```
0043  C
0044        WRITE (LUCRT,4)
0045        READ (LUCRT,*) ICON
0046        IF (ICON .NE. 1) GO TO 17
0047           DO 14 I=1,3,2
0048           WRITE (LUCRT,5)
0049           READ (LUCRT,*) POS(I+1)
0050           CALL EXEC (1,LUAD4,IPT,90,2000B)
0051           POS(I)=0.0
0052              DO 15 J=1,88,3
0053              POS(I)=POS(I)+FLOAT(IPT(J))/1638.4
0054     15       CONTINUE
0055           POS(I)=POS(I)/30
0056     14    CONTINUE
0057     17 CONTINUE
0058        ICLK=LUAD1+3000B
0059        IBUFL=NPPC1*NCH1
0060  C
0061  C
0062  C...  SPECIFY A/D THROUGHPUT RATE IN HERTZ
0063  C
0064        WRITE (LUCRT,7)
0065        READ (LUCRT,*) HERTZ
0066  C
0067  C
0068  C...  COMPUTE CLOCK DIVISOR
0069  C
0070        ICDV=IFIX(1.0E+07/HERTZ)
0071        HERTZ=1.0E+07/FLOAT(ICDV)
0072        WRITE (LUCRT,8) HERTZ
0073  C
0074  C
0075  C...  SET CLOCK DIVISOR
0076  C
0077        CALL EXEC (3,ICLK,ICDV)
0078        IRUN=0
0079     13 CONTINUE
0080        WRITE (LUCRT,6)
0081        READ (LUCRT,*) ICON
0082        IF (ICON .EQ. -1) GO TO 16
0083        IRUN=IRUN+1
0084  C
```

```
0085  C
0086  C...  READ POSITION AND TEMPERATURE
0087  C
0088        CALL EXEC (1,LUAD4,IPT,NCH4*NPPC4,2000B)
0089  C
0090  C
0091  C...  READ IBUFL SAMPLES INTO IBUFR, BEGIN AT FIRST CHANNEL
0092  C
0093        CALL EXEC (3,LUAD1+3100B,NCH1-1)
0094        CALL EXEC (1,LUAD4,TRIG,2,2077B)
0095        CALL EXEC (1,LUAD1,IBUFR,IBUFL)
0096  C
0097  C
0098  C...  GET STATUS AND TRANSMISSION LOG(WORD COUNT)
0099  C
0100        CALL ABREG(ISTAT,ITLOG)
0101        ISTAT=IAND(ISTAT,1)
0102  C
0103  C
0104  C...  ISTAT SHOULD BE EQUAL TO ONE. IF NOT WE DID NOT END ON LAST
0105  C...  CHANNEL
0106  C
0107  C
0108  C
0109  C...  READ POSITION AND TEMPERATURE
0110  C
0111        CALL EXEC (1,LUAD4,IPT(91),NCH4*NPPC4,2000B)
0112  C
0113  C
0114  C...  READ DATE
0115  C
0116        CALL TODAY(IB)
0117        WRITE (LUCRT,1) IRUN
0118  C
0119  C
0120  C...  WRITE TO TAPE
0121  C
0122        CALL EXEC (2,LUMT,ITITLE,19)
0123        CALL EXEC (2,LUMT,HEAD,20)
0124        CALL EXEC (2,LUMT,IPT,180)
0125        CALL EXEC(2,LUMT,IBUFR,IBUFL)
0126  C
```

```
0127  C
0128  C...  WRITE EOF
0129  C
0130        CALL EXEC(3,LUMT+100B)
0131        GO TO 13
0132     16 CONTINUE
0133        STOP
0134        END
```

FTN4 COMPILER: HP92060-16092 REV. 1926 (790430)

** NO WARNINGS ** NO ERRORS ** PROGRAM = 04700 COMMON = 00196

```
0135          END$
```

2. Data Reducation for a One Beam Experiment

This step had to be divided into three programs due to memory limitations. Program DC12 converts from binary into decimal and rearranges the sequential arrays into separate ones for each device. It eliminates the points taken by the A/D converter before and after the laser scan and calibrates the position and temperature. Program FT12 fits the experimental data with a theoretically derived fit with a least squares routine ZXSSQ supplied by IMSL. Program PL12 plots the theoretical curve, the experimental tunnel and atomic beam data, the theoretical line strengths for the six D_2 transitions and residuals.

```
0001  FTN4,L
0002        PROGRAM DC12
0003  C     CHANGES DATA FROM BINARY INTO DECIMAL.
0004  C     WRITES ONTO DISK
0005  C     RUNS FITTING AND PLOTTING PROGRAMS FOR 1000 POINTS (ONE BEAMS)
0006        COMMON ICOM(196)
0007        REAL VOLT(1000,4),H(10),P(60),T(60),TW(60),SLOPE(5),
0008       1     CCL(100,2),CCR(100,2)
0009        INTEGER PARMS(5),ITITLE(54),IVOLT(4000),IPT(180)
0010        EQUIVALENCE (PARMS(1),LUCRT)
0011        EQUIVALENCE (ITITLE(16),ISCAN),(ITITLE(18),REFL),
0012       1            (ITITLE(32),REFR),
0013       2            (ITITLE(34),XPOS),
0014       3            (EXMI,ITITLE(38)),(EXM,ITITLE(40)),
0015       4            (ITITLE(42),TA),(ITITLE(44),TB),
0016       5            (ITITLE(46),TC),(ITITLE(48),TD),
0017       6            (ITITLE(54),K1)
0018        DATA LUMT /8/
0019      1 FORMAT (16I6)
0020      2 FORMAT (' ',1P10E13.4)
0021      3 FORMAT (10F12.4)
0022      4 FORMAT (" ENTER NUMBER OF RUNS TO BE FITTED AND PLOTTED <39")
0023      5 FORMAT (" HIT CR TO PLOT. ENTER -1 OTHERWISE.")
0024      6 FORMAT (" HIT CR FOR HISTOGRAM-DISTRIBUTION. ENTER -1 OTHERWISE.")
0025      7 FORMAT (" HIT CR FOR RAMP NOISE FILTER. ENTER -1 OTHERWISE.")
0026  C
0027  C
0028  C...  DETERMINE CONSOLE
0029  C
0030        CALL RMPAR(PARMS)
0031        IF (LUCRT .LE. 0) LUCRT=1
0032  C
0033  C
0034  C...  HISTOGRAM-DISTRIBUTION?
0035  C
0036        WRITE (LUCRT,6)
0037        READ (LUCRT,*) N5
0038  C
0039  C
0040  C...  RAMP NOISE FILTER?
0041  C
0042        WRITE (LUCRT,7)
```

```
0043          READ (LUCRT,*) NS
0044    C
0045    C
0046    C...  ALLOCATE DISK TRACKS WITH SUSPENSION
0047    C
0048          CALL EXEC (15,3,ISTRK,IDISK,ISECT)
0049    C
0050    C
0051    C...  DETERMINE NUMBER OF RUNS TO BE FITTED AND PLOTTED
0052    C
0053          WRITE (LUCRT,4)
0054          READ (LUCRT,*) N1
0055          DO 14 K1=1,N1
0056    C
0057    C
0058    C...  READ TITLE FROM TAPE
0059    C
0060          CALL EXEC (1,LUMT,ITITLE,19)
0061    C
0062    C
0063    C...  READ POSITION AND FREQUENCY CALIBRATION FROM TAPE
0064    C
0065          CALL EXEC (1,LUMT,H,20)
0066    C
0067    C
0068    C...  READ DATA FROM TAPE
0069    C
0070          CALL EXEC (1,LUMT,IPT,180)
0071          CALL EXEC(1,LUMT,IVOLT,4000)
0072    C
0073    C
0074    C...  FORWARD SPACE MAG. TAPE FILE
0075    C
0076          CALL EXEC (3,LUMT+1300B)
0077    C
0078    C
0079    C...  CONVERT TO FLOAT
0080    C
0081          K=0
0082             DO 10 I=1,1000
0083                DO 20 J=1,4
0084                M=K+J
```

```
0085                VOLT(I,J)=FLOAT(IVOLT(M)/8)/409.6
0086     20         CONTINUE
0087             K=K+4
0088     10      CONTINUE
0089  C
0090         DO 16 I=1,60
0091         P(I)=FLOAT(IPT((I-1)*3+1))/1638.4
0092         T(I)=FLOAT(IPT((I-1)*3+2))/1638.4
0093         TW(I)=FLOAT(IPT((I-1)*3+3))/1638.4
0094     16 CONTINUE
0095  C
0096  C
0097  C...  FIND MAX. VOLTAGE ON RAMP.
0098  C
0099         A=0.
0100            DO 12 I=1,1000
0101            IF (VOLT(I,1) .LT. A) GO TO 12
0102            A=VOLT(I,1)
0103            ISMAX=I
0104     12 CONTINUE
0105         WRITE (6,2) A
0106  C
0107  C
0108  C...  FIND SCAN STARTING POINT
0109  C
0110            DO 21 I=1,5
0111            J=ISMAX-I+1
0112            SLOPE(I)=(VOLT(J,1)-VOLT(J-10,1))/10
0113     21     CONTINUE
0114         ISMIN=ISMAX
0115            DO 22 I=2,ISMAX
0116            IF (SLOPE(5) .LT. SLOPE(1)/5) GO TO 24
0117            J=ISMAX-I+1
0118            ISMIN=J
0119               DO 23 K=1,4
0120               SLOPE(K)=SLOPE(K+1)
0121     23        CONTINUE
0122            SLOPE(5)=(VOLT(J-4,1)-VOLT(J-14,1))/10
0123     22     CONTINUE
0124     24 CONTINUE
0125         ISMIN=ISMIN-4
0126         ISCAN=ISMAX-ISMIN+1
```

```
0127        WRITE (6,1) ISCAN
0128  C
0129  C
0130  C...  RESTRUCTURE ARRAYS
0131  C
0132           DO 25 J=1,4
0133              DO 26 I=1,ISCAN
0134              VOLT(I,J)=VOLT(ISMIN+I-1,J)
0135     26       CONTINUE
0136     25    CONTINUE
0137  C
0138  C
0139  C...  ELIMINATE NONSCANNING TERMS
0140  C
0141           DO 13 J=1,4
0142              DO 15 I=ISCAN+1,1000
0143              VOLT(I,J)=0
0144     15       CONTINUE
0145     13    CONTINUE
0146  C
0147  C
0148  C...  FILTER OUT NOISE IN RAMP
0149  C
0150        IF (N6 .EQ. -1) GO TO 32
0151           DO 11 I=11,ISCAN-10
0152           V=VOLT(I-10,1)
0153              DO 19 J=1,20
0154              V=V+VOLT(I-10+J,1)
0155     19       CONTINUE
0156           VOLT(I,1)=V/21.
0157     11    CONTINUE
0158     32 CONTINUE
0159  C
0160  C
0161  C...  MAX OF LASER INTENSITY
0162  C
0163        LMAX=VOLT(1,4)
0164           DO 30 I=1,ISCAN
0165           IF (VOLT(I,4) .LT. LMAX) GO TO 30
0166           ILMAX=VOLT(I,1)
0167           LMAX=VOLT(I,4)
0168     30    CONTINUE
```

```
0169  C
0170  C
0171  C...  NORMALISE LASER INTENSITY
0172  C
0173           DO 31 I=1,ISCAN
0174           VOLT(I,4)=VOLT(I,4)/LMAX
0175     31    CONTINUE
0176  C
0177  C
0178  C...  DIVIDE OUT LASER INTENSITY FROM TUNNEL DATA
0179  C
0180           DO 111 I=1,ISCAN
0181           IF (VOLT(I,4) .EQ. 0) GO TO 111
0182           VOLT(I,3)= VOLT(I,3)/VOLT(I,4)
0183    111    CONTINUE
0184  C      WRITE (6,2) (VOLT(I,3),I=1,700)
0185  C
0186  C
0187  C...  AVERAGE POSITION AND STAGNATION TEMPERATURE ARRAYS
0188  C
0189  C
0190        VPOS=0.0
0191        T1=0.0
0192        T2=0.0
0193        T3=0.0
0194        T4=0.0
0195           DO 113 I=1,30
0196           VPOS=VPOS+P(I)+P(I+30)
0197           T1=T1+T(I)
0198           T2=T2+T(I+30)
0199           T3=T3+TW(I)
0200           T4=T4+TW(I+30)
0201    113 CONTINUE
0202        VPOS=VPOS/60
0203        T1=T1/30
0204        T2=T2/30
0205        T3=T3/30
0206        T4=T4/30
0207        XPOS=(H(4)-H(2))*(VPOS-H(1))/(H(3)-H(1))
0208  C
0209  C
0210  C...  ADJUST TEMPERATURE READINGS FOR AMPLIFICATION
```

```
0211  C
0212        T1=T1*.003
0213        T2=T2*.003
0214        T3=T3*.003
0215        T4=T4*.003
0216  C
0217  C
0218  C...  CALIBRATE TEMPERATURES
0219  C
0220        TA=CRALM(T1,-1,IER1)
0221        TB=CRALM(T2,-1,IER2)
0222        TC=CRALM(T3,-1,IER3)
0223        TD=CRALM(T4,-1,IER4)
0224  C
0225  C
0226  C...  CALIBRATE EXPERIMENTAL FREQUENCY
0227  C
0228        CF1=3.0552
0229        CF2=532.74
0230        DO 18 I=1,ISCAN
0231           CALL CAL (CF1,CF2,VOLT(I,1),FR)
0232           VOLT(I,1)=FR
0233     18    CONTINUE
0234  C
0235  C
0236  C...  MAX. FREQUENCY
0237  C
0238        EXM=0.0
0239        DO 66 I=1,ISCAN
0240        IF (VOLT(I,1) .GT. EXM) EXM=VOLT(I,1)
0241     66 CONTINUE
0242  C
0243  C
0244  C...  MIN. FREQUENCY
0245  C
0246        EXMI=EXM
0247        DO 68 I=1,ISCAN
0248        IF (VOLT(I,1) .LT. EXMI) EXMI=VOLT(I,1)
0249     68 CONTINUE
0250  C
0251  C
0252  C
```

```
0253  C
0254  C...  MAX. ON LEFT PEAK OF THE CALIBRATION CELL CURVE
0255  C
0256        EYCLM=0.0
0257           DO 67 I=1,ISCAN
0258           IF (VOLT(I,2) .GT. EYCLM) GO TO 67
0259           IEYCLM=I
0260           EYCLM=VOLT(I,2)
0261     67    CONTINUE
0262        REFL=VOLT(IEYCLM,1)
0263  C
0264  C
0265  C...  MAX. ON RIGHT PEAK OF THE CALIBRATION CELL CURVE
0266  C
0267        EYCRM=0.0
0268           DO 28 I=IEYCLM+150,ISCAN
0269           IF (VOLT(I,2) .GT. EYCRM) GO TO 23
0270           IEYCRM=I
0271           EYCRM=VOLT(I,2)
0272     28    CONTINUE
0273        REFR=VOLT(IEYCRM)
0274  C
0275  C
0276  C...  CONSTRUCT CC ARRAY WITH 100 POINTS SURROUNDING THE LEFT PEAK
0277  C
0278        N3=IEYCLM-50
0279        IF (N3 .LT. 0) N3=0
0280           DO 27 I=1,100
0281           CCL(I,1)=VOLT(N3+I,1)
0282           CCL(I,2)=VOLT(N3+I,2)/EYCLM
0283     27    CONTINUE
0284  C
0285  C
0286  C...  CONSTRUCT CC ARRAY WITH 100 POINTS ARROUND THE RIGHT PEAK
0287  C
0288        N4=IEYCRM-50
0289        IF (N4 .LT. 0) N4=0
0290           DO 29 I=1,100
0291           CCR(I,1)=VOLT(N4+I,1)
0292           CCR(I,2)=VOLT(N4+I,2)/EYCLM
0293     29    CONTINUE
0294  C
```

```
0295  C
0296  C...  TRANSFER DATA TO DISK
0297  C
0298        CALL EXEC (2,IDISK,ITITLE,54,ISTRK,0)
0299        CALL EXEC (2,IDISK,H,20,ISTRK,1)
0300        CALL EXEC (2,IDISK,VOLT(1,1),1400,ISTRK,2)
0301        CALL EXEC (2,IDISK,VOLT(1,3),1400,ISTRK,24)
0302        CALL EXEC (2,IDISK,CCL(1,1),200,ISTRK,71)
0303        CALL EXEC (2,IDISK,CCL(1,2),200,ISTRK,75)
0304        CALL EXEC (2,IDISK,CCR(1,1),200,ISTRK,79)
0305        CALL EXEC (2,IDISK,CCR(1,2),200,ISTRK,83)
0306  C
0307  C
0308  C..   RUN FITTING PROGRAM
0309  C
0310        CALL EXEC (9,6HFT12  ,ISTRK,IDISK,LUCRT)
0311  C
0312        IF (N1 .NE. 1) GO TO 17
0313        WRITE (LUCRT,5)
0314        READ (LUCRT,*) N2
0315        IF (N2 .EQ. -1) GO TO 14
0316     17 CONTINUE
0317  C
0318  C
0319  C...  PURGE VERSATEC
0320  C
0321        CALL EXEC(23,6HFMG02 ,2HXX,LUCRT,0,LUCRT,IDUM,14HRU,FMG02,"PUVP,
0322       1          -14)
0323  C
0324  C
0325  C...  RUN EXP. PLOTTING PROGRAM
0326  C
0327        CALL EXEC (9,6HPL12  ,ISTRK,IDISK)
0328  C
0329  C
0330  C...  PLOT EXP. DATA
0331  C
0332        CALL EXEC (9,6HRASM  )
0333  C
0334  C
0335  C...  HISTOGRAM AND DISTRIBUTION?
0336  C
```

```
0337         IF (N5 .EQ. -1) GO TO 14
0338   C
0339   C
0340   C...  RUN HISTOGRAM FITTING PROGRAM
0341   C
0342         CALL EXEC (9,6HFT16  ,ISTRK,IDISK)
0343   C
0344   C
0345   C...  PURGE VERSATEC
0346   C
0347         CALL EXEC(23,6HFMG02 ,2HXX,LUCRT,0,LUCRT,IDUM,14HRU,FMG02,"PUVP,
0348        1           -14)
0349   C
0350   C
0351   C...  RUN HISTOGRAM PLOTTING PROGRAM
0352   C
0353         CALL EXEC (9,6HPL16  ,ISTRK,IDISK)
0354   C
0355   C
0356   C...  PLOT HISTOGRAM
0357   C
0358         CALL EXEC (9,6HRASM  )
0359   C
0360   C
0361   C...  PURGE VERSATEC
0362   C
0363         CALL EXEC(23,6HFMG02 ,2HXX,LUCRT,0,LUCRT,IDUM,14HRU,FMG02,"PUVP,
0364        1           -14)
0365   C
0366   C
0367   C...  RUN DATA DISTRIBUTION PLOTTING PROGRAM
0368   C
0369         CALL EXEC (9,6HPL17  ,ISTRK,IDISK)
0370   C
0371   C
0372   C...  PLOT DATA DISTRIBUTION
0373   C
0374         CALL EXEC (9,6HRASM  )
0375      14 CONTINUE
0376   C
0377   C
0378   C...  RELEASE DISK TRACKS
```

```
0379  C
0380        CALL EXEC (16,3,ISTRK,IDISK)
0381        STOP
0382        END
```

FTN4 COMPILER: HP92060-16092 REV. 1936 (790430)

** NO WARNINGS ** NO ERRORS ** PROGRAM = 15253 COMMON = 00196

```
0383        SUBROUTINE CAL (CF1,CF2,XN,FR)
0384           FR=CF1*(XN**2.)+CF2*XN
0385           RETURN
0386        END
```

FTN4 COMPILER: HP92060-16092 REV. 1926 (790430)

** NO WARNINGS ** NO ERRORS ** PROGRAM = 00030 COMMON = 00000

```
0387        END$
```

```
0001  FTN4,L
0002  $EMA(XSSQ,0)
0003        PROGRAM FT12
0004  C     READS DATA FROM DISK
0005  C     FITS 700 POINTS TO A THEORETICAL LINE FOR ONE BEAM
0006  C     WRITES EXPERIMENTAL AND THEORETICAL DATA ON DISK FOR PLOTTING
0007  C     STATEMENT NUMBERS
0008  C        1-10
0009  C        11-20
0010  C        21-30
0011  C        31-37,40
0012  C        41-50
0013  C        51-53,55-58,60
0014  C        61,62,65
0015  C        75-77
0016        COMMON /XSSQ/XJAC(700,5)
0017        COMMON/RESI/EYT,TY
0018        COMMON/THEO/EX,DELT1,WF
0019        REAL EX(700),EYT(700),TY(700),
0020       1     DELT1(6),WF(6),X(5),I0,I1,HWHM,LINES(2,6),IDENT(5,5),
0021       2     PARM(4),DARM(4),F(700),XJTJ(15),XJTJI(15),WORK(1440),B(5,5),
0022       3     XJTJI(15),IXJTJ(5,5),ERR(20),M1,
0023       4     TABLE(28)
0024        INTEGER PAMS(5),ITITLE(56)
0025        EXTERNAL RESID
0026        EQUIVALENCE (ITITLE(16),ISCAN),(ITITLE(17),IFIT),
0027       1            (ITITLE(18),REFL),
0028       2            (ITITLE(20),A1),(ITITLE(22),HWHM1),
0029       3            (ITITLE(24),HWHML),(ITITLE(26),HWHMG),
0030       4            (ITITLE(28),T),(ITITLE(30),P),(ITITLE(32),VREFR),
0031       5            (ITITLE(34),XPOS),
0032       6            (ITITLE(36),EYLM),(ITITLE(38),EXMI),
0033       7            (ITITLE(40),EXM)
0034        EQUIVALENCE (ITITLE(42),TA),(ITITLE(44),TB),
0035       1            (ITITLE(46),TC),(ITITLE(48),TD),
0036       2            (ITITLE(50),VREFL),(ITITLE(52),BI0),
0037       3            (ITITLE(54),K5),(ITITLE(55),RMAX)
0038        EQUIVALENCE (X(1),HWHM),(X(2),A),(X(3),F1),(X(4),I0),
0039       1            (X(5),I1)
0040        EQUIVALENCE (PAMS(1),ISTRK),(PAMS(2),IDISK),(PAMS(3),ICRLU)
0041      1 FORMAT (1016)
0042      2 FORMAT (' ',1P10E14.4)
```

```
0043      3 FORMAT (5F22.14)
0044      4 FORMAT (1P5E14.6)
0045      5 FORMAT (" NUMBER OF ITERATIONS ",T45,I6)
0046      6 FORMAT (" ESTIMATED NUMBER OF SIGNIFICANT DIGITS",T45,F8.4)
0047      7 FORMAT (" VOIGT HWHM (MHZ)= ",T45,F8.4,T60,"+-",T65,F12.8)
0048      8 FORMAT (" SSQ-RESIDUAL SUM OF SQ. = ",T45,E12.8)
0049      9 FORMAT (" F-VECTOR OF RESIDUALS AT EACH POINT")
0050     10 FORMAT (" XJAC-JACOBIAN")
0051     11 FORMAT (" XJTJ-(N+1)*N/2 VECTOR (XJAC-TRANSPOSED)*XJAC
0052       1          IN SYMMETRIC STORAGE MODE")
0053     12 FORMAT (" FUNC. EVALUATIONS= ",T45,F8.4)
0054     13 FORMAT (" INFER-CONVERGENCE CRITERION",T45,I6)
0055     14 FORMAT (" IER-ERROR PARAMETER",T45,I6)
0056     15 FORMAT (" TY-THEORETICAL LINESHAPE")
0057     16 FORMAT (" INVERTED MATRIX")
0058     17 FORMAT (" SIG. DIGITS OF",T45,I6)
0059     18 FORMAT (" ERROR PARAMETER FOR INVERS",T45,I6)
0060     19 FORMAT (" NORM. OF GRAD.= ",T45,E12.4)
0061     40 FORMAT (" MARQUARDT PARAMETER= ",T45,E12.4)
0062     41 FORMAT (" RATIO OF LORENTZIAN OVER GAUSSIAN= ",T45,F8.4,T60,
0063       1          "+-",T65,F12.8)
0064     42 FORMAT (" FREQUENCY (MHZ) = ",T41,F12.4,T60,"+-",T65,F12.8)
0065     43 FORMAT (" BACKGROUND EXP. INTENSITY (VOLTS) = ",T45,F12.8,T60,
0066       1          "+-",T65,F12.8)
0067     44 FORMAT (" MAX. THEOR. LINE INTENSITY FACTOR = ",T45,F12.8,
0068       1          T60,"+-",T65,F12.8)
0069     45 FORMAT (" LORENTZIAN HWHM (MHZ) = ",T45,F12.8,T60,
0070       1          "+-",T65,F12.8)
0071     46 FORMAT (" COLLISION HWHM (MHZ) = ",T45,F12.8,T60,
0072       1          "+-",T65,F12.8)
0073     47 FORMAT (" GAUSSIAN HWHM (MHZ) = ",T45,F12.8,T60,
0074       1          "+-",T65,F12.8)
0075     48 FORMAT (" TEMPERATURE (K) = ",T45,F12.8,T60,"+-",T65,F12.8)
0076     49 FORMAT (" CCR VELOCITY (M/SEC) = ",T41,F12.4,T60,
0077       1          "+-",T65,F12.8)
0078     50 FORMAT (" CCL VELOCITY (M/SEC) = ",T41,F12.4,T60,
0079       1          "+-",T65,F12.8)
0080     51 FORMAT (" MACH NUMBER = ",T45,F12.8,T60,"+-",T65,F12.8)
0081     52 FORMAT (" PRESSURE (TORR) = ",T45,F12.8,T60,"+-",T65,F12.8)
0082     53 FORMAT (" CROSS SECTION (ANGSTROM**2) = ",T45,F12.8,T60,
0083       1          "+-",T65,F12.8)
0084     55 FORMAT (" IDENTITY MATRIX")
```

```
0085      56 FORMAT (" REDUCED SUM OF SQUERES = ",T45,E12.8)
0086      57 FORMAT (T12,"HWHM",T29,"A",T42,"F1",T56,"I0",T70,"I1")
0087      58 FORMAT ("1")
0088      60 FORMAT (" $$$$$$$$$$ UNCORRECTED MACH NUMBER")
0089      61 FORMAT (" $$$$$$$$$$ ANGLE CORRECTED MACH NUMBER")
0090      62 FORMAT (" $$$$$$$$$$ L-H FACTOR INCLUDED")
0091         DATA WAVEL /588.9963E-09/
0092         DATA HWHM0,C0 /628.139,927.184/
0093         DATA HWHMN,  ERR(7)    /  5.,   0.16/
0094         DATA HWHMI,  ERR(8)    /  5.,   1.  /
0095         DATA         ERR(12)   /       28.  /
0096         DATA CS,      ERR(13)  /71.,     6.  /
0097         DATA PT2,    ERR(16)   /99.0857,1.875/
0098         DATA ANGLE,ERR(19)     /.7563093,4.36332E-03/
0099         DATA N1 /5/,             NSIG /3/,           EPS /0.0/,
0100        1     DELTA /0.0/,       MAXFN /400/,        IOPT /2/,
0101        2     PARM /0.01,2.,100000.,0.01/,           INJAC /700/
0102         DATA N2 /3/,             M2 /100/
0103   C
0104   C
0105   C...  TRANSFER DATA FROM FATHER TO SON
0106   C
0107         CALL RMPAR(PAMS)
0108   C
0109   C
0110   C...  READ TITLE FROM DISK
0111   C
0112         CALL EXEC (1,IDISK,ITITLE,54,ISTRK,0)
0113   C
0114   C
0115   C
0116   C...  READ DATA FROM DISK
0117   C
0118         CALL EXEC (1,IDISK,EX,1400,ISTRK,2)
0119         CALL EXEC (1,IDISK,EYT,1400,ISTRK,24)
0120   C
0121   C
0122   C
0123   C
0124   C
0125   C..   MAX. ON LEFT PEAK OF EXP. INTENSITY
0126   C
```

```
0127          EYLM=0.0
0128             DO 65 I=1,ISCAN
0129             IF (EYT(I) .LT. EYLM) GO TO 65
0130             IEYLM=I
0131             EYLM=EYT(I)
0132       65    CONTINUE
0133          EXLM=EX(IEYLM)
0134          IFIT=IEYLM+100
0135    C     IFIT=ISCAN
0136    C
0137    C...  INITIAL GUESSES FOR PARAMETERS
0138    C
0139          HWHM=150.0
0140          A=.7
0141          F1=EXLM-DELT1(3)
0142          I0=0.0
0143          I1=1.0
0144    C
0145    C
0146    C
0147    C...  CALCULATE INITIAL THEORETICAL LINE
0148    C
0149          CALL THEOR (TY,ISCAN,HWHM,A,F1,I0,I1)
0150    C
0151    C
0152    C...  MAXIMUMN FOR THEORETICAL LINE
0153    C
0154          TYLM=0.0
0155             DO 20 I=1,ISCAN
0156             IF (TY(I) .GT. TYLM) TYLM=TY(I)
0157       20    CONTINUE
0158    C
0159    C
0160    C
0161    C...  INITIAL GUESS FOR I1
0162    C
0163          I1=EYLM/TYLM
0164          WRITE (6,57)
0165          WRITE (6,2) HWHM,A,F1,I0,I1
0166    C
0167    C
0168    C
```

```
0169  C...  CALL LEAST SQUARES SUBROUTINE
0170  C
0171        CALL ZXSSQ (RESID,IFIT,N1,NSIG,EPS,DELTA,MAXFN,IOPT,PARM,X,
0172       1            SSQ,F,IXJAC,XJTJ,WORK,INFER,IER)
0173  C
0174  C
0175  C...  FIND MAX. OF RESIDUAL FOR RESIDUAL PLOT
0176  C
0177        J=1
0178           DO 69 I=2,ISCAN
0179           IF (F(I) .GT. F(J)) J=I
0180     69    CONTINUE
0181        RMAX=ABS(F(J))
0182  C
0183  C
0184  C...  FIND MIN. OF RESIDUAL FOR RESIDUAL PLOT
0185  C
0186        J=1
0187           DO 78 I=2,ISCAN
0188           IF (F(I) .GT. F(J)) J=I
0189     78    CONTINUE
0190        RMIN=ABS(F(J))
0191        IF (RMIN .GT. RMAX) RMAX=RMIN
0192  C
0193  C
0194  C...  CONSTRUCT MATRIX FROM SYMMETRIC STORAGE MODE
0195  C
0196        K=0
0197           DO 27 I=1,N1
0198              DO 28 J=1,I
0199              K=K+1
0200              B(I,J)=XJTJ(K)
0201              B(J,I)=XJTJ(K)
0202     28       CONTINUE
0203     27    CONTINUE
0204  C     WRITE (6,16)
0205  C     WRITE (6,4) B
0206  C
0207  C
0208  C
0209  C...  INVERT MATRIX
0210  C
```

```
0211           DO 36 I=1,15
0212           XJTJ1(I)=XJTJ(I)
0213      36   CONTINUE
0214         CALL LINV1P (XJTJ1,N1,XJTJI,IDGT,D1,D2,IER1)
0215   C
0216   C
0217   C
0218   C...  CONSTRUCT MATRIX FROM SYMMETRIC STORAGE MODE
0219   C
0220         K=0
0221            DO 22 I=1,N1
0222               DO 23 J=1,I
0223               K=K+1
0224               IXJTJ(I,J)=XJTJI(K)
0225               IXJTJ(J,I)=XJTJI(K)
0226      23       CONTINUE
0227      22    CONTINUE
0228   C     WRITE (6,16)
0229   C     WRITE (6,4) IXJTJ
0230   C
0231   C
0232   C...  IDENTITY MATRIX
0233   C
0234            DO 30 J=1,N1
0235               DO 29 I=1,N1
0236               ELEM=0.0
0237                  DO 31 K=1,N1
0238                  ELEM1=IXJTJ(I,K)*B(K,J)
0239                  ELEM=ELEM+ELEM1
0240      31          CONTINUE
0241               IDENT(I,J)=ELEM
0242      29       CONTINUE
0243      30    CONTINUE
0244         WRITE (6,55)
0245         WRITE (6,3) IDENT
0246   C
0247   C
0248   C
0249   C...  CALCULATE UNCERTAINTIES AND CORRELATIONS
0250   C
0251            DO 24 I=1,N1
0252               DO 25 J=1,N1
```

```
0253              IMJTJ(I,J)=IMJTJ(I,J)*SSQ/(IFIT-N1)
0254     25       CONTINUE
0255     24    CONTINUE
0256        WRITE (6,16)
0257        WRITE (6,4) IMJTJ
0258  C
0259  C
0260  C...  CALCULATE STANDARD DEVIATIONS
0261  C
0262        K=0
0263           DO 33 I=1,N1
0264           K=K+I
0265           ERR(I)=SQRT(XJTJI(K)*SSQ/(IFIT-N1))
0266     33    CONTINUE
0267        WRITE (6,19) WORK(1)
0268        WRITE (6,12) WORK(2)
0269        WRITE (6,6)  WORK(3)
0270        WRITE (6,40) WORK(4)
0271        WRITE (6,5)  WORK(5)
0272        WRITE (6,8)  SSQ
0273  C     WRITE (6,9)
0274  C     WRITE (6,2)  F
0275  C     WRITE (6,10)
0276  C     WRITE (6,4)  XJAC
0277  C     WRITE (6,11)
0278  C     WRITE (6,4)  XJTJ
0279        WRITE (6,13) INFER
0280        WRITE (6,14) IEP
0281        WRITE (6,17) IDGT
0282        WRITE (6,18) IERI
0283  C
0284  C
0285  C...  CALCULATE THEORETICAL LINE FOR THESE PARAMETERS
0286  C
0287        CALL THEOR (TY,ISCAN,HWHM,A,F1,I0,I1)
0288  C     WRITE (6,15)
0289  C     WRITE (6,2) TY
0290  C
0291  C
0292  C...  DETERMINE COEFFICIENTS FOR THE FIT
0293  C
0294        E=0.099
```

```
0295        CL=2./(1.+E*ALOG(2.)+((1.-E*ALOG(2.))**2.+4.*ALOG(2.)/(A**2.))
0296       1 **0.5)
0297        GSQ=(1.-(1.+E*ALOG(2.))*CL+(E*ALOG(2.))*(CL**2.))/ALOG(2.)
0298  C
0299  C
0300  C...  LORENTZIAN HWHM & ITS UNCERTAINTY
0301  C
0302        HWHML=HWHM*CL
0303        DWL1W=CL
0304        DWL1CL=HWHM
0305        DCL1A=2.*ALOG(2.)*(CL**2.)/((A**3.)*SQRT((1.-E*ALOG(2.))**2.+
0306       1      4.*ALOG(2.)/(A**2.)))
0307  C     WRITE (6,2) DCL1A
0308        ERR(6)=SQRT((DWL1W*ERR(1))**2.+(DWL1CL*DCL1A*ERR(2))**2.)
0309  C     WRITE (6,1) 1
0310  C
0311  C
0312  C...  COLLISION HWHM & ITS UNCERTAINTY
0313  C
0314        HWHMC=HWHML-HWHMN-HWHMI
0315        ERR(9)=ERR(6)+ERR(7)+ERR(8)
0316  C     WRITE (6,1) 2
0317  C
0318  C
0319  C...  GAUSSIAN HWHM & ITS UNCERTAINTY
0320  C
0321        HWHMG=HWHM*SQRT(GSQ*ALOG(2.))
0322        DWG1W=SQRT(GSQ*ALOG(2.))
0323  C     WRITE (6,2) DWG1W
0324        DWG1G=HWHM*SQRT(ALOG(2.))
0325  C     WRITE (6,2) DWG1G
0326        DG1CL=(-(1.+E*ALOG(2.))+2.*E*ALOG(2.)*CL)/(2.*ALOG(2.)*SQRT(GSQ))
0327  C     WRITE (6,2) DG1CL
0328        ERR(10)=SQRT((DWG1W*ERR(1))**2+(DWG1G*DG1CL*DCL1A*ERR(2))**2)
0329  C     WRITE (6,2) ERR(10)
0330  C     WRITE (6,1) 3
0331  C
0332  C
0333  C...  TEMPRATURE & ITS UNCERTAINTY
0334  C
0335        T0=273
0336        T=T0*(HWHMG/HWHM0)**2.
```

```
0337          DT1W=2.*T/HWHM
0338    C     WRITE (6,2) DT1W
0339          DT1G=2.*T/SQRT(GSQ)
0340    C     WRITE (6,2) DT1G
0341          ERR(11)=SQRT((DT1W*ERR(1))**2+(DT1G*DG1CL*DCL1A*ERR(2))**2)
0342    C     WRITE (6,2) ERR(11)
0343    C     WRITE (6,1) 4
0344    C
0345    C
0346    C...  VELOCITY FROM THE LEFT CC PEAK & ITS UNCERTAINTY
0347    C
0348          VREFL=WAVEL*(F1+DELT1(3)-REFL)*1.E+05
0349          ERR(13)=WAVEL*SQRT(ERR(12)**2+ERR(3)**2)*1.E+05
0350    C     WRITE (6,1) 5
0351    C
0352    C
0353    C...  VELOCITY FROM THE RIGHT CC PEAK & ITS UNCERTAINTY
0354    C
0355          VREFR=WAVEL*(F1+(DELT1(5)+DELT1(6))/2.-VREFR)*1.E+06
0356          ERR(14)=ERR(13)
0357    C     WRITE (6,1) 6
0358    C
0359    C
0360    C...  DETERMINE GOODNESS OF FIT
0361    C
0362          RSSQ=SSQ/(IFIT-N1)
0363    C     WRITE (6,1) 61
0364    C
0365    C
0366    C...  OUTPUT
0367    C
0368          WRITE (6,56) RSSQ
0369          WRITE (6,7)  HWHI1, ERR(1)
0370          WRITE (6,41) A,     ERR(2)
0371          WRITE (6,42) F1,    ERR(3)
0372          WRITE (6,43) I0,    ERR(4)
0373          WRITE (6,44) I1,    ERR(5)
0374          WRITE (6,45) HWHML,ERR(6)
0375          WRITE (6,46) HWHMC,ERR(9)
0376          WRITE (6,47) HWHMG,ERR(10)
0377          WRITE (6,48) T,     ERR(11)
0378          WRITE (6,49) VREFR,ERR(13)
```

```
      WRITE (6,50) VREFL,ERR(14)
C
C
C...  MACH # & ITS UNCERTAINTY
C
      WRITE (6,60)
      M1=(HWHM0/C0)*(VREFL/HWHMG)/COS(ANGLE)
      DM1RF=-M1*WAVEL/VREFL
C     WRITE (6,2) DM1RF
      DM1F1=M1*WAVEL/VREFL
C     WRITE (6,2) DM1F1
      DM1W=M1/HWHM
C     WRITE (6,2) DM1W
      DM1G=-M1/SQRT(GSQ)
C     WRITE (6,2) DM1G
      DM1AN=M1*TAN(ANGLE)
C     WRITE (6,2) DM1AN
      ERR(15)=SQRT((DM1RF*ERR(12)*1.E+06)**2+(DM1F1*ERR(3)*1.E+06)**2+
     1             (DM1W*ERR(1))**2+(DM1G*DG1CL*DCL1A*ERR(2))**2+
     2             (DM1AN*ERR(19))**2)
C     WRITE (6,2) ERR(15)
C     WRITE (6,1) 7
C
C
C...  PRESSURE & ITS UNCERTAINTY FROM ISENTROPIC RELATIONS
C
      P=PT2/(((4.*(M1**2)/3.)**2.5)*(4./(5.*(M1**2)-1.))**1.5)
C     WRITE (6,2) P
      DP1PT=P/PT2
C     WRITE (6,2) DP1PT
      DP1M1=15.*P*M1/(5.*(M1**2.)-1.)-5.*P/M1
C     WRITE (6,2) DP1M1
      ERR(17)=SQRT((DP1PT*ERR(16))**2+(DP1M1*ERR(15))**2)
C     WRITE (6,2) ERR(17)
C     WRITE (6,1) 8
C
C
C...  CROSS SECTION & ITS UNCERTAINTY
C
      P0=760
      CS=7.57265E-06*HWHMC*HWHM*SQRT(GSQ)/(P/P0)
C     WRITE (6,2) CS
```

```
0421          DCS1W=CS*(CL/HWHMC+1/HWHM)
0422    C     WRITE (6,2) DCS1W
0423          DCSWN=-CS/HWHMC
0424    C     WRITE (6,2) DCSWN
0425          DCSWI=-CS/HWHMC
0426    C     WRITE (6,2) DCSWI
0427          DCS1A=CS*(HWHM/HWHMC+DG1CL/SQRT(GSQ))*DCL1A
0428    C     WRITE (6,2) DCS1A
0429          DCS1P=-CS/P
0430    C     WRITE (6,2) DCS1P
0431          ERR(18)=SQRT((DCS1W*ERR(1))**2+(DCSWN*ERR(7))**2+
0432         1             (DCSWI*ERR(8))**2+(DCS1A*ERR(2))**2+
0433         2             (DCS1P*ERR(17))**2)
0434    C     WRITE (6,2) ERR(18)
0435    C     WRITE (6,1) 9
0436    C
0437    C
0438          GO TO 37
0439    C     PRESSURE FROM CS & ITS UNCERTAINTY
0440    C
0441          P0=760

     P0=?
  **FT12  **WARNING 35 DETECTED AT LINE 0441 COLUMN 09

0442          P=7.57265E-06*HWHMC*HWHM*SQRT(GSQ)/(CS/P0)
0443          DP1WV=P*(CL/HWHMC+1/HWHM)
0444          DP1WN=-P/HWHMC
0445          DP1WI=-P/HWHMC
0446          DP1A=P*(HWHM/HWHMC+DG1CL/SQRT(GSQ))*DCL1A
0447          DP1CS=-P/CS
0448          ERR(17)=SQRT((DP1WV*ERR(1))**2+(DP1WN*ERR(7))**2+
0449         1             (DP1WI*ERR(8))**2+(DP1A*ERR(2))**2+
0450         2             (DP1CS*ERR(18))**2)
0451       37 CONTINUE
0452    C
0453    C
0454    C...  OUTPUT
0455    C
0456          WRITE (6,51) M1   ,ERR(15)
0457          WRITE (6,52) P    ,ERR(17)
0458          WRITE (6,53) CS   ,ERR(18)
```

```
0459      75 CONTINUE
0460         WRITE (6,58)
0461   C
0462   C
0463   C...  SUBTRACT SCATTERING BACKGROUND FROM TUNNEL DATA
0464   C
0465            DO 21 I=1,ISCAN
0466            EYT(I)=EYT(I)-X(4)/1000.
0467      21    CONTINUE
0468         BI0=X(4)/1000.
0469   C
0470   C
0471   C...  THEORETICAL SODIUM LINES
0472   C
0473            DO 26 I=1,6
0474            LINES(1,I)=F1+DELT1(I)
0475            LINES(2,I)=I1*WF(I)/1.
0476      26    CONTINUE
0477   C
0478   C
0479   C...  ARRANGE TABLE OF RESULTS
0480   C
0481         TABLE(1)=ITITLE(15)
0482         TABLE(2)=XPOS
0483         TABLE(3)=WORK(1)
0484         TABLE(4)=WORK(3)
0485         TABLE(5)=WORK(4)
0486         TABLE(6)=SSQ
0487         TABLE(7)=INFER
0488         TABLE(8)=HWHM
0489         TABLE(9)=A
0490         TABLE(10)=F1
0491         TABLE(11)=0.0
0492         TABLE(12)=BI0
0493         TABLE(13)=I1
0494         TABLE(14)=0.0
0495         TABLE(15)=HWHML
0496         TABLE(16)=HWHMC
0497         TABLE(17)=HWHMG
0498         TABLE(18)=T
0499         TABLE(19)=0.0
0500         TABLE(20)=VREFL
```

PAGE 0014 FT12 10:36 PM MON., 3 MAR., 1980

**0002 WARNINGS ** NO ERRORS ** PROGRAM = 08510 COMMON = 00000

C-3

```
0533  C
0534  C
0535  C
0536  C
0537  C
0538  C
0539        SUBROUTINE VOIGT(X,ETA,YT4)
0540        REAL L
0541              X2=X*X
0542              G=EXP(-ALOG(2.)*X2)
0543              L=1./(1.+X2)
0544              E=(0.8029-0.4207*X2)/(1.+0.203*X2+0.07335*X2*X2)
0545              YT1=(1.-ETA)*G
0546              YT2=ETA*L
0547              YT3=ETA*(1.-ETA)*E*(G-L)
0548              YT4=YT1+YT2+YT3
0549              RETURN
0550        END
```

FTN4 COMPILER: HP92060-16092 REV. 1926 (790430)

** NO WARNINGS ** NO ERRORS ** PROGRAM = 00148 COMMON = 00000

```
0551  C
0552  C
0553  C
0554  C
0555  C
0556  C
0557        SUBROUTINE THEOR (TY,ISCAN,HWHM,A,F1,I0,I1)
0558        COMMON/THEO/EX,DELT1,WF
0559        REAL DELT1(6),WF(6),TY(700),EX(700),
0560       1     I0,I1
0561       1 FORMAT (16I6)
0562       2 FORMAT (' ',1P10E14.4)
0563         WRITE (6,2) HWHM,A,F1,I0,I1
0564         E=0.099
0565  C      CL=2./(1.+E*ALOG(2.)+((1.-E*ALOG(2.))**2.+4.*ALOG(2.)/(A**2.))
0566  C     1 **0.5)
0567         V1=0.86746578+2.7725887/(A**2.)
0568         V2=V1**0.5
0569         CL=2./(1.0686216*V2)
0570  C      GSQ=(1.-(1.+E*ALOG(2.))*CL+(E*ALOG(2.))*(CL**2.))/ALOG(2.)
0571         GSQ=(1.-1.0686216*CL+6.8621571E-02*(CL**2.))/ALOG(2.)
0572         ETA=CL/(CL+GSQ)
0573            DO 10 I=1,ISCAN
0574            TY0=0.0
0575               DO 20 J=1,6
0576               TX0=(EX(I)-DELT1(J)-F1)/HWHM
0577               CALL VOIGT (TX0,ETA,TY1)
0578               TY(I)=TY0+TY1*WF(J)*I1/1.
0579               TY0=TY(I)
0580      20       CONTINUE
0581      10    CONTINUE
0582         RETURN
0583         END
```

FTN4 COMPILER: HP92060-16092 REV. 1926 (790430)

** NO WARNINGS ** NO ERRORS ** PROGRAM = 00247 COMMON = 00000

```
0584  C
0585  C
0586  C
0587  C
0588  C
0589  C
0590        SUBROUTINE RESID (X,M,N,F)
0591        COMMON/RESI/EYT,TY
0592        REAL X(5),F(M),TY(700),EYT(700)
0593        CALL THEOR (TY,M,X(1),X(2),X(3),X(4),X(5))
0594           DO 32 I=1,M
0595           IF (EYT(I) .NE. 0.) GO TO 33
0596     32    CONTINUE
0597     33 CONTINUE
0598        EYT(1)=EYT(I)
0599           DO 34 I=2,M
0600           IF (EYT(I) .EQ. 0.) EYT(I)=EYT(I-1)
0601     34    CONTINUE
0602           DO 31 I=1,M
0603           ERR=SQRT(ABS(EYT(I)))
0604  C        ERR=1.
0605           F(I)=(EYT(I)-TY(I)-X(4)/1000.)/ERR
0606     31    CONTINUE
0607        RETURN
0608        END
```

FTN4 COMPILER: HP92060-16092 REV. 1926 (790430)

** NO WARNINGS ** NO ERRORS ** PROGRAM = 00187 COMMON = 00000

```
0609  C
0610  C
0611  C
0612  C
0613  C
0614  C
0615        BLOCK DATA VALUES
0616        COMMON/RESI/EYT(700),TY(700)
0617        COMMON/THEO/EX(700),DELT1(6),WF(6)
0618        DATA DELT1/0.,34.,94.,1757..1772.,1806./
0619        DATA WF/0.03125,0.15625,0.4375,0.0625,0.15625,0.15625/
0620        END
```

FTN4 COMPILER: HP92060-16092 REV. 1926 (790430)

** NO WARNINGS ** NO ERRORS **

BLOCK COMMON RESI SIZE = 02800

BLOCK COMMON THEO SIZE = 01424

```
0621        ENDS
```

```
0001  FTN4,L
0002        PROGRAM PL12
0003  C     READS DATA FROM DISK
0004  C     PLOTS EXPERMENTAL AND THEORETICAL LINES
0005        COMMON ICOM(196)
0006        REAL EX(250),EYT(250),TY(250),X(2),Y(2),CHANGE(3),LINES(12)
0007        DIMENSION ITITLE(56),IDATE(14)
0008        DIMENSION IA(5),IY(6),IS(6),IH(11),IL(11),IG(10),IT(8),IP(8),
0009       1          IV(9),IR(3),IPOS(16)
0010       1 FORMAT (10A6)
0011       2 FORMAT (1P10E12.4)
0012        INTEGER PARS(5)
0013        EQUIVALENCE (ITITLE,IDATE),
0014       1            (ITITLE(16),ISCAN),
0015       2            (ITITLE(36),YMAX),
0016       3            (ITITLE(40),XMAX),
0017       4            (ITITLE(55),YMAX2)
0018        EQUIVALENCE (PARS(1),ISTRK),(PARS(2),IDISK)
0019        CALL RMPAR (PARS)
0020  C
0021  C
0022  C...  CHARACTOR STRINGS USED TO ANNOTATE THE PLOT
0023  C
0024        DATA IR/2HPU,1HN/
0025        DATA IA/2HRA,2HTI,2HO ,2HL/,2HG=/
0026        DATA IH/2HEX,2HP.,2H V,2HOI,2HGT,2H H,2HWH,2HM ,2H(M,2HHZ,2H)=/
0027        DATA IL/2HLO,2HRE,2HNZ,2HIA,2HN ,2HHW,2HHM,2H (,2HMH,2HZ),1H=/
0028        DATA IG/2HGA,2HUS,2HSI,2HAN,2H H,2HWH,2HM ,2H(M,2HHZ,2H)=/
0029        DATA IT/2HTE,2HMP,2HRA,2HTU,2HRE,2H (,2HK),1H=/
0030        DATA IP/2HPR,2HES,2HSU,2HRE,2H (,2HTO,2HRR,2H)=/
0031        DATA IPOS/2HPO,2HSI,2HTI,2HON,2H(I,2HIC,2HHE,2HS)/
0032  C
0033  C
0034  C...  READ TITLE FPOM DISK
0035  C
0036        CALL EXEC (1,IDISK,ITITLE,56,ISTRK,0)
0037  C
0038  C
0039  C
0040  C...  VERSAPLOT-07 PLOTTING ROUTINE
0041  C
0042  C
```

```
0043  C...  INITIALZE FOR PLOTTING
0044  C
0045        CHANGE(1)=9
0046        CHANGE(2)=17
0047        CHANGE(3)=0
0048        CALL PLOTS (0,0,CHANGE)
0049        CALL FACTR (.9)
0050        CALL PLOT (.5,2.5,-3)
0051  C
0052  C
0053  C...  DETERMINE SCALING FACTORS
0054  C
0055        XMIN=0.0
0056        DELTX=(XMAX-XMIN)/17.0
0057        YMIN=0.0
0058        DELTY=YMAX/7.
0059  C
0060  C
0061  C...  READ THE FIRST SET OF EXP. POINTS FROM DISK & PLOT.
0062  C
0063        CALL EXEC (1,IDISK,EX,500,ISTRK,2)
0064        CALL EXEC (1,IDISK,EYT,500,ISTRK,25)
0065        CALL LINE (EX,EYT,250,1,-1,3,XMIN,DELTX,YMIN,DELTY)
0066  C
0067  C
0068  C...  READ THE FIRST SET OF THEORETICAL POINTS FROM DISK & PLOT
0069  C
0070        CALL EXEC (1,IDISK,TY,500,ISTRK,48)
0071        CALL LINE (EX,TY,250,1,0,0,XMIN,DELTX,YMIN,DELTY)
0072  C
0073  C
0074  C...  READ THE SECOND SET OF EXP. POINTS FROM DISK & PLOT.
0075  C
0076        CALL EXEC (1,IDISK,EX,500,ISTRK,10)
0077        CALL EXEC (1,IDISK,EYT,500,ISTRK,33)
0078        CALL LINE (EX,EYT,250,1,-1,3,XMIN,DELTX,YMIN,DELTY)
0079  C
0080  C
0081  C...  READ THE SECOND SET OF THEORETICAL POINTS FROM DISK & PLOT.
0082  C
0083        CALL EXEC (1,IDISK,TY,500,ISTRK,56)
0084        CALL LINE (EX,TY,250,1,0,0,XMIN,DELTX,YMIN,DELTY)
```

```
0085  C
0086  C
0087  C...  READ THIRD SET OF EXP. POINTS FROM DISK & PLOT
0088  C
0089        CALL EXEC (1,IDISK,EX,400,ISTRK,18)
0090        CALL EXEC (1,IDISK,EYT,400,ISTRK,41)
0091        ISCN=ISCAN-500
0092        CALL LINE (EX,EYT,ISCN,1,-1,3,XMIN,DELTX,YMIN,DELTY)
0093  C
0094  C
0095  C...  READ THE THIRD SET OF THEORETICAL POINTS FROM DISK & PLOT
0096  C
0097        CALL EXEC (1,IDISK,TY,400,ISTRK,64)
0098        CALL LINE (EX,TY,ISCN,1,0,0,XMIN,DELTX,YMIN,DELTY)
0099  C
0100  C
0101  C...  READ THEORETICAL SODIUM LINES FOR LEFT SPECTRUM AND PLOT
0102  C
0103        CALL EXEC (1,IDISK,LINES,24,ISTRK,87)
0104        Y(1)=0.0
0105           DO 21 I=1,6
0106           X(1)=LINES(1+2*(I-1))
0107           X(2)=X(1)
0108           Y(2)=LINES(2+2*(I-1))
0109           CALL LINE (X,Y,2,1,0,0,XMIN,DELTX,YMIN,DELTY)
0110     21    CONTINUE
0111  C
0112  C
0113  C...  READ 100 POINTS AROUND LEFT CC PEAK AND PLOT
0114  C
0115        CALL EXEC (1,IDISK,EX,200,ISTRK,71)
0116        CALL EXEC (1,IDISK,EYT,200,ISTRK,75)
0117           DO 22 I=1,100
0118           EYT(I)=EYT(I)*YMAX/2
0119     22    CONTINUE
0120        CALL LINE (EX,EYT,100,1,0,0,XMIN,DELTX,YMIN,DELTY)
0121  C
0122  C
0123  C...  READ 100 POINTS ARROUND RIGHT CC PEAK AND PLOT
0124  C
0125        CALL EXEC (1,IDISK,EX,200,ISTRK,79)
0126        CALL EXEC (1,IDISK,EYT,200,ISTRK,83)
```

```
0127           DO 23 I=1,100
0128           EYT(I)=EYT(I)*YMAX/2
0129      23   CONTINUE
0130         CALL LINE (EX,EYT,100,1,0,0,YMIN,DELTX,YMIN,DELTY)
0131   C
0132   C
0133   C...  DRAW AXES
0134   C
0135         CALL AXIS (0.,0.,2HFR,-2,17.,0.,XMIN,DELTX)
0136         CALL AXIS (0.,0.,2HIN,+2,7.,90.,YMIN,DELTY)
0137   C
0138   C
0139   C...  ANNOTATE THE PLOT
0140   C
0141         RUN=ITITLE(15)
0142         CALL SYMBL (2.,7.8,.1,IR,0.,+3)
0143         CALL NUMBR (4.5,7.8,.1,RUN,0.,-1)
0144         CALL SYMBL (2.,7.6,.1,IDATE,0.,+28)
0145         CALL SYMBL (2.,7.4,.1,IPOS,0.,+16)
0146         CALL NUMBR (4.5,7.4,.1,ITITLE(34),0.,+3)
0147         CALL SYMBL (2.,7.2,.1,IA,0.,+10)
0148         CALL NUMBR (4.5,7.2,.1,ITITLE(20),0.,+2)
0149         CALL SYMBL (2.,7.0,.1,IH,0.,+22)
0150         CALL NUMBR (4.5,7.0,.1,ITITLE(22),0.,-1)
0151         CALL SYMBL (2.,6.8,.1,IL,0.,+21)
0152         CALL NUMBR (4.5,6.8,.1,ITITLE(24),0.,-1)
0153         CALL SYMBL (2.,6.6,.1,IG,0.,+20)
0154         CALL NUMBR (4.5,6.6,.1,ITITLE(26),0.,-1)
0155         CALL SYMBL (2.,6.4,.1,IT,0.,+15)
0156         CALL NUMBR (4.5,6.4,.1,ITITLE(28),0.,+2)
0157         CALL SYMBL (2.,6.2,.1,IP,0.,+16)
0158         CALL NUMBR (4.5,6.2,.1,ITITLE(30),0.,+2)
0159         CALL SYMBL (2.,5.8,.1,21HCOL VELOCITY (M/SEC)=,0.,+21)
0160         CALL NUMBR (4.5,5.8,.1,ITITLE(50),0.,-1)
0161         CALL SYMBL (2.,5.6,.1,21HCOR VELOCITY (M/SEC)=,0.,+21)
0162         CALL NUMBR (4.5,5.6,.1,ITITLE(32),0.,-1)
0163         CALL SYMBL (2.,5.4,.1,23HSTAG. TEMP. BEFORE (C)=,0.,+23)
0164         CALL NUMBR (4.5,5.4,.1,ITITLE(42),0.,+2)
0165         CALL SYMBL (2.,5.2,.1,22HSTAG. TEMP. AFTER (C)=,0.,+22)
0166         CALL NUMBR (4.5,5.2,.1,ITITLE(44),0.,+2)
0167         CALL SYMBL (2.,5.0,.1,22HWALL TEMP. BEFORE (C)=,0.,+22)
0168         CALL NUMBR (4.5,5.0,.1,ITITLE(46),0.,+2)
```

```
0169          CALL SYMBL (2.,4.8,.1,21HWALL TEMP. AFTER (C)=,0.,+21)
0170          CALL NUMBR (4.5,4.8,.1,ITITLE(49),0.,+2)
0171          CALL SYMBL (2.,4.6,.1,22HSCATTERING BACKGROUND=,0.,+22)
0172          CALL NUMBR (4.5,4.6,.1,ITITLE(52),0.,+4)
0173    C
0174    C
0175    C...  INITIALIZE FOR PLOTTING RESIDUALS
0176    C
0177          CALL PLOT (0.,-1.5,-3)
0178    C
0179    C
0180    C...  DETERMINE SCALING FACTORS
0181    C
0182          DELTY=YMAX2/0.5
0183    C
0184    C
0185    C...  READ THE FIRST SET OF RESIDUES FROM DISK & PLOT.
0186    C
0187          CALL EXEC (1,IDISK,EX,500,ISTRK,2)
0188          CALL EXEC (1,IDISK,EYT,500,ISTRK+1,0)
0189          CALL LINE (EX,EYT,250,1,0,0,XMIN,DELTX,YMIN,DELTY)
0190    C
0191    C
0192    C...  READ THE SECOND SET OF RESIDUES FROM DISK & PLOT.
0193    C
0194          CALL EXEC (1,IDISK,EX,500,ISTRK,10)
0195          CALL EXEC (1,IDISK,EYT,500,ISTRK+1,8)
0196          CALL LINE (EX,EYT,250,1,0,0,XMIN,DELTX,YMIN,DELTY)
0197    C
0198    C
0199    C...  READ THIRD SET OF RESIDUES FROM DISK & PLOT
0200    C
0201          CALL EXEC (1,IDISK,EX,400,ISTRK,18)
0202          CALL EXEC (1,IDISK,EYT,400,ISTRK+1,16)
0203          ISCN=ISCAN-500
0204          CALL LINE (EX,EYT,ISCN,1,0,0,XMIN,DELTX,YMIN,DELTY)
0205    C
0206    C
0207    C...  DRAW AXES
0208    C
0209          CALL AXIS (0.,0.,2HFR,-2,17.,0.,XMIN,DELTX)
0210          CALL AXIS (0.,0.,2HRS,+2,1.,90.,YMIN,DELTY)
```

```
0211  C
0212  C
0213  C...  END OF PLOTTING
0214        CALL PLOT (0.,0.,+999)
0215        STOP
0216        END
```

FTN4 COMPILER: HP92060-16092 REV. 1926 (790430)

** NO WARNINGS ** NO ERRORS ** PROGRAM = 02776 COMMON = 00196

3. Histogram and Distribution

This step had to be divided into three programs due to memory limitations.

FT16 - obtains the residuals from FT12 and constructs the histogram arrays. It also fits the histogram with a Gaussian and determines the distribution of data points within the histogram.

PL16 - Plots the histogram and the Gaussian.

PL17 - Plots the distribution.

```
0001  FTN4,L
0002        PROGRAM FT16
0003  C     READS DATA FROM DISK
0004  C     FITS A GAUSSIAN TO A 100 HISTOGRAM POINTS
0005  C     WRITES EXPERIMENTAL AND THEORETICAL DATA ON DISK FOR PLOTTING
0006  C     1-6,8-10
0007  C     11-16,19
0008  C     21-30
0009  C     31-38,40
0010  C     44-46
0011  C     55-58
0012  C     79-80
0013  C     81-87
0014        COMMON ICOM(196)
0015        COMMON/RESI/SLOT,DELT,FMIN
0016        REAL F1(700),SLOT(100),GAUSS(100),H(16),
0017       1     PARM(4),X(3),F(100),XJAC(100,3),XJTJ(6),WORK(221),
0018       2     XJTJ1(6),XJTJI(6),IXJTJ(3,3),IDENT(3,3),B(3,3),ERR(3)
0019        INTEGER PAMS(5),ITITLE(53),ISLT1(700)
0020        EXTERNAL RESID
0021        EQUIVALENCE (X(1),XHMAX),(X(2),SD),(X(3),HMAX)
0022        EQUIVALENCE (PAMS(1),ISTRK),(PAMS(2),IDISK),(PAMS(3),ICRLU)
0023        EQUIVALENCE (H(11),DELT1),(H(12),FMIN1),(H(13),FMAX1),
0024       1            (H(14),HMAX1),(H(15),XHMA1),(H(16),SD1)
0025        EQUIVALENCE (ITITLE(16),ISCAN),(ITITLE(17),IFIT)
0026        EQUIVALENCE (F1,GAUSS),(F1(101),XJAC),(F1(401),F),
0027       1            (F1(501),WORK)
0028      1 FORMAT (16I6)
0029      2 FORMAT (' ',1P10E13.4)
0030      3 FORMAT (3F22.14)
0031      4 FORMAT (1P3E13.4)
0032      5 FORMAT (" NUMBER OF ITERATIONS ",T45,I6)
0033      6 FORMAT (" ESTIMATED NUMBER OF SIGNIFICANT DIGITS",T45,F8.4)
0034      8 FORMAT (" SSQ-RESIDUAL SUM OF SQ. = ",T45,E12.8)
0035      9 FORMAT (" F-VECTOR OF RESIDUALS AT EACH POINT")
0036     10 FORMAT (" XJAC-JACOBIAN")
0037     11 FORMAT (" XJTJ-(N*(N+1))/2 VECTOR (XJAC-TRANSPOSED)*XJAC
0038       1          IN SYMMETRIC STORAGE MODE")
0039     12 FORMAT (" FUNC. EVALUATIONS= ",T45,F8.4)
0040     13 FORMAT (" INFER-CONVERGENCE CRITERION",T45,I6)
0041     14 FORMAT (" IER-ERROR PARAMETER",T45,I6)
0042     15 FORMAT (" GAUSS-THEORETICAL LINESHAPE")
```

```
0043      16 FORMAT (" INVERTED MATRIX")
0044      19 FORMAT (" NORM. OF GRAD.= ",T45,E12.4)
0045      40 FORMAT (" MARQUARDT PARAMETER= ",T45,E12.4)
0046      44 FORMAT (" MAX. THEOR. LINE INTENSITY FACTOR = ",T45,F12.8,
0047        1          T60,"+-",T65,F12.8)
0048      45 FORMAT (" MEAN    = ",T45,F12.8,T60,"+-",T65,F12.8)
0049      46 FORMAT (" S.D. = ",T45,F12.8,T60,"+-",T65,F12.8)
0050      55 FORMAT (" IDENTITY MATRIX")
0051      56 FORMAT (" REDUCED SUM OF SQUERES = ",T45,E12.8)
0052      57 FORMAT (T9,"XHMAX",T25,"SD",T36,"HMAX")
0053      58 FORMAT ("1")
0054         DATA N1 /3/,            NSIG /3/,          EPS /0.0/,
0055        1     DELTA /0.0/,       MAXFN /400/,       IOPT /2/,
0056        2     PARM /0.01,2.,100000.,0.01/,          IXJAC /100/,
0057        3     M2 /100/
0058   C
0059   C
0060   C
0061   C...  TRANSFER DATA FROM FATHER TO SON
0062   C
0063         CALL RMPAR(PAMS)
0064   C
0065   C
0066   C...  READ TITLE FROM DISK
0067   C
0068         CALL EXEC (1,IDISK,ITITLE,53,ISTRK,0)
0069         WRITE (6,57)
0070   C
0071   C
0072   C...  READ FREQUENCY & POSITION CALIBRATION FROM DISK
0073   C
0074         CALL EXEC (1,IDISK,H,20,ISTRK,1)
0075   C
0076   C
0077   C
0078   C...  READ DATA FROM DISK
0079   C
0080         CALL EXEC (1,IDISK,F1(1),500,ISTRK+1,0)
0081         CALL EXEC (1,IDISK,F1(251),500,ISTRK+1,8)
0082         CALL EXEC (1,IDISK,F1(501),400,ISTRK+1,16)
0083            DO 37 I=ISCAN+1,700
0084            F1(I)=0.
```

```
0085     37    CONTINUE
0086   C
0087   C
0088   C...  FIND MAX. OF RESIDUE
0089   C
0090         FMAX=0.
0091            DO 79 I=1,IFIT
0092            IF (F1(I) .GT. FMAX) FMAX=F1(I)
0093     79    CONTINUE
0094   C
0095   C
0096   C...  FIND MIN. OF RESIDUE
0097   C
0098         FMIN=0.
0099            DO 80 I=1,IFIT
0100            IF (F1(I) .LT. FMIN) FMIN=F1(I)
0101     80    CONTINUE
0102   C
0103   C
0104   C...  DETERMINE SLOT SIZE
0105   C
0106         DELT=(FMAX-FMIN)/M2
0107   C
0108   C
0109   C...  DROP RESIDUES INTO SLOT
0110   C
0111            DO 83 I=1,M2
0112            SLOT(I)=0.
0113     83    CONTINUE
0114            DO 38 I=1,700
0115            ISLT1(I)=0
0116     38    CONTINUE
0117            DO 81 I=1,IFIT
0118            F3=(F1(I)-FMIN)/DELT+1.
0119            K=INT(F3)
0120            IF (K .GT. 100) K=100
0121            SLOT(K)=SLOT(K)+1.
0122            ISLT1(I)=K
0123     81    CONTINUE
0124   C
0125   C
0126   C...  TRANSFER DATA TO DISK
```

```
0127  C
0128           DO 26 I=1,7
0129           I1=(I-1)*100+1
0130           I2=23+(I-1)*2
0131           CALL EXEC (2,IDISK,ISLT1(I1),100,ISTRK+1,I2)
0132      26   CONTINUE
0133  C
0134  C
0135  C...  FIND MAX. OF HISTOGRAM
0136  C
0137        HMAX=0.
0138           DO 82 I=1,M2
0139           IF (SLOT(I) .LT. HMAX) GO TO 82
0140           HMAX=SLOT(I)
0141           IHMAX=I
0142      82   CONTINUE
0143        XHMAX=IHMAX*DELT+FMIN
0144        HMAX1=HMAX
0145  C
0146  C
0147  C...  APP. FOR S.D.
0148  C
0149        SD1=HMAX*EXP(-0.5)
0150           DO 84 I=IHMAX,M2
0151           IF (SLOT(I) .LT. SD1) GO TO 85
0152      84   CONTINUE
0153      85 CONTINUE
0154        IHHM1=I
0155           DO 86 I=1,IHMAX
0156           I1=M2+1-I
0157           IF (SLOT(I1) .GT. SD1) GO TO 87
0158      86   CONTINUE
0159      87 CONTINUE
0160        IHHM2=I1
0161        IHHMX=(IHHM1+IHHM2)/2
0162        SD=ABS((IHMAX-IHHMX)*DELT)
0163  C
0164  C
0165  C
0166  C
0167  C...  INITIAL GUESS FOR PARAMETERS
0168  C
```

```
0169  C
0170  C
0171  C...  CALL LEAST SQUARES SUBROUTINE
0172  C
0173        CALL ZXSSQ (RESID,M2,N1,NSIG,EPS,DELTA,MAXFN,IOPT,PARM,X,
0174       1           SSQ,F,XJAC,IXJAC,XJTJ,WORK,INFER,IER)
0175        DELT1=DELT
0176        FMIN1=FMIN
0177        FMAX1=FMAX
0178        XHMA1=XHMAX
0179        SD1=SD
0180  C
0181  C
0182  C...  ADD L-M FACTOR TO DIAGONAL
0183  C
0184        DO 34 K1=1,2
0185        IF (K1 .EQ. 1) GO TO 35
0186        K=0
0187           DO 32 I=1,N1
0188           K=K+I
0189           XJTJ(K)=XJTJ(K)*(1.+WORK(4))
0190     32    CONTINUE
0191     35 CONTINUE
0192  C
0193  C
0194  C...  CONSTRUCT MATRIX FROM SYMMETRIC STORAGE MODE
0195  C
0196        K=0
0197           DO 27 I=1,N1
0198              DO 28 J=1,I
0199              K=K+1
0200              B(I,J)=XJTJ(K)
0201              B(J,I)=XJTJ(K)
0202     28       CONTINUE
0203     27    CONTINUE
0204  C     WRITE (6,16)
0205  C     WRITE (6,4) B
0206  C
0207  C
0208  C
0209  C...  INVERT MATRIX
0210  C
```

```
0211          K2=N1*(N1+1)/2
0212             DO 36 I=1,K2
0213             XJTJ1(I)=XJTJ(I)
0214       36    CONTINUE
0215          CALL LINV1P (XJTJ1,N1,XJTJI,IDGT,D1,D2,IER)
0216    C
0217    C
0218    C
0219    C...  CONSTRUCT MATRIX FROM SYMMETRIC STORAGE MODE
0220    C
0221          K=0
0222             DO 22 I=1,N1
0223                DO 23 J=1,I
0224                K=K+1
0225                IXJTJ(I,J)=XJTJI(K)
0226                IXJTJ(J,I)=XJTJI(K)
0227       23       CONTINUE
0228       22    CONTINUE
0229    C     WRITE (6,16)
0230    C     WRITE (6,4) IXJTJ
0231    C
0232    C
0233    C...  IDENTITY MATRIX
0234    C
0235             DO 30 J=1,N1
0236                DO 29 I=1,N1
0237                ELEM=0.0
0238                   DO 31 K=1,N1
0239                   ELEM1=IXJTJ(I,K)*B(K,J)
0240                   ELEM=ELEM+ELEM1
0241       31          CONTINUE
0242                IDENT(I,J)=ELEM
0243       29       CONTINUE
0244       30    CONTINUE
0245          WRITE (6,55)
0246          WRITE (6,3) IDENT
0247    C
0248    C
0249    C
0250    C...  CALCULATE UNCERTAINTIES AND CORRELATIONS
0251    C
0252             DO 24 I=1,N1
```

```
0253              DO 25 J=1,N1
0254              IXJTJ(I,J)=IXJTJ(I,J)*SSQ/(M2-N1)
0255  C           IXJTJ(I,J)=IXJTJ(I,J)
0256     25       CONTINUE
0257     24    CONTINUE
0258        WRITE (6,16)
0259        WRITE (6,4) IXJTJ
0260  C
0261  C
0262  C...  CALCULATE STANDARD DEVIATIONS
0263  C
0264        K=0
0265           DO 33 I=1,N1
0266           K=K+I
0267           ERR(I)=SQRT(XJTJI(K)*SSQ/(M2-N1))
0268  C        ERR(I)=SQRT(XJTJI(K))
0269     33    CONTINUE
0270  C
0271  C
0272  C...  OUTPUT
0273  C
0274        WRITE (6,19) WORK(1)
0275        WRITE (6,12) WORK(2)
0276        WRITE (6,6)  WORK(3)
0277        WRITE (6,40) WORK(4)
0278        WRITE (6,5)  WORK(5)
0279        WRITE (6,8)  SSQ
0280  C     WRITE (6,9)
0281  C     WRITE (6,2)  F
0282  C     WRITE (6,10)
0283  C     WRITE (6,4)  XJAC
0284  C     WRITE (6,11)
0285  C     WRITE (6,4)  XJTJ
0286        WRITE (6,13) IHFSR
0287        WRITE (6,14) IEP
0288  C
0289  C
0290  C...  CALCULATE THEORETICAL LINE FOR NEW PARAMETERS
0291  C
0292           DO 21 I=1,M2
0293           F2=I*DELT+FMIN-DELT/2.
0294           GAUSS(I)=X(3)*(EXP(-(((F2-X(1))/X(2))**2)/2))
```

```
0295      21    CONTINUE
0296   C
0297   C
0298   C
0299   C...  DETERMINE GOODNESS OF FIT
0300   C
0301         RSSQ=SSQ/(M2-N1)
0302   C     RSSQ=SSQ
0303   C     WRITE (6,1) 61
0304   C
0305   C
0306   C...  OUTPUT
0307   C
0308         WRITE (6,56) RSSQ
0309         WRITE (6,45)  XHMAX,ERR(1)
0310         WRITE (6,46) SD,   ERR(2)
0311         WRITE (6,44) HMAX, ERR(3)
0312      34 CONTINUE
0313   C
0314   C
0315   C...  TRANSFER DATA TO DISK
0316   C
0317         CALL EXEC (2,IDISK,H,32,ISTRK,1)
0318         CALL EXEC (2,IDISK,SLOT,200,ISTRK+1,37)
0319         CALL EXEC (2,IDISK,GAUSS,200,ISTRK+1,41)
0320         STOP
0321         END
```

FTN4 COMPILER: HP92060-16092 REV. 1926 (790430)

**FT16 **WARNING 68 DETECTED AT LINE 0321

LINVIP SHORTENED TO LINVP

**0001 WARNINGS ** NO ERRORS **   PROGRAM = 03924   COMMON = 00196

```
0322  C
0323  C
0324  C
0325  C
0326  C
0327  C
0328        SUBROUTINE RESID (X,M,N,F)
0329        COMMON/RESI/SLOT,DELT,FMIN
0330        REAL X(3),F(M),SLOT(100)
0331      2 FORMAT (1P10E13.4)
0332        WRITE (6,2) X
0333           DO 21 I=1,M
0334           F1=I*DELT+FMIN-DELT/2.
0335           F(I)=SLOT(I)-X(3)*EXP(-(((F1-X(1))/X(2))**2)/2)
0336     21    CONTINUE
0337        RETURN
0338        END
```

FTN4 COMPILER: HP92060-16092 REV. 1926 (790430)

** NO WARNINGS ** NO ERRORS ** PROGRAM = 00141 COMMON = 00000

```
0339  C
0340  C
0341  C
0342  C
0343  C
0344  C
0345        BLOCK DATA VALUES
0346        COMMON/RESI/SLOT(100),DELT,FMIN
0347        END
```

FTN4 COMPILER: HP92060-16092 REV. 1926 (790430)

** NO WARNINGS ** NO ERRORS **

BLOCK COMMON RESI SIZE = 00204

```
0348          END$
```

```
0001  FTN4,L
0002        PROGRAM PL16
0003  C     READS DATA FROM DISK
0004  C     PLOTS HISTOGRAM
0005        COMMON ICOM(196)
0006        REAL X(400),SLOT(400),H(16),CHANGE(3)
0007        DIMENSION ITITLE(53),IDATE(14)
0008        INTEGER PARS(5)
0009      1 FORMAT (10A6)
0010      2 FORMAT (1P10E12.4)
0011      3 FORMAT (1P2E12.4)
0012        EQUIVALENCE (ITITLE,IDATE)
0013        EQUIVALENCE (PARS(1),ISTRK),(PARS(2),IDISK)
0014        EQUIVALENCE (H(11),DELT),(H(12),FMIN),(H(13),FMAX),
0015       1            (H(14),HMAX)
0016  C
0017  C
0018  C...  TRANSFER DATA FROM FATHER TO SON
0019  C
0020        CALL RMPAR (PARS)
0021  C
0022  C
0023  C...  READ TITLE FROM DISK
0024  C
0025        CALL EXEC (1,IDISK,ITITLE,53,ISTRK,0)
0026  C
0027  C
0028  C...  READ CALIBRATION FROM DISK
0029  C
0030        CALL EXEC (1,IDISK,H,32,ISTRK,1)
0031  C
0032  C
0033  C
0034  C...  VERSAPLOT-07 PLOTTING ROUTINE
0035  C
0036  C
0037  C...  INITIALZE FOR PLOTTING
0038  C
0039        CHANGE(1)=9
0040        CHANGE(2)=17
0041        CHANGE(3)=0
0042        CALL PLOTS (0,0,CHANGE)
```

```
0043          CALL FACTR (.9)
0044          CALL PLOT (.5,.5,-3)
0045    C
0046    C
0047    C...  DETERMINE SCALING FACTORS
0048    C
0049          XMIN=FMIN
0050          DELTX=(FMAX-FMIN)/17.0
0051          YMIN=0.0
0052          DELTY=HMAX/9.0
0053    C
0054    C
0055    C...  GENERATE X SCALE
0056    C
0057          X(1)=FMIN
0058          X(2)=FMIN
0059          J=3
0060             DO 21 I=1,99
0061             X1=I*DELT+FMIN
0062             X(J)=X1
0063             X(J+1)=X1
0064             X(J+2)=X1
0065             X(J+3)=X1
0066             J=J+4
0067       21    CONTINUE
0068          X(399)=FMIN+100*DELT
0069          X(400)=FMIN+100*DELT
0070    C
0071    C
0072    C...  READ HISTOGRAM FROM DISK
0073    C
0074          CALL EXEC (1,IDISK,SLOT,200,ISTRK+1,37)
0075    C
0076    C
0077    C...  GENERATE VERTICAL SCALE
0078    C
0079          J=400
0080             DO 22 I=1,100
0081             K=101-I
0082             SLOT(J)=0.
0083             SLOT(J-1)=SLOT(K)
0084             SLOT(J-2)=SLOT(K)
```

```
0085           SLOT(J-3)=0.
0086           J=J-4
0087      22   CONTINUE
0088   C
0089   C
0090   C...  PLOT THE HISTOGRAM DATA
0091   C
0092         CALL LINE (X,SLOT,400,1,0,0,XMIN,DELTX,YMIN,DELTY)
0093   C
0094   C
0095   C...  GENERATE X SCALE
0096   C
0097           DO 23 I=1,100
0098           X(I)=I*DELT+FMIN-DELT/2.
0099      23   CONTINUE
0100   C
0101   C...  READ THEORETICAL LINE FROM DISK & PLOT
0102   C
0103         CALL EXEC (1,IDISK,SLOT,200,ISTRK+1,41)
0104         CALL LINE (X,SLOT,100,1,0,0,XMIN,DELTX,YMIN,DELTY)
0105   C
0106   C
0107   C
0108   C...  DRAW AXES
0109   C
0110         CALL AXIS (0.,0.,2HRS,-2,17.,0.,XMIN,DELTX)
0111         CALL AXIS (0.,0.,2HHS,+2,9.,90.,YMIN,DELTY)
0112   C
0113   C
0114   C...  ANNOTATE THE PLOT
0115   C
0116         RUN=ITITLE(15)
0117         CALL SYMBL (2.,8.8,.1,3HRUN,0.,+3)
0118         CALL NUMBR (4.5,8.8,.1,RUN,0.,-1)
0119         CALL SYMBL (2.,8.6,.1,IDATE,0.,+28)
0120         CALL SYMBL (2.,8.4,.1,19HPOSITION (INCHES) =,0.,+19)
0121         CALL NUMBR (4.5,8.4,.1,ITITLE(34),0.,+3)
0122   C
0123   C
0124   C...  END OF PLOTTING
0125         CALL PLOT (0.,0.,+999)
0126         STOP
```

```
 PAGE 0004  PL16  10:42 PM  MON.,  3  MAR., 1980

0127        END


  FTN4 COMPILER: HP92060-16092 REV. 1926 (790430)

  **  NO WARNINGS **  NO ERRORS **   PROGRAM = 02190      COMMON = 00196
```

```
0128          END$
```

```
0001  FTN4,L
0002        PROGRAM PL17
0003  C     READS DATA FROM DISK
0004  C     PLOTS HISTOGRAM
0005        COMMON ICOM(196)
0006        REAL SLOT(100),H(16),CHANGE(3),X(2),Y(2)
0007        DIMENSION ITITLE(53),IDATE(14)
0008        INTEGER PARS(5),ISLT1(100)
0009      1 FORMAT (10I6)
0010      2 FORMAT (1P10E12.4)
0011      3 FORMAT (1P2E12.4)
0012        EQUIVALENCE (ITITLE,IDATE),(ITITLE(16),ISCAN),
0013       1            (ITITLE(17),IFIT)
0014        EQUIVALENCE (PARS(1),ISTRK),(PARS(2),IDISK)
0015        EQUIVALENCE (H(11),DELT),(H(12),FMIN),(H(13),FMAX),
0016       1            (H(14),HMAX)
0017  C
0018  C
0019  C...  TRANSFER DATA FROM FATHER TO SON
0020  C
0021        CALL RMPAR (PARS)
0022  C
0023  C
0024  C...  READ TITLE FROM DISK
0025  C
0026        CALL EXEC (1,IDISK,ITITLE,53,ISTRK,0)
0027  C
0028  C
0029  C...  READ CALIBRATION FROM DISK
0030  C
0031        CALL EXEC (1,IDISK,H,32,ISTRK,1)
0032  C
0033  C
0034  C
0035  C...  VERSAPLOT-07 PLOTTING ROUTINE
0036  C
0037  C
0038  C...  INITIALZE FOR PLOTTING
0039  C
0040        CHANGE(1)=9
0041        CHANGE(2)=17
0042        CHANGE(3)=0
```

```
      CALL PLOTS (0,0,CHANGE)
      CALL FACTR (.9)
      CALL PLOT (.5,.5,-3)
C
C
C...  DETERMINE SCALING FACTORS
C
      XMIN=0.0
      DELTX=ISCAN/17.0
      YMIN=0.0
      DELTY=HMAX/9.0
C
C
C...  READ VERTICAL SCALE  FROM DISK
C
      CALL EXEC (1,IDISK,SLOT,200,ISTRK+1,37)
C
C
C...  READ HORISONTAL SCALE FROM DISK
C
      I5=0
         DO 21 I=1,7
         I4=23+(I-1)*2
         CALL EXEC (1,IDISK,ISLT1,100,ISTRK+1,I4)
         I1=(I-1)*100
            DO 22 I2=1,100
            I5=I5+1
            IF (I5 .GT. IFIT) GO TO 23
            I3=I1+I2
            X(1)=I3
            X(2)=X(1)
            Y(1)=0.
            Y(2)=SLOT(ISLT1(I2))
            CALL LINE (X,Y,2,1,0,0,XMIN,DELTX,YMIN,DELTY)
   22       CONTINUE
   21    CONTINUE
   23 CONTINUE
C
C
C
C...  DRAW AXES
C
```

```
0085        CALL AXIS (0.,0.,2HRS,-2,17.,0.,XMIN,DELTX)
0086        CALL AXIS (0.,0.,2HHS,+2,9.,90.,YMIN,DELTY)
0087  C
0088  C
0089  C...  ANNOTATE THE PLOT
0090  C
0091        RUN=ITITLE(15)
0092        CALL SYMBL (2.,8.8,.1,3HRUN,0.,+3)
0093        CALL NUMBR (4.5,8.8,.1,RUN,0.,-1)
0094        CALL SYMBL (2.,8.6,.1,IDATE,0.,+28)
0095        CALL SYMBL (2.,8.4,.1,19HPOSITION (INCHES) =,0.,+19)
0096        CALL NUMBR (4.5,8.4,.1,ITITLE(34),0.,+3)
0097  C
0098  C
0099  C...  END OF PLOTTING
0100        CALL PLOT (0.,0.,+999)
0101        STOP
0102        END
```


FTN4 COMPILER: HP92060-16092 REV. 1926 (790430)

** NO WARNINGS ** NO ERRORS ** PROGRAM = 00772 COMMON = 00196

```
0103          END$
```

References

1. R.C. Pankhurst, D.W. Holder, "Wind tunnel techniques", Pitman, London, 1952.

2. C.F. Dewey, Jr., AGARD Conference Proceedings No. 193 on "Applications of Non-Intrusive Instrumentation in Fluid Flow Research", AGARD CP-193 (Hanfor House, London, 1976), paper 17-1.

3. F.R. Owen in Reference 2, paper 27-1.

4. E.P. Muntz, AGARD ograph, 132, 1968 (unpublished).

5. T. Kimura, M. Nishio, T. Fujita, R. Maeno, AIAA J., 15, 611, 1977.

6. J.A. Smith, J.F. Driskoll, J. Fluid Mech., 72, 695, 1975.

7. V. Natiello Thesis, A.M.S. Department, Princeton University.

8. W. Merzkirch, Flow Visualization, Academic, London, 1974.

9. G. Blendstrup, D. Bershader, AIAA J., Vol. 16, No. 10, 1106, October 1978.

10. W.J. Yanta, B.J. Crapo, Refernce, 2, paper 2-1.

11. W. Gregor, Disa Inf. No. 26, p. 39, December 1977.

12. R.B. Miles, Phys. of Fluids, Vol. 18, No. 6, June 1975.

13. R.B. Miles, E. Udd, M. Zimmermann, Appl. Phys. Lett. Vol. 32, No. 5, March 1978.

14. C.P. Wang, Combustion Science Tech., Vol. 13, p. 211, 1976.

15. W.M. Fairbanks, Jr., T.W. Hansch, A.L. Schalow, J. Opt. Soc. Amer., Vol. 65, No. 2, p. 199, February 1975.

16. A.C.G. Mitchell, M.W. Zemansky, "Resonant Radiation and Excited Atoms", Dover, 1961.

17. H. Schlichtling, "Boundary Layer Theory", McGraw-Hill, 1968.

18. A.H. Shapiro, "The Dynamics and Thermodynamics of Compressible Fluid Flow", Ronald, 1953.

19. C.F. Dewey, Int. J. Heat Mass Trans., Vol. 8, p. 245, 1965.

20. W.G. Vincenti, C.H. Kruger, "Introduction to Phys. Gas Dynamics", R.E. Krieger, 1975.

21. J.P. Holman, "Heat Transfer", McGraw-Hill, 1972.

22. K.F. Smith, "Molecular Beams", London:Methuen, 1955.

23. I. Estemann, D.C. Simpson, O. Stem, Phys. Rev. 71, 238, 1947.

24. S.A. Korff, Astrophysical J., Vol. 76, p. 124, 1933.

25. D.G. McCartan, J.M. Farr, J. Phys. B, Atom. Molec. Phys., Vol. 9, No. 6, 1976.

26. D.W. Posner, Aust. J. Phys., 12, 184, 1959.

27. A. Yariv, "Introduction to Optical Electronics", Holt, Rinehart and Winston, Inc., 1971.

28. C. Young, J. Quant. Spec. Rad. Trans., Vol. 5, p. 549, 1965.

29. R. Huang, "Statistical Mechanics", John Wiley and Sons, 1963.

30. P. Materna, "Hot Wire Anemometry in a Low Density Hypersonic Turbulent Boundary Layer", Thesis, Department of Mechanical and Aerospace Engineering, Princeton University, April 1979.

31. A. Henderson, Jr., D.O. Braswell, "Charts for conical and two dimensional oblique-shock flow parameters in Helium at Mach numbers from about 1 to 100", NASA Technical Note D-819, 1961.

32. Spectra Physics, "Frequency Stabilization Techniques for Single Frequency Dye Lasers", March 1977.

33. J.F. Kielkopf, J.O.S.A., Vol. 63, No. 8, p. 987, August 1973.

34a. K. Levenberg, Quant. Appl. Math., 2, p. 164-168, 1944.

34b. D.W. Marquardt, J. SIAM, Vol. II, No. 2, June 1963.

34c. K.M. Brown, J.E. Dennis, Numerische Mathematic, Vol. 18, p. 289, 1972.

35. International Mathematical and Statistical Libraries Inc., Suite 510, 6200 Hilcroft, Houston, Texas 77036.

36. P.A. Thompson, "Compressible Fluid Dynamics", McGraw-Hill, 1972.

37. J.N. Mueller, "Equations Tables and Figures for Use in the Analysis of Helium Flow at Supersonic and Hypersonic Speeds", NACA Technical Note 4063, 1957.

38. C.L. Mehta, "Lectures in Theoretical Physics", Vol. XII-A, p. 95, Ed. R.T. Mahanthapa, W.E. Brittin, 1971.

39. S.D. Silvey, "Statistical Interference", Halsted Press, 1975.

40. R.A. Arndt, M.H. McGregor, "Nucleon-Nucleon Phase Shift Analysis by Chi-Squared Minimization", Method in Computational Physics, Vol. 6, p. 253, Academic Press, 1966.

41. P.R. Bevington, "Data Reduction and Error Analysis for the Physical Sciences", McGraw-Hill, 1969.

42. E.L. Lewis, L.F. McNamara, Phys. Rev. A, Vol. 5, No. 6, June 1972.

43. F. Biraben, B. Cagnac, G. Grynberg, Phys. Rev. Lett., Vol. 32 No. 12, p. 643, 1974.
M.D. Levenson, N. Bloemberger, Phys. Rev. Lett., Vol. 32, No. 12, p. 645, 1974.
D. Pritchard, J. Apt., T.W. Ducas, Phys. Rev. Lett., Vol. 32, No. 12, p. 641, 1974.

44. M.D. Levenson, Post Deadline Session, Q.2, IEEE/OSA, June 12, 1974.

45. R.B. Miles, "Optical third harmonic generation in metal vapors", Microwave Laboratory Report No. 2069, W.W. Hansen Laboratories of Physics, Stanford University, 1972.

46. R.C. Weast, C.R.C. "Handbook of Chemistry and Physics" 1976-1977.
N.I. Sax, "Dangerous Properties of Industrial Materials", Reinhold.

47. W.H. Lin, Thesis, A.M.S. Department, Princeton University, 1974.

48. A. Corney,"Atomic and Laser Spectroscopy", Clarendon Press, Oxford, 1977.

49. R.M. Schneider, A. Lurio, W. Happer, A. Kladjavi, Phys. Rev. A, Vol. 2, No. 4, 1970.

50. M.S. Sargent, M.D. Schully, W.E. Lamb, Jr., "Laser Physics", Addison-Wesley, 1974.

51. J.D. Jackson, "Classical Electrodynamics", John Wiley and Sons, 1975.

52. V. Weisskopf, E. Wigner, Zeitschrift fur Physik, Vol. 63, p. 54, 1930.

53. A. Messiah, "Quantum Mechanics", John Wiley, 1958.

54. B.P. Ribble, G. Copley, L. Krause, Phys. Rev., 153, 9, 1967.

55. J.L. Hall, "Lectures in Theoretical Physics", Vol. XII-A, p. 161, Ed.: K.T. Mahanthapa, W.E. Brittin, 1971.

56. W.R. Hindmarsh, J.M. Farr, "Collision Broadening of Spectral Lines by Neutral Atoms", Progress in Quantum Electronics", Ed.: J.H. Sanders, S. Stenholm, Pergamon Press, 1972.

57. A.E. Siegman, "An Introduction to Lasers and Masers", McGraw-Hill, 1971.

58. W.E. Baylis, J. Chem. Phys., Vol. 51, No. 6, 15 September 1969.

59. A.L. Schawlow, C.H. Townes, Phys. Rev., Vol. 12, No. 6, p. 1940, 1958.

60. J.L. Hall, S.A. Lee, J. Helmcke, F. Kowalski, Conference of Laser Engineering and Applications, IEEE/OSA, Washington, D.C., 1979.

61. V. Weisskopf, Physikalische Zeitschrift, 34, 1, 1933.

62. A.P. Thorne, "Spectrophysics", Chapman and Hall, London, 1974.

63. V. Weisskopf, E. Wigner, Zeitschrift fur Physik, Vol. 63, p. 54, 1930.

64. E.M. Pugh, G.H. Winslow, "The Analysis of Physical Measurement", Addison-Wesley, 1966.

Publications Issued During the

Course of Research

Quantitative flow visualization in sodium vapor seeded hypersonic helium[a)]

R. B. Miles, E. Udd,[b)] and M. Zimmermann

Department of Aerospace and Mechanical Sciences, Princeton University, Princeton, New Jersey 08540
(Received 29 August 1977; accepted for publication 4 January 1978)

Sodium vapor seeded into a hypersonic helium flow through an orifice on a model is used as a tracer to determine velocity profiles. A narrow-linewidth tunable dye laser is scanned across the Doppler-shifted absorption line of the sodium and the resonant fluorescence is observed. Curves showing the velocity-shifted pressure- and temperature-broadened absorption lines at several points in the flow are presented. Fluorescence is strong enough to use this technique for quantitative flow visualization: at each laser frequency, a specific velocity component is highlighted and easily observed by eye.

PACS numbers: 47.40.Ki, 32.70.Jz, 51.70.+f, 06.30.Gv

We report here the development of a new technique for the measurement of high-speed flow parameters including velocity, pressure, and temperature, and the quantitative visualization of the flow field. Atomic sodium vapor seeded into the flow has a Doppler-shifted temperature- and pressure-broadened absorption profile at any point within the flow. An expanded narrow-linewidth laser beam will cause all regions of the seeded flow with a specific velocity component in the illumination direction to fluoresce brightly enough to be easily seen with the eye. Tuning the laser frequency selects different velocity profiles.

Fluorescence for flow visualization has been found useful for both qualitative and quantitative studies in incompressible fluid flows into which fluorescing dyes are seeded and observed under laser illumination.[1,2] For the gas phase, researchers have relied on electron-beam fluorescence,[3] electric-discharge-induced fluorescence,[4] and index-of-refraction techniques,[5] such as Schlieren, shadowgraphs, and interferometry for flow visualization. Of these methods, electron-beam fluorescence has also given quantitative density, temperature, and velocity information in low-density gases,[6] and index-of-refraction techniques have given density information in high-density gases. The standard laser Doppler velocimeter is limited in low-density high-speed facilities by particle lag and low signal intensities.[7] The technique presented in this paper applies to both high- and low-density flows and has virtually no particle lag problem.

In this experiment a concentrated high-temperature mixture of sodium and helium is injected through a model into a Mach 16 helium flow and illuminated by a narrow-linewidth tunable dye laser. As the laser frequency is scanned through the hyperfine lines of the D_2 transition at 589 nm, the absorption profile of the sodium line is determined by observing the resonant fluorescence. The choices of a hypersonic helium flow and injection through the model were made for simplicity since helium does not quench sodium and the model-mounted injector is easy to fabricate. The technique is amenable to high-speed dry nitrogen and air flows, and full flowfield seeding appears to be feasible. The use of tunable lasers to observe sodium lines is well developed,[8,9] and the theory of this technique has been discussed previously.[10,11]

An argon-ion-pumped Spectra Physics 580 dye laser beam is expanded through a spatial filter and telescope and passed through the wind tunnel at 40° to the flow axis. The laser frequency is set first using a spectrometer, then a hot sodium cell, and finally an atomic beam. An optical spectrum analyzer monitors the frequency stability of the laser. Fluorescence is observed when the laser frequency is tuned to a Doppler-shifted absorption line of the sodium. The flow velocity component in the illumination direction is found by a straightforward comparison of the fluorescence versus frequency from the seeded flow with that from the atomic beam.

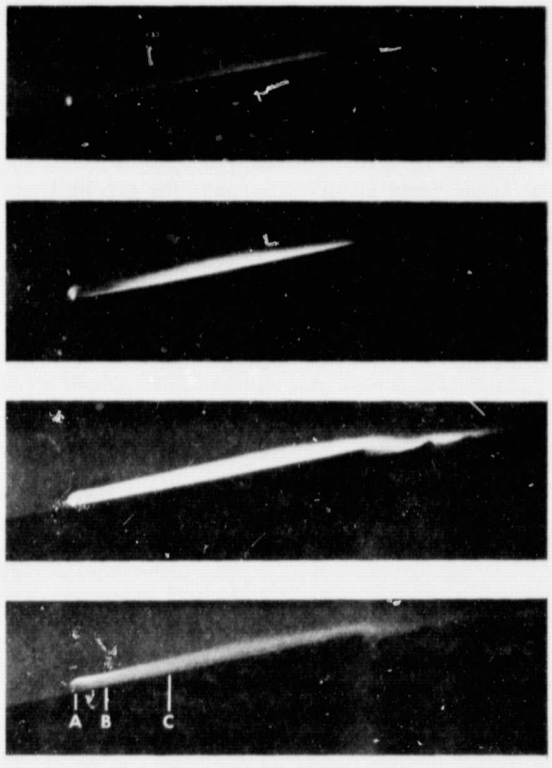

FIG. 1. Composite photograph of the seeded flow. From top to bottom the frequency is increased, thus highlighting sequentially higher-velocity components. Point A is the injection orifice; points B and C are the locations of the velocity surveys 5.3 mm and 18 mm downstream of the injection point.

 0003-6951/78/3205-0317$00.50

A 10° half-angle cone model is mounted in a 1.6×10^6 N/m^2 room-temperature-plenum Mach 16 helium tunnel for this experiment. A heated sodium oven is located inside the model. High-purity helium flows at 0.01 g/sec with a back pressure of 1.3×10^5 N/m^2 into the oven through a resistively heated stainless-steel tube and mixes with the sodium vapor. The sodium-helium mixture then passes through another resistively heated stainless-steel capillary and is injected into the flow through a 0.9-mm-diam orifice on the model. The sodium density reaches self-trapping levels at an oven temperature of 220 °C, so normal operation is in the region of 190 °C. The capillary is maintained at approximately 500 °C to avoid clogging.

With the flow, the hot sodium-helium jet is swept downstream. Fluorescence can be seen all the way along the cone and continuing down the tunnel. As the laser is tuned, different velocity components of the flow are highlighted. Figure 1 is a composite of four pictures of the seeded region illuminated at different wavelengths. The corresponding highlighted velocity components vary from low velocity in the top picture to high velocity in the bottom picture.

For velocity measurements, a cylindrical lens is placed in the beam and the laser focused to a line over the axis of the cone. A detection system is focused to intersect the line so a point in the flow directly over the cone is observed. The calibration cell scan of the D_2 hyperfine lines shown in Fig. 2 is compared with the scans from points 0.25 mm, 0.75 mm, 1.25 mm, 1.75 mm, 2.25 mm, and 2.75 mm above the cone 5.3 mm and 18 mm downstream of the injection point. In Fig. 3 the scans 18 mm downstream are shown normalized, vertically offset, and scaled so that 0 MHz corresponds to no Doppler shift. The overall line shape is a combination of the temperature- and pressure-broadened profiles of the six hyperfine transitions of the D_2 manifold. These transitions are used because the strong line ($3^2S_{1/2}[F=2]$ to $3^2P_{3/2}[F=3]$) seen in Fig. 2 provides a convenient reference wavelength.

The axial velocity at a point may be determined by measuring the frequency shift of the peaks and using simple geometry. Figure 4 gives the axial velocities

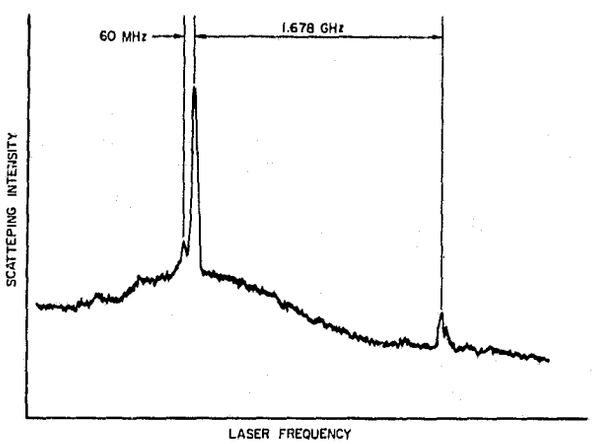

FIG. 2. Atomic beam calibration cell scan of the hyperfine D_2 lines of sodium vapor.

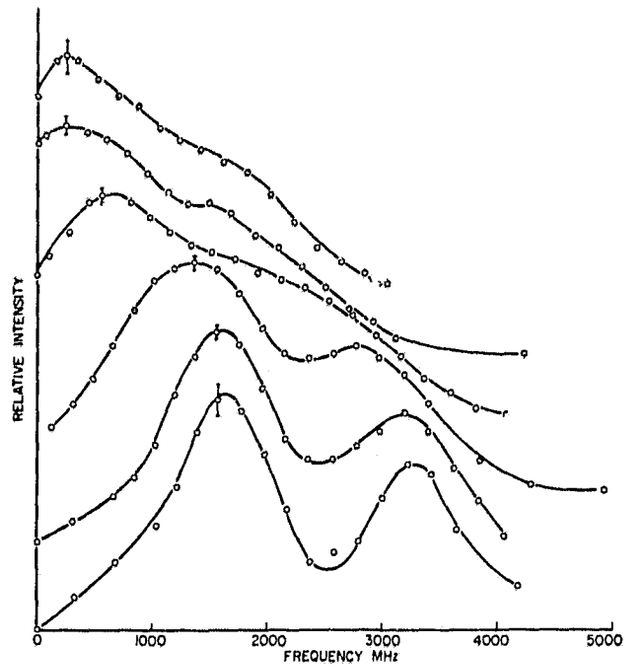

FIG. 3. Fluorescence as a function of laser frequency off resonance from points 0.25 ± 0.25 mm, 0.75 ± 0.25 mm, 1.25 ± 0.25 mm, 1.76 ± 0.25 mm, 2.25 ± 0.25 mm, and 2.75 ± 0.25 mm from the surface 18 mm behind the sodium-helium injection point. The top curve is closest to the surface. The error bar on the top point of each curve applies to all points in the curve. The curves are sketched through the points for clarity.

at various heights above the surface 5.3 mm and 18 mm downstream of the injection point. The error bars are large because the detector aperture sampled a 0.25-mm-diam region and the data reduction was done by hand. The scattered signal was bright enough to require attenuation before entering the detecting photomultiplier, so volumes several orders of magnitude smaller should be observable.

The observed Voigt linewidth is a convolution of pressure and temperature broadening of the sodium vapor plus additional terms due to turbulence, the linewidth of the illuminating laser, and the natural linewidth of the

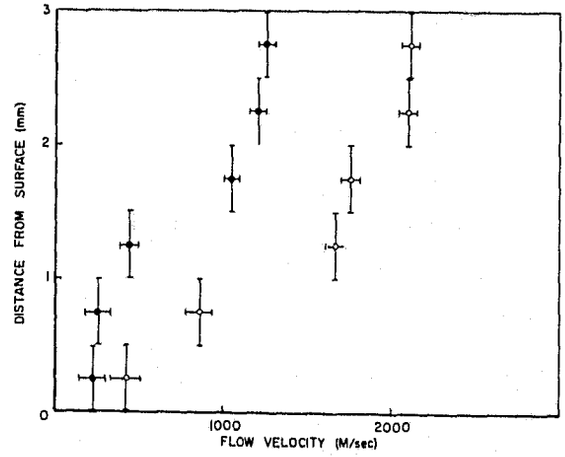

FIG. 4. Measured velocities above a point 5.3 mm (circles) and 18 mm (dots) downstream of the injection orifice.

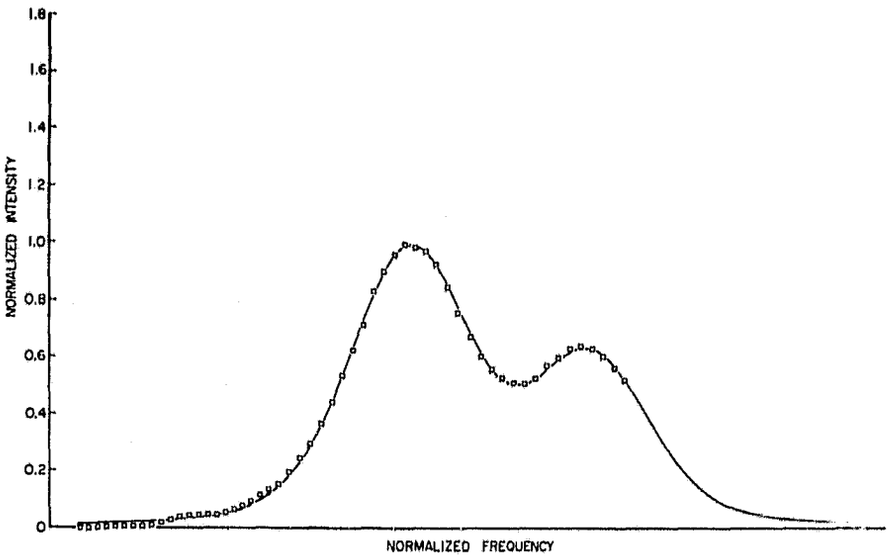

FIG. 5. Normalized computer-generated fit to the experimental points taken 18 mm downstream of the sodium-helium injection point and 1.25 mm above the surface.

sodium. The calibration cell scan (Fig. 2) shows that the combined laser and natural full widths at half-maximum are not broader than 25 MHz and therefore can be ignored relative to pressure and temperature broadening. Pressure broadening of sodium by helium is[12]

$$\Delta f_p = 4.2\times10^{10}\, P/P_0(T_0/T)^{1/2},$$

where P_0 and T_0 are the pressure and temperature at STP and Δf_p is the full linewidth at half-maximum. The full width at half-maximum of temperature-broadened sodium is

$$\Delta f_t = 1.25\times10^9(T/T_0)^{1/2}.$$

A normalized computer-generated fit to the experimental points at 1.25 mm above the surface and 18 mm downstream is shown in Fig. 5. The best fit yields a Voigt linewidth of 1396 MHz made up of a pressure-broadened (Lorentzian) component of 416 MHz and a temperature-broadened (Gaussian) component of 1157 MHz. The corresponding temperature and pressure are 233 °K ± 8% and 9 Torr ± 12%. The sensitivities are determined from the variation of pressure and temperature among acceptable fits and are strongly dependent on experimental noise. The temperature drops to 190 °K ± 15% $\frac{1}{2}$ mm farther into the flow; however, the pressure remains approximately the same. Fits at other points show the temperature decreasing farther out into the flow; however, due to increased noise in our measurements, values of temperature and pressure could not be determined for these points.

The measurement of velocity close to the cone surface under these circumstances is difficult by other techniques. Pitot surveys tend to interfere with the flow and require the temperature and static pressure in order to deduce the velocity. Electron-beam fluorescence is hampered by scattering of electrons from the surface.

This technique virtually eliminates the particle lag problems associated with standard LDV and opens exciting possibilities for measurement of multiple velocity components, turbulence, temperature, pressure, and density. Since seeding through the model perturbs the flow, noninteractive flowfield seeding techniques are currently under development in our laboratory and the expansion to dry nitrogen and air flows seems promising.

The authors wish to thank G.K. Bienkowski, S.M. Bogdonoff, F.R. Hama, S.H. Lam, G.S. Settles, and particularly J.A. Smith for technical and editorial suggestions. W.C. Honaker, J.C. Hoppe, and W.W. Hunter at NASA Langley have interacted closely with this work, giving strong encouragement and suggesting experimental configurations.

[1]C.F. Dewey, Jr., *AGARD Conference Proceedings No. 193 on Applications of Non-Intrusive Instrumentation in Fluid Flow Research*, AGARD CP-193 (Harford House, London, 1976), paper 17-1.
[2]F.K. Owen, in Ref. 1, paper 27-1.
[3]E.P. Muntz, AGARDograph 132, 1968 (unpublished).
[4]T. Kimura, M. Nishio, T. Fujita, and R. Maeno, AIAA J. 15, 611 (1977).
[5]W. Merzkirch, *Flow Visualization* (Academic, London, 1974).
[6]J.A. Smith and J.F. Driscoll, J. Fluid Mech. 72, 695 (1975); Ref. 1, paper 16-1.
[7]J.F. Meyers and W.V. Feller, Laser Doppler Workshop, Purdue University, 1972, p. 445 (unpublished).
[8]F.Y. Wu and S. Ezekiel, 1977 IEEE/OSA Conference on Laser Engineering and Applications, 1977, Paper No. 716 (unpublished).
[9]F. Schuda, M. Hercher, and C.R. Stroud, Jr., Appl. Phys. Lett. 22, 360 (1973).
[10]R.B. Miles, Phys. Fluids 18, 751 (1975).
[11]R.B. Miles, in Ref. 1, paper 19-1.
[12]S. Chen and P. Henry, J. Quant. Spectrosc. Radiat. Transfer 13, 135 (1973).

Resonant Doppler velocimeter

Richard B. Miles

Aerospace and Mechanical Sciences Department, Princeton University, Princeton, New Jersey 08540
(Received 15 October 1974; final manuscript received 26 February 1975)

Narrow linewidth tunable lasers augur a new kind of laser Doppler velocimetry employing resonant absorption and fluorescence from trace atomic species rather than scattering from particles. This technique may provide better turbulence and small volume information than present velocimetry.

A narrow bandwidth tunable dye laser incident in the direction opposed to a flow seeded with trace amounts of sodium vapor will be absorbed at the Doppler-shifted resonant frequency of the sodium and the light will be rapidly reradiated in all directions. The fluorescence intensity may be correlated with the absorption; the maximum fluorescence occurring when the tunable laser is matched to the Doppler-corrected resonant absorption line center of the observed region. Measurement of the laser frequency, then, will yield the velocity of the gas in the observed region. Pressure and temperature discontinuities will also be observable as intensity variations, rendering this tool a convenient device for qualitative flow visualization as well as quantitative measurements. Similar applications have been suggested for the study of plasmas,[1] and experiments using a tunable dye laser to study hyperfine structure in a sodium atomic beam have demonstrated the feasibility of the technique.[2,3]

The Doppler shift for sodium is 1.7 MHz for each meter/sec of flow velocity. Since the natural linewidth is 9.8 MHz, the limiting resolution of the resonant Doppler technique is several meters/sec. Pressure and thermal broadening will substantially decrease the minimum velocity sensitivity. Several experimental configurations with these minimum velocity resolutions and other pertinent information are given in Table I for helium and nitrogen.

Laser stability is not expected to be a limitation. Bjorkholm and Ashkin[4] achieved stable operation to within 20 MHz for times up to 30 sec and were able to repeatedly scan through the sodium resonance lines. Wu *et al.*[5] were able to operate their dye laser with a short term jitter of 200 kHz and observe the hyperfine structure of iodine to one part in 10^9. Commercially available lasers now produce single mode electronically scanned beams at the sodium resonance frequencies with scan rates up to 40 msec and resolutions of less than 10 MHz.

The hyperfine structure of the sodium is on the order of the frequency shifts to be measured and therefore must be taken into account. Splitting of the $3^2P_{1/2}$ level is 192 MHz and, if unresolvable, will cause a 100 m/sec indeterminacy. Splitting of the $3^2S_{1/2}$ level is 1.77 GHz and should pose no problem. Either splitting may be used to calibrate the instrument. A sodium atomic beam calibration cell may be used in which $P_{1/2}$ state splitting is easily observable.[2,3] The wind tunnel flow will be both pressure and temperature broadened so $P_{1/2}$ state splitting will generally not be observable; therefore, the most desirable line to observe is the $3^2S_{1/2}$ $(F=1)$ to $3^2P_{1/2}$ $(F=2)$ line since its companion is a factor of five lower and should not cause difficulty in accuracy.

Rows 1–4 of Table I list operating conditions in typical wind tunnels of interest. The velocity sensitivity in Row 5 is determined from the pressure and thermally broadened linewidth. Full width at half maximum values are

$$\Delta f_t = f_0\left(8\ln 2\,\frac{kT}{Mc^2}\right)^{1/2} = 757\left(\frac{T}{100}\right)^{1/2}\text{MHz}\,, \tag{1}$$

$$\Delta f_p = \delta_p\,\frac{N}{N_0}\left(\frac{T}{100}\right)^{1/2} + \delta_N\,, \tag{2}$$

where $\delta_p = 0.89\times10^{10}$ for N_2,[6] $\delta_p = 1.27\times10^{10}$ for He,[7] and $\delta_N = 9.76\times10^6$ is the sodium natural linewidth. $N_0 = 2.69\times10^{19}$ molecules/cc and N is the static number density of nitrogen. $f_0 = 5.085\times10^{14}$ Hz. A square root dependence on temperature is assumed, although at very low temperatures this may not be accurate. The velocity sensitivity is rather arbitrarily chosen to be $\pm10\%$ of the full width at half maximum of the combined thermal and pressure (Voigt) linewidth profile plus the natural linewidth with which the fluorescence is being compared.

$$\Delta v \cong \pm 0.1\left(\frac{\Delta f_p + \delta_N}{1.7\times10^6}\right)\,. \tag{3}$$

Pressure effects cause a shift of the resonance line to the red in the case of nitrogen and to the blue for helium.[7]

$$\delta f_{N_2} = -0.39\times10^{10}\,\frac{N}{N_0}\left(\frac{T}{100}\right)^{1/2}\,, \tag{4}$$

$$\delta f_{He} = 0.073\times10^{10}\,\frac{N}{N_0}\left(\frac{T}{100}\right)^{1/2}\,. \tag{5}$$

These shifts produce a velocity correction factor shown in Table I.

Maximum collected signal intensities will depend on the incident laser power density, the sodium atom density, static temperature and pressure, quenching, and on the collection optics. The incident laser power density should be held below the saturation level of the sodium, particularly for pressure dominated broadening since saturation further broadens the resonance. Assuming the $3^2S_{1/2}$ $(F=1)$ to $3^2P_{1/2}$ $(F=2)$ line contributes 5/48 to the total $3S$-$3P$ oscillator strength $f = 0.982$,[8] the line center cross section for this naturally broadened line is $\sigma = 1.77\times10^{-10}$ cm^2. The unquenched

TABLE I. Velocity sensitivity and signal level for various wind tunnel configurations.

	Helium				Nitrogen		
Mach number	8	10	16	20.7	2.9	10	20
Stagnation pressure (Atm)	20	108	20	102	6.8	50	100
Stagnation temperature (°K)	300	256	300	297	291	1000	2000
Free stream velocity (m/sec)	1725	1606	1753	1748	616	1407	2027
Velocity sensitivity	±3%	±7%	±0.6%	±0.6%	±49%	±2.3%	±1.1%
Velocity correction (m/sec)	+27	+67	+1.8	+3.3	−1128	−9.3	−0.2
Fluorescence per atom (photons/sec)	6.33×10^{4}	2.58×10^{4}	3.68×10^{4}	3.30×10^{4}	2.45×10^{2}	1.08×10^{5}	1.99×10^{4}
Maximum sodium density (atoms/cc)	4.69×10^{10}	1.15×10^{11}	8.06×10^{9}	9.01×10^{9}	2.91×10^{11}	2.05×10^{10}	1.47×10^{10}
Maximum detected signal from 1 cc (W)	2.5×10^{-6}	2.5×10^{-6}	2.5×10^{-6}	2.5×10^{-6}	6.0×10^{-8}	1.9×10^{-6}	2.5×10^{-6}
Mass flow ratio	1.7×10^{7}	2.3×10^{7}	1.3×10^{7}	2.8×10^{7}	6.1×10^{7}	1.1×10^{7}	5.1×10^{5}

lifetime of sodium is 16.3 nsec so the saturation intensity is approximately 0.06 W/cm^2. Quenching and broadening will increase the saturation level; however, for maximum signal calculations, an intensity of 0.01 W/cm^2 was assumed for convenience.

The number of photons scattered per atom, n, is determined by the cross section at the maximum of the Voigt broadened line, the incident flux density, and the quenching factor Q:

$$n=\frac{(0.01\ \mathrm{W/cm^2})}{hf_0}\sigma(f=f_0)Q\ . \tag{6}$$

$Q=[1+72.1(T/100)^{1/2}N/N_0]^{-1}$ for nitrogen[9] and $Q=1$ for helium. The Voigt broadened maximum may be determined from the thermal linewidth Δf_t and the pressure broadened linewidth Δf_p by

$$\sigma(f=f_0)=\frac{5}{48}\frac{fe^2\eta}{2m_e}\frac{(\ln 2)^{1/2}}{\pi^{1/2}\Delta f_t}\exp\left(\ln 2\,\frac{\Delta f_p^2}{\Delta f_t^2}\right)\times\left(1-\mathrm{erf}\,\frac{\Delta f_p(\ln 2)^{1/2}}{\Delta f_t}\right) \tag{7}$$

$$=\frac{2.55\times10^{-3}}{\Delta f_t}\left[\exp\left(0.069\,\frac{\Delta f_p^2}{\Delta f_t^2}\right)\right]\times\left(1-\mathrm{erf}\,\frac{0.833\Delta f_p}{\Delta f_t}\right)(\mathrm{cm}^2) \tag{8}$$

where f is the oscillator strength, e is the electron charge, η is the free space impedance = 377, and m_e is the electron mass.

From the number of photons scattered/atom, the maximum signal may be determined for any experimental arrangement. Collection optics, of course, only subtend a small portion of the scattering angle. The $f/5$ optics assumed here reduce the number of photons seen by 400; however, the signal varies as the inverse square of the collect f number. The density is limited by the condition that the medium be optically thin. This is specified by limiting the absorption length to longer than the wind tunnel distances: $1/N_{N_2}\sigma\geq l$. l has been chosen as 10 cm for sodium density and mass flow ratio calculations presented. The scattering volume observed is assumed to be 1 cm^3, but the detected intensity simply scales with the volume. The large calculated intensities suggest that very small volumes or low atom concentrations are observable. This is consistent with observations by Fairbank *et al.*,[10] who have measured sodium densities as low as 10^5 atoms/cc with a signal-to-noise ratio of better than 1000.

It is apparent from Table I that substantial inaccuracies occur for low Mach number of high pressure conditions. This limitation is due to thermal and pressure broadened linewidths causing uncertainty in the measurement of the velocity associated frequency shift. Heavier vapors or gases may be used to overcome the thermal broadening; for example, iodine vapor will reduce it by 70%. The lower cross sections of these molecular gases may be compensated for by higher incident laser power densities. The major loss in performance will be the higher tracer gas densities required to offset the thermally distributed ground state populations. To achieve similar signal levels in iodine vapor, the incident laser power density would have to be increased about 3000 times, and the iodine vapor density would have to be 1000 to 4000 times greater than the sodium atom density.[11] Since iodine and chlorine do not react with air, either may be a reasonable candidate for supersonic low pressure air wind tunnels.

I would like to thank F. Hama, J. Smith, and I. Vas of the Gas Dynamics Laboratory, Princeton University for many helpful discussions.

This work was supported by research grant Number NSG 1070 from the National Aeronautics and Space Administration Langley Research Center, Hampton, Virginia.

[1]D. Dimock, E. Hinnov, and L. C. Johnson, Phys. Fluids 12, 1730 (1969).
[2]W. Hartig and H. Walther, Appl. Phys. 1, 171 (1973).
[3]F. Schuda, M. Herscher, and C. R. Stroud, Jr., Appl. Phys. Lett. 22, 360 (1973).
[4]J. Bjorkholm and A. Ashkin, Phys. Rev. Lett. 32, 129 (1974).
[5]F. Y. Wu, R. E. Grove, and S. Ezekiel, Appl. Phys. Lett. 25, 73 (1974).
[6]S. Ch'en and M. Takeo, Rev. Mod. Phys. 29, 20 (1957).
[7]S. Ch'en and P. Henry, J. Quant. Spectrosc. Radiat. Transfer 13, 385 (1973).
[8]W. Wiese, M. Smith, and B. Miles, Atomic Transition Probabilities, National Standard Reference Data Series No. 22, National Bureau of Standards (1969), Vol. II.
[9]B. Kibble, G. Copely, and L. Krause, Phys. Rev. 159, 11 (1967).
[10]W. Fairbank, Jr., T. Hansch, and A. Schawlow, Bull. Am. Phys. Soc. 18, 1587 (1973).
[11]S. Ezekiel and R. Weiss, Phys. Rev. Lett. 20, 91 (1968).

NORTH ATLANTIC TREATY ORGANIZATION

ADVISORY GROUP FOR AEROSPACE RESEARCH AND DEVELOPMENT

(ORGANISATION DU TRAITE DE L'ATLANTIQUE NORD)

AGARD Conference Proceedings No.193

APPLICATIONS OF NON-INTRUSIVE INSTRUMENTATION IN FLUID FLOW RESEARCH

Papers and Discussion of the Fluid Dynamics Panel Symposium held at the French-German Research Institute (ISL), Saint-Louis, France 3–5 May 1976.

RESONANT DOPPLER VELOCIMETER

Richard B. Miles
Princeton University
Princeton, N. J.
08540

SUMMARY

Resonance fluorescence is a potentially useful tool for studying hypersonic flowing gases. This paper discusses the measurement of velocities and demonstrates visualization techniques using sodium seeded into helium flows. A narrow linewidth dye laser is tuned onto the sodium resonance line. The doppler shift of the absorption frequency yields the velocity profile, and the fluorscence provides direct flow visualization. Other flow properties such as the turbulence frequency, temperature, etc. may also be measured.

I. Introduction

Tracer particles in a flowing gas have extensively been used for laser doppler velocimetry in subsonic and transonic flow. In the hypersonic regime, however, these particles tend to lose their ability to follow the flow. This "particle lag" becomes more serious as the flow velocities increase and makes standard laser doppler velocimetry a rather inaccurate tool for monitoring low density high velocity flows and high turbulence frequencies. To overcome this problem, smaller particles must be used. As the size of the particle decreases, however, its effectiveness as a visible light scatterer also decreases, thereby lowering the signal levels until finally with particles less than .1 micron the signal levels virtually disappear. Thus, the ideal tracer particle is useless as a scatterer.

Work currently underway at Princeton University's Gas Dynamics Laboratory is investigating the possibility of seeding hypersonic gas flows with atomic sodium and using resonance fluorescence rather than Mie scattering to generate high signal intensities. The strongly resonant sodium D lines have been studied since before the turn of the century. These lines are so strong that number densities as low as several thousand sodium atoms per cubic centimeter have been detected in the laboratory.[1] Sodium atoms introduced into foreign gases such as helium and nitrogen quickly equilibrate thermally with the foreign gas and tend to follow the flow closely. Currently available narrow linewidth dye lasers can be used to probe the sodium tracer atoms. Since the absorption frequency is doppler shifted in the direction of the incident light, monitoring the fluorescence intensity as a function of the incident laser wavelength gives the velocity component in the incident light direction. The wavelength of the fluorescence may also be monitored to give the component of the velocity in the observation direction. Other characteristics of the sodium absorption and fluorescence profile give additional information about the gas mixture; for example the fluorescence intensity may be related to the number density, the temperature and the pressure. Illumination of the entire flow field will produce fluorescence which may be useful for flow visualization.

In the laboratory, (Figure 1) a beam from a narrow linewidth tunable dye laser

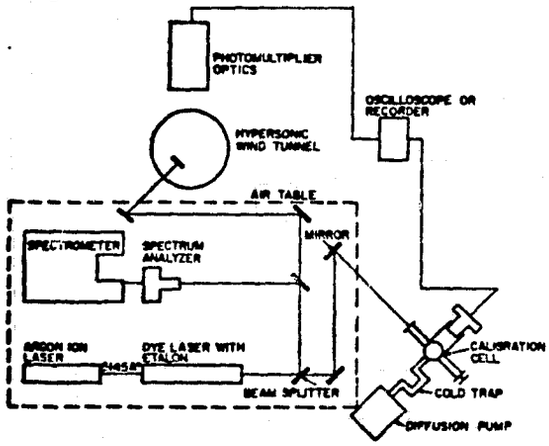

is split into two components. The first is directed axially down the wind tunnel and fluorescence from that beam is monitored in a transverse direction. The second beam is directed into a sodium atomic beam calibration cell. The fluorescence from the sodium atoms mixed with the helium or nitrogen gas flow within the wind tunnel is compared to the fluorescence of the pure sodium atomic beam in the calibration cell. By sweeping the frequency of the dye laser, the frequency offset of the fluorescence maximum from the wind tunnel will give the velocity of the gas mixture within the tunnel. The observed linewidth difference will give information about the pressure and the temperature of the mixture within the tunnel. If the dye laser is tuned onto the maximum of the fluorescence profile from the tunnel, fluorescence intensity fluctuations can be correlated with turbulence. Various single and two photon processes may be conceived to measure other parameters of the flow.

II. Discussion

Flows seeded with particles depend, of course, on the Mie scattering cross section. This cross section is strongly dependent on the size of the particle, and for particles less than .5μ in diameter, falls off at approximately the fourth power of the diameter if the flow is illuminated with visible light.[2] On the other hand, the ability of a seed particle to follow the flow is strongly enhanced as the size is decreased. For example, for water droplets in air, the relative mean square error at 10 KHz drops from 2.7% for a 1.0μ diameter droplet to .02% for a .3μ diameter droplet.[3] In hypersonic flows, turbulence frequencies up to a megahertz or more must be measured. Even at 100 KHz, the .3μ particle cannot follow the flow,[4] and at 1 MHz the true frequency spectra cannot be measured. To overcome particle lag and low scattering cross sections, very high densities of < .3μ particles must be used. Such high densities are prone to particle agglomeration and may also affect the character of the flow.

An atomic species seeded into the flow will equilibrate in several collisions, therefore there is virtually no particle lag. Although the resonant scattering cross section is low ($\sigma \cong 10^{-12}cm^2$), the mass of the atoms is small so large numbers ($>10^{10}/cc$) of tracer particles may be used without affecting the flow characteristics.

Due to the nature of atomic fluorescence, the gas mixture, and the illuminating laser, various broadening processes are observed which limit the accuracy of the measurement.

A. Lifetime broadening.

The larger the absorption cross section, the shorter the lifetime in the excited state. Thus an atom will re-emit the radiation within several tens of nanoseconds. This means that the "observation time" cannot be longer than several tens of nanoseconds.

B. Collision broadening.

In a gas mixture, a collision with another particle dephases the seed atom and causes the "observation time" to be reduced to the time between collisions. Even if the atom remains in the excited state, these collisions cause the energy level to be more uncertain and therefore broader.

C. Thermal broadening.

At any instant of time, each atom has some instantaneous velocity. The distribution of instantaneous velocities is centered around the average velocity; the width of the distribution is determined by the temperature and mass of the atoms. Since the absorption line center for each atom is doppler shifted by the instantaneous velocity, the absorption profile for the mixture is broadened.

D. Laser broadening.

Our ability to measure the absorption profile is limited by the bandwidth and stability of the laser. Current tunable dye laser systems have output linewidths in the 10-20 MHz range. Some dye lasers have been stabilized to 250 KHz.[5]

E. Velocity fluctuation broadening.

Fluctuations in the average velocity will be caused by turbulent eddys. These fluctuations look similar to the thermal broadening and will cause the absorption profile to broaden yet further. They differ, however, in that the thermal broadening occurs in time comparable with the atom-atom collision frequency, and velocity broadening occurs in time comparable with the turbulence frequency.

In general all these ambiguities are mixed together to produce some measured absorption linewidth with its peak shifted by the average velocity. Although they may make the accurate determination of the velocity difficult, thermal, collision, and velocity broadening yield additional information about the flow.

III. Example - Sodium in Helium

The strong sodium D lines are split into ten hyperfine lines as shown in figure 2.[1]

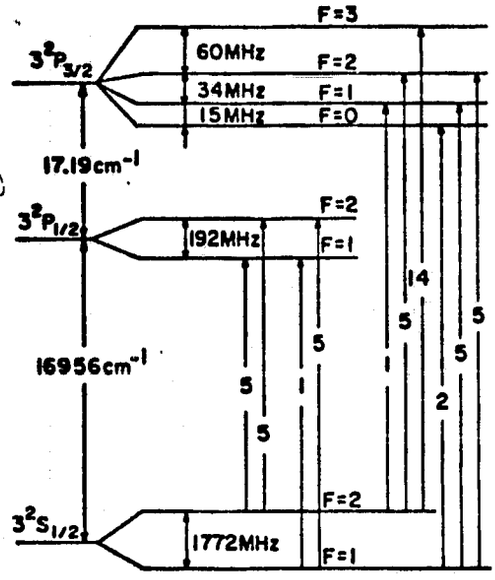

Figure 2 Sodium Resonant Line Strengths and Energy Levels

Theoretical line strengths and spacings are shown in the figure. With tunable dye lasers and atomic beam cells, these lines have been measured down to 10% of their natural width of 9.6 MHz.[5] In the flow, these lines will be substantially broadened by collisions, thermal broadening, and velocity fluctuations. A calibration cell is necessary to provide a comparison between the unperturbed line and the wind tunnel.

Although any of the lines will suffice, two are of particular interest. The $^2S_{1/2}(F=1)$ to $^2P_{1/2}(F=2)$ line is paired with a line with an intensity lower by a factor of five and is removed by at least 1.77 GHz from other strong lines. Thus this line provides an easy unambiguous reference. A problem occurs, however, if the atom is excited numerous times within the observation region. Since the selection rules permit $\Delta F=0, \pm 1$, after several excitations, the probability is high that the atom will relax to the $^2S_{1/2}(F=2)$ state and effectively be lost. This phenomena is called resonant pumping, and to avoid it the $^2S_{1/2}(F=2)$ to $^2P_{3/2}(F=3)$ line may be chosen. Any atom reaching the $F = 3$ state can only relax back to the $F = 2$ state from which it came.

Assuming the $^2S_{1/2}(F=1)$ to $^2P_{1/2}(F=2)$ line is observed, the line center value of the absorption cross section is[6]

$$\sigma(f=f_o) = \frac{2.55 \times 10^{-3}}{\Delta f_t} \left[\exp\left(0.833 \frac{\Delta f_c}{\Delta f_t}\right)^2\right] \times \left(1-\mathrm{erf}\ \frac{.833\Delta f_c}{\Delta f_t}\right)$$

where σ is in cm^2, Δf_c and Δf_t are the collision and thermal linewidths in Hertz. The flow is assumed to be non turbulent. The error function arises from the combination of the thermal and collision broadening into a Voigt profile. Using the $^2S_{1/2}(F=2)$ to $^2P_{3/2}(F=3)$ line will increase this cross section by a factor of 2.8.

Absorption is detected by observing the fluorescence from the atoms relaxing back to the ground level. In the absence of quenching all the photons absorbed are reradiated into 4π steradians. It has been shown that helium does not quench sodium, so the detected signal can be straightforwardly calculated from the incident photon flux, the cross section, and the detection aperature.

It is apparent that the scattering intensity increases as the number of sodium atoms increases and as the incident photon flux increases. As the density of atoms becomes large, the fluoresced light is itself reabsorbed and subsequently reradiated. This is the self trapping or "optically thick" regime. Since the region to be observed must fluoresce and these photons must be able to reach the detector, the sodium number density must be maintained low enough to permit a photon to pass from the observation region to the window without being absorbed. In general, sodium densities in excess of 10^{10}/cc or so cause self trapping over distances of 10 cm.

Table 1 shows calculations for several helium tunnels.[6] The velocity correction is due to a slight shift in the absorption peak caused by the helium ambient pressure. The velocity sensitivity is chosen to be one tenth the sum of the full width half maximum linewidths of the calibration cell fluorescence and fluorescence from the tunnel.

TABLE I

Velocity Sensitivity and Sodium Density for Various Wind Tunnel Configurations in Helium

	Mach 8	Mach 10	Mach 16	Mach 20.7
Stagnation pressure (Atm)	20	108	20	102
Stagnation temperature (^oK)	300	256	300	297
Free Stream velocity (m/sec)	1725	1606	1753	1748
Velocity sensitivity	±3%	±7%	±0.6%	±0.6%
Velocity correction (m/sec)	+27	+67	+1.8	+3.3
Maximum sodium density (atoms/cc)	4.69×10^{10}	1.15×10^{11}	8.06×10^{9}	9.01×10^{9}
Mass flow ratio	1.7×10^{7}	2.3×10^{7}	1.3×10^{7}	2.8×10^{7}

As the laser intensity is increased into the saturation region, the collision broadened linewidth begins to increase as $\sqrt{1 + I/I_{sat}}$ and the peak absorption decreases as $1/(1 + I/I_{sat})$.[7] Thus as the intensity is pushed farther into the saturation regime, the sensitivity drops due to the linewidth increase.

A saturation intensity of .06 watts/cm^2 is calculated from the naturally broadened sodium atom cross section. The temperature and pressure broadening substantially decrease the on-line center cross section and therefore increase the saturation intensity. For each configuration a saturation intensity must be calculated, and these are given for several helium wind tunnels in row 1 of Table II. If the laser intensity is increased to the saturated intensity, the absorption cross section drops to 1/2 its unsaturated value and the linewidth increases by $\sqrt{2}$. This may be considered the maximum signal level per unit volume before sensitivity is lost. Row 2 of Table II gives the

TABLE II

Saturation Intensities and Maximum Signal From the Minimum Volume

	Mach 8	Mach 10	Mach 16	Mach 20.7
$I_{sat}(w/cm^2)$	5.1	1.23×10^{1}	8.5×10^{-1}	9.6×10^{-1}
$\sigma(f=f_o)(cm^2)$	2.1×10^{-12}	8.6×10^{-13}	1.24×10^{-11}	1.1×10^{-11}
Max Signal from 1 cc at $I=I_{sat}(w)$	6.3×10^{-4}	1.6×10^{-3}	1.1×10^{-4}	1.2×10^{-4}
Beam Area from 10 mw laser at $I = I_{sat}(cm^2)$	2.0×10^{-3}	8.1×10^{-4}	1.2×10^{-2}	1.0×10^{-2}
Smallest Sample Volume(cc)	1.0×10^{-4}	2.6×10^{-5}	1.4×10^{-3}	1.2×10^{-3}
Maximum Signal (w)	6.3×10^{-8}	4.0×10^{-8}	1.5×10^{-7}	1.4×10^{-7}

on line center value of saturated cross sections for each configuration. If the intensity is chosen at this level, the maximum detected signal from one cubic centimeter is shown in row 3, assuming the number density of sodium atoms is still confined to the optically thin region.

The output from a commercial tunable dye laser is approximately 30 mW. If 10 mW passes through the sample volume, the beam area needed to reach saturation is shown in row 4. Assuming the detection optics is arranged to look at a cylindrical volume with a length equal to the diameter, the detected signal is given in row 6, calculated from the sample volume given in row 5, and assuming f/5 collection optics. Thus the volumes shown in row 5 represent minimum observation volumes before saturation begins to dominate with a 10 mW laser; of course smaller volumes may be observed by simply throwing away some of the scattered signal. It is important to note that the detected light corresponds to a rather large photon flux and can be enhanced by a factor of 25 by going from f/5 to f/1 optics.

IV. Turbulence Measurements

From Table II it is apparent that rather small volumes may be observed without substantially reducing the collected signal. Sample regions are on the order of a millimeter or less.

If the incident laser frequency and amplitude are held constant, fluctuations in the output fluorescence intensity will be caused by temperature, pressure, density, and velocity fluctuations within the flow, assuming the sodium is well mixed. The frequency spectrum may then be read directly from an electronic spectrum analyzer connected to the detector.

Since the detected signals of 10^{-7} and 10^{-8} watts correspond to between 3×10^{10} and 3×10^{11} photons/sec, even fluctuations in the megahertz region have sufficient photon flux to eliminate statistical noise. All the minimum sample volumes shown have more than 10^{6} sodium particles, so again scattering is not masked by low particle density statistics.

V. Seeding

The choice of which atomic or molecular vapor to use as a seed is presently limited by the availability of tunable narrow linewidth lasers. By far the most successful and

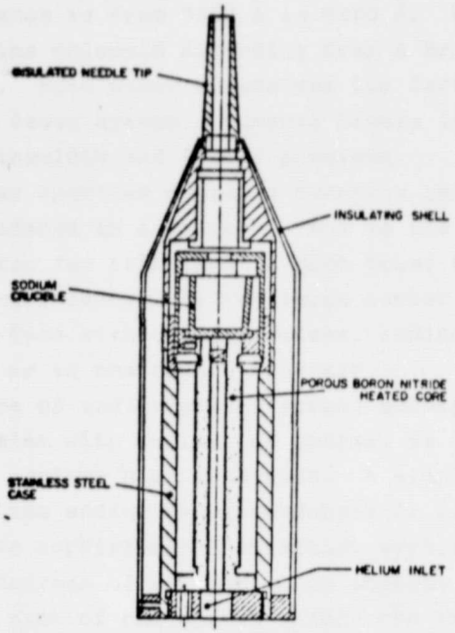

Figure 3 Sodium Injector Oven

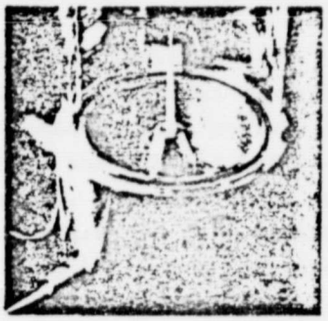

Figure 4 Sodium-Helium Jet from the Injector Oven into Atmospheric Helium Illuminated by Sodium Vapor Lamp.

Figure 5 Sodium-Helium Jet from the Injector Oven into 4 Torr Helium Illuminated by Laser on Resonance.

of helium and sodium emerging from the oven into one atmosphere of helium. This plume is transparent under standard illumination, but appears opaque when illuminated with a sodium vapor lamp. The density of sodium atoms is high enough to cause the plume to become optically thick and appear opaque.

In Figure 5 the oven is placed in a low pressure (4 torr) chamber and observed through windows. The dye laser is tuned onto resonance and strong fluorescence from the free jet is visible. Again the jet is optically thick so the laser beam cannot pass through. The multiple beams come from reflections in the dye laser and beam steering optics.

VIII. Conclusion

The possibility of using an atomic gas as a seed for doppler velocimetry seems particularly attractive now that narrow linewidth tunable dye lasers are commercially

dependable laser system is the argon laser driven cw dye laser. With the several dyes available, the operable range is from 5400 Å to 6400 Å. Within this range lie the resonant lines of the iodine molecule extending over a broad range around 5535 Å and the sodium atom at 5890 Å. Most other resonances lie farther toward the ultraviolet and cannot be reached by this laser system. Tunable lasers in the ultraviolet are pulsed and therefore have inherent linewidth and jitter problems.

The iodine molecular spectrum contains numerous rotational vibrational lines, many of which overlap when broadened in a mixture. Due to the nature of molecular resonances, the absorption cross section for each line is much lower than the atomic cross section,[8] and the absorption is further reduced by the large number of ground states over which the molecule is distributed. Even with these problems, iodine may prove desirable if sodium seeding is too complicated or if the tunnel uses air.

The atomic resonance of sodium yields strong absorption and fluorescence and unambiguous lines. The problem with sodium, of course, is its reactive nature and the high temperatures necessary to achieve high densities. A simple oven in the stagnation chamber does not work because the sodium vapor condenses or is lost in other ways before it reaches the throat. A more sophisticated injection system is required which either introduces the sodium downstream of the throat or injects it into the flow just before the throat. The resident time of the sodium within the tunnel must be short compared with the condensation time or any reaction rate with impurities. At velocities in the thousand meter per second range, the sodium must remain in atomic form for the order of a millisecond.

If the gas flow is pure helium, then the loss mechanism is dominated by the formation of dimers assuming the sodium is fully vaporized in the injection oven. Dimer formation, however, requires a three body collision, two sodium atoms and one helium or sodium atom to take away the excess energy. At the sodium densities of interest, this three body reaction occurs slowly.

Sodium particles of even submicron size may not be seen, but do provide agglomeration and condensation centers in the flow. Particle concentrations depend on the oven temperature and ambient gas pressure, but it seems certain that particles are almost always present. Duthler et al. conjecture that particles in the range of .005μ exist in the hot mixture and grow depending on the cooling rate of the mixture.[9] These particles tend to keep the vapor pressure of the sodium in equilibrium with the ambient temperature. At the low static temperatures in the observation region (generally below 10°K), equilibrium vapor pressures of sodium are negligible. Thus the equilibrium rate must be slow compared to 1 millisecond for the seeding to work.

Sodium also will react with oxygen or water impurities in the flow. Generally impurity levels must be kept lower than 50 ppm to avoid losing the sodium between the injection point and the observation region.

VI. Experimental Configuration

Figure 1 shows a sketch of the experimental configuration. The laser is mounted on a vibration isolation table to facilitate frequency stability in the wind tunnel laboratory. The laser fequency is swept through the sodium resonance, and the signal from the calibration cell is compared with that from the wind tunnel.

Currently work is concentrating on the sodium seeder oven. The newest configuration is shown in figure 3. Pure helium enters at the bottom and passes through a heating core. The crucible is heated by the helium, and the hot sodium-helium mixture passes through a double walled insulated injector needle. This oven is designed to be placed in the stagnation chamber with the needle reaching just below the throat.

VII. Flow Visualization

The usefulness of the sodium vapor as a flow visualization technique is demonstrated in figures 4 and 5. The fluorescent plume apparent in figure 4 shows a mixture

available. If seeding difficulties can be overcome, this device may be used to monitor not only the flow velocity, but turbulence frequencies as well.

With sodium vapor in the tunnel, numerous spectroscopic techniques become available to further characterize the flow. Two photon absorption, for example, may be used to eliminate thermal and velocity fluctuation broadening. If the incident power density is increased far above saturation, the fluorescence intensity depends only on the number density of sodium atoms and not on the pressure, temperature, or velocity. Specific velocity components may be selected by two step absorption using two lasers. Other nonlinear spectroscopic tricks may be used to look only at the pressure, temperature, and velocity.

IX. References

1. W. M. Fairbank, Jr., T. W. Hansch, and A. L. Schawlow, "Absolute Measurement of Very Low Sodium Vapor Densities Using Laser Resonance Fluorescence". J. Opt. Soc. Am. 65, 199-204 (Feb. 75).

2. M. Born and E. Wolf, Principles of Optics, (Pergamon Press, 1965), p. 654.

3. H. S. Berman, "Particle Fluctuations in Turbulent Flows", Laser Doppler Workshop, Purdue University, 1972, p. 530.

4. J. F. Meyers and W. V. Feller, "Wind Tunnel Measurements LDV Characteristics", Laser Doppler Workshop, Purdue University, 1972, p. 445.

5. F. Y. Wu, R. E. Grove, and S. Ezekiel, "Investigation of the Spectrum of Resonant Fluorescence Induced by a Monochromatic Field", Phys. Rev. Lett. 35, 1426 (24 Nov. 1975).

6. R. B. Miles, "Resonant Doppler Velocimeter", Phys. of Fluids 18, 751 (June 1975).

7. R. H. Pantell and H. E. Puthoff, Fundamentals of Quantum Mechanics, (John Wiley and Sons, 1969).

8. C. P. Wang, "Laser Applications to Turbulent Reactive Flows: Density Measurement by Resonant Absorption and Scattering Techniques." Aerospace Corp. Report SAMSO-TR-75-150 (to appear in Combustion Science & Technology).

9. C. J. Duthler, S. E. Johnson, and H. P. Broida, "Plasma Resonance Scattering from Small Sodium Particles Formed in a Flowing Gas Stream", Phys. Rev. Lett., 26, 1236 (May 17, 1971).

X. Acknowledgements

This research was supported by the NASA Langley Research Center under grant NSG 1070.